CRACK TURNING IN INTEGRALLY STIFFENED AIRCRAFT STRUCTURES

A Dissertation

Presented to the Faculty of the Graduate School

of Cornell University

in Partial Fulfillment of the Requirements for the Degree of

Doctor of Philosophy

by

Richard Glen Pettit

August 2000

CRACK TURNING IN INTEGRALLY STIFFENED AIRCRAFT STRUCTURES

Richard Glen Pettit, Ph.D.

Cornell University 2000

Current emphasis in the aircraft industry toward reducing manufacturing cost has created a renewed interest in integrally stiffened structures. Crack turning has been identified as an approach to improve the damage tolerance and fail-safety of this class of structures. A desired behavior is for skin cracks to turn before reaching a stiffener, instead of growing straight through. A crack in a pressurized fuselage encounters high T-stress as it nears the stiffener--a condition favorable to crack turning. Also, the tear resistance of aluminum alloys typically varies with crack orientation, a form of anisotropy that can influence the crack path.

The present work addresses these issues with a study of crack turning in two-dimensions, including the effects of both T-stress and fracture anisotropy. Both effects are shown to have relation to the process zone size, an interaction that is central to this study.

Following an introduction to the problem, the T-stress effect is studied for a slightly curved semi-infinite crack with a cohesive process zone, yielding a closed form expression for the future crack path in an infinite medium. For a given initial crack tip curvature and tensile T-stress, the crack path instability is found to increase with process zone size.

Fracture orthotropy is treated using a simple function to interpolate between the two principal fracture resistance values in two-dimensions. An

extension to three-dimensions interpolates between the six principal values of fracture resistance. Also discussed is the transition between mode I and mode II fracture in metals. For isotropic materials, there is evidence that the crack seeks out a direction of either local symmetry (pure mode I) or local asymmetry (pure mode II) growth. For orthotropic materials the favored states are not pure modal, and have mode mixity that is a function of crack orientation.

Drawing upon these principles, two crack turning prediction approaches are extended to include fracture resistance orthotropy--a second-order linear elastic method with a characteristic length parameter to incorporate T-stress/process-zone effects, and an elastic-plastic method that uses the Crack Tip Opening Displacement (CTOD) to determine the failure response. Together with a novel method for obtaining enhanced accuracy T-stress calculations, these methods are incorporated into an adaptive-mesh, finite-element fracture simulation code.

A total of 43 fracture tests using symmetrically and asymmetrically loaded double cantilever beam specimens were run to develop crack turning parameters and compare predicted and observed crack paths.

BIOGRAPHICAL SKETCH

Richard Glen Pettit was born and raised in Pasadena, California. As a young man, he attended Brigham Young University, graduating with Bachelors and Masters Degrees in Mechanical Engineering. Interrupting his studies for time, he also served as a missionary in Argentina for two years.

Mr. Pettit has nearly 15 years experience in the aerospace industry, working for McDonnell Douglas and Boeing in research related to the design and analysis of advanced metallic structures. Before coming to Cornell, he was sent to NASA for two years to study the damage tolerance of integral fuselage structure, an effort that eventually led him to the present undertaking.

Mr. Pettit and his wife, Lori, are the parents of five children.

to Lori, Sarah, Laura, Jacob, Stephen, and Elizabeth . . .

ACKNOWLEDGMENTS

I would like to sincerely thank my advisor, Professor Anthony R. Ingraffea, for his support, enthusiasm, insight, and candid review of this work during its various stages of completion. Thanks also to Professors Herbert Hui, Alan Zehnder, and Teoman Pekoz who served on my committee.

Numerous others in the Cornell Fracture Group and Cornell Community also provided much needed help along the way. In particular, David Chen, Bruce Carter, and Paul Wawrzyneck, mentored me through many of the technical and programming aspects of the present work. Also, Tim Bond, supervisor of the Winter Laboratory, played a vital role in the set-up, calibration and instrumentation work related to the mechanical test program.

This work was supported by funding from NASA Langley Research Center, indirectly through the Boeing Company as part of the Integral Airframe Structures (IAS) Program, and also through contracts NAG-1-2013 and NAG-1-2268. Sincere thanks to Jim Newman, Phil Bogert, and Marcia Domack at NASA Langley Research Center, and Keith Wilkins, Jian-Juei Wang, Chin Toh, John Munroe, and Trent Logan at the Boeing Company who provided valuable input and support.

I am deeply thankful for the blessing that has been given me to return to school and complete this program of study and research. A community of dear friends has surrounded myself and my family, providing thoughtful words of encouragement, and acts of service small and great. Special thanks to my wife Lori, and each of the children for their patience and support during this endeavor, and to God for His sustaining influence.

TABLE OF CONTENTS

LIST OF TABLES

LIST OF FIGURES

CHAPTER 1.0

BACKGROUND

1.1 Manufacturing Trends

About a third of the direct operating cost of a commercial aircraft is associated with the manufacturing cost, which is probably the most critical competitive parameter with regard to market share [1]. In the past, the airframe design process in the U.S. has been focused on riveted aluminum skin and stringer construction, a structural concept dating from the 1940's. Design and manufacturing processes based on this concept have become highly mature, and therefore difficult to reduce significantly in cost without substantial deviations from conventional practice. Nevertheless, metallic structure is also well proven, and the industry will likely retain extensive metallic production capability for the foreseeable future.

The continual need for low acquisition cost and the emergence of high speed machining and other technologies has brought about a renewed interest in large, integral, metallic structures for aircraft applications. An example of an integral fuselage concept developed under the NASA Integral Airframe Structures (IAS) Program [1] is shown in Figure 1.1, consisting of only two detail parts—skin and frames. The conventional baseline structure is shown in Figure 1.2, and requires the separate fabrication and assembly of skin, stringers, frames, stringer clips, and tear straps. Integrating multiple parts into larger pieces of structure offers inherent savings and flexibility, which is made increasingly more attractive as the labor required to machine the parts is reduced by faster machines. Nevertheless, application of low-cost integral structures has been inhibited in many applications by a perceived lack of damage tolerance.

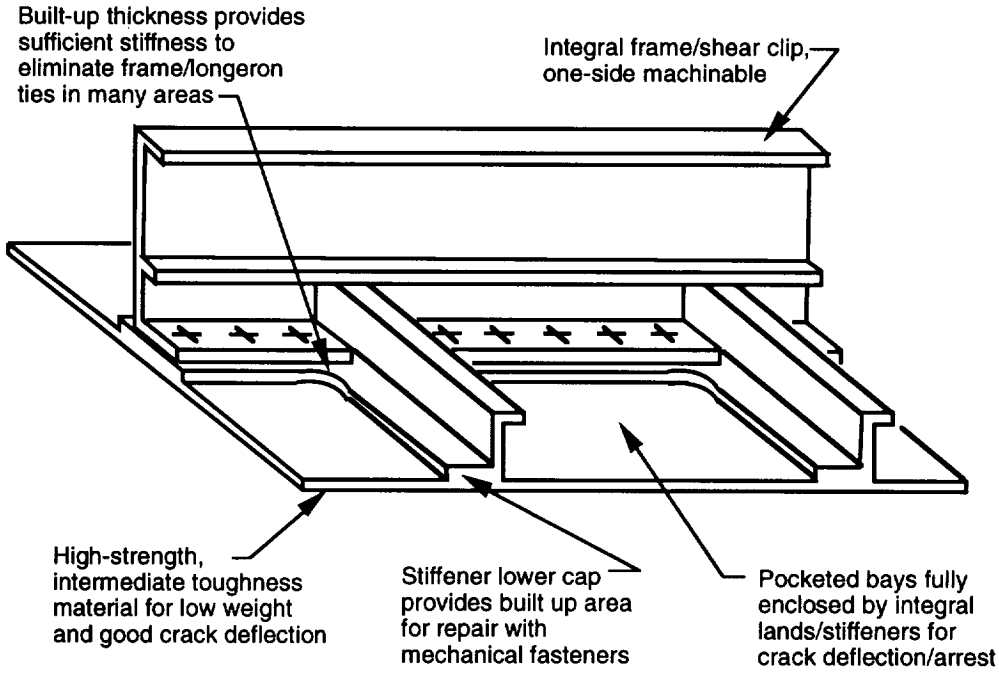

Figure 1.1 IAS Integral Fuselage Panel Concept [1]

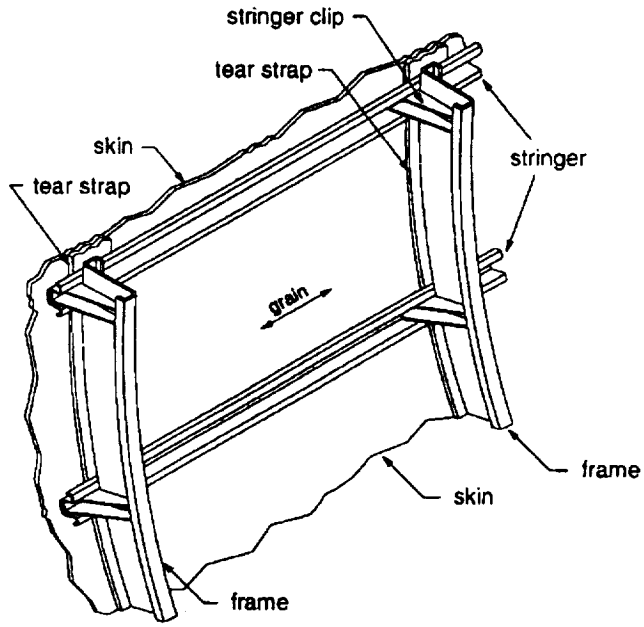

Figure 1.2 IAS Baseline Fuselage Panel Concept [1]

1.2 Damage Tolerance and Integral Structures

Properly designed integral structures with attention to fillet radii and other life-limiting features, can potentially achieve very long fatigue lives. Nevertheless, damage tolerance has long been a concern for integral structures [2], which have been particularly shunned in critical areas like the fuselage. This concern was largely based on NASA fatigue crack growth tests [3,4] which showed that a skin crack slows more when crossing a mechanically fastened stiffener than an integral stiffener. Multi-bay panels were seen to crack through considerably faster in integral construction, compared to multi-piece designs. The NASA data would infer that catastrophic failure of integral structure would likely develop more quickly than in built up structure--that is, if the cracks grow straight through the stiffeners as they did in the NASA tests.

1.3 Crack Turning as a Mechanism to Enhance Damage Tolerance and Fail Safety

On the contrary, crack turning has long been recognized as a potentially important crack arrest mechanism for pressurized aircraft fuselage structure, and for longitudinal cracks can result in the turning and flapping behavior shown in Figure 1.3 as reported by Maclin [5]. This behavior contains the damage, vents the pressure in a controlled manner, and results in obvious damage which can be subsequently repaired. Flapping was observed to occur reliably enough during tests of thin skinned, relatively narrow-body fuselages that it was utilized as a fail-safe criterion on the 707, 727, and 737 fuselages for regions excluding the joint areas. Similar phenomena have been observed in unstiffened cylinders by Swift [6, 7], who also reported turning and cracking in an experimental fuselage with adhesively bonded stiffeners [2], Kosai et al [8], who studied crack turning in stiffened cylinders, and Pettit [9], who observed crack turning and arrest in integrally stiffened fuselage structure with transverse cracks.

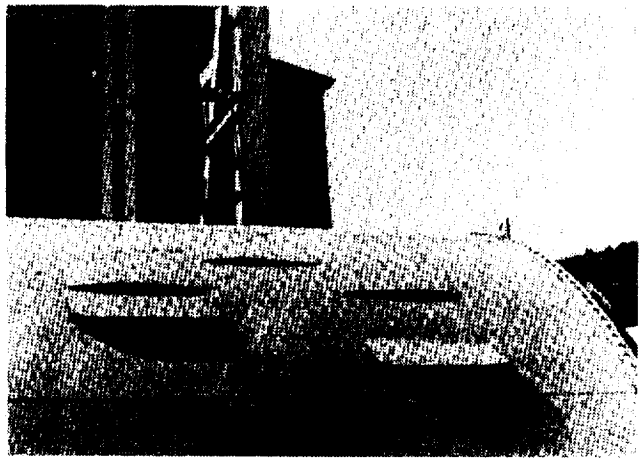

Figure 1.3 Crack Turning and Flapping in a Boeing 707 Test Panel [5]

These behaviors were observed in tests, but have been troublesome to model adequately. Turning and flapping was observed in narrow-body aircraft (skin thicknesses down to 0.04 inches or so), but not wide-body aircraft like the 747 aircraft. Also, it was found that aging aircraft develop multi-site damage, which can potentially alter the crack turning and flapping performance [10]. The need for an accurate crack trajectory modeling capability was evident.

In the last decade, a sequence of authors have studied the fuselage flapping phenomenon, including Kosai et al [11], Miller et al [12], Potyondy et al [13], Knops [14], and Chen [15]. Beginning with Potyondy, an adaptive mesh finite element code was used similar to that proposed by Wawrzynek and Ingraffea [16] but extended to three-dimensional shell problems, which allows the trajectory of the crack to develop naturally in accordance with a user-selected crack turning theory. Potyondy used the first order maximum tangential stress theory of Erdogan and Sih [17] to predict the crack trajectory of an adhesively bonded narrow-body fuselage panel tested at Boeing. He was able to approximate the actual behavior fairly well in the gently curving region

until the crack grew near to the tear strap, but was unable to predict the sharp turning radius observed as the crack grew parallel to the tear strap, resulting in flapping.

The work of Kosai, Knops and others gave substantial evidence that to more accurately model crack turning behavior in pressurized cylinders, a second-order theory was needed such as that described by Finnie and Saith [18]. (Here, second-order refers to the inclusion of the second term, or T-stress, in the asymptotic stress field in the vicinity of the crack tip, which is neglected in the Erdogan and Sih theory.) Knops was the first to implement this theory in an adaptive mesh finite element code[1], and showed that for simulations of various specimens with tensile T-stress, the second-order theory predicted that the crack would turn more sharply than the first order theory, improving correlation with test results. Yet despite the improved theory, his results for the Boeing narrow body panel test compared very closely with those of Potyondy. Like Potyondy, he was unable to simulate the small turning radius of the crack in the vicinity of the tear strap, and the resulting flapping phenomenon.

Pettit [9] observed a similar rapid turning phenomenon when testing integrally stiffened fuselage test panels with a symmetric, two-bay, circumferential crack. The panels were loaded with pressure and axial tension. Crack turning was attributed to the T-stress, which was shown to be significant as the crack passed through a narrow region (on the order of a ten skin thicknesses) immediately adjacent to the edge of an arresting stiffener. The analyses also indicated that the presence of the T-stress was largely driven by geometrically nonlinear behavior (pressure pillowing) which would not occur if the panels were unpressurized. In the pressurized panel, which turned (but did not flap) at both crack tips, a 23 percent increase in residual strength was observed.

[1] Adaptive mesh, in this context, refers to a code that remeshes the area around the crack tip as it grows, allowing the crack to follow a natural path.

Nevertheless, some spurious turning results were also observed that indicated a need to take into account fracture toughness anisotropy.

Pettit et al [1] later combined the 2nd order turning criterion of Finnie and Saith with the orthotropic theory of Buczek and Herakovich [19] to formulate a second-order crack turning criterion with fracture toughness orthotropy that will be described in more detail in Chapter 5. This theory was implemented by Chen [15] into a 3D shell adaptive mesh environment similar to that of Potyondy, and subsequently used to model the same Boeing test panel studied by previous authors. His results, comparing first and second-order isotropic theories, and second order theory for both isotropic and orthotropic cases are presented in Figure 1.4. Note that in the second-order isotropic run, he was for the first time able to negotiate the fairly tight turn observed in the test data as the crack approaches the tear strap. In the second-order orthotropic case, he matched the first part of the trajectory considerably better, but was still unable to simulate crack turning at the tear strap, because the crack was growing in the preferred direction of the 2024-T3 fuselage skin, and the effect of the T-stress was insufficient to turn the crack. Despite this shortcoming, the ability to simulate crack deflection by a tear strap for the isotropic case was a significant first.

While there were various differences in the finite element implementation, it appears that the main difference in Chen's isotropic analysis which enabled him to show turning and flapping where Knops did not was the characteristic length, r_c, chosen for use in the analysis. Chen used a value of 0.09 inches which was found during finite element simulations to correlate fairly well with crack paths observed in double cantilever beam specimens reported by Pettit [9], whereas Knops used a value of 0.05 inches[2].

[2] Actually, Knops is not explicit with regard to the value of r_c utilized for 2024-T3. However, he did quote a value for PMMA plastic plate of 1.3 mm (0.05 inches) based on the results of Ramulu and

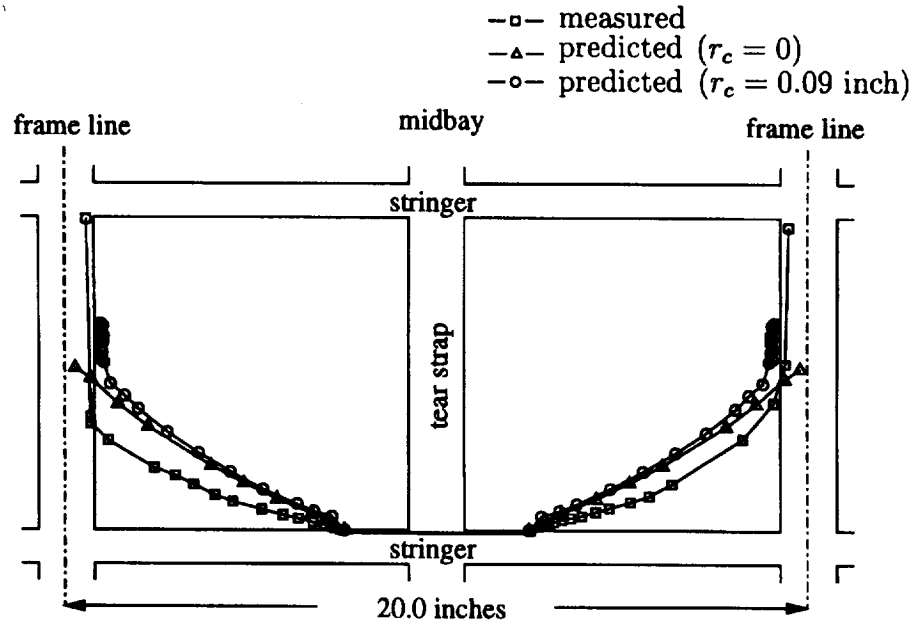

a.) 1st order (rc=0) and 2nd order (rc=0.9) isotropic fracture simulations

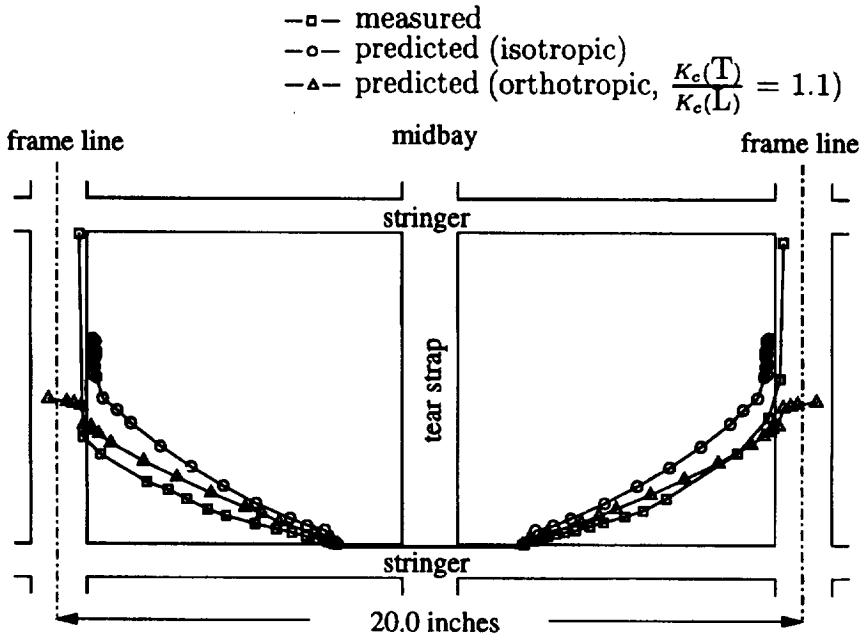

b) 2nd order fracture simulations with and without toughness orthotropy

Figure 1.4. Comparison of Narrow Body Fuselage Panel Test Data with Fracture Simulations, After Chen [15]

Kobayashi [20] . Kosai, Kobayashi and Ramulu [8] later gave the same value for 2024 aluminum, and it is appears that Knops used this value for both materials.

Attempts in the literature to evaluate r_c often give contradictory results, as will be discussed at length in Chapter 5. While presumably associated with some process zone dimension, the phenomenological basis by which the process zone affects the crack path has not been well understood. Nevertheless, comparison of fatigue and static tearing crack paths in aluminum under a high T-stress environment have shown a pronounced difference in crack path [9] (the statically torn specimens turning more sharply), confirming at least the notion that increased process zone size should promote crack turning.

1.4 Program Focus and Scope

The present study will focus on the crack turning problem in the context of a crack growing in a large integral metallic panel, with specific focus on factors that decrease the radius of turning. The basic phenomenology of crack turning will be explored, with the primary hypothesis that process zone effects result in the acceleration of crack turning in the presence of T-stress. It is hoped that the present study will result in greater understanding of that role, as well as provide improved methods for more accurate simulation of crack turning. In a broader sense, the following factors are believed to be potentially important with respect to crack turning behavior.

1. Mode mixity (load asymmetry)
2. T-stress
3. The size and nature of the inelastic fracture process zone at the crack tip
4. Fracture toughness anisotropy
5. Transition between competing fracture modes

An important theme that will be underlying this work is the observation that tensile T-stress often arises as a crack nears an integral stiffener, particularly in a stiffened skin arrangement loaded under lateral pressure, such as an aircraft fuselage. As will be described in Chapter 2, tensile T-stresses cause the crack to become directionally unstable[21], potentially resulting in the desired turning behavior. The more T-stress, the sharper the crack is likely to turn. From a damage tolerance and residual strength perspective, it is desirable for the crack to turn until it is oriented parallel, or nearly parallel to the stiffener. However, the region of the crack path over which the T-stresses arise is often quite small [9], perhaps on the order of ten skin thicknesses or less. Thus it may be necessary for the crack to turn at a fairly small radius if it is to miss the stiffener, or impinge upon it at a sufficiently grazing angle to effectively blunt the damage. It has been observed that the process zone size can have a significant effect on the crack path [9], with larger process zones in a high T-stress environment turning the crack far more sharply than commonly used linear elastic theories predict. In view of the need for the crack to turn with a small radius, proper understanding of this effect is considered to be critical.

Engineering materials often exhibit fracture resistance anisotropy, which has been shown to strongly affect the crack path [22]. An attempt will be made to extend the most promising theories to include fracture resistance orthotropy, a special (and very common) case where the toughness function exhibits symmetry in an orthonormal basis. This will be discussed in two and three dimensions in Chapter 4.

While cracks most often propagate in-plane in a nearly pure crack opening mode (mode I), it is possible for a crack in a ductile material to grow in a crack sliding mode (mode II) when the crack is heavily shear loaded. While transition between the two modes is rarely observed in practice, it has been observed in laboratory

experiments, may provide an alternative method to achieve crack turning, and is given limited attention in Chapters 4 and 5.

Drawing upon the foregoing, a practical, second-order linear elastic theory for the prediction of crack trajectory, including T-stress and fracture toughness orthotropy, will be developed in Chapter 5, including methods developed concurrently by the author under the NASA IAS program. Also included is a modification of an elastic-plastic crack trajectory method to include fracture resistance orthotropy.

Chapter 6 describes the implementation of elastic and elastic-plastic crack turning theories into the FRANC2D/L fracture simulation code. A method is also presented to enhance the accuracy of the T-stress calculation utilized by the elastic theories. Simulations are compared to test data in Chapter 7, including selected data from the NASA IAS program.

Chapter 8 will provide a concluding discussion, and recommendations for future work.

CHAPTER 2.0

ISOTROPIC CRACK TURNING THEORY IN TWO-DIMENSIONS

2.1 Linear Elastic Crack Kinking Due to Mixed-Mode Loading Without T-Stress

The mixed-mode expressions for the two-dimensional elastic stress field around a crack tip (Figure 2.1) are given to the first two terms [23] as

$$\sigma_r = \frac{1}{\sqrt{2\pi r}}\cos\frac{\theta}{2}\left[K_I\left(1+\sin^2\frac{\theta}{2}\right)+\frac{3}{2}K_{II}\sin\theta-2K_{II}\tan\frac{\theta}{2}\right]+\frac{T}{2}(1+\cos 2\theta) \tag{2.1}$$

$$\sigma_\theta = \frac{1}{\sqrt{2\pi r}}\cos\frac{\theta}{2}\left[K_I\cos^2\frac{\theta}{2}-\frac{3}{2}K_{II}\sin\theta\right]+\frac{T}{2}(1-\cos 2\theta) \tag{2.2}$$

$$\sigma_{r\theta} = \frac{1}{2\sqrt{2\pi r}}\cos\frac{\theta}{2}\left[K_I\sin\theta+K_{II}(3\cos\theta-1)\right]-\frac{T}{2}\sin 2\theta \tag{2.3}$$

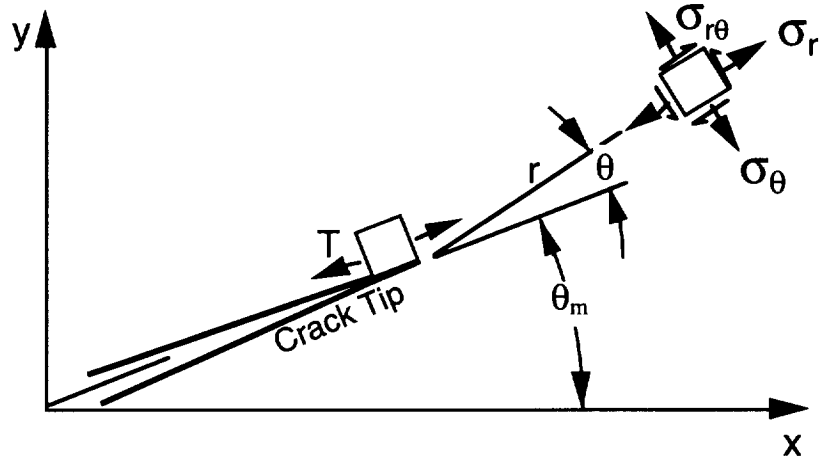

Figure 2.1 Crack Tip Coordinate and Stress Notation

where K_I and K_{II} are the stress intensity factors associated with mode I and mode II loading as illustrated in Figure 2.2. The T-stress is the constant component of the stress field, and oriented parallel to the crack tip as shown in Figure 2.1.

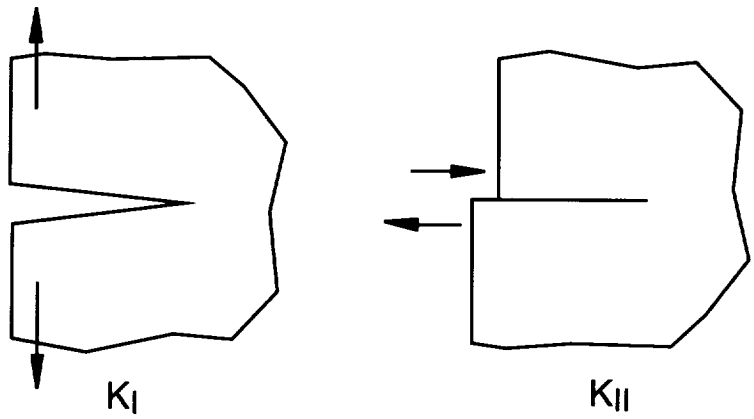

Figure 2.2 Illustration of Crack Tip Loading Modes (Shown with Positive Sense)

Most of the studies related to crack turning found in the literature focus on determining the kink angle that occurs when a crack is loaded with in-plane asymmetry. The leading stress terms are singular in r, thus dominating crack tip stresses in the elastic solution. Thus, with the tacit assumption that the mechanism by which the crack is directed occurs at or very close to the physical crack tip, the second and higher order terms are often neglected, even though they may be significant at some distance from the crack tip. In these first-order turning theories, the asymmetry is characterized exclusively in terms of the mode mixity, K_{II}/K_I. For the time being, we will postpone our discussion of second-order kinking theories, which assume a process zone size large enough that T affects the kink angle.

The classical first-order maximum tangential stress ($\sigma_{\theta\theta}$ max) theory, proposed by Erdogan and Sih [17] for isotropic materials, asserts that the crack will grow toward the location of the maximum tangential tensile stress. By differentiating the first term in Equation (2.2) with respect to theta and setting it to zero (equivalent to setting $\sigma_{r\theta}=0$) they obtained (shown somewhat rearranged)

$$\frac{K_{II}}{K_I} = \frac{-\sin\Delta\theta_c}{(3\cos\Delta\theta_c - 1)} \tag{2.4}$$

or [24]

$$\Delta\theta_c = 2\tan^{-1}\left(\frac{1-\sqrt{1+8(K_{II}/K_I)^2}}{4(K_{II}/K_I)}\right) \tag{2.5}$$

where $\Delta\theta_c$ is the kink angle. This expression predicts straight crack growth unless $K_{II}\neq 0$, as in asymmetric loading or in the case of a crack with a perturbed trajectory.

Equation (2.5) is plotted in Figure 2.3, along with two other well-known first order linear elastic theories, the maximum energy release rate ($G(\theta)_{max}$) theory proposed by Hussain *et al.* [25], and the minimum strain energy density theory (S(θ)min) proposed by Sih [26]. For convenience, the data is plotted using the mode mixity parameter

$$M^e = \frac{2}{\pi}\tan^{-1}\left(\frac{K_I}{K_{II}}\right) \tag{2.6}$$

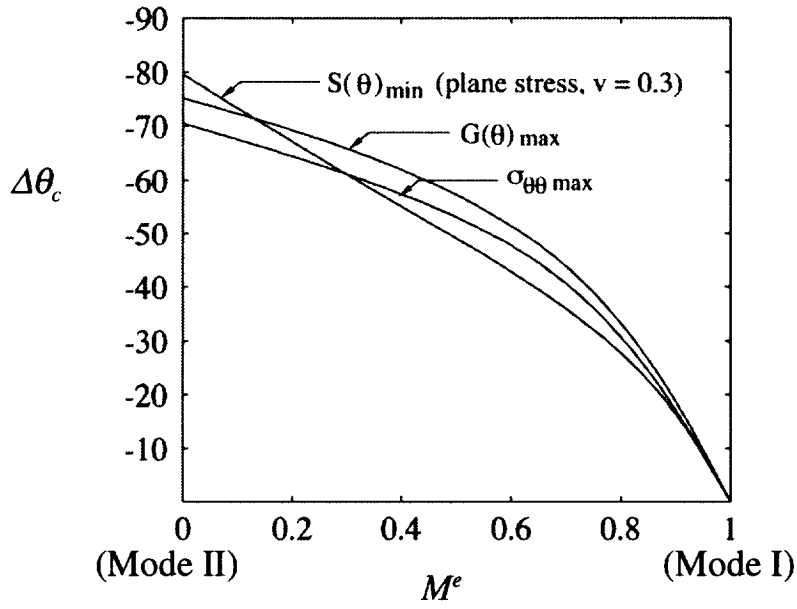

Figure 2.3 Comparison of First-Order Linear Elastic Crack Kinking Theories

By assuming other quantities, such as maximum principle stress, maximum hoop strain and/or void growth, numerous first-order kinking criteria have been proposed [e.g. 27, 28, 29].

For the most part, all these theories predict quite similar kink angles, particularly as $K_{II} << K_I$. Nevertheless, the data of many authors have been correlated with the various theories [28, 29] in an attempt to determine the most accurate. Noteworthy among the empirical studies in this respect is the very meticulous work of Maccagno and Knott [30, 31], who, unlike most authors, chose a specimen geometry with near zero T-stress in order to minimize higher-order effects. They also designed their specimens of sufficient thickness to ensure a plain strain state of stress near the crack tip. Their work included testing of plexiglass at room temperature, and various grades of steel at low temperature (–196°C, resulting in transgranular cleavage fracture), and showed that even for moderate amounts of ductility, the initial kink angle was well predicted by the maximum tangential stress theory of Erdogan and Sih. This was true even when the ductility was sufficiently high that they had to resort to an elastic-plastic failure criterion to correlate the fracture initiation loads. However, they cautioned that while this was true of the transgranular cleavage failure mode, it might not be true of other failure mechanisms (more on this momentarily).

Pook [32], and Liu [33] provided crack kinking data for aluminum alloys that also correlates well with the maximum tangential stress theory, at least in the predominately mode I regime.

2.2 Elastic-Plastic Crack Kinking

Huchinson [34] studied the stress field at the tip of a crack in a strain hardening material which follows the Ramberg Osgood constitutive law

$$\frac{\varepsilon}{\varepsilon_o} = \frac{\sigma}{\sigma_o} + \alpha\left(\frac{\sigma}{\sigma_o}\right)^n \tag{2.7}$$

where σ and ε are the stress and strain, and σ_o and ε_o are the corresponding yield values. A theoretical description of the asymptotic stress field was developed of the form

$$\sigma_{ij} = \frac{K_m}{r^{1/(n+1)}} f_{ij}(\theta) \tag{2.8}$$

An equivalent theoretical development was concurrently published by Rice and Rosengren [35], thus (2.8) is has become known as the HRR stress field. The HRR theory assumes proportional loading, and thus is not valid for a propagating crack, but provides insight into the crack behavior at initiation.

Shih [36] extended the HRR theory to include mixed mode loading under plane strain conditions, and applied it to develop a maximum circumferential stress theory for elastic-plastic crack initiation. Note that the HRR fields assumes that T and higher-order terms are zero in the far-field elastic stress field, and represents only the leading term in the elastic-plastic stress field. Thus, though it includes a process zone, the elastic-plastic theory of Shih is still a first order theory. The results of his work are reproduced in Figure 2.4, and revert to the theory of Erdogan and Sih for n=1. For higher values of n, the kink angle predicted is still not dramatically different from the linear elastic theory, thus the observation that the linear elastic theory may adequately predict the kink angle even in the presence of significant plasticity is not surprising.

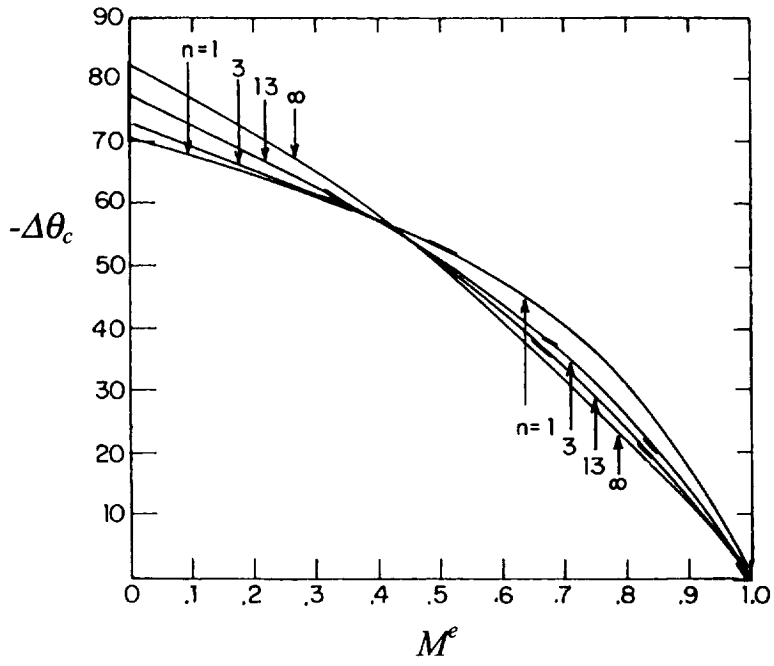

Figure 2.4 Elastic-Plastic Crack Kinking Theory, After [36]

As mentioned earlier, there remains the issue of the failure mode. Aware that the tearing failure mode of HY 130 steel at room temperature would involve void growth and decohesion along planes of maximum shear, as opposed to the transgranular cleavage failure mode observed in earlier work, Maccagno and Knott proceeded to run otherwise identical room temperature tests [31]. While large-scale plasticity was found to exist in the specimens, the failure mode clearly followed planes of maximum shear, rather than maximum tension. For mode I loading, this resulted in a zigzag pattern directed macroscopically along the original crack plane. However, increased proportions of mode II loading resulted eventually resulted in straight crack growth along the plane of maximum shear. Subsequent tests by other investigators [37, 38, 39, 40] have shown that various aluminum alloys also fail macroscopically along the direction of local symmetry when loaded predominately in mode I, and the direction of local asymmetry when loaded mostly in mode II, with transition between

the modes occurring at some intermediate mode-mixity. This modal transition behavior will be discussed in greater detail in Chapter 4. Nevertheless, mode II dominant crack propagation is rarely if ever observed in aircraft structures (and probably most structures), thus attention will be given primarily to mode I dominant crack propagation.

2.3 Linear Elastic Crack Path Instability in a Positive T-stress Environment

Notwithstanding the foregoing discussion of crack kinking theories, the crack turning problems encountered in many real structural applications are not really crack kinking problems. In an average macroscopic sense, cracks typically initiate normal to the maximum tensile stress, and propagate in a rather smoothly curving fashion as the crack negotiates its way among the structural features of the part. Since the first-order isotropic theories predict crack kinking for non-zero K_{II}, it would appear that the only way for a crack to propagate smoothly is for the crack to follow a path along which $K_{II}=0$. Since all the first-order isotropic theories agree exactly for this condition, the crack path is apparently independent of any first-order theory.

While it is true that at a sufficiently small scale the crack path is not smooth due to material inhomogeneities, microscopic failure phenomena, or fluctuations about a mean loading orientation, these anomalies are may be considered random in nature, and may be viewed as perturbations[3] to the crack path. Nevertheless, short of characterizing these perturbations and including them explicitly in a probabilistic analysis, it would appear that the best deterministic estimate of the crack path in an average sense would be the path for which $K_{II}=0$.

---

[3] It is duly noted that in the late stages of catastrophic failure of an assemblage, failure of secondary members, crack branching, multiple crack coalescence, and other major load or path disruptions may occur, and are beyond the scope of the present discussion.

The above conclusion seems quite intuitive, and was suggested at least as early as Cotterell and Rice [21] , who further proved that for crack propagating in pure mode I, the strain energy release rate is locally maximized for a straight crack extension. They started with an approximate kinked crack solution for infinitesimal kinks,

$$\begin{aligned} K_I &= C_{11}k_I + C_{12}k_{II} \\ K_{II} &= C_{21}k_I + C_{22}k_{II} \end{aligned} \tag{2.9}$$

where k_I and k_{II} are the stress intensities of the lead (unkinked) crack, K_I and K_{II} are the resulting stress intensities at the kink tip, and

$$\begin{aligned} C_{11} &= \tfrac{1}{4}\left[3\cos(\Delta\theta/2) + \cos(3\Delta\theta/2)\right] \\ C_{12} &= -\tfrac{3}{4}\left[\sin(\Delta\theta/2) + \sin(3\Delta\theta/2)\right] \\ C_{21} &= \tfrac{1}{4}\left[\sin(\Delta\theta/2) + \sin(3\Delta\theta/2)\right] \\ C_{22} &= \tfrac{1}{4}\left[\cos(\Delta\theta/2) + 3\cos(3\Delta\theta/2)\right] \end{aligned} \tag{2.10}$$

which was shown accurate to the second order in $\Delta\theta$. For small angles

$$\begin{aligned} K_I &= C_{11}k_I = k_I\left[1 - \frac{3}{8}(\Delta\theta^2)\right] + O(\Delta\theta^3) \\ K_{II} &= C_{21}k_I = -\frac{\Delta\theta}{2}k_I + O(\Delta\theta^3) \end{aligned} \tag{2.11}$$

The strain energy release rate is (plane stress)

$$\begin{aligned} G &= \frac{1}{E}\left(K_I^2 + K_{II}^2\right) \\ &= \frac{1}{E}\left(1 - \frac{\Delta\theta^2}{2}\right)K_I^2 + O(\Delta\theta^3) \end{aligned} \tag{2.12}$$

which is clearly maximized for $\Delta\theta = 0$.

Cotterell and Rice then considered the future path of an (initially straight) crack propagating in pure mode I as shown in Figure 2.5, subject to a small perturbation in k_{II} as the crack reaches the origin of the local coordinate system

indicated. They retained the T-stress term in their calculations to observe its influence on the crack path.

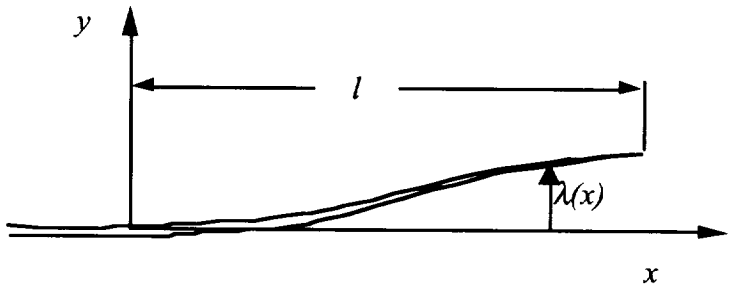

Figure 2.5 Schematic of a Growing Crack

Based on a formulation of their own derivation which integrates the tractions due to the lead crack stress field over the developing crack path to obtain the stress intensity factors at the crack tip, they obtained for K_{II},

$$K_{II} = k_{II} + \frac{1}{2}\lambda'(l)k_I - \sqrt{\frac{2}{\pi}}\,T\int_0^l \frac{\lambda'(l)}{\sqrt{l-x}}\,dx \tag{2.13}$$

accurate to the first order in λ'. Cotterell and Rice gave evidence that this solution was accurate to within about five percent up until the slope of the extending crack crack exceeds 15 degrees. Setting $K_{II}=0$ at the developing crack tip,

$$\theta_o = \lambda'(l) - \frac{\beta}{\sqrt{\pi}}\int_0^l\left[\frac{\lambda'(l)}{\sqrt{l-x}}\right]dx \tag{2.14}$$

where

$$\theta_o = -2\frac{k_{II}}{k_I}$$
$$\beta = 2\sqrt{2}\frac{T}{k_I} \tag{2.15}$$

Note that the expression for the small perturbation angle, θ_o, has been defined in such a way as to be in agreement with the Equation (2.5) as K_{II} becomes small

compared to K_I (see also (2.11)). Solving (2.14) for $\lambda(x)$ using the method of Laplace Transforms, Cotterell and Rice obtained[4]

$$\lambda(x) = \frac{\theta_o}{\beta^2}\left[\exp\left(\beta^2 x\right) erfc\left(-\beta\sqrt{x}\right) - 1 - 2\beta\sqrt{\frac{x}{\pi}}\right] \tag{2.16}$$

which is plotted in normalized format in Figure 2.6.

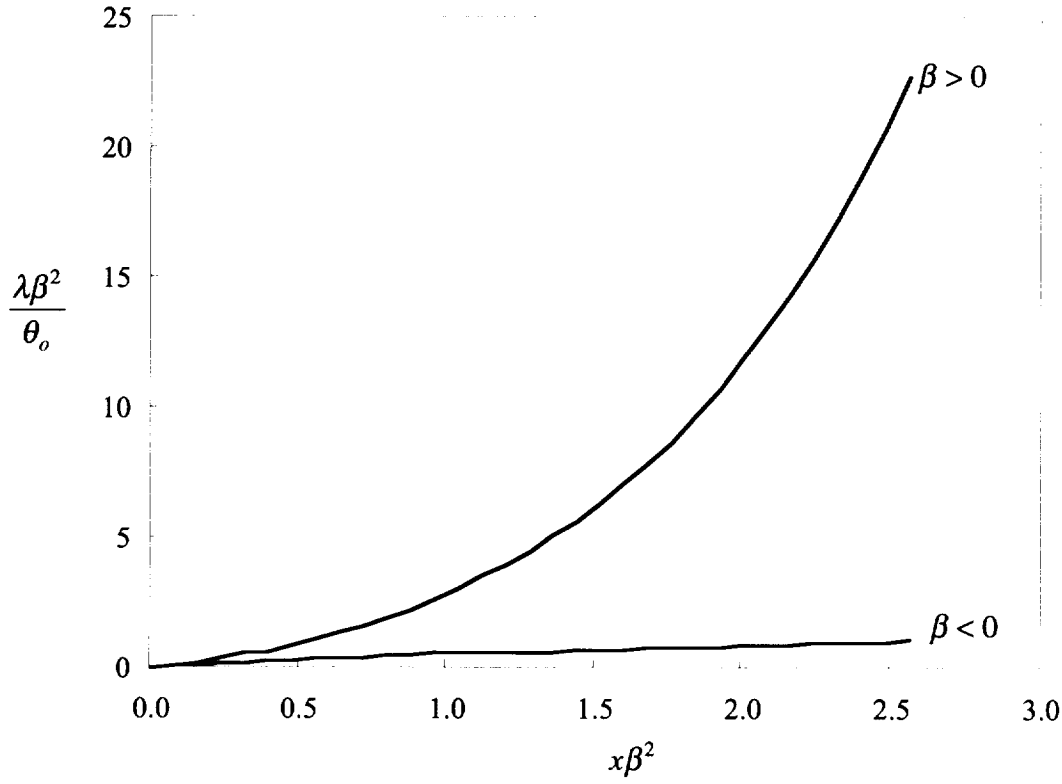

Figure 2.6 Normalized Plot of the Perturbed Crack Path of Cotterell and Rice

The primary conclusion drawn is that if T>0, the crack path diverges, if T<0, the crack path turns back toward a relatively straight trajectory after the initial perturbation. These behaviors are in qualitative agreement with test data [41]. The predicted rate of divergence is proportional to the perturbation and the square of the T-stress. A similar analysis was performed by Sumi [42], who included one additional

[4] Equation (2.13) differs slightly from the published result due to a typographical error.

higher order term in the stress field expansion, and was able to obtain additional information about whether the crack was approaching a region of greater stability or instability.

Based on the foregoing, we observe that given a set of initial conditions k_I, k_{II} (small compared to k_I), T, and higher order terms should one desire to include them, there is only one path for which $K_{II}=0$. Yet, crack paths observed in nominally self-similar specimens with tensile (positive) T-stress indicate a process zone size effect. To illustrate this, crack path data [9] from 2024-T3 double cantilever beam (DCB) specimens is re-plotted in Figure 2.7, shown slightly translated so that the initial notch tips are superimposed. The value of β was about 0.37 for both specimens.

Neglecting the roughness of the crack paths observed in measurements taken from both faces, both paths initially grow straight ahead, and then turn in a relatively smooth fashion. However, the stable tearing crack path, which would be associated with the larger process zone condition due to the higher loading, turns much more sharply than the fatigue cracked specimen. Both specimens were of the same (T-L) grain orientation, and presumably had similar (though unknown) perturbations. The paths of only two specimens are shown, but qualitatively similar behavior was noted in comparable specimens from this and other aluminum materials [1].

The Cotterell and Rice solution is for an infinite plate, and would therefore not be valid for a large enough crack extensions within the DCB specimen to render useful any quantitative comparison of the predicted and observed paths. Nevertheless, postulating that the tiny process zone associated with fatigue crack growth might result in something approximating a $K_{II}=0$ path (neglecting fracture orthotropy for the time being), we must now ask on what phenomenological basis the more sharply turning crack could be anticipated due to a larger process zone.

compared to K_I (see also (2.11)). Solving (2.14) for $\lambda(x)$ using the method of Laplace Transforms, Cotterell and Rice obtained[4]

$$\lambda(x) = \frac{\theta_o}{\beta^2}\left[\exp(\beta^2 x)erfc(-\beta\sqrt{x}) - 1 - 2\beta\sqrt{\frac{x}{\pi}}\right] \tag{2.16}$$

which is plotted in normalized format in Figure 2.6.

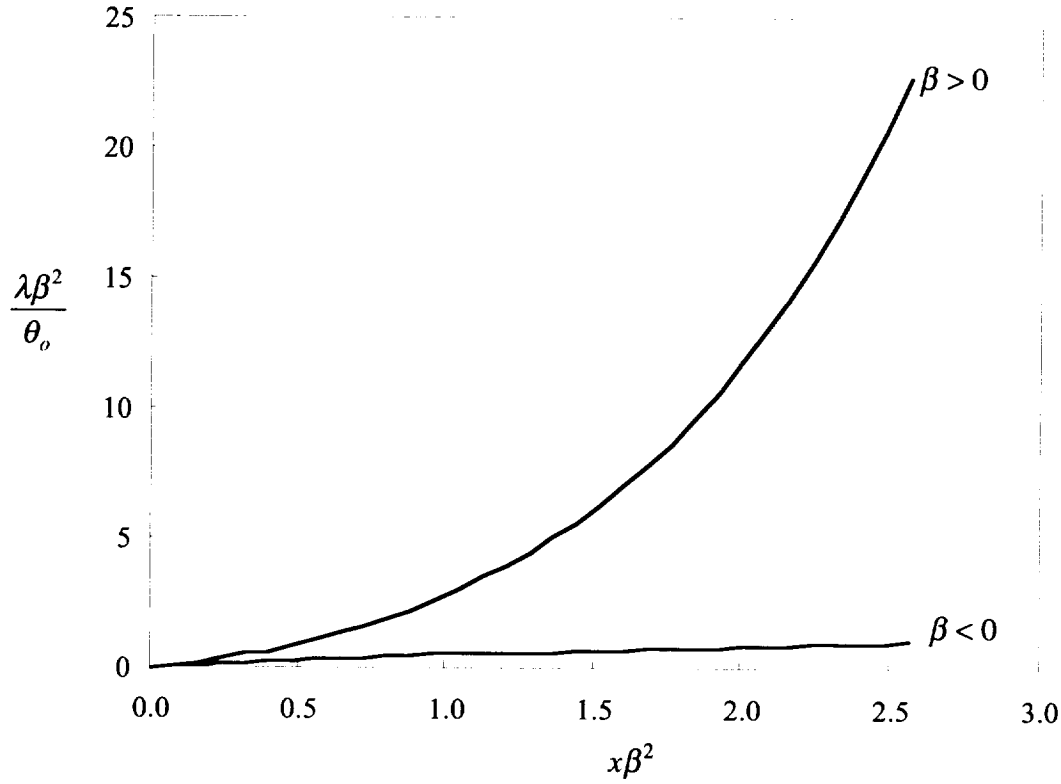

Figure 2.6 Normalized Plot of the Perturbed Crack Path of Cotterell and Rice

The primary conclusion drawn is that if T>0, the crack path diverges, if T<0, the crack path turns back toward a relatively straight trajectory after the initial perturbation. These behaviors are in qualitative agreement with test data [41]. The predicted rate of divergence is proportional to the perturbation and the square of the T-stress. A similar analysis was performed by Sumi [42], who included one additional

[4] Equation (2.13) differs slightly from the published result due to a typographical error.

higher order term in the stress field expansion, and was able to obtain additional information about whether the crack was approaching a region of greater stability or instability.

Based on the foregoing, we observe that given a set of initial conditions k_I, k_{II} (small compared to k_I), T, and higher order terms should one desire to include them, there is only one path for which $K_{II}=0$. Yet, crack paths observed in nominally self-similar specimens with tensile (positive) T-stress indicate a process zone size effect. To illustrate this, crack path data [9] from 2024-T3 double cantilever beam (DCB) specimens is re-plotted in Figure 2.7, shown slightly translated so that the initial notch tips are superimposed. The value of β was about 0.37 for both specimens.

Neglecting the roughness of the crack paths observed in measurements taken from both faces, both paths initially grow straight ahead, and then turn in a relatively smooth fashion. However, the stable tearing crack path, which would be associated with the larger process zone condition due to the higher loading, turns much more sharply than the fatigue cracked specimen. Both specimens were of the same (T-L) grain orientation, and presumably had similar (though unknown) perturbations. The paths of only two specimens are shown, but qualitatively similar behavior was noted in comparable specimens from this and other aluminum materials [1].

The Cotterell and Rice solution is for an infinite plate, and would therefore not be valid for a large enough crack extensions within the DCB specimen to render useful any quantitative comparison of the predicted and observed paths. Nevertheless, postulating that the tiny process zone associated with fatigue crack growth might result in something approximating a $K_{II}=0$ path (neglecting fracture orthotropy for the time being), we must now ask on what phenomenological basis the more sharply turning crack could be anticipated due to a larger process zone.

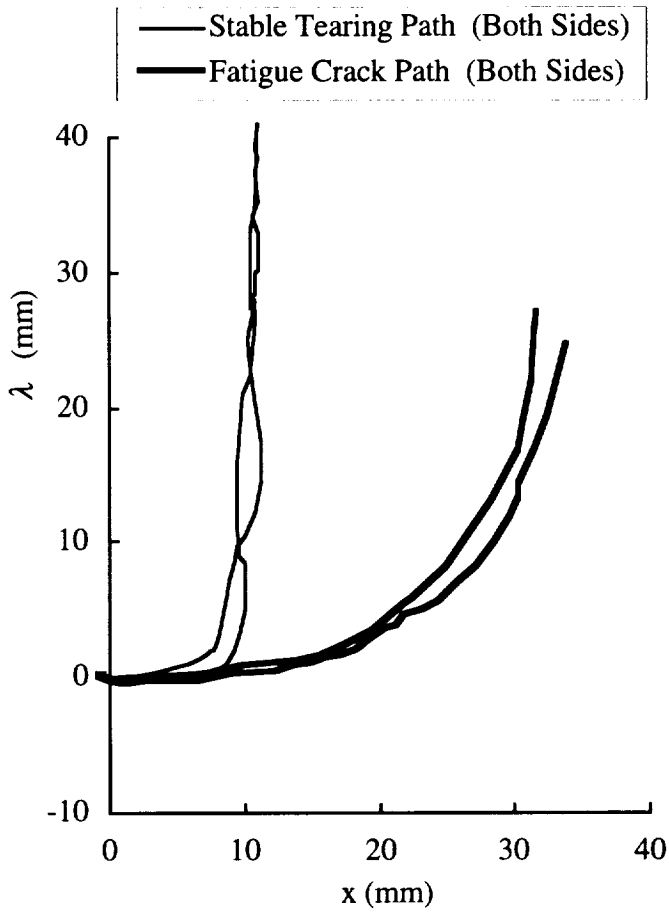

Figure 2.7 Crack Paths Observed in Reference [9], β=.37

2.4 Summary

First-order linear elastic and elastic-plastic crack kinking theories have been presented. First-order refers in this sense to the absence of the T-stress or higher order crack tip field parameters in the crack kinking expression. This infers that the theory either assumes a process zone of negligible size, or allows a finite process zone, but excludes or neglects the presence of higher order terms in the in the analysis. All first order theories predict kinking for non-zero K_{II}, thus inferring that the crack path will be smooth only if K_{II}=0.

Crack path instability theory has been presented in the case where the linear elastic crack kinking theory is construed to admit the presence of T-stress, but (tacitly) with vanishing process zone size so that the kinking theory is first order (K_{II}=0). A divergent crack path is predicted in the presence of positive (tensile) T-stress, which is in qualitative agreement with observation. This behavior will be referred to hereafter as the "first-order crack path instability" associated with the T-stress.

Lastly, test data is presented showing that when the process zone is large and the crack grows in a strong T-stress environment, the crack may turn smoothly along a much sharper radius. This now motivates a discussion of mechanisms by which such accelerated turning may occur.

CHAPTER 3.0

CRACK PATH INSTABILITY IN A MATERIAL WITH A COHESIVE PROCESS ZONE

While the fact that cracks tend to exhibit directional instability in tensile T-stress environments has been well established, there is some disagreement as to the role of the process zone. The theory of Finnie and Saith[5] [18] requires the use of a process-zone related characteristic length, r_c, to explain the directional instability. On the other hand, Cotterell and Rice [21] explained the T-stress-related path instability for linear elastic cracks devoid of any process zone assumptions. Notably, the former theory predicts that given sufficient T-stress, the crack can turn sharply from a symmetric starting configuration—whereas the latter theory predicts a smoothly turning crack resulting from a small perturbation in a self-similar crack path. Initially symmetric fracture tests tend to show smooth crack paths, but indicate that turning is accelerated if the process zone size is increased, as noted in differences between fatigue crack growth and stable tearing crack paths in otherwise identical specimens [9]. There is also evidence that the accelerated turning behavior plays a significant role in observed fuselage flapping tests [9, 14, 15, 43].

In order to study the effects of process zone size on the crack path, it was desired to extend the more rigorous approach taken by Cotterell and Rice to include the effects of a process zone. The following development will be discussed in the context of plasticity, with focus on metallic materials. Nevertheless, the general principles described could likely be applied to materials that fracture by way of micro-cracking or other inelastic effects.

[5] This theory will be discussed in greater detail in Chapter 5

3.1 Strain Localization Concept

A simple tensile test of a strain hardening material yields the familiar engineering and true stress-strain plots shown schematically in Figure 3.1. In

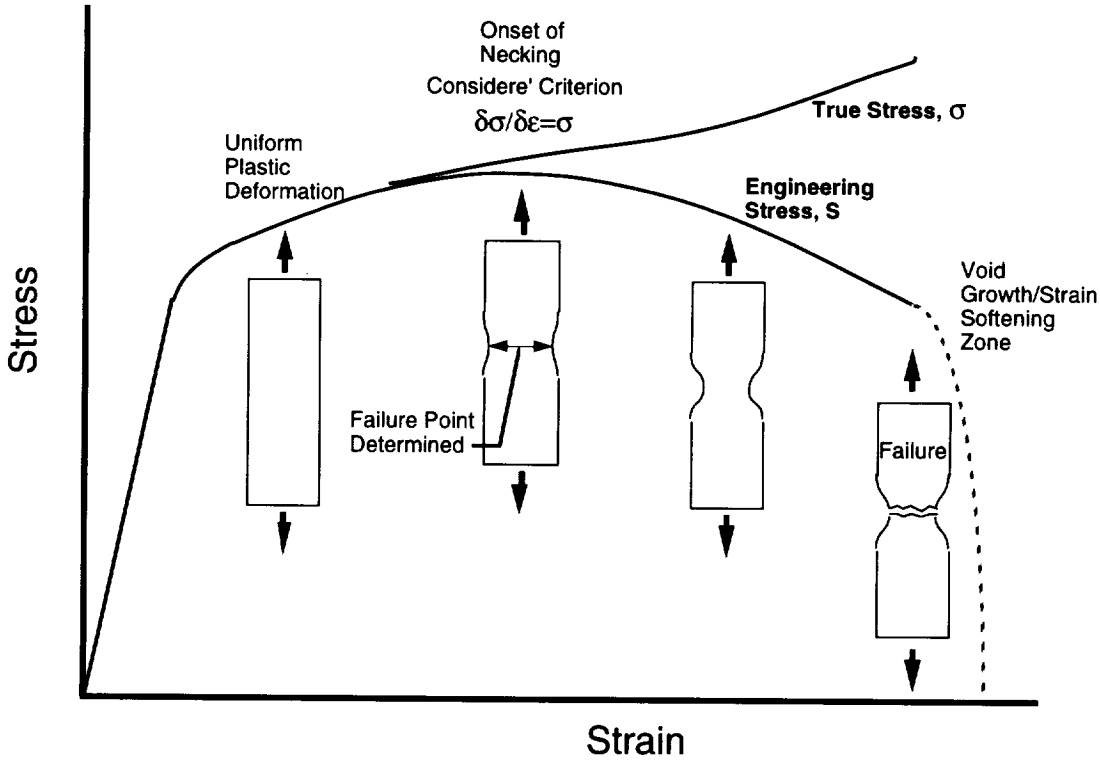

Figure 3.1 Schematic of Typical Tensile Test of Strain Hardening Material

accordance with a well-known plastic instability theory attributed to Considere, the maximum load, F, occurs when the specimen rate of area reduction equals the rate of strain hardening [44]

$$dF = \sigma dA + Ad\sigma = 0$$

Rearranging,

$$\frac{d\sigma}{\sigma} = -\frac{dA}{A} \equiv d\varepsilon$$

$$\frac{d\sigma}{d\varepsilon} = \sigma \tag{3.1}$$

It is equally well established in this context that the point of maximum load also defines the onset of localized deformation or necking in the specimen. This can be clearly illustrated by likening the specimen to a series of nonlinear springs of unit length, as illustrated in Figure 3.2. Each spring may be considered to have a local spring constant $\frac{dF}{d\varepsilon}$. As the series is stretched, all the springs elongate in proportion to their compliance, $\frac{d\varepsilon}{dF}$. Obviously, as the stiffness of any one of the springs becomes zero, then its compliance becomes infinite, all the other springs unload, and only that spring elongates. All along the specimen a stiffness of zero is approached as the maximum load is approached, but due to some imperfection one segment reaches that point first, and strain localization (necking) begins there. Once strain localization has begun, the failure location is set. If the specimen is pulled continuously to failure, the failure will occur through the location where the onset of strain localization first occurred.

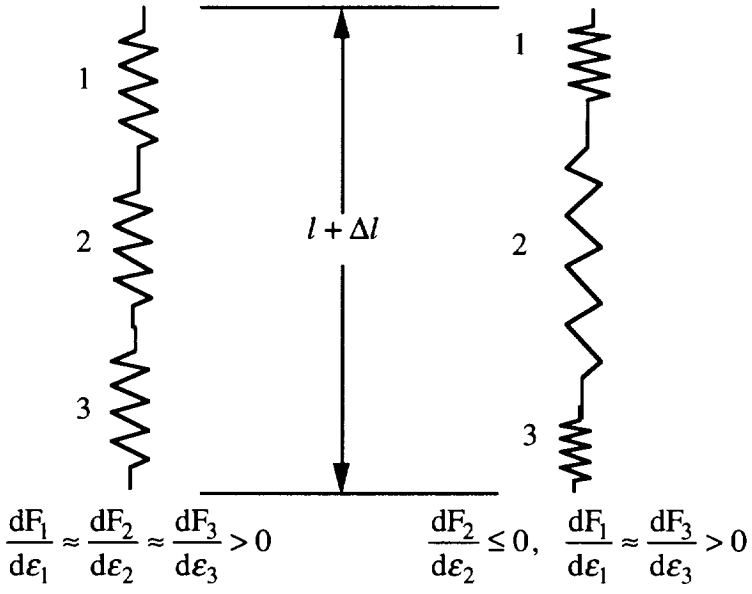

Figure 3.2 Illustration of Instability Principle Using Nonlinear Springs

Strain localization ahead of a crack tip may occur by a necking or dimpling phenomenon, as illustrated in Figure 3.3, and/or by other mechanisms such as void growth, which also results in strain softening. An attempt to quantify the distance ahead of the crack tip, r_c, over which strain localization occurs by necking is presented in Appendix 1.0, though it is approximate even within the rather severe limitations of the HRR elastic-plastic theory. Nevertheless, the principle that where failure is, strain localization once was, must be true for all but the most brittle material states. Thus the future path of the crack is set for the distance ahead of the crack within which strain localization has occurred[6], and the stress field in the vicinity of the point of onset of strain localization decides the future path of the crack. Due to the nature of the phenomena that result in strain localization, it is expected to occur at a length scale considerably smaller than the plastic zone size.

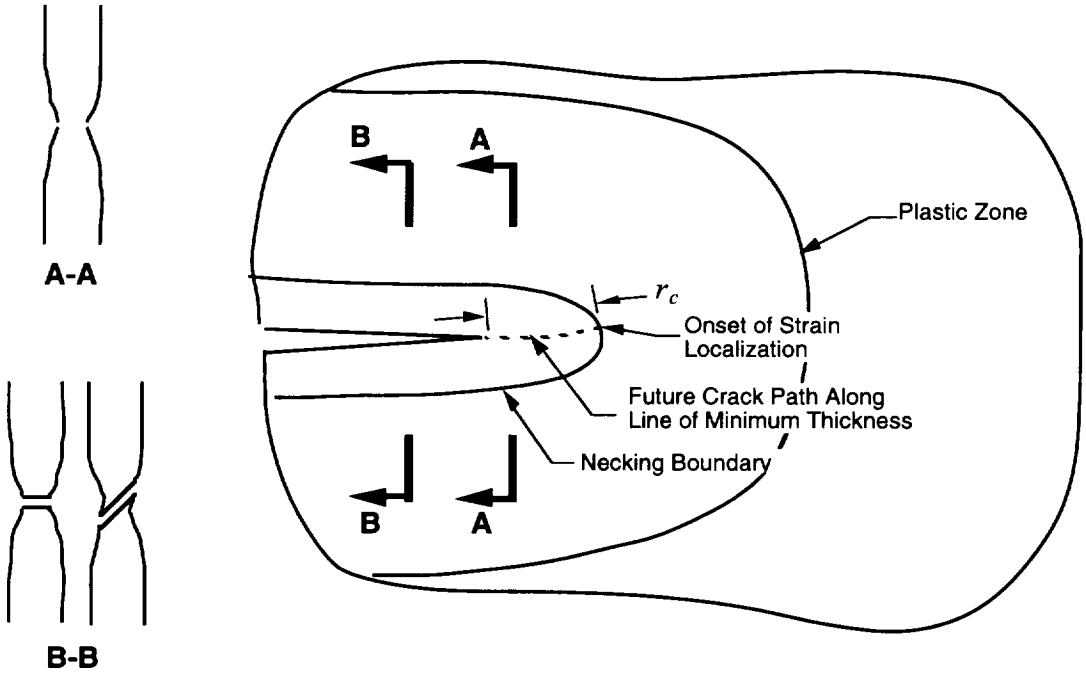

Figure 3.3 Schematic of Physical Process Zones in the Vicinity of a Propagating Crack

[6] Note that this assertion may not be true if the loading on the crack tip is suddenly changed, causing strain localization and failure to reinitiate along an alternate path.

3.2 Proposed Cohesive Crack Model

We can simulate this mechanism by modeling the strain localization point as the crack tip in a linear elastic material, trailed by a region of cohesive tractions acting to close the crack in a manner similar to the Dugdale-Barenblatt model. The primary difference is that, unlike the Dugdale-Barenblatt model [45, 46], the resultant of the tractions in the strain localization (cohesive) zone accounts only for a fraction, η, of the total stress intensity factor (because the strain localization zone length, r_c, is likely smaller than the plastic zone size, r_p, given by the Dugdale model).

$$\eta = \frac{-K_I^{\,p}}{K_I} \qquad (\eta < 1) \tag{3.2}$$

Here $K_I{}^p$ is the component of mode I stress intensity factor resulting at the cohesive crack tip from the tractions in the cohesive zone, and is negative because it acts to close the crack. Any plasticity in the physical problem outside of the cohesive strain localization zone is neglected. The stress intensity, K_I, represents the total stress intensity that would act at the crack tip if the cohesive zone were not present, and for a propagating crack equals the effective fracture toughness of the material. We will further impose as an initial condition that the process zone is fully developed. That is, the proposed model assumes that the crack has torn statically for a sufficient distance prior to the beginning of the analysis that the process zone has reached a steady-state condition, and K_I, K_I^p, and the strain localization zone size remain constant as the crack propagates.

In order to determine the future crack path from some initial position of the crack, we apply the assertion that a naturally curving crack follows a path that results in local symmetry of the stress and displacement fields at the crack tip. Thus, the mode II stress intensities due to external loads and cohesive stresses must cancel.

$$K_{II} + K_{II}{}^{p} = 0 \tag{3.3}$$

Cotterell and Rice developed a framework to solve this problem (in the absence of K_{II}^{P}) for a slightly curved extension of a perturbed crack. They used an expression for K_{II} that was accurate to the first order with respect to deviations from a straight crack path, and provided evidence that this expression was accurate to within five percent for angular deviations up to 15 degrees. In order to account for the strain-localization zone effect a comparable first-order approximation must first be derived for K_{II}^{P}. Other investigators [47,48] have proposed mixed-mode Dugdale models, allowing the cohesive zone to lie along a linear extension of the crack, but none are suitable for the curved crack problem at hand.

Cotterell and Rice, Erdogan and Sih, and others have shown that small angle changes in crack path are of the same order as K_{II}/K_{I}. With the restriction to a slightly curving crack, the absolute magnitudes of K_{II} and K_{II}^{P} must likewise be small compared to K_{I}, thus only first order terms in K_{II}, K_{II}^{P} and the corresponding tractions will likewise be retained in the analysis. As will be shown, K_{II}^{P} is not a constant, but varies with the curvature of the cohesive zone. Further, the effect of the variance of the mode II tractions within an otherwise "steady state" cohesive zone will be shown to have an influence on the mode I tractions of less than first order. Thus K_{I}^{P} remains constant to the first order for a constant cohesive zone length as previously inferred.

An expression for K_{II}^{P} can be obtained in terms of the tractions within the cohesive zone. These tractions are a function of the crack flank displacements, which displacements include contributions both from the far field loading and from the local tractions. A constitutive model for the cohesive material is then required, which provides the additional relationship between the tractions and the displacements necessary to obtain a solution for a given crack configuration. In the next four subsections, these individual building blocks are assembled, setting the stage for the solution of the future crack path in the remainder.

3.2.1 A First Order Solution for the Slightly Curved Crack with Opposing Crack Flank Tractions

A solution for this problem has already been provided by Cotterell and Rice, but will be derived by an alternative means here in order to set the stage for further development. We will begin by developing a solution for the opposing point load case illustrated in Figure 3.4. Equal and opposite point loads act at point $B = (-b, \lambda(b))$ on the upper and lower surfaces of the crack, which lies with its tip tangent to the x-axis.

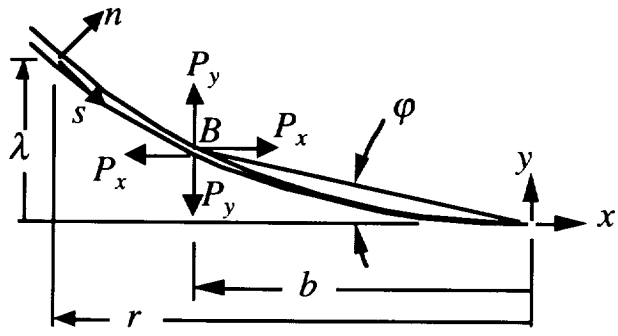

a. Actual Curved Crack

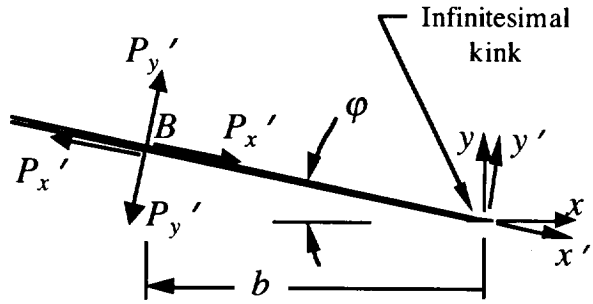

b. First-Order Representation of Crack Corresponding to Point Load Location

Figure 3.4 Slightly Curved Crack Loaded with Opposing Point Loads

The crack is assumed to deviate only slightly from a straight path (λ(r)<< r along the crack path), and we seek a solution of first order accuracy in λ. For such a solution, the crack path need only (indeed can only) be represented to the first order--that is, as a straight line. The characteristic line for the problem is that which passes through the load point and the crack tip. Presumably, all slightly curved crack paths passing through and loaded in the same manner at B, and terminating at the origin tangent to the x-axis, must have the same stress intensity solution to the first order in λ (to say otherwise would require information of higher order in the solution).

A special case that meets this description is a straight crack passing through B, and terminating at the origin with an infinitesimal kink in the positive x direction as shown in Figure 3.4b. The stress intensity at the kink tip can be easily determined from two known solution. Erdogan gave the solution for the stress intensity of a straight, semi-infinite crack in an infinite medium with opposing point loads [49]

$$\begin{Bmatrix} k_I \\ k_{II} \end{Bmatrix} = \sqrt{\frac{2}{\pi b}} \begin{Bmatrix} P_y' \\ P_x' \end{Bmatrix} \tag{3.4}$$

where P_x' and P_y' are the components of the point load parallel and normal to the straight crack, as shown in Figure 3.4b. Lower case k is used to denote stress intensities of the main crack, as opposed to the stress intensity at the kink tip, which will be referred to in upper case. Rewriting this expression in terms of P_x and P_y to the first order in $\varphi(b)$

$$\begin{Bmatrix} k_I \\ k_{II} \end{Bmatrix} = \sqrt{\frac{2}{\pi b}} \begin{Bmatrix} P_y + \varphi(b)P_x \\ P_x - \varphi(b)P_y \end{Bmatrix} \tag{3.5}$$

The stress intensity at the tip of the infinitesimal kink at angle φ to the main crack is given in terms of the far field stress intensity of the main crack by [21]

$$\begin{Bmatrix} K_I \\ K_{II} \end{Bmatrix} = \begin{bmatrix} C_{11} & C_{12} \\ C_{21} & C_{22} \end{bmatrix} \begin{Bmatrix} k_I \\ k_{II} \end{Bmatrix} \tag{3.6}$$

where

$$C_{11} = \tfrac{1}{4}\left[3\cos(\varphi/2) + \cos(3\varphi/2)\right]$$
$$C_{12} = -\tfrac{3}{4}\left[\sin(\varphi/2) + \sin(3\varphi/2)\right]$$
$$C_{21} = \tfrac{1}{4}\left[\sin(\varphi/2) + \sin(3\varphi/2)\right]$$
$$C_{22} = \tfrac{1}{4}\left[\cos(\varphi/2) + 3\cos(3\varphi/2)\right]$$

Cotterel and Rice showed (3.6) to be accurate to better than first order in φ. Since only first order accuracy is required here, we expand C_{ij} about $\varphi = 0$, so that (3.6) simplifies to

$$\begin{Bmatrix} K_I \\ K_{II} \end{Bmatrix} = \begin{Bmatrix} k_I \\ k_{II} \end{Bmatrix} + \frac{\varphi}{2} \begin{Bmatrix} -3k_{II} \\ k_I \end{Bmatrix} \tag{3.7}$$

Combining (3.5) and (3.7) and retaining only first order terms we obtain for the kinked crack representation of the crack tip

$$\begin{Bmatrix} K_I \\ K_{II} \end{Bmatrix} = \sqrt{\frac{2}{\pi b}} \left[\begin{Bmatrix} P_y \\ P_x \end{Bmatrix} - \frac{1}{2} \begin{Bmatrix} P_x \\ P_y \end{Bmatrix} \varphi(b) \right] \tag{3.8}$$

For the cohesive crack problem at hand, tractions T_x and T_y act over a distance r_c trailing the crack tip. Letting $t = b/r_c$ and recognizing that $dP_j = T_j db = (T_j/r_c)dt$, we can find the stress intensity factors at the crack tip due to the cohesive tractions by integration of (3.8) over the cohesive zone.

$$\begin{Bmatrix} K_I{}^P \\ K_{II}{}^P \end{Bmatrix} = \sqrt{\frac{2r_c}{\pi}} \int_o^1 \left[\begin{Bmatrix} T_y \\ T_x \end{Bmatrix} - \frac{1}{2} \begin{Bmatrix} T_x \\ T_y \end{Bmatrix} \varphi(t) \right] \frac{1}{\sqrt{t}} dt \tag{3.9}$$

Using a more rigorous stress function approach, Cotterell and Rice developed an equation for the stress intensity factors at the end of a slightly curved finite crack in an infinite plate

$$\begin{Bmatrix} K_I \\ K_{II} \end{Bmatrix} = \sqrt{\frac{2}{\pi L}} \int_o^L \left[\begin{Bmatrix} T_y \\ T_x \end{Bmatrix} \left(\frac{L-r}{r} \right)^{1/2} + \frac{1}{2} \begin{Bmatrix} T_x \\ T_y \end{Bmatrix} \left(\varphi(L) - \frac{\varphi(r)L}{r} \right) \left(\frac{r}{L-r} \right)^{1/2} \right] dr \qquad (3.10)$$

where L is the total crack length. By letting r become vanishingly small compared to L in (10), and integrating over a cohesive process zone from $r=0$ to r_c with $t=r/r_c$ it can be verified that (3.10) reduces to (3.9), thus confirming the foregoing development.

3.2.2 Determination of Crack Tip Opening Displacement Due to Far-Field Loading

Encouraged by the preceding result, we shall now use a similar approach to obtain the crack opening displacements of a slightly curved crack associated with the far field stress intensity factors K_I, K_{II}. The analogous first-order representation of the crack pertaining to the displacements at a point on the crack flanks is illustrated in Figure 3.5. The stress intensities at the tip of the infinitesimal kink are taken to represent the stress intensities at the tip of the curved crack to the first order, and for the present are assumed to be given. Equation (3.7) can then be solved for the stress intensities corresponding to the main crack in terms of the kinked crack stress intensities.

$$\begin{Bmatrix} k_I \\ k_{II} \end{Bmatrix} = \begin{Bmatrix} K_I \\ K_{II} \end{Bmatrix} + \frac{\varphi}{2} \begin{Bmatrix} 3K_{II} \\ -K_I \end{Bmatrix} \qquad (3.11)$$

For the straight (main) crack, the displacements are expressed in circular coordinates by (neglecting terms of order $r^{3/2}$ and above)

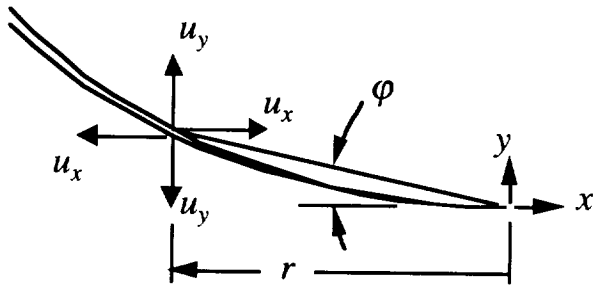

a. Actual Curved Crack

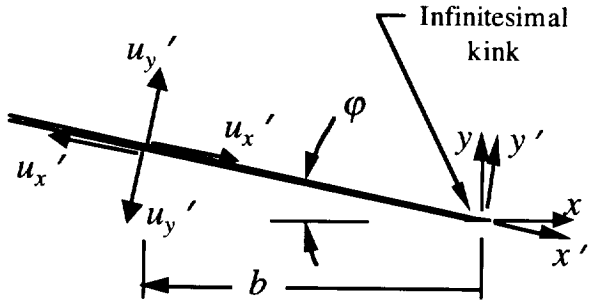

b. First-Order Representation of Crack Corresponding to Point Load Location

Figure 3.5 Deflections of Slightly Curved Crack Associated with Stress Intensity Due to Far-Field Loading

$$u_x' = \frac{1}{4G}\sqrt{\frac{r}{2\pi}}\left\{k_I\left[(2\kappa-1)\cos\frac{\theta}{2}-\cos\frac{3\theta}{2}\right]+k_{II}\left[(2\kappa+3)\sin\frac{\theta}{2}+\sin\frac{3\theta}{2}\right]\right\}+\frac{Tr(\kappa+1)}{8G}\cos\theta$$

$$u_y' = \frac{1}{4G}\sqrt{\frac{r}{2\pi}}\left\{k_I\left[(2\kappa+1)\sin\frac{\theta}{2}-\sin\frac{3\theta}{2}\right]+k_{II}\left[(2\kappa-3)\cos\frac{\theta}{2}+\cos\frac{3\theta}{2}\right]\right\}-\frac{Tr(3-\kappa)}{8G}\sin\theta \tag{3.12}$$

where G is the shear modulus, ν is Poisson's ratio, and

$$\kappa = \begin{cases} 3-4\nu & (\textit{plane strain}) \\ (3-\nu)/(1+\nu) & (\textit{plane stress}) \end{cases} \tag{3.13}$$

Evaluating these displacements at $\theta=\pm\pi$, the crack opening displacement, $\Delta u_j' = u_j'(\pi) - u_j'(-\pi)$ at r is given by

$$\begin{Bmatrix} \Delta u'_y(r) \\ \Delta u'_x(r) \end{Bmatrix} = \frac{(\kappa+1)}{G}\sqrt{\frac{r}{2\pi}}\begin{Bmatrix} k_I \\ k_{II} \end{Bmatrix} \tag{3.14}$$

Note that the T-stress terms are symmetric, and have been carried here only to illustrate that they make no contribution to the crack opening for the first order representation of the crack. The displacements Δu_x and Δu_y in the original coordinate system can be expressed in terms of their primed counterparts to the first order by

$$\begin{Bmatrix} u_y(r) \\ u_x(r) \end{Bmatrix} = \begin{Bmatrix} u'_y(r) - \varphi(r)u'_x \\ u'_x(r) + \varphi(r)u'_y \end{Bmatrix} \tag{3.15}$$

Combining Equations (3.11), (3.14) and (3.15) and disregarding higher order terms, we obtain

$$\begin{Bmatrix} \Delta u_y{}^k(r) \\ \Delta u_x{}^k(r) \end{Bmatrix} = \frac{(\kappa+1)}{G}\sqrt{\frac{r}{2\pi}}\left[\begin{Bmatrix} K_I \\ K_{II} \end{Bmatrix} + \varphi(r)\frac{1}{2}\begin{Bmatrix} K_{II} \\ K_I \end{Bmatrix}\right] \tag{3.16}$$

The superscript k is introduced to denote crack opening components due to the stress intensity induced by far-field loading. With the further restriction that the stress intensity approaches pure mode I or pure mode II, we can write the normalized expressions

$$\frac{\Delta u_x{}^k(r)}{\Delta u_y{}^k(r)} = \frac{K_{II}}{K_I} + \frac{\varphi(r)}{2} \qquad \text{for } K_{II} << K_I \tag{3.17}$$

$$\frac{\Delta u_y{}^k(r)}{\Delta u_x{}^k(r)} = \frac{K_I}{K_{II}} + \frac{\varphi(r)}{2} \qquad \text{for } K_I << K_{II} \tag{3.18}$$

Equation (3.17) should be applicable to the case of a naturally curving mode I crack. To check the accuracy of these expressions, we run finite element analyses of non-rectilinear cracks and to plot the normalized crack opening displacements as a function of φ. A 20 x 20 inch plate was modeled in FRANC2D/L [50] with a 2.0 inch

center crack. As illustrated in Figure 3.6, a kink projecting 0.01 inches along the crack axis was modeled at one end of the crack. The relative scales of the panel, crack and kink were selected so that that finite width and finite crack length effects on the kinked crack stress intensity would remain well below one percent.

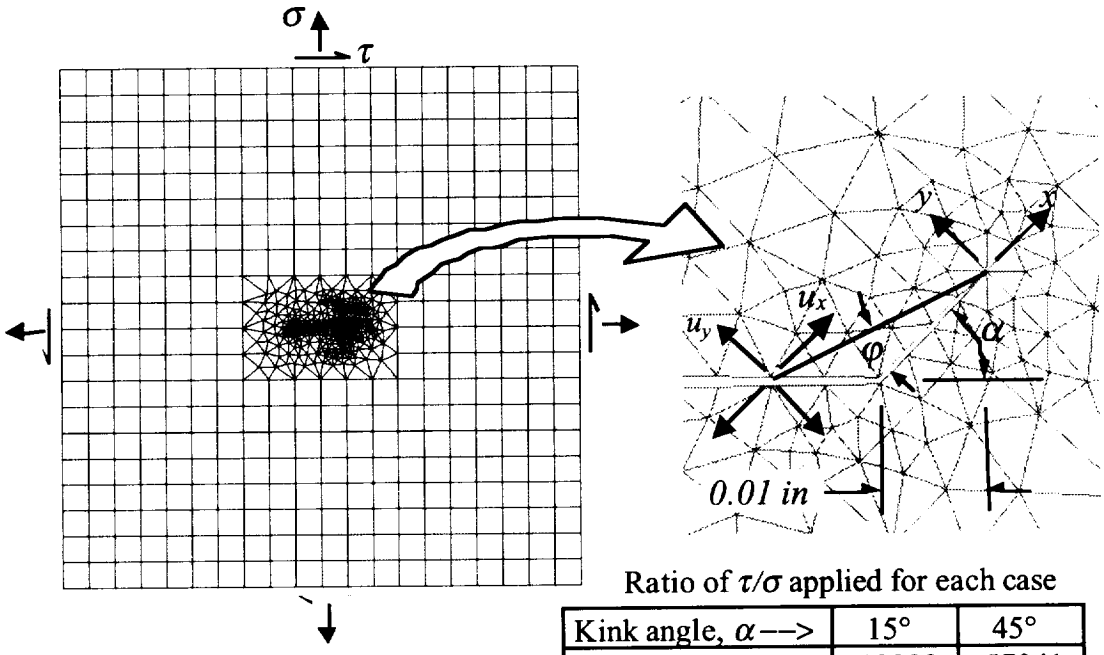

Ratio of τ/σ applied for each case

Kink angle, α -->	15°	45°
K_{II}=0	-.13398	-.57041
K_I=0	2.5231	.80077

Figure 3.6 FRANC2D/L Finite Element Model of Crack with Finite Kink

Two kink configurations were modeled, a 15 degree kink to represent a minimum standard for which the first order solution should hold, and a 45 degree kink. To isolate the first order term in φ, only pure modal cases were run. The loading scenarios consisted of a biaxial tension stress of unity, coupled with a shear stress determined based on the results of Isida and Nishino [51] to result in pure mode I or pure mode II stress intensity at the kink tip (including the small finite crack length effect). The crack tip opening displacements were measured at the kink corner ($\varphi = 0$),

and at six additional points along the main crack in the immediate vicinity of the kink, corresponding to different values of φ. The results, plotted in Figure 3.7, show excellent correlation with the first order theory for the 15 degree kink, but degrade as the deviation from straightness increases.

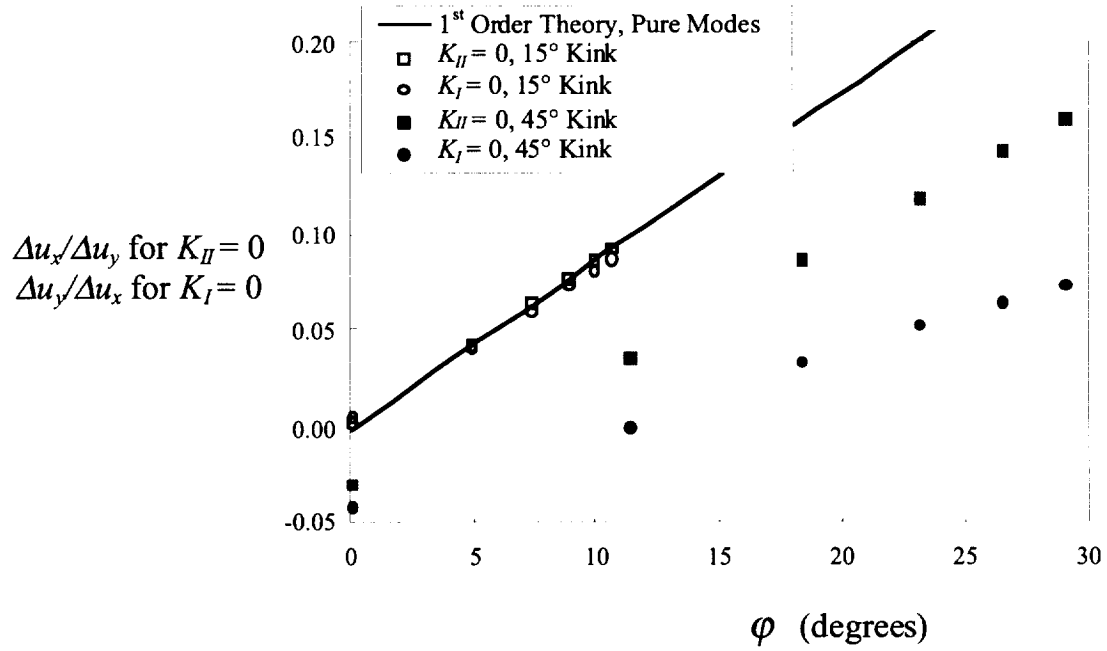

Figure 3.7 Correlation of FEM Results with First Order Crack Tip Opening Expression Corresponding to Far-Field Loading

3.2.3 Determination of Crack Tip Opening Displacement Due to Cohesive Tractions

Having solved for the crack tip opening displacements due to the far field loads, we now need an expression for the displacement components due to the cohesive tractions imposed near the crack tip. An approximate expression will suffice if it can be shown that the effect of these tractions on the overall solution is small. Such an expression may be deduced from the straight crack solution. For a straight crack

loaded with opposing point loads (a special case of Figure 3.4a), Irwin [52] gives the Westergaard stress functions

$$\begin{Bmatrix} Z_I \\ Z_{II} \end{Bmatrix} = -\frac{2}{\pi}\begin{Bmatrix} P_y \\ P_x \end{Bmatrix}\tan^{-1}\sqrt{\frac{b}{z}}$$

where $z = x + iy$ and b is the distance trailing the crack tip at which the point loads are applied. This yields the displacements

$$\begin{Bmatrix} u_y \\ u_x \end{Bmatrix} = \frac{1}{4G}\begin{Bmatrix} (\kappa+1)\,\mathrm{Im}\,Z_I \\ (\kappa-1)\,\mathrm{Re}\,Z_I \end{Bmatrix} - y\begin{Bmatrix} \mathrm{Re}\,Z_I' \\ \mathrm{Im}\,Z_I' \end{Bmatrix} \qquad \text{(mode I)}$$

$$\begin{Bmatrix} u_y \\ u_x \end{Bmatrix} = \frac{1}{4G}\begin{Bmatrix} -(\kappa-1)\,\mathrm{Re}\,Z_{II} \\ (\kappa+1)\,\mathrm{Im}\,Z_{II} \end{Bmatrix} + y\begin{Bmatrix} -\mathrm{Im}\,Z_{II}' \\ \mathrm{Re}\,Z_{II}' \end{Bmatrix} \qquad \text{(mode II)}$$

Setting $y=0^{\pm}$, and defining r=-x, we evaluate the deflections along the crack flanks

$$\begin{Bmatrix} u_y^{\pm}(r) \\ u_x^{\pm}(r) \end{Bmatrix} = \pm\frac{(\kappa+1)}{4G\pi}\begin{Bmatrix} P_y \\ P_x \end{Bmatrix}\log\left|\frac{1+\sqrt{r/b}}{1-\sqrt{r/b}}\right| + \frac{(\kappa-1)}{4G}\begin{Bmatrix} -P_x \\ P_y \end{Bmatrix}H(r-b) \qquad (3.19)$$

where the first term is equivalent to that given by Tada [53]. In the second term, *H(x)* is the Heaviside step function (omitting the point of load application). The term is antisymmetric, and thus drops out when calculating the relative displacements between adjacent points on the upper and lower crack faces, leaving

$$\begin{Bmatrix} \Delta u_y(r) \\ \Delta u_x(r) \end{Bmatrix} = \frac{(\kappa+1)}{2G\pi}\begin{Bmatrix} P_y \\ P_x \end{Bmatrix}\log\left|\frac{1+\sqrt{r/b}}{1-\sqrt{r/b}}\right| \qquad (3.20)$$

For the slightly curved crack, it is not unreasonable to assume that the corresponding antisymmetric terms can likewise be disregarded, and postulate that an approximate solution to the first order in φ would take the form.

$$\begin{Bmatrix}\Delta u_y(r)\\ \Delta u_x(r)\end{Bmatrix}=\frac{(\kappa+1)}{2G\pi}\begin{Bmatrix}P_y+\varphi(r)C_{yr}+\varphi(b)C_{yb}\\ P_x+\varphi(r)C_{xr}+\varphi(b)C_{xb}\end{Bmatrix}\log\left|\frac{1+\sqrt{r/b}}{1-\sqrt{r/b}}\right| \tag{3.21}$$

where coefficients C_{ij} remain to be determined. An initial approach to obtain coefficients is to observe that as $r\rightarrow 0$, the deflections due to the singular stress field must dominate at the crack tip, thus Equation (3.16) must be satisfied in the limit, requiring that for r<<b

$$\sqrt{\frac{2}{\pi b}}\begin{Bmatrix}P_y+\varphi(r)C_{yr}+\varphi(b)C_{yb}\\ P_x+\varphi(r)C_{xr}+\varphi(b)C_{xb}\end{Bmatrix}=\left[\begin{Bmatrix}K_I\\ K_{II}\end{Bmatrix}+\varphi(r)\frac{1}{2}\begin{Bmatrix}K_{II}\\ K_I\end{Bmatrix}\right] \tag{3.22}$$

The stress intensity factors in this case are those incurred by the point forces, as given by Equation (3.8), which, neglecting higher order terms, yields the tentative relation

$$\begin{Bmatrix}\Delta u_y(r)\\ \Delta u_x(r)\end{Bmatrix}=\frac{(\kappa+1)}{2G\pi}\left[\begin{Bmatrix}P_y\\ P_x\end{Bmatrix}-\frac{1}{2}[\varphi(b)-\varphi(r)]\begin{Bmatrix}P_x\\ P_y\end{Bmatrix}\right]\log\left|\frac{1+\sqrt{r/b}}{1-\sqrt{r/b}}\right| \tag{3.23}$$

Equation (3.23) was checked using the same finite element model as before, but with four different kink configurations as illustrated in Figure 3.8. The predicted deflections from Equation (3.23) and the finite element analysis for Case #4 are presented in Figure 3.9. Note that the finite element results exhibit the expected symmetry between pure modal load states, and also that the deflections corresponding to the primary loading mode are accurately represented. For displacements transverse to the load axis, however, Equation (3.23) approaches the correct solution very near the crack tip, but does very poorly everywhere else. Similar results were observed for the other cases. By allowing the solution to differ on either side of the point load, a modified expression was obtained.

$$\begin{Bmatrix}\Delta u_y(r)\\ \Delta u_x(r)\end{Bmatrix}=\frac{(\kappa+1)}{2G\pi}\left[\begin{Bmatrix}P_y\\ P_x\end{Bmatrix}-\left[0.25\varphi(b)+0.50|\varphi(b)-\varphi(r)|\right]\begin{Bmatrix}P_x\\ P_y\end{Bmatrix}\right]\log\left|\frac{1+\sqrt{r/b}}{1-\sqrt{r/b}}\right| \tag{3.24}$$

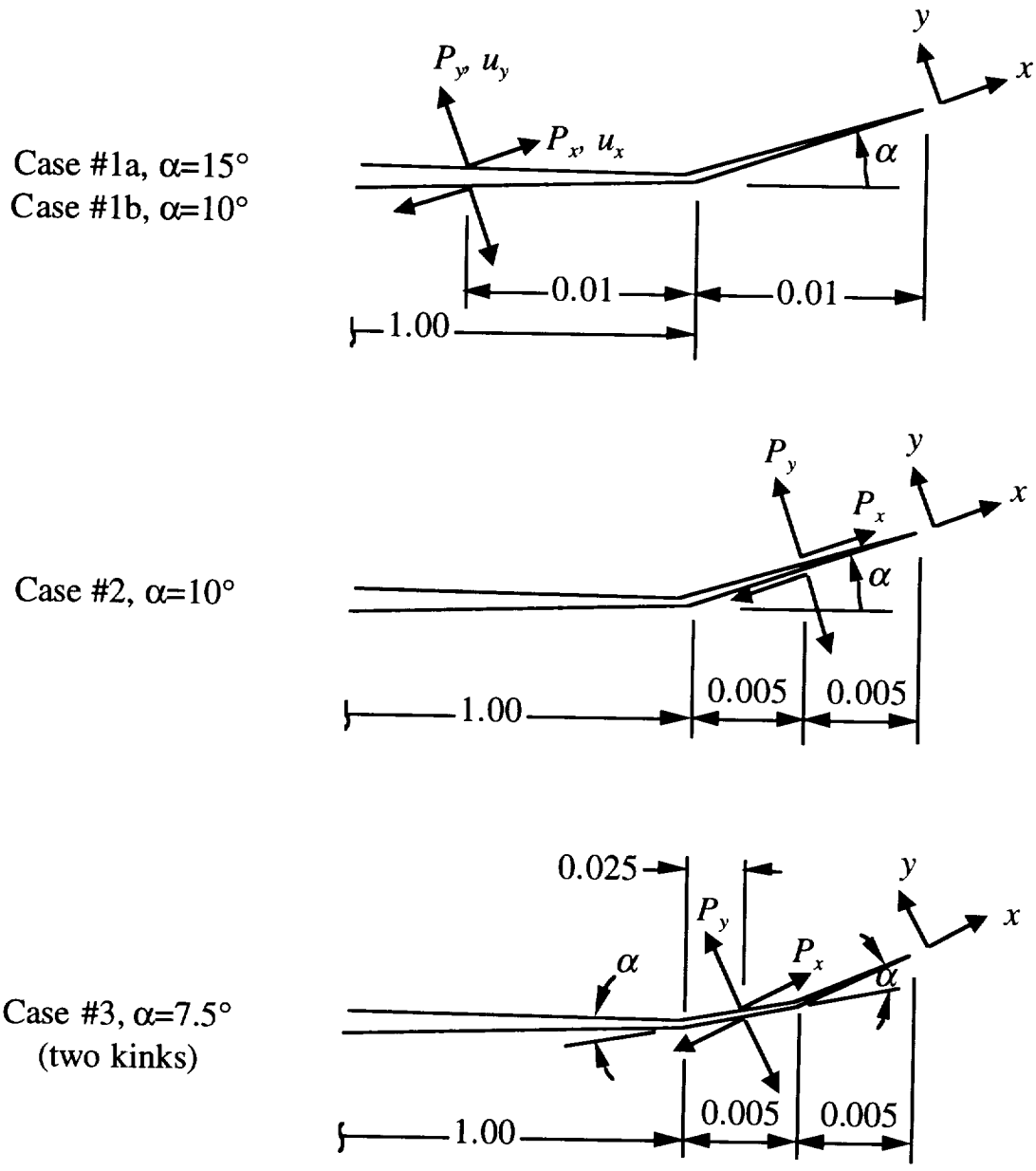

Figure 3.8 Crack Tip/Point Load Configurations for Finite Element Analysis

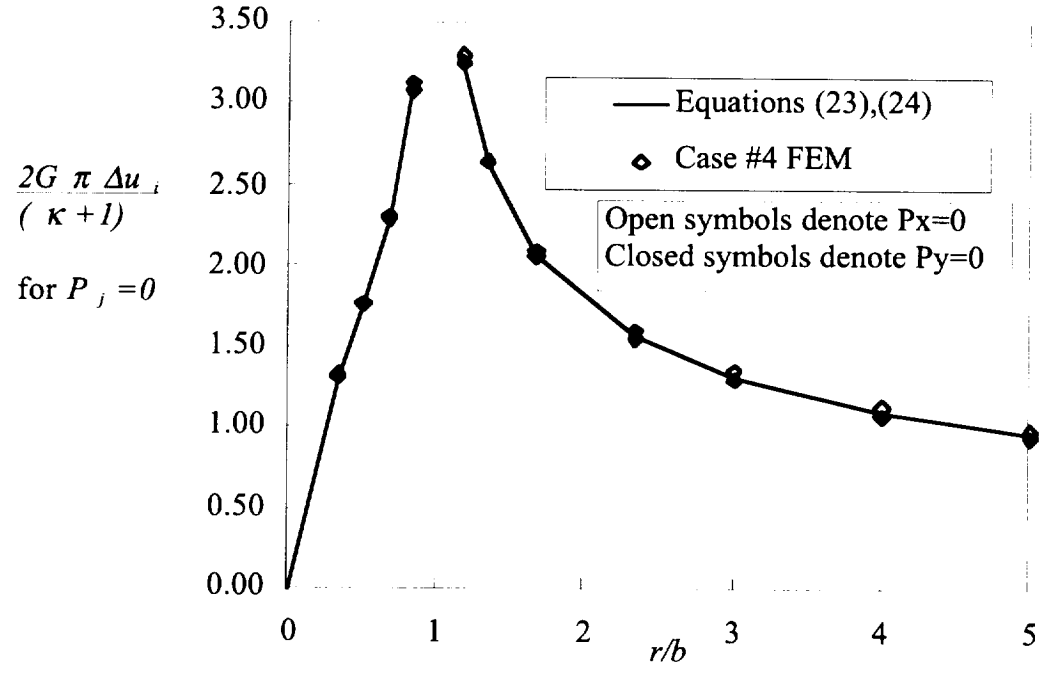

a. Displacement Parallel to Load

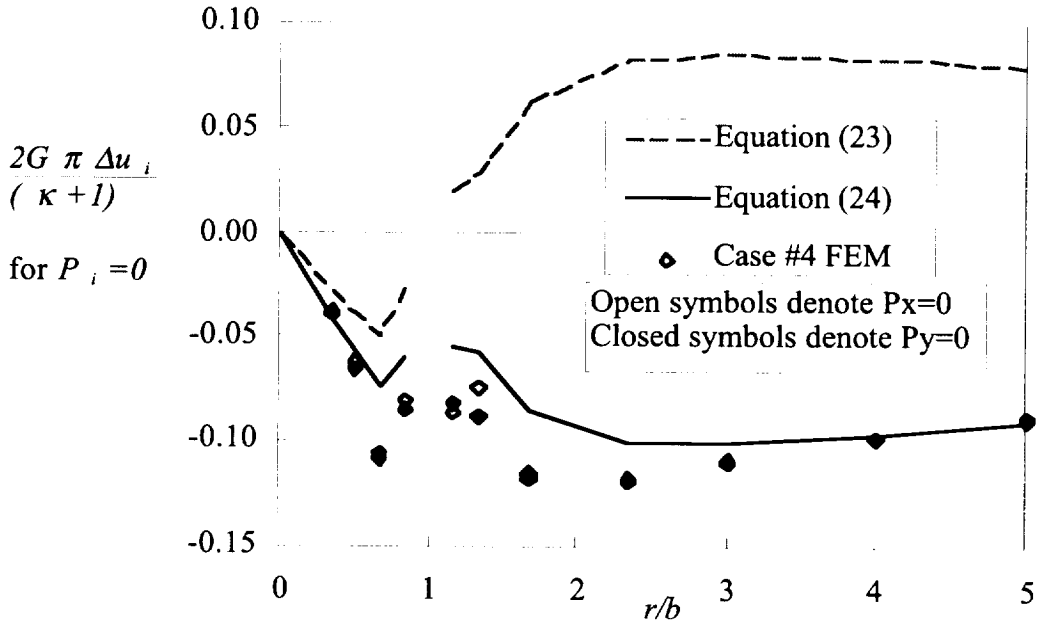

b. Displacement Transverse to Load

Figure 3.9 Case #3 Finite Element Crack Tip Opening Results Due to Point Load Compared with First-Order Approximations

A least squares fit could slightly improve the fit on the average over the entire region where data was taken, but worsened the fit as r>>b and b>>r. Equation (3.24) is also plotted in Figure 3.9b, showing much improved correlation. Yet, while the coefficients look suspiciously familiar, the solution is considerably more approximate than the equations derived previously for stress intensity due to local loading, and deflections due to far-field loading. Nevertheless, based on (3.24), we can write for pure modal loading,

$$\frac{\Delta u_i(r)}{\Delta u_j(r)} + 0.25\varphi(b) = 0.5\left|\varphi(b) - \varphi(r)\right| \qquad \text{where} \quad P_i = 0 \tag{3.25}$$

The transverse deflection data from pure mode loading of all configurations is correlated in this manner in Figure 3.10, showing good agreement overall. As will be shown, the present solution will be sufficient for the present purpose[7].

As mentioned previously for the naturally curving crack, K_{II}, and K_{II}^{P} must be of the order of φK_I. Consequently, the mode II deflections and tractions along the cohesive zone must be small compared to the corresponding mode I values, allowing us to neglect φP_x terms. Further recognizing that $dP_j = T_j db$ and integrating (3.24) over the cohesive process zone, we obtain an approximate expression for the overall displacements due to the cohesive tractions.

$$\begin{Bmatrix} \Delta u_y^{\,p}(r) \\ \Delta u_x^{\,p}(r) \end{Bmatrix} = \frac{(\kappa+1)}{2G\pi}\int_0^{r_c} \begin{Bmatrix} T_y \\ T_x - T_y\left[0.25\varphi(b) + 0.5\left|\varphi(b) - \varphi(r)\right|\right] \end{Bmatrix} \log\left|\frac{1+\sqrt{r/b}}{1-\sqrt{r/b}}\right| db$$

$$= \frac{(\kappa+1)}{2G\pi} r_c \int_0^1 \begin{Bmatrix} T_y \\ T_x - T_y\left[0.25\varphi(t) + 0.5\left|\varphi(t) - \varphi(r/r_c)\right|\right] \end{Bmatrix} \log\left|\frac{1+\sqrt{(r/r_c)/t}}{1-\sqrt{(r/r_c)/t}}\right| dt \tag{3.26}$$

[7] A more precise solution could possibly be obtained by further development of the Muskhelishvili stress functions discussed by Cotterell and Rice.

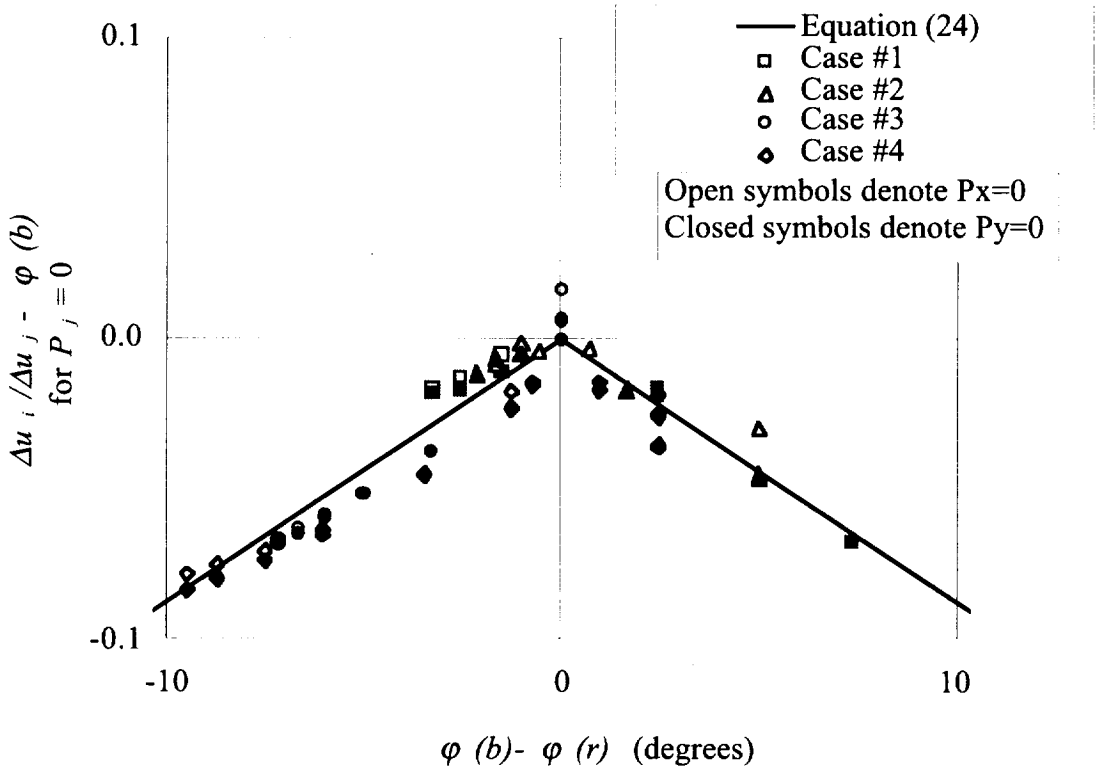

Figure 3.10 Finite Element Crack Tip Opening Results from all Cases Correlated with Modified First Order Approximation

The total relative displacement at any point along the crack face is thus given by superposition of Equations (3.16) and (3.26)

$$\Delta u_j^{tot} = \Delta u_j^{k} + \Delta u_j^{p} \tag{3.27}$$

with the stress intensities in (3.16) construed as those that would exist if the cohesive zone were absent. The total displacement distribution is then imposed (implicitly) on the cohesive zone as a boundary condition to determine the tractions.

3.2.4 Relationship Between Crack Tip Opening Deflections and Cohesive Tractions

For the present investigation, we will model the cohesive zone as a strip of perfectly plastic material that is narrow with respect to the radius of crack curvature. If the imposed displacements are expressed in terms of the local coordinate system, *(s,n)* shown in Figure 3.4a, we observe that

$$\frac{\gamma_{sn}}{\varepsilon_{nn}} = 2\frac{\varepsilon_{sn}}{\varepsilon_{nn}} = \frac{\Delta u_s^{\,tot}}{\Delta u_n^{\,tot}} \qquad \left|\frac{d\varepsilon_{sn}}{d\varepsilon_{nn}}\right| << 1 \qquad \left|\frac{d\varepsilon_{ss}}{d\varepsilon_{nn}}\right| << 1 \tag{3.28}$$

where ε_{ij} are plastic strains in the cohesive zone, with γ_{sn} the engineering shear strain. The first inequality follows from the prior observation that for a slightly curving crack propagating in mode I, the shear displacements must be small compared to normal displacements (which must also be true of the respective differentials). The second inequality follows from the assumption of strain localization—that is, the normal cohesive strains are large as the crack opens, and strain in the cohesive region parallel to the crack is resisted by the comparatively rigid crack flanks.

We define the yield surface, F, according to the Von Mises yield criterion

$$F = \left(\frac{1}{2}s_{ij}s_{ij} - \tau_o^{\,2}\right)$$

where τ_o is the shear flow stress, and s_{ij} are the components of the deviatoric stress tensor,

$$s_{ij} = \sigma_{ij} - \frac{1}{3}\sigma_{kk}\delta_{ij}$$

For plane stress, this yields

$$\frac{1}{2}s_{ij}s_{ij} = \frac{1}{3}\left(\sigma_{nn}^{\,2} - \sigma_{nn}\sigma_{ss} + \sigma_{ss}^{\,2}\right) + \frac{1}{2}\left(\sigma_{sn}^{\,2} + \sigma_{ns}^{\,2}\right) \tag{3.29}$$

Employing the Prandtl-Reuss flow rule

$$d\varepsilon_{ij} = (d\lambda)s_{ij} = (d\lambda)\frac{\partial F}{\partial \sigma_{ij}}$$

where $d\lambda$ is a scalar multiplier, we obtain the incremental strain components in two dimensions

$$\begin{aligned} d\varepsilon_{nn} &= \frac{d\lambda}{3}(2\sigma_{nn} - \sigma_{ss}) \\ d\varepsilon_{ss} &= \frac{d\lambda}{3}(2\sigma_{ss} - \sigma_{nn}) \\ d\varepsilon_{sn} &= d\varepsilon_{ns} = (d\lambda)\sigma_{sn} \end{aligned} \tag{3.30}$$

Normalizing these equations with respect to ε_{nn}

$$\frac{d\varepsilon_{ss}}{d\varepsilon_{nn}} = \frac{2\sigma_{ss} - \sigma_{nn}}{2\sigma_{nn} - \sigma_{ss}}$$

$$\frac{d\varepsilon_{sn}}{d\varepsilon_{nn}} = \frac{3\sigma_{sn}}{2\sigma_{nn} - \sigma_{ss}} \tag{3.31}$$

we can then solve for the corresponding normalized stress ratios

$$\frac{\sigma_{ss}}{\sigma_{nn}} = \frac{\dfrac{d\varepsilon_{ss}}{d\varepsilon_{nn}} + \dfrac{1}{2}}{1 + \dfrac{1}{2}\dfrac{d\varepsilon_{ss}}{d\varepsilon_{nn}}} = \frac{1}{2} + \frac{3}{4}\frac{d\varepsilon_{ss}}{d\varepsilon_{nn}} + 0\left[\left(\frac{d\varepsilon_{ss}}{d\varepsilon_{nn}}\right)^2\right] \tag{3.32}$$

$$\frac{\sigma_{sn}}{\sigma_{nn}} = \frac{1}{3}\frac{d\varepsilon_{sn}}{d\varepsilon_{nn}}\left(2 - \frac{\sigma_{ss}}{\sigma_{nn}}\right) = \frac{1}{2}\frac{d\varepsilon_{sn}}{d\varepsilon_{nn}} + 0\left[\frac{d\varepsilon_{ss}}{d\varepsilon_{nn}}\frac{d\varepsilon_{sn}}{d\varepsilon_{nn}}\right] \tag{3.33}$$

Retaining only first order terms and applying (3.32) and (3.33) to the von Mises yield criterion (F=0), we note that

$$\sigma_{nn} = 2\tau_o \tag{3.34}$$

Assuming proportional loading, the ratios of the strain increments may be approximated by ratios of the total strains, and we obtain from Equations (3.28) and (3.33),

$$\frac{T_s}{T_n} = \frac{\sigma_{sn}}{\sigma_{nn}} = \frac{1}{2}\frac{d\varepsilon_{sn}}{d\varepsilon_{nn}} \approx \frac{1}{2}\frac{\varepsilon_{sn}}{\varepsilon_{nn}} = \frac{1}{4}\frac{\Delta u_s}{\Delta u_n} \tag{3.35}$$

or

$$\frac{T_s}{T_n} = c\frac{\Delta u_s}{\Delta u_n} \tag{3.36}$$

where c has a nominal value of 1/4 for the plane stress case. One should bear in mind that this represents an ideal condition, not only with regard to the extent of strain localization, but also with regard to the foregoing assumption of a perfectly plastic cohesive zone in plane stress (and the assumption of proportional loading). Conceivably, this factor could vary for different types of cohesive zones and shall therefore be carried as a constant. For example, a derivation given in Appendix 2.0 shows that for a slant crack deforming along a shear slip plane (a common failure mode for thin sheet materials), c = 1/2.

To add further realism to the cohesive model, we note that the normal traction may not be constant as might be suggested by (3.34), but in fact decrease due to necking, void growth or other phenomena from a maximum value, T_c, at the cohesive crack tip, down to zero as the cohesive zone separates at $r=r_c$. This can be written

$$T_n = -T_c f(r/r_c) \tag{3.37}$$

where the cohesive softening function $f(t)$ presumably varies between $f(0)=1$ and $f(1)=0$, and is assumed to represent a steady-state characteristic of the material. The

negative sign indicates that T_n acts to close the crack for positive T_c. A suggested form for $f(t)$ capable of representing a broad range of softening behaviors is

$$f(t) = 1 - t^m \tag{3.38}$$

which is plotted in Figure 3.11 for various values of m.

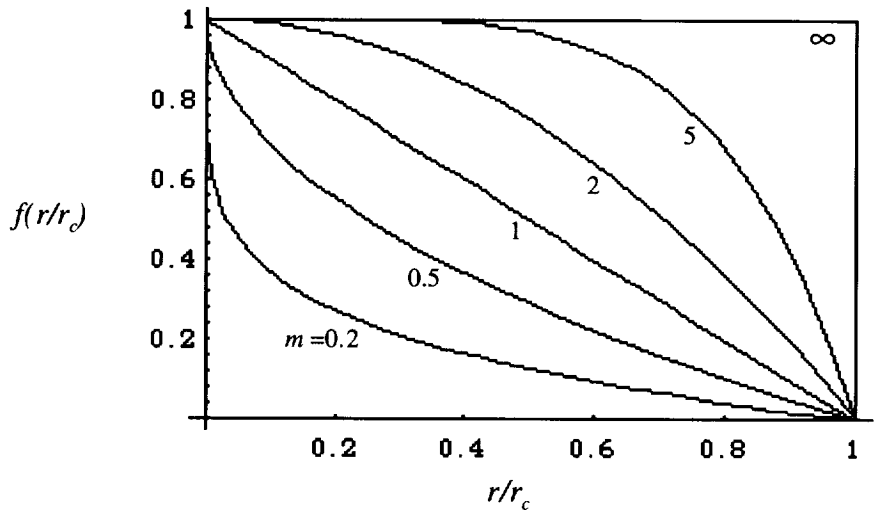

Figure 3.11 Suggested Softening Function, $f(r/r_c)$

Expressing the normal and shear tractions and displacements in terms of their x and y components to the first order in λ', where prime here denotes differentiation with respect to r,

$$\begin{aligned} T_n &= T_y + T_x\lambda' & u_n &= u_y + u_x\lambda' \\ T_s &= T_x - T_y\lambda' & u_s &= u_x - u_y\lambda' \end{aligned} \tag{3.39}$$

we can rewrite Equation (3.36), neglecting 2nd and higher order terms in λ'.

$$\frac{T_x}{T_y} = c\frac{\Delta u_x^{tot}}{\Delta u_y^{tot}} \tag{3.40}$$

Also $T_x << T_y$, thus $T_x \lambda'$ may be considered of second order and can be neglected, allowing us to write

$$T_y = -T_c f(r/r_c)$$
$$T_x = -T_c f(r/r_c) c \frac{\Delta u_x^{tot}}{\Delta u_y^{tot}} \tag{3.41}$$

3.2.4 Estimating the Cohesive Components of Stress Intensity

The cohesive contribution to the mode one stress intensity, K_I^p, can be now be obtained to the first order by combining equations (3.9), (3.38), and (3.41).

$$K_I^p = -T_c \sqrt{\frac{2r_c}{\pi}} \int_o^1 \frac{f(t)}{\sqrt{t}} dt = -T_c \sqrt{\frac{2r_c}{\pi}} \left(\frac{4m}{1+2m} \right) \tag{3.42}$$

The crack path plays no first-order role, and the steady-state value of K_I^p may be considered constant for the slightly curved crack as previously claimed. For the special case where T_y is constant throughout the cohesive zone (m approaching infinity), we further observe that

$$\eta = \sqrt{\frac{r_c}{r_p}} \tag{3.43}$$

where r_p is the Dugdale-Barenblatt plastic zone size

$$r_p = \frac{\pi}{8} \left(\frac{K_I}{T_c} \right)^2 \tag{3.44}$$

On the other hand, K_{II}^p is dependent entirely on the crack path, thus requiring a further assumption to obtain an estimate for it. For the gently curving crack, the radius of curvature, R, at the crack tip must be large compared to r_c, and may be considered to

be approximately constant within the process zone. Recognizing that $\varphi(t)=\lambda(t)/r$, This is equivalent to assuming

$$\varphi(r/rc)=A\frac{r}{r_c} \tag{3.45}$$

or

$$\lambda(r/r_c)=A\frac{r^2}{r_c}$$

Thus,

$$\frac{1}{R}=\frac{\partial^2\lambda}{\partial r^2}=2\frac{A}{r_c}$$

$$A=\frac{r_c}{2R}$$

and

$$\varphi(t)=\frac{r_c t}{2R} \tag{3.46}$$

Equations (3.9), (3.17), (3.26), (3.27), (3.40), and (3.41) can be solved iteratively to converge on the actual traction and displacement distributions until a sufficiently accurate solution is obtained. As a first iteration, we assume only the displacements associated with K_I, and set $K_{II}^{(0)}=K_{II}^{p(0)}=0$ (numeric superscripts denoting iteration number). Combining (3.40) and (3.17), we obtain the first approximation for the tractions

$$\frac{T_x^{(1)}}{T_y}=c\frac{\Delta u_x^{(1)}}{\Delta u_y^{(1)}}=c\frac{\varphi}{2} \tag{3.47}$$

Employing these tractions in Equations (3.41) and (3.9), and afterwards employing (3.38) and (3.46), we obtain a first estimate for K_{II}^{p}.

$$
\begin{aligned}
K_{II}{}^{p(1)} &= -T_c\sqrt{\frac{2r_c}{\pi}}\int_o^1\left(\frac{T_x^{(1)}}{T_y}-\frac{1}{2}\varphi(t)\right)\frac{f(t)}{\sqrt{t}}dt \\
&= -T_c\sqrt{\frac{2r_c}{\pi}}\int_o^1\left(\frac{c}{2}\varphi(t)-\frac{1}{2}\varphi(t)\right)\frac{f(t)}{\sqrt{t}}dt \\
&= \frac{(1-c)}{2}T_c\sqrt{\frac{2r_c}{\pi}}\int_o^1\frac{\varphi(t)(1-t^m)}{\sqrt{t}}dt \\
&= \frac{(1-c)}{4}\frac{r_c}{R}T_c\sqrt{\frac{2r_c}{\pi}}\left(\frac{4m}{9+6m}\right)
\end{aligned}
\tag{3.48}
$$

In view of Equations (3.42) and (3.2) this can also be written

$$
\begin{aligned}
K_{II}{}^{p(1)} &= -\frac{(1-c)}{4}\frac{r_c}{R}K_I{}^{p}\left(\frac{1+2m}{9+6m}\right) \\
&= \frac{(1-c)}{4}\frac{r_c}{R}\eta K_I\left(\frac{1+2m}{9+6m}\right)
\end{aligned}
\tag{3.49}
$$

Because the total mode II stress intensity at the crack tip must be zero for the naturally curving crack, we now assume a revised remote loading configuration that results in just enough K_{II} to offset $K_{II}{}^{p}$, maintaining local symmetry at the cohesive crack tip

$$K_{II}{}^{(i)} = -K_{II}{}^{p(i)}$$

Including the mode I and mode II tractions associated with $K_I{}^{p}$ and $K_{II}{}^{p\,(1)}$, we now invoke Equations (3.40), (3.16), (3.26) and (3.27), to obtain a second estimate of the tractions.

$$\frac{T_x^{(2)}}{T_y} = c\frac{\Delta u_x{}^{k(1)} + \Delta u_x{}^{p(1)}}{\Delta u_y{}^{k} + \Delta u_y{}^{p}}$$

$$= \frac{c\left(\frac{\kappa+1}{G}\right)\left[\sqrt{\frac{r}{2\pi}}\left(K_{II}{}^{(1)} + \frac{\varphi}{2}K_I\right) - T_c\frac{r_c}{2\pi}\int_0^1 f(t)\left(\frac{T_x^{(1)}}{T_y} - .25\varphi(t) - .5\left|\varphi(t) - \varphi(r/r_c)\right|\right)\log\left|\frac{1+\sqrt{(r/r_c)/t}}{1-\sqrt{(r/r_c)/t}}\right|dt\right]}{\left(\frac{\kappa+1}{G}\right)\left[\sqrt{\frac{r}{2\pi}}K_I - T_c\frac{r_c}{2\pi}\int_0^1 f(t)\log\left|\frac{1+\sqrt{(r/r_c)/t}}{1-\sqrt{(r/r_c)/t}}\right|dt\right]}$$

$$= c\frac{\frac{K_{II}{}^{(1)}}{K_I} + \frac{\varphi(r/r_c)}{2} - \frac{T_c}{K_I}\sqrt{\frac{r_c}{2\pi(r/r_c)}}\int_0^1 f(t)\left(c\frac{\varphi(t)}{2} - .25\varphi(t) - .5\left|\varphi(t) - \varphi(r/r_c)\right|\right)\log\left|\frac{1+\sqrt{(r/r_c)/t}}{1-\sqrt{(r/r_c)/t}}\right|dt}{1 - \frac{T_c}{K_I}\sqrt{\frac{r_c}{2\pi(r/r_c)}}\int_0^1 f(t)\log\left|\frac{1+\sqrt{(r/r_c)/t}}{1-\sqrt{(r/r_c)/t}}\right|dt}$$

$$= c\frac{-\frac{(1-c)r_c}{4R}\frac{T_c}{K_I}\sqrt{\frac{2r_c}{\pi}}\left(\frac{4m}{9+6m}\right) + \frac{r_c}{4R}\frac{r}{r_c} - \frac{T_c}{K_I}\frac{r_c}{4R}\sqrt{\frac{r_c}{2\pi(r/r_c)}}\int_0^1 f(t)\left[t(c-.5) - \left|t - \frac{r}{r_c}\right|\right]\log\left|\frac{1+\sqrt{(r/r_c)/t}}{1-\sqrt{(r/r_c)/t}}\right|dt}{1 - \frac{T_c}{K_I}\sqrt{\frac{r_c}{2\pi(r/r_c)}}\int_0^1 f(t)\log\left|\frac{1+\sqrt{(r/r_c)/t}}{1-\sqrt{(r/r_c)/t}}\right|dt}$$

$$= \left(\frac{cr_c}{4R}\right)\frac{\frac{r}{r_c} - \frac{T_c}{K_I}\sqrt{\frac{2r_c}{\pi}}\left\{(1-c)\left(\frac{4m}{9+6m}\right) - \frac{1}{2}\sqrt{\frac{1}{r/r_c}}\int_0^1 f(t)\left[t(.5-c) + \left|t - \frac{r}{r_c}\right|\right]\log\left|\frac{1+\sqrt{(r/r_c)/t}}{1-\sqrt{(r/r_c)/t}}\right|dt\right\}}{1 - \frac{T_c}{K_I}\sqrt{\frac{r_c}{2\pi(r/r_c)}}\int_0^1 f(t)\log\left|\frac{1+\sqrt{(r/r_c)/t}}{1-\sqrt{(r/r_c)/t}}\right|dt}$$

$$= \frac{T_x^{(1)}}{T_y}g\left(\frac{r}{r_c}\right)$$

where

$$g\left(\frac{r}{r_c}\right) = \frac{1 - \frac{\eta}{r/r_c}\left(\frac{1+2m}{4m}\right)\left\{(1-c)\left(\frac{4m}{9+6m}\right) - \frac{1}{2}\sqrt{\frac{1}{r/r_c}}\int_0^1 (1-t^m)\left[t(.5-c) + \left|t - \frac{r}{r_c}\right|\right]\log\left|\frac{1+\sqrt{(r/r_c)/t}}{1-\sqrt{(r/r_c)/t}}\right|dt\right\}}{1 - \frac{\eta}{2}\sqrt{\frac{1}{r/r_c}}\int_0^1 (1-t^m)\log\left|\frac{1+\sqrt{(r/r_c)/t}}{1-\sqrt{(r/r_c)/t}}\right|dt} \tag{3.50}$$

The function *g(t)* was numerically evaluated using Mathematica®, and is plotted in Figure 3.12 for $m=2$, $c=1/4$, and various values of η.

Mathematica® is a trademark of Wolfram Research, Inc.

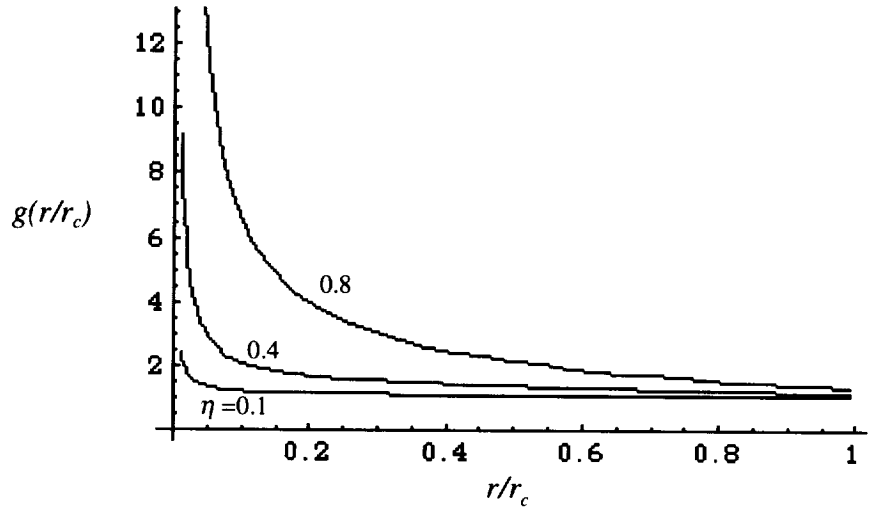

Figure 3.12 Function $g(r/r_c)$ Plotted for m=2, c=1/2

From the second estimate of the tractions, we obtain a second estimate of K_{II}^{p}.

$$
\begin{aligned}
K_{II}^{p(2)} &= -T_c\sqrt{\frac{2r_c}{\pi}}\int_o^1\left(\frac{T_x^{(1)}}{T_y}g(t)-\frac{1}{2}\varphi(t)\right)\frac{f(t)}{\sqrt{t}}dt \\
&= -T_c\sqrt{\frac{2r_c}{\pi}}\int_o^1\left(\frac{c}{2}\varphi(t)g(t)-\frac{1}{2}\varphi(t)\right)\frac{f(t)}{\sqrt{t}}dt \\
&= \frac{r_c}{4R}T_c\sqrt{\frac{2r_c}{\pi}}\int_o^1[1-c\,g(t)](1-t^m)\sqrt{t}\;dt
\end{aligned}
\tag{3.51}
$$

from which we obtain a first estimate of the error in $K_{II}^{p(1)}$

$$
\chi^{(1)} = \frac{K_{II}^{p(1)}}{K_{II}^{p(2)}} - 1 = \frac{4m(1-c)}{9+6m}\left\{\int_o^1[1-c\,g(t)](1-t^m)\sqrt{t}\;dt\right\}^{-1} - 1 \tag{3.52}
$$

Equation (3.52) was numerically evaluated and is plotted as a function of η for various values of m and c in Figure 3.13. Clearly, $K_{II}^{p(1)}$ is a sufficiently accurate

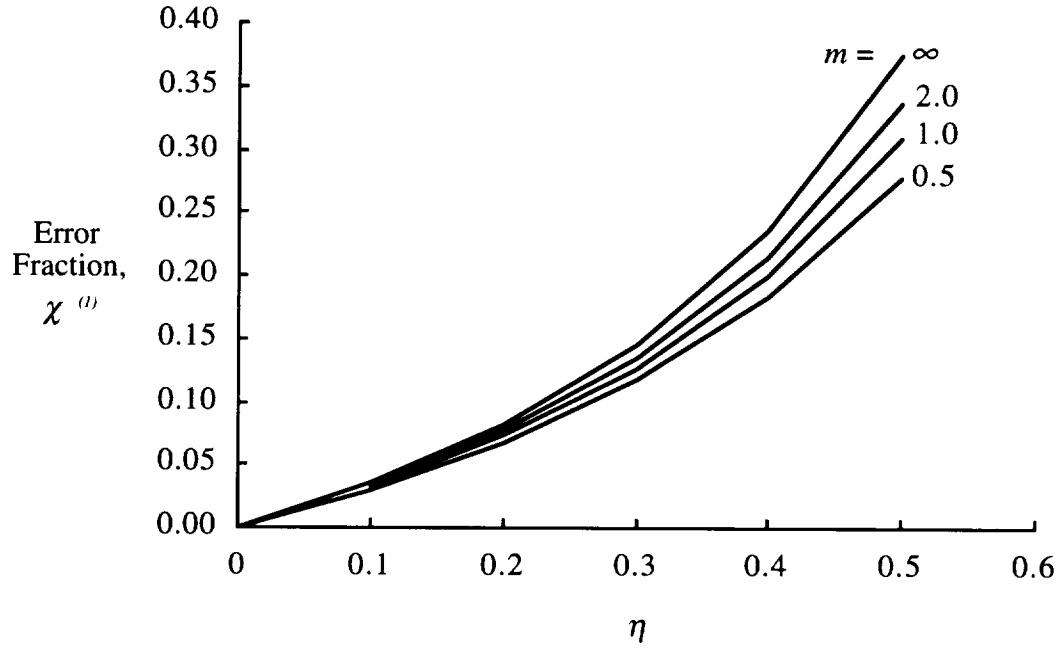

a. Plotted for c= 1/4, various values of m

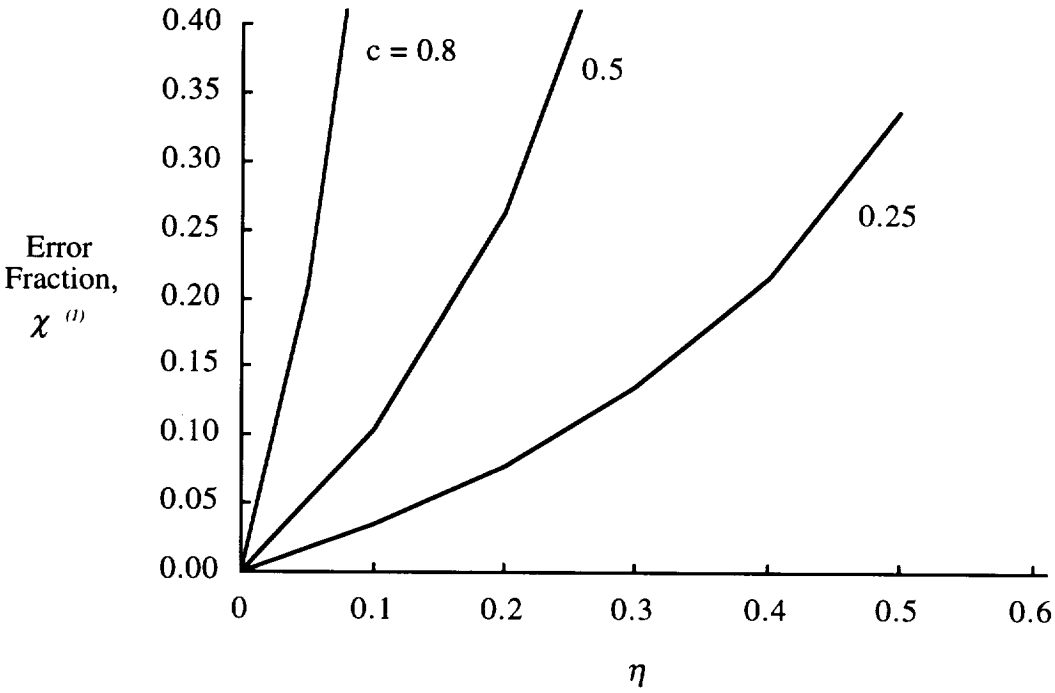

b. Plotted for m=2, various values of c

Figure 3.13 First Estimate of Error in K_{II}^{P} when Evaluated Using Equation (3.36)

approximation only for small values of η. For higher values of η, it is possible to use χ to correct ${K_II}^{P(1)}$

$$ {K_II}^{P} = \frac{{K_II}^{P(1)}}{1+\chi} \tag{3.53} $$

However, assuming a second iteration would yield additional error on the order of $(\chi^{(1)})^2$, the first estimate of χ is likely to provide an increasingly poor estimate beyond a value of about 0.2. Nevertheless, from the foregoing it is apparent that χ is independent of the curvature. Thus, if by further iteration, sufficiently accurate values of χ were to be obtained for higher values of η, ${K_II}^{P}$ could be obtained from (3.53).

3.3 Solution for Future Path of a Naturally Curving Crack

We now consider a gently curving cohesive crack propagating naturally in an isotropic medium. Defining coordinate axes tangent and normal to the cohesive crack tip at an initial position, we now wish to determine the future path of the crack, $\lambda(x)$, as shown in Figure 3.14. In the absence of a cohesive crack tip, Cotterell and Rice expressed the mode II stress intensity at the crack tip to the first order in λ as

$$ K_{II} = k_{II} + \frac{1}{2}\lambda'(l)k_I - \sqrt{\frac{2}{\pi}}\, T \int_0^l \frac{\lambda'(l)}{\sqrt{l-x}}\, dx \tag{3.54} $$

where the lower case k 's are the stress intensities that would act at the initial crack tip in the absence of a cohesive zone, T is the T-stress of the initial crack tip, and l is the length of crack extension beyond the initial crack tip. In keeping with the assertion of a naturally curving cohesive crack, we impose Equation (3.3) to obtain

$$0 = k_{II} + \frac{1}{2}\lambda'(l)k_I - \sqrt{\frac{2}{\pi}}\,T\int_0^l \frac{\lambda'(l)}{\sqrt{l-x}}\,dx + {K_{II}}^p \tag{3.55}$$

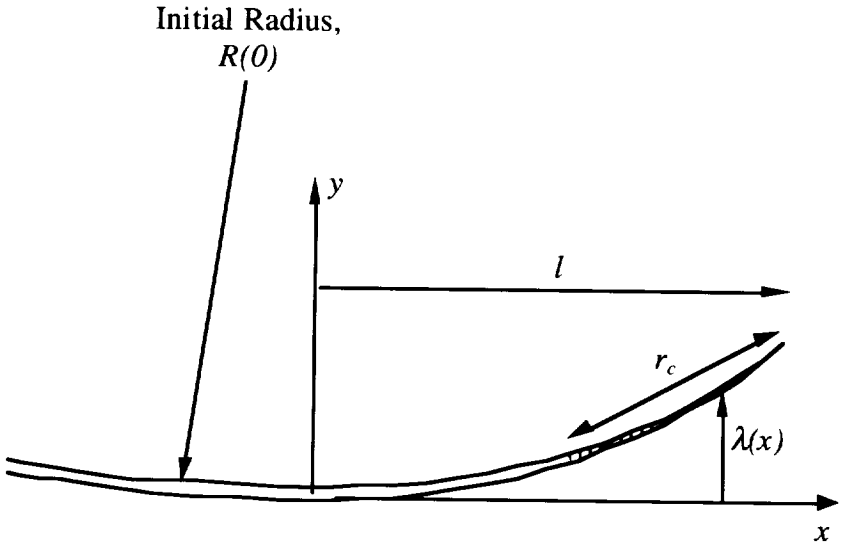

Figure 3.14 Schematic of Curvilinear Crack Problem

Cotterell and Rice give the equation for K_I in terms of k_I for the slightly curved semi-infinite crack. To the first order, the equation is identical to the solution for a straight crack, thus k_I=K_I. Further recognizing that $\lambda''(l) = 1/R$ to the first order in $\lambda'(l)$, and substituting this result and Equation (3.49) into (3.55), we obtain

$$\theta_o = \lambda'(l) - \frac{\beta}{\sqrt{\pi}}\int_0^l \left[\frac{\lambda'(l)}{(l-x)^{1/2}}\right]dx + \rho\lambda''(l) \tag{3.56}$$

where

$$\theta_o = -2\frac{k_{II}}{k_I} = \frac{\rho}{R(0)}$$

$$\beta = 2\sqrt{2}\,\frac{T}{k_I}$$

$$\rho = \frac{\eta r_c(1-c)}{2(1+\chi)}I_c \tag{3.57}$$

$$\eta = -\frac{{K_I}^p}{K_I} = -\frac{{K_I}^p}{k_I}$$

and

$$I_c = \frac{\int_0^1 f(t)\sqrt{t}\,dt}{\int_0^1 \frac{f(t)}{\sqrt{t}}dt} = \frac{1+2m}{9+6m}$$

The latter expression for I_c assumes $f(t)$ is of the form given by Equation (3.38). It should be observed that the perturbation, θ_o, is of a different nature in the present work in that the total mode II stress intensity at the cohesive crack tip is never non-zero, and the crack never kinks as in the solution of Cotterell and Rice. The initial slope of the extending crack is thus zero, and θ_o relates to the initial curvature at the crack tip, rather than an initial kink.

Taking the Laplace transform of Equation (3.56) we obtain (imposing zero initial slope)

$$\frac{\theta_o}{s} = s\bar{\lambda}(s) - \frac{\beta}{\sqrt{s}}s\bar{\lambda}(s) + \rho s^2\bar{\lambda}(s) \tag{3.58}$$

or

$$s\bar{\lambda}(s) = \frac{\theta_o}{\sqrt{s}\left(-\beta + \sqrt{s} + \rho s\sqrt{s}\right)} \tag{3.59}$$

Recognizing the parenthetical expression in the denominator as a cubic polynomial in $\sqrt{s}$, with roots

$$\begin{aligned} a_1 &= \sqrt{s_1} = \frac{d^2 - 3\rho}{3\rho d} \\ a_2 &= \sqrt{s_2} = \frac{3\rho - d^2}{6\rho d} + \sqrt{3}\frac{3\rho + d^2}{6\rho d}i \\ a_3 &= \sqrt{s_3} = \frac{3\rho - d^2}{6\rho d} - \sqrt{3}\frac{3\rho + d^2}{6\rho d}i \end{aligned} \tag{3.60}$$

where $d = \left(\frac{27\rho^2\beta + \sqrt{108\rho^3 + 729\rho^4\beta^2}}{2} \right)^{\frac{1}{3}}$

we can rewrite (3.59) as

$$s\bar{\lambda}(s) = \frac{\theta_o}{\sqrt{s}\left(\sqrt{s} - a_1\right)\left(\sqrt{s} - a_2\right)\left(\sqrt{s} - a_3\right)} \tag{3.61}$$

This can be expanded as partial fractions

$$s\bar{\lambda}(s) = -\theta_o \left\{ \frac{1}{a_1 a_2 a_3 \sqrt{s}} + \sum_{j=1}^{3} \frac{p_j}{\left(a_j - \sqrt{s}\right)} \right\} \tag{3.62}$$

where

$$\begin{aligned} p_1 &= \frac{1}{a_1(a_1 - a_2)(a_1 - a_3)} \\ p_2 &= \frac{1}{a_2(a_2 - a_3)(a_2 - a_1)} \\ p_3 &= \frac{1}{a_3(a_3 - a_1)(a_3 - a_2)} \end{aligned} \tag{3.63}$$

Taking the inverse Laplace transform of Equation (3.62) we obtain

$$\frac{\lambda'(x)}{\theta_o} = -\frac{1}{a_1 a_2 a_3 \sqrt{\pi x}} + \sum_{j=1}^{3} p_j \left[\frac{1}{\sqrt{\pi x}} + \exp\left(a_j{}^2 x\right) erfc\left(-a_j \sqrt{x}\right) \right]$$

$$\frac{\lambda(x)}{\theta_o} = -\frac{2}{a_1 a_2 a_3} \sqrt{\frac{x}{\pi}} + \sum_{j=1}^{3} \frac{p_j}{a_j} \left[\exp\left(a_j{}^2 x\right) erfc\left(-a_j \sqrt{x}\right) - 1 \right] \tag{3.64}$$

When equation (3.64) is evaluated, imaginary parts vanish and only real parts remain. The future crack path predicted by Equation (3.64) is plotted in dimensionless format in Figure 3.15.

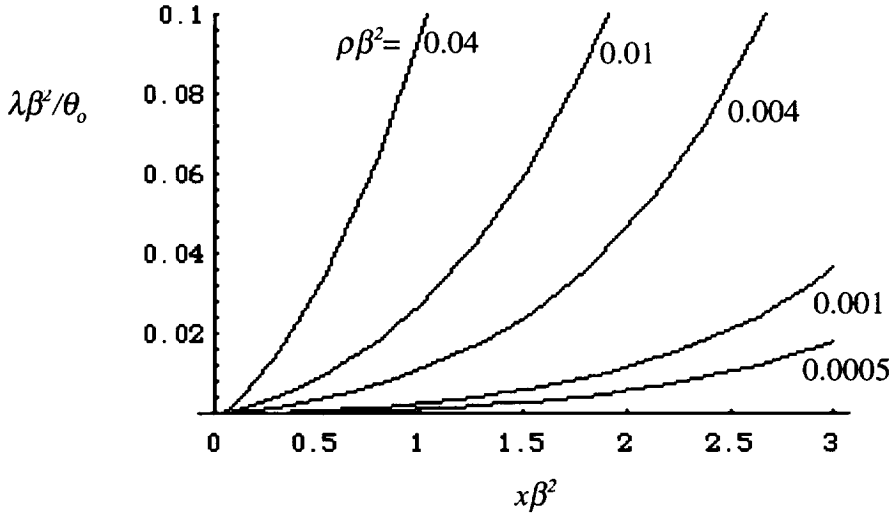

a. T > 0

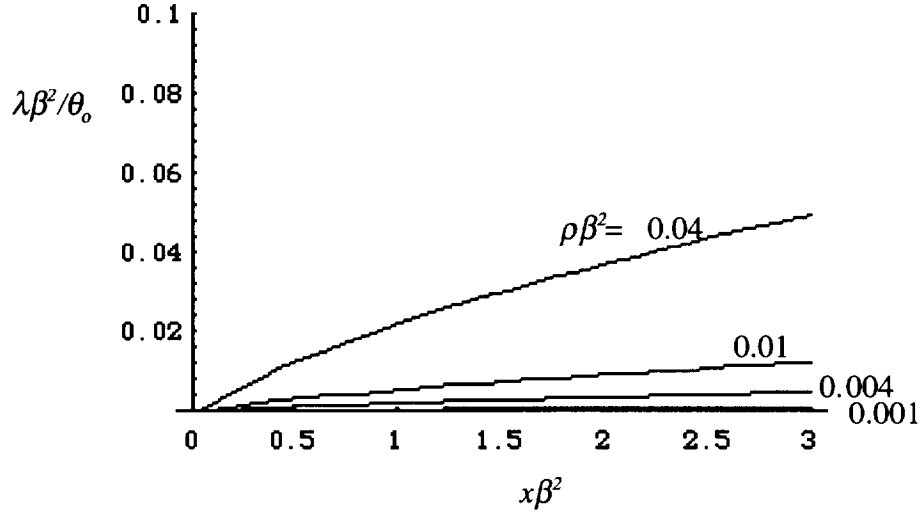

b. T < 0

Figure 3.15 Normalized Plots of Curvilinear Crack Path for Positive and Negative T-Stress

3.4 Discussion

The results shown in Figure 3.15 illustrate that crack path perturbation sensitivity in a positive T-stress environment is influenced by process zone phenomena. The process zone size parameter, ρ, has units of length, and presumably scales with the plastic zone size. Despite potential errors arising from assumptions made in the analyses of the parameters included within ρ in Equation (3.57), the form of the equation (3.56) should be correct. Thus, the larger the process zone, the faster the crack is expected to diverge from a straight path in a tensile T-stress environment. It is also predicted that a compressive T-stress environment tends to stabilize the crack path as suggested by previous investigators, but the present analysis indicates that for the same perturbation magnitude, θ_o, specimens with larger process zone size exhibit greater path disruption.

Qualitatively, this result matches experimental findings given in [9] for Double Cantilever Beam (DCB) specimens made of 2024-T3 aluminum sheet. The present analysis is for a semi-infinite crack in an infinite medium, and is not sufficiently valid for the finite size specimen to warrant direct quantitative comparison. Nevertheless, crack paths observed during stable tearing in static tests turned much more sharply then crack paths developed by fatigue cracking, as shown in Figure 2.7. This confirms the predicted result inasmuch as the loads required to achieve stable tearing were much higher than those imposed during the fatigue cracking process, and thus the process zone would have been much larger, corresponding to faster turning. For both tests, the normalized T-stress corresponded to $\beta \cong 0.37$ mm$^{-1/2}$. The present theory is only valid for the first 10-15 degrees of turning, though the predicted trends would be expected to perpetuate.

As mentioned previously, the perturbation, θ_o is of a different nature than that of Cotterel and Rice, representing an initial curvature, rather than an initial kink angle.

Thus, the present solution cannot be directly compared to their prior solution. In fact, if there is no cohesive zone, $\rho=0$, and the present solution reverts to an unperturbed crack.

3.5 Summary

A boundary layer solution has been developed for a slightly curved cohesive crack propagating in an elastic medium with a cohesive constitutive relationship generalized from a plane stress von Mises plasticity theory to simulate a strain localization zone. An approximate expression for crack face deflections due to the cohesive tractions was developed for the slightly curved crack with zero mode II stress intensity at the crack tip, and it was shown that the stress intensity resultant of the tractions is insensitive to the cohesion induced deflections as long as the strain localization region is small compared to the plastic zone size. Correction factors were provided to estimate the effect of cohesive tractions, extending the solution to somewhat larger cohesive zone sizes.

By enforcing zero mode II stress intensity at the cohesive crack tip, and neglecting the curvature gradient within the cohesive zone, an approximate solution for the future crack path was obtained. The crack path solution predicts that increasing the size of the strain localization zone will amplify crack path instability in a positive T-stress environment, a result that agrees qualitatively with test data.

CHAPTER 4.0

FRACTURE RESISTANCE ORTHOTROPY AND MODAL TRANSITION

4.1 Fracture Orthotropy in Two Dimensions

In general, materials may exhibit elastic anisotropy as well as anisotropy in fracture resistance. Nevertheless, many materials, such as wrought metal products, are virtually isotropic elastically, but have a preferred direction of (mode I) crack propagation resulting from the manner in which the material is processed. Often, as for rolled sheet or plate, the processing is of symmetric character, and the two-dimensional relation describing the crack growth resistance as a function of orientation has two axes of symmetry. This special case is referred to hereafter as two-dimensional fracture orthotropy. For convenience, the orientation describing the crack angle in material coordinates is measured from the longitudinal grain direction, which corresponds to the rolling direction for rolled products. The crack growth resistance is maximum for growth across the rolling direction (θ=90°, or L-T) and minimum for growth parallel to the rolling direction (0°, or T-L) [54, 1]. Materials produced by other processes, such as extrusion, and to a lesser extent forgings, would be expected to exhibit comparable symmetries, at least locally.

We can approximate the orthotropic crack growth resistance as a function of θ of the form [15]

$$K_p(\theta)^n\left(\frac{\cos^2\theta}{K_p(0°)^n}+\frac{\sin^2\theta}{K_p(90°)^n}\right)=1 \tag{4.1}$$

where n is a constant exponent. For the present study, K_p is taken to represent the stress intensity at which the crack propagates. It is proposed [1], that K_p is a material-dependent function of the orientation of the crack tip consistent with the

regime of crack growth. Thus, for fatigue crack growth, K_p represents the stress intensity at which the crack propagates at a given rate; for stable tearing, K_p represents the fracture toughness.

In the context of a maximum stress theory, Buczek and Herakovich [19] suggested a fracture orthotropy relation equivalent to setting n=(-1). They deduced the form of the equation by requiring that the toughness function be independent of θ for isotropic materials, and that it possess the desired orthogonal symmetry, collocating to $K_p(0)$ and $K_p(90)$ values. Kfouri [55] used the more familiar form of an ellipse (n=2). Either case produces a nearly identical oblong shape in polar coordinates for fairly small orthotropy ratios, as illustrated in Figure 4.1. However, for severe values of orthotropy, positive exponents result in an unjustifiably spiked

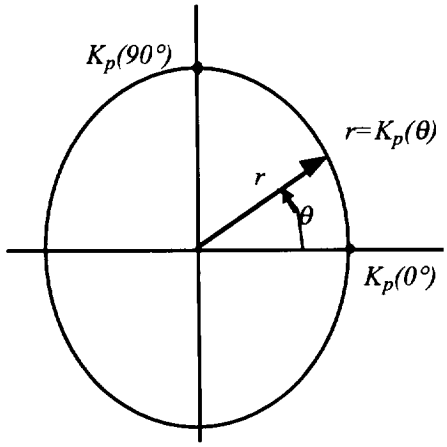

Figure 4.1 Assumed Elliptical Function Describing Crack Growth Resistance as a Function of Orientation for Materials with Fracture Orthotropy

relationship, as illustrated in Figure 4.2, plotted in a normalized format given below. In the absence of data to show otherwise, the use of n=(-1) is favored, or

$$K_p(\theta) = K_p(0°)\cos^2\theta + K_p(90°)\sin^2\theta \tag{4.2}$$

For the two-dimensional problem we define the normalized crack growth resistance as

$$\overline{K}(\theta) \equiv \frac{K_p(\theta)}{K_p(0^o)} \tag{4.3}$$

which varies between unity and $\overline{K}_m$, where $\overline{K}_m$ is the fracture orthotropy ratio defined by

$$\overline{K}_m \equiv \frac{K_p(90°)}{K_p(0°)} \tag{4.4}$$

We can rewrite (4.1) in normalized form as

$$\overline{K}(\theta) = \left(\cos^2\theta + \overline{K}_m^{-n}\sin^2\theta\right)^{-1/n} \tag{4.5}$$

or, for n=(-1)

$$\overline{K}(\theta) = \cos^2\theta + \overline{K}_m \sin^2\theta \tag{4.6}$$

Unless otherwise specified, $\overline{K}$ and $\overline{K}_m$ will be assumed to apply to mode I dominated crack growth, and could thus be designated $\overline{K}_I$ and $\overline{K}_{Im}$. For convenience, the modal subscripts will be omitted unless clarity requires them.

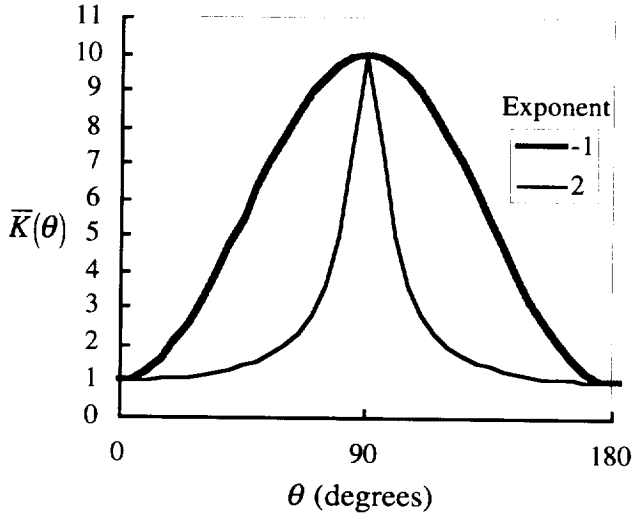

Figure 4.2 The Orthotropic Toughness Function, $\overline{K}(\theta)$, Evaluated for $\overline{K}_m = 0.1$

4.2 Extension to Three Dimensions

In a three-dimensional body a crack may be non-planar, and oriented arbitrarily. At any point along the crack front in an orthotropic material, however, we can characterize the local orientation in terms of the tangent plane and the crack front normal vector within that plane, defined relative to the principal axes of the material.

For an orthotropic material such as a rolled or extruded plate, there are three orthogonal planes of symmetry. Within each of these planes there are thus two orthogonal axes of symmetry. This results in six principal fracture toughness values. The material is assumed to be homogeneous, thus the toughness for a given orientation relative to these principal planes is invariant with regard to translation.

Following the convention established for metals [56], the principle values of fracture toughness are written in a two-letter code (i-j) where the first letter refers to the principle axis normal to the crack plane, and the second subscript identifies the principle axis corresponding to the direction of propagation. These designations have already been mentioned. The standard principal axes for rectangular products (plate, extrusion and forging) correspond to the longitudinal grain orientation (L), the long transverse grain orientation (T), and the short transverse grain orientation (S). Thus, a crack growing normal to the width in the rolling direction of a plate corresponds to the T-L orientation. The (mode I) fracture resistance in this direction we shall designate as K_{TL}. For convenience and generality, we will use numeric subscripts (1,2,3) in place of the metallurgical (L,T,S). The six principal fracture resistances are thus K_{12}, K_{21}, K_{23}, K_{32}, K_{13}, and K_{31}.

What is needed is a function to interpolate the fracture resistance for arbitrary orientations in terms of these principal values. As illustrated in Figure 4.3, a crack (or

a point on an arbitrary crack front) may propagate in an arbitrary direction defined by unit vector

$$\mathbf{a} = a_1\mathbf{i} + a_2\mathbf{j} + a_3\mathbf{k} \tag{4.7}$$

where **i**, **j**, and **k** are unit vectors corresponding to the principal material axes x_1, x_2, and x_3. Vector **a** lies within a plane tangent to the developing crack surface at the crack front, which plane is uniquely described by its unit normal vector

$$\mathbf{n} = n_1\mathbf{i} + n_2\mathbf{j} + n_3\mathbf{k} \tag{4.8}$$

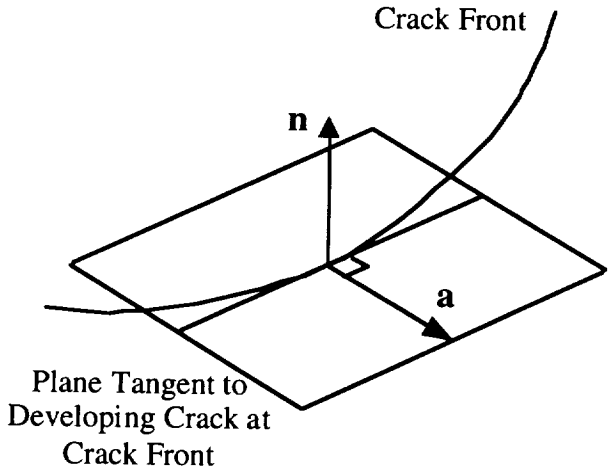

Figure 4.3 Geometry of Crack Orientation at a Point on an Arbitrary Crack Front

The crack orientation is uniquely defined by the direction cosines a_i and n_i. Following the work of Buczek and Herakovich, the interpolation function must

1. Be independent of a_i and n_i for an isotropic material
2. Return the principal fracture resistances for cracks in the corresponding principal orientations.

We seek the lowest order function that can achieve this. Presumably such a function must revert to the two-dimensional form of Equation 4.2 (for this development, we shall assume $n = -1$).

The angles (using right hand rule) describing the trace of **a** on the principle planes are given by

$$\tan(\theta_1) = \frac{a_3}{a_2} \qquad \tan(\theta_2) = \frac{a_1}{a_3} \qquad \tan(\theta_3) = \frac{a_2}{a_1} \tag{4.9}$$

where the angle subscript refers to the axis normal to the principal plane. The fracture resistance of a crack, were it to lie in a principal plane normal to axis x_k and propagate in the direction of the corresponding trace defined in (4.9), can be interpolated in two dimensions in a manner analogous to Equation (4.2)

$$K_k(\theta_k) = K_{ki}\cos^2\theta_k + K_{kj}\sin^2\theta_k \tag{4.10}$$

Further observing the trigonometric identity

$$\begin{aligned}\cos^2\left(\tan^{-1}\frac{b}{c}\right) &= \frac{c^2}{b^2+c^2}\\ \sin^2\left(\tan^{-1}\frac{b}{c}\right) &= \frac{b^2}{b^2+c^2}\end{aligned} \tag{4.11}$$

and the property of direction cosines

$$a_1^2 + a_2^2 + a_3^2 = 1 \tag{4.12}$$

we can combine (4.10) and (4.11) to write

$$\begin{aligned}K_1(\mathbf{a}) &= \frac{1}{1-a_1^2}\left(K_{12}a_2^2 + K_{13}a_3^2\right)\\ K_2(\mathbf{a}) &= \frac{1}{1-a_2^2}\left(K_{23}a_3^2 + K_{21}a_1^2\right)\\ K_3(\mathbf{a}) &= \frac{1}{1-a_3^2}\left(K_{31}a_1^2 + K_{32}a_2^2\right)\end{aligned} \tag{4.13}$$

In essence, these may be considered as the fracture resistance components of **a** in the principal planes, as illustrated in Figure 4.4. Presumably, they must be summed

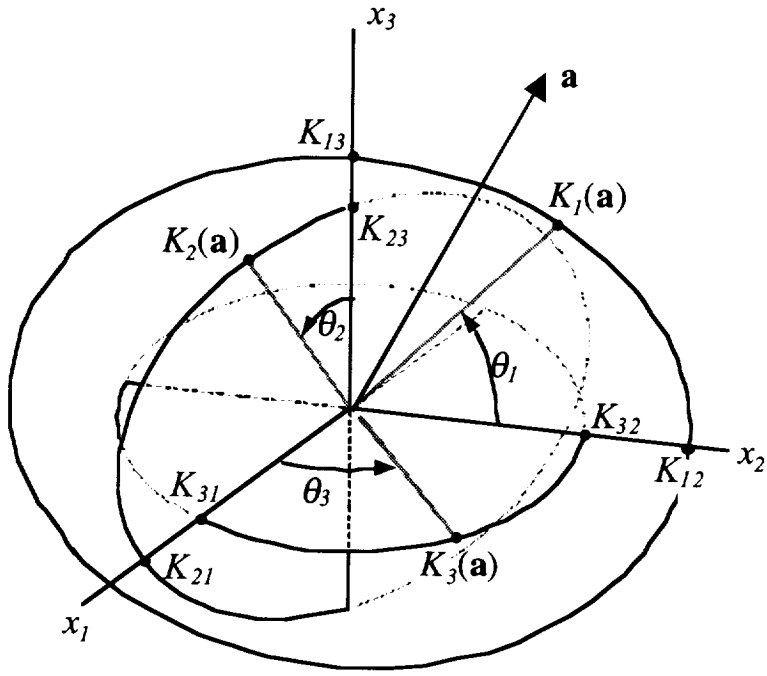

Figure 4.4 Principal Orthotropic Components of Crack Growth Resistance for Crack Growth Parallel to Unit Vector **a**

in some weighted combination based on crack-plane normal **n** to obtain the effective fracture resistance, $K_p(\mathbf{a},\mathbf{n})$. Since the weight factors must sum to unity to satisfy the isotropic case, it seems reasonable to write

$$K_p(\mathbf{a},\mathbf{n}) = K_1 n_1^2 + K_2 n_2^2 + K_3 n_3^2$$

$$= \frac{n_1^2}{1-a_1^2}\left(K_{12}a_2^2 + K_{13}a_3^2\right) + \frac{n_2^2}{1-a_2^2}\left(K_{23}a_3^2 + K_{21}a_1^2\right) + \frac{n_3^2}{1-a_3^2}\left(K_{31}a_1^2 + K_{32}a_2^2\right) \tag{4.14}$$

An inspection of (4.14) shows that it satisfies the criteria previously outlined.

4.3 Modal Transition and Fracture Mode Asymmetry

The first-order isotropic crack turning theories described earlier all predict that the crack will seek out a direction of local symmetry in the stress and strain fields (pure mode I). For the most part cracks are observed to grow in a mode I dominated fashion from a macroscopic point of view. Fracture experiments have shown that this is particularly true of materials failing in a so-called brittle material state, even when the crack is initially loaded in nearly pure mode II. The maximum hoop stress theory (Equation 2.4) predicts that as K_I vanishes,

$$|\theta_c| = \cos^{-1}(1/3) = 70.5° \tag{4.15}$$

where the sign of the θ_c is opposite the sign of K_{II}. Vaughn [57], validated this result for plexiglass (PMMA) within 1° for each of 30 samples tested in pure mode II.

Mixed mode testing of materials in more ductile states, however, can result in straight mode II propagation when the mode mixity includes a sufficiently large mode II component. This was demonstrated in HY130 structural steel at room temperature by Maccagno and Knott [58], who observed that even in mode I loaded static tests, the failure mode clearly followed planes of maximum shear, rather than maximum tension, resulting in zig-zag crack extension macroscopically parallel to the starter crack. With additional mode II loading, crack propagation became less zig-zag, eventually extending in planar fashion along the plane of maximum shear. The failure mode in the regime tested involved void growth and decohesion along planes of maximum shear. Prior work by the same authors [31] noted that mode II propagation was not observed under transgranular cleavage fracture conditions when identical tests were run at low temperature.

In aluminum alloys, crack propagation in mode I under static loading involves void growth and coalescence. Several investigators have observed mode II propagation in aluminum alloys when statically loaded with a large proportion of mode II loading. Among the more recent studies, Hallback and Nilsson [37] observed a transition from mode I to mode II propagation in 7075-T6 at a mode mixity $M^c = .56$, where M^c is as given in Equation (2.6). Their results from 9.5 mm thick Arcan [59] and compact tension/shear specimens showed that crack kinking at initiation followed the maximum tangential stress criterion in the mode I critical regime, and a maximum shear stress criterion in the mode II critical regime. They studied the transition phenomena using a plane strain, small-scale yielding, large-deformation theory to predict shear localization, and obtained results qualitatively similar to the observed behavior.

Amstutz *et al* [38,60] presented the results of mixed mode fracture experiments using 2.3 mm thick 2024-T3 aluminum, showing modal transition to occur at $M^c = 0.24$.

For an initially smooth notch tip loaded under mixed mode static loading, Dalle Donne & Doker [39] described two competing failure modes—a self sharpening phenomenon in the region of maximum shear stress, and a blunting zone in the region of maximum tensile stress. They studied modal transition behavior for the initiation of sharp cracks in 6mm thick StE 550 steel and 5 mm thick 2024-T3 aluminum alloy sheet using biaxial cruciform specimens. While their results did not allow precise determination of the transition mode-mixity parameter, it was about 0.7 to 0.8 for the steel, and somewhere between 0.2 and 0.5 for the aluminum.

In most structural applications cracks initiate and grow macroscopically in such a way that mode I loading dominates. Nevertheless, the preceding information has been provided as a guide to when mode II propagation might become a factor. Also, Dalle Donne and Doker suggested that higher order crack tip stress field parameters

associated with part geometry might affect the transition mode mixity. This concept was studied further by Hallback [61], who also gave a thorough review of related work in modal transition. It should also be mentioned that the transition may not always represent a sharp discontinuity in behavior, but that there may be an intermediate regime where mode I and mode II failure mechanisms may coexist, as discussed by Ghosal and Narasimhan [62].

While the processes that result in modal transition appear to be inelastic phenomena associated with the process zone, it is possible to view the problem in the context of linear elasticity. Kfouri and Brown [63] explained transition-like behavior as a result of the critical fracture toughness being a (smooth) function of mode mixity. In a later paper Kfouri [55] extended the theory to also include fracture toughness orthotropy, and coined the term "fracture mode assymetry" to describe the condition when the critical fracture toughness differs between fracture modes.

Chao and Liu [64] also recognized the potential for fracture mode asymmetry to exist, but rather than defining a smooth-function interaction between modes, they asserted, based on the experimental results of Amstutz and others, that the crack would propagate in the most critical of modes I or II. They defined competing failure modes based on a critical tangential stress or shear stress at a characteristic length from the crack tip (we shall call this r_c). The transition from mode I to mode II fracture would thus be predicted to occur according to the criterion

$$\left.\frac{\sigma_{\theta\theta}(\Delta\theta, r_c)}{\sigma_{crit}}\right|_{\max} \leq \left.\left|\frac{\sigma_{r\theta}(\Delta\theta, r_c)}{\tau_{crit}}\right|\right|_{\max} \tag{4.16}$$

The value of $\Delta\theta$ corresponding to the dominant mode based on (4.16) would be the predicted kink angle. This is shown schematically in Figure 4.4, where the competing failure criteria may be determined from either linear elastic or elastic-plastic (HRR)

stress field solutions. When the crack is critical with respect to the maximum tangential stress, then the crack kinks in the direction in which the maximum tangential stress occurs, as given by Equation (2.5) or Figure 2.4, depending on whether elastic or elastic-plastic theory is used. Otherwise, the crack propagates in direction of maximum shear stress. Based on the Von Mises yield criterion, Chao and Liu further argue that the ratio between the critical stresses for metals would be $\tau_{crit}/\sigma_{crit}=0.577$, which infers for the linear elastic case that transition occurs at $M^e= 0.54$.

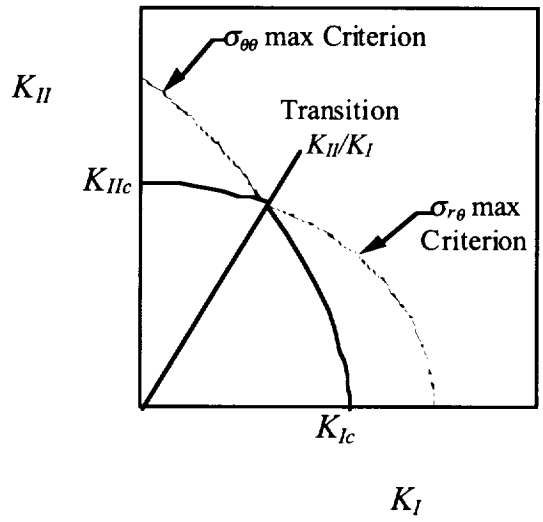

Figure 4.5 Modal Transition Theory, After Chao and Liu [64]

4.4 Summary

Orthotropic interpolation functions have been presented to estimate the fracture toughness for cracks of arbitrary orientation in terms of known principal fracture toughness values. The two-dimensional interpolation approach defined was

extended to three dimensions to support future work in three-dimensional crack turning simulation.

Various literature references have been cited showing that under ambient conditions steel and aluminum alloys fail macroscopically along the direction of local symmetry when loaded primarily in mode I, and the direction of local asymmetry when loaded primarily in mode II, with transition between the modes occurring at some intermediate mode-mixity. The transition mode-mixity may be treated either as a material property, or as a result of differences in critical fracture toughness between the different modes.

CHAPTER 5.0

CRACK TURNING THEORIES WITH PROCESS ZONE EFFECTS AND FRACTURE RESISTANCE ORTHOTROPY

It is the purpose of this chapter to develop practical approaches to simulate crack turning in two dimensions, including process zone effects and fracture orthotropy. The discussion of Chapter 3 provides valuable insights into at least one mechanism by which crack path instability in a positive T-stress environment may be accelerated by the action of a process zone. Nevertheless, the approach has severe geometric limitations, and appears to underestimate the rate at which the crack path diverges.

It was decided to explore two options with regard to crack path simulation, a second-order linear elastic approach which includes a single empirical process zone parameter [18], and a fully elastic-plastic approach which directs the crack based on the crack tip opening displacement [40, 65]. In order to be useful in practical problems, both methods are extended to account for fracture toughness orthotropy, based on the two-dimensional approach of Chapter 4. To a lesser degree, fracture mode asymmetry is also treated where possible.

Both linear-elastic and elastic-plastic methods are later implemented into the FRANC2D or FRANC2D/L adaptive mesh, finite element fracture simulation environment, building on the work of previous researchers. Therefore, it is appropriate to begin with a brief discussion of the piecewise linear manner in which cracks are represented in such simulations.

5.1 Representation of a Curvilinear Crack by a Series of Segments

Following a discussion of crack kinking theories in Chapter 2, the statement was made that "the crack turning problems encountered in many structural applications are not really crack kinking problems". From the first-order theoretical perspective, this meant that a "real" smoothly curving crack followed K_{II}=0 regardless of the kinking theory used, suggesting that the kinking theories are virtually irrelevant. With the exception of the initial kink angle when a crack initiates from a mixed-mode load state, and provided that process zone effects and toughness anisotropy effects are absent, this is largely true.

Nevertheless, when simulating the crack path, it is typically convenient to represent the curved crack as union of a series of linear segments, thus involving a series of kinks. In the FRANC2D environment, the need to kink reflects a limitation of the quadratic element type used, as well as to the fact that the small amount of mode II stress intensity detected at each step is used to determine the incremental path of the crack by virtue of some kinking theory. The program remeshes in the region of the crack tip for each step. Ideally, the path so determined should converge to the "true" crack path as the step size and element size is reduced.

For the isotropic case, following the K_{II}= 0 criterion, a method was proposed by Stone and Babuska [66] to model the crack path as a C^1 continuous (kink free) series of polynomial segments, and implemented their approach in a p-element finite element program using quadratic segments. Two of the three coefficients associated with the quadratic polynomial of each segment were defined to make the path C^1 continuous. The remaining coefficient was iterated to drive K_{II} at the tip of the crack extension to zero within some tolerance.

Stone and Babuska provided theoretical and numerical evidence to substantiate that this method indeed converges to an arbitrarily accurate approximation (limited by the accuracy of the stress intensity solution) of the true crack path so long as the junctions between segments are at least C^1 continuous. Kinks, of course, are only C^0 continuous, and the theory could not prove convergence in this case. Nevertheless, Stone and Babuska performed a highly accurate analysis of a curvilinear crack spanning an arc of about 27 degrees, and compared the path with paths developed by various sequences of quadratic segments, and also by sequences of linear segments using the kinking criterion of Equation (2.4). As the step size was reduced, the kink angles also reduced, thus approaching a smooth crack path. While the curvilinear method was seen to converge more rapidly (with fewer segments) than the kinked crack approximation, it seems apparent from their results that if the kink angles are below 10 degrees for the propagating crack, the path is probably of sufficient accuracy for most engineering purposes. With adaptive mesh codes, such convergence is easily obtained, as observed by Wawrzynek and Ingraffea [16], and Knops [14], among others.

This is not surprising in view of the results presented in Chapter 3, where it is found that in many respects, a slightly curved crack (limited to a threshold of 15 degrees arc by Cotterell and Rice) can be represented to the first order in arc angle by a straight line with an infinitesimal kink at the tip, aligned with the tip of the true curved crack. Thus, one might expect that a slightly curved segment would be sufficiently well represented by a straight segment with an infinitesimal kink oriented tangent to the direction of the next segment (determined according to the criterion K_{II}=0). Note that for small K_{II}/K_I, Equation (2.5) predicts turning angles resulting in K_{II}=0 to the first order in $\Delta\theta$, as can be verified be Equations (2.11).

The above discussion is based on first order, isotropic crack kinking theory, but at least provides support to the notion that for other crack kinking theories, an assemblage of straight segments should converge to a correct theoretical crack path if, as the segment length is reduced, the discrete turning angles become small in regions of curvilinear growth. Of course, this restriction does not apply at the first kink of a crack loaded with mixed mode loading, where the physical fracture response is well represented by a kink.

5.2 Second-Order Linear Elastic Maximum Stress Kinking Theory

5.2.1 Isotropic Maximum Tangential Stress Theory (Mode I Dominated)

The mixed mode expressions for the elastic stress field around a crack tip were introduced in Chapter 2, and are repeated here for convenience, including the first two terms.

$$\sigma_r = \frac{1}{\sqrt{2\pi r}}\cos\frac{\Delta\theta}{2}\left[K_I\left(1+\sin^2\frac{\Delta\theta}{2}\right)+\frac{3}{2}K_{II}\sin\Delta\theta-2K_{II}\tan\frac{\Delta\theta}{2}\right]+\frac{T}{2}(1+\cos 2\Delta\theta) \tag{5.1}$$

$$\sigma_\theta = \frac{1}{\sqrt{2\pi r}}\cos\frac{\Delta\theta}{2}\left[K_I\cos^2\frac{\Delta\theta}{2}-\frac{3}{2}K_{II}\sin\Delta\theta\right]+\frac{T}{2}(1-\cos 2\Delta\theta) \tag{5.2}$$

$$\sigma_{r\theta} = \frac{1}{2\sqrt{2\pi r}}\cos\frac{\Delta\theta}{2}\left[K_I\sin\Delta\theta+K_{II}(3\cos\Delta\theta-1)\right]-\frac{T}{2}\sin 2\Delta\theta \tag{5.3}$$

The classical first-order maximum tangential stress theory given by Equation (2.5) maximizes only the first (singular) term of the tangential stress. This expression predicts straight crack growth unless $K_{II}\neq 0$, as in asymmetric loading or in the case of a perturbed crack.

Williams and Ewing [67] proposed that the crack would propagate in the direction corresponding to the location of maximum tangential stress evaluated at a material dependent finite distance, r_c, ahead of the crack tip, and included the second term in the crack tip stress field expansion. Note the similarity in function of Williams and Ewing's r_c to the parameter of the same name in Chapter 3. Finnie and Saith [18] corrected the formulation of Williams and Ewing for the angled crack problem, and Kosai, Kobayashi and Ramulu [8] later derived a more general formulation of the same second-order theory by forcing the $\Delta\theta$ derivative of (5.2) to zero at $r=r_c$ to obtain the implicit expression

$$\frac{K_{II}}{K_I} = \frac{-2\sin\dfrac{\Delta\theta_c}{2}}{\left(3\cos\Delta\theta_c - 1\right)}\left[\cos\frac{\Delta\theta_c}{2} - \frac{8}{3}\frac{T}{K_I}\sqrt{2\pi r_c}\cos\Delta\theta_c\right] \tag{5.4}$$

Note that according to this expression, the crack may turn with sufficient T-stress even if $K_{II}=0$. In this case, Equation (5.4) yields $\Delta\theta_c > 0$ only if Finnie and Saith's inequality is satisfied[8].

$$r_c > r_o = \frac{9}{128\pi}\left(\frac{K_I}{T}\right)^2 \tag{5.5}$$

where, for $T>0$, r_o represents the distance forward of the crack tip at which the angle of maximum tangential stress becomes non-zero. In Figure 5.1, equation (5.4) is plotted in normalized format using the dimensionless parameter (defined to result in a bifurcation value of unity)

[8] It is observed that K_I^2 in Equation (5.5) could be replaced with $(K_I^2 + K_{II}^2)$ in order to more conveniently represent the behavior in the vicinity of pure mode II. Nevertheless, the present formulation has been chosen to be consistent with previous authors, recognizing also that the theory is not likely valid as $K_I \to 0$.

$$\overline{T} \equiv \frac{8}{3}\frac{T}{K_I}\sqrt{2\pi r_c} = \frac{T}{|T|}\sqrt{\frac{r_c}{r_o}} \tag{5.6}$$

Equation (5.4) can be rewritten in terms of $\overline{T}$

$$\overline{T} = \frac{\sin\Delta\theta_c + \frac{K_{II}}{K_I}(3\cos\Delta\theta_c - 1)}{2\sin\frac{\Delta\theta_c}{2}\cos\Delta\theta_c} \tag{5.7}$$

From Figure 5.1, straight crack growth is predicted only for the case where K_{II}=0, and $r_o > r_c$. As r_o approaches r_c, the predicted path becomes very sensitive to small amounts of K_{II}.

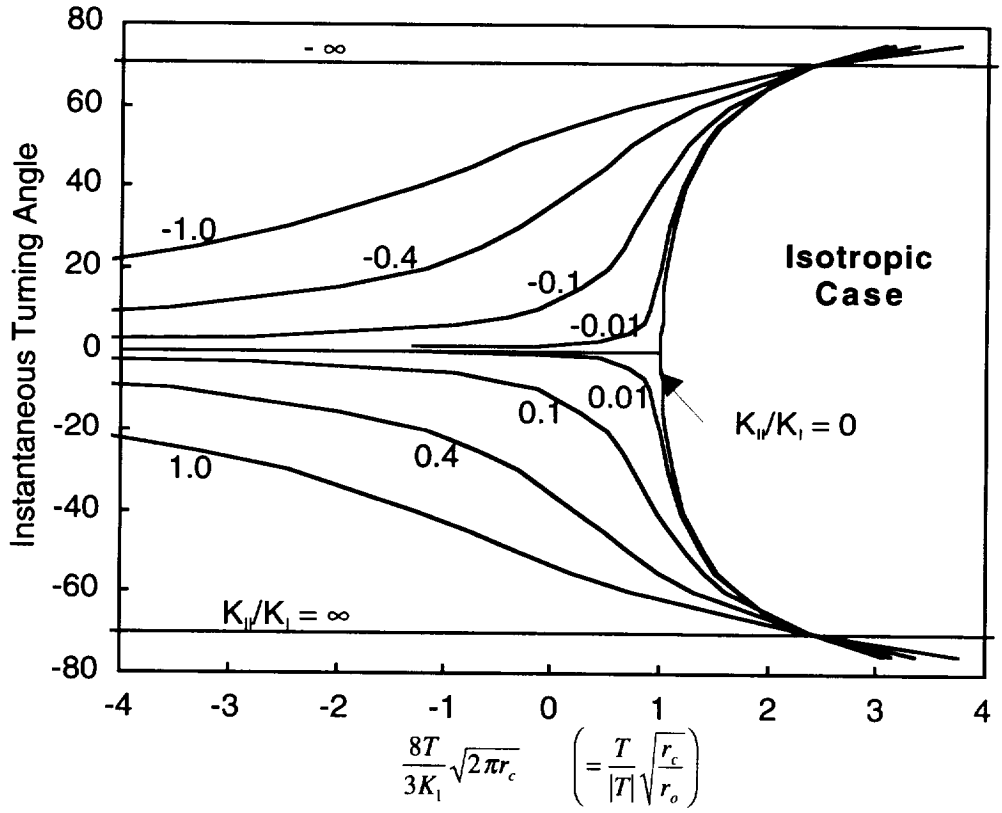

Figure 5.1 Normalized Crack Turning Plot for Isotropic Material Based on the Formulation of Kosai et al [8]

As should be the case, with $T=0$ or $r_c=0$, the maximum tangential stress theory of Equation (5.7) reduces to the first order theory of Equation (2.4). As has been mentioned, Equation (2.4) can be derived either by maximizing σ_θ or by setting $\sigma_{r\theta}=0$. In the case of finite T-stress, one might likewise consider enforcing $\sigma_{r\theta}=0$ to obtain

$$\overline{T}_{(\sigma_{r\theta}\to 0)} = \frac{4}{3}\left(\frac{\sin\Delta\theta_c + \frac{K_{II}}{K_I}\left(3\cos\Delta\theta_c - 1\right)}{2\sin\frac{\Delta\theta_c}{2}\cos\Delta\theta_c} \right) = \frac{4}{3}\overline{T} \tag{5.8}$$

which indicates that the two criteria predict identical kink angles if one recognizes that the applicable characteristic lengths are related by

$$r_{c_{(\sigma_{r\theta}\to 0)}} = \frac{16}{9} r_c \tag{5.9}$$

where the unsubscripted r_c is the characteristic length pertaining to the maximum tangential stress theory defined previously. Thus, the definition of the characteristic length may vary with the criterion used. Before formulating the extension to fracture orthotropy, a discussion with regard to the physical basis and determination of the characteristic length is in order.

5.2.2 The Characteristic Length, r_c, of the Second-Order Maximum Tangential Stress Theory

Irwin [68], Dugdale [45] and others gave approximate expressions for the size of plastic zone in front of a crack tip in elastic-plastic materials. Reasoning that r_c is

related to some failure process, it seems probable that the characteristic length associated with the maximum tangential stress crack turning theory should be no larger than the inelastic zones identified.

Rice and Johnson [69] discussed the role of various characteristic lengths associated with microscopic failure mechanisms in elastic plastic materials, including the crack blunting radius and void spacing, in the context of plain strain fracture problems.

As mentioned previously, the characteristic length associated with crack turning was proposed by Williams and Ewing. As an estimate of the characteristic length for PMMA (plexiglass), they referenced a previous work by Constable, Williams, and Culver [70] which identified equivalent flaw sizes based on fatigue thresholds in polyvinyl chloride of the order of 0.0025 inches. Constable et al conjectured that the equivalent flaw effect might be associated with crazing.

Using photoelastic methods to observe path instability of a nominally symmetric specimen, Ramulu and Kobayashi [71] experimentally determined r_c for PMMA[9] to be 0.05 inches. This was a considerably larger value than those obtained by prior authors, but Theocaris and Andrianopolis [72] independently obtained similar results. While the independent corroboration of r_c data from these authors would seem encouraging, the characteristic length estimate was more than an order of magnitude larger than the plane stress Irwin plastic zone size for this material. Further, based on the fracture toughness and critical T-stress for crack path instability in PMMA given by Selvarathinam and Goree [73], Equation (5.5) would yield a value of r_c= 0.1 inches.

---

[9] Actually, the material used by Ramulu and Kobayashi is designated as "Homelite 100" which the author understands is a commercial form of PMMA. Also, their experiments were dynamic in nature, though they claimed that static values of r_c would be comparable.

While the cohesive, strain softening nature of fracture in this material could enlarge the process zone somewhat, these values of r_c would seem too large based on the scale of any known failure mechanism in that material.

Because imperfections or perturbations giving rise to small amounts of K_{II} can be found in any real specimen, the onset of path instability in nominally symmetric specimens would be expected to occur at an r_o value in excess of r_c. Note from Figure 5.1 that the predicted sensitivity even to very small amounts of K_{II} is substantial as one nears the bifurcation. The more sensitive the manner in which the onset of path instability is detected, the larger the overestimate of r_c that might be expected.

Also using photoelastic methods to observe the onset of path instability in symmetric specimens, Streit and Finnie [74] determined r_c for 7075-T651 aluminum plate to be 0.010 inches. They described r_c as the distance at which void growth or crack initiation will occur, referencing Rice and Johnson and others. Using values of strength and toughness they provided, their value of r_c is about 0.7 times the size of the plane strain Irwin plastic zone radius (plane strain assumed based on their specimen configuration).

Kosai, Kobayashi, and Ramulu [8] later estimated r_c for 2024-T3 and 7075-T6 sheet to be 0.06 inches based on the lengths of micro-crack branches observed along dynamic fracture surfaces of test specimens. This is considerably larger than the value given by Streit and Finnie for 7075-T651 plate, but the method of determination of r_c is completely different than previous methods, and the thickness of the material used would justify a plane stress assumption. In this case, the characteristic length estimate is about a third of the plane stress Irwin plastic zone size for 7075-T6, and more than an order of magnitude less than the plastic zone size of 2024-T3.

Pettit et al [9], found that severe path instability occurred consistently in 2024-T3[10] double cantilever beam specimens at values of r_o at least as high as 0.11 inches (the specimen with the shortest crack, and lowest T-stress tested). To obtain an estimate of r_c, the turning radius was plotted as a function of r_o, and extrapolated to zero turning radius (a sharp kink), at critical value of $r_o = 0.05$ inches. This was subsequently used as a conservative estimate of r_c, though it tended to underestimate crack turning in crack turning simulations. Chen [15] used an r_c value of 0.09 to obtain improved correlation with Pettit's results. A larger r_c would have further improved correlation, but there was concern that r_c was growing too large compared to the K-T dominant zone of the specimen. Also, spurious oscillation was observed in the predicted crack path, and increased with higher values of r_c.

The disagreement in the literature with regard to values of r_c for the various materials tested, and the apparent disparity between some of the values derived from test data and the assumed physical significance of r_c begs reconsideration of the significance of this parameter. The possibility of the onset of plastic instability was considered as a motivating phenomenon as described in Appendix 1.0 (see also Chapter 3). While this concept has merit, it also gives r_c values that are somewhat small with regard to correlating fracture simulations with test data.

Nevertheless, from the equivalence of Equation 5.9, we realize that the characteristic length may not correspond to the actual size of any particular physical damage phenomenon, but that its use in the maximum tangential stress theory is simply a surrogate for something more complex than the theory describes. However, if the

---

[10] More precisely, the material was of NASA vintage stock made to the earlier 24ST designation.

theory is even a decent surrogate, it would be expected that the r_c would be at least proportional in size to some phenomenological length scale. In a later Chapter, r_c will be treated as a state variable, determined to best correlate simulations and test data.

5.2.3 2nd Order Maximum Tangential Stress Theory for Materials with Fracture Orthotropy (Mode I Dominated)

Whereas the isotropic crack turning theory maximizes tangential stress, Buczek and Herakovich [19] suggested that the crack path in anisotropic materials would follow the maximum of the ratio of the tangential stress to the crack growth resistance obtained by

$$\frac{d}{d(\Delta\theta)}\left(\frac{\sigma_\theta(\Delta\theta)}{\overline{K}(\theta+\Delta\theta)}\right)=0 \tag{5.10}$$

Separating variables, we obtain

$$\frac{1}{\sigma_\theta(\Delta\theta)}\frac{d\sigma_\theta}{d\theta}=\frac{1}{\overline{K}(\theta+\Delta\theta)}\frac{d\overline{K}}{d\theta}\equiv\Psi \tag{5.11}$$

Ψ can be obtained in terms of $\overline{K}_m$ using Equation (4.5)

$$\Psi(\theta+\Delta\theta_c)=\left(\frac{2}{n}\right)\frac{\beta\sin 2(\theta+\Delta\theta_c)}{1+\beta\cos 2(\theta+\Delta\theta_c)} \quad \text{where} \quad \beta=\frac{\overline{K}_m{}^n-1}{\overline{K}_m{}^n+1} \tag{5.12}$$

To simplify notation, the argument of Ψ will not be shown explicitly unless it differs from that given above or is required for clarity. Based on the discussion of Chapter 4, a value of n=-1 will be used. Defining Ψ_I with reference to the mode I orthotropy ratio $\overline{K}_{Im}$, evaluating the left hand side of (5.11) with use of Equation (5.2), and solving for $\overline{T}$,

$$\overline{T} = \frac{\sin\Delta\theta_c + \frac{K_{II}}{K_I}\left(3\cos\Delta\theta_c - 1\right) - 2\Psi_I\left[\frac{K_{II}}{K_I}\sin\Delta\theta_c - \frac{1}{3}\left(1+\cos\Delta\theta_c\right)\right]}{\sin\left(\frac{\Delta\theta_c}{2}\right)\left(2\cos\Delta\theta_c - \Psi_I\sin\Delta\theta_c\right)} \tag{5.13}$$

Note that for $\overline{K}_{Im}$=1, Ψ_I =0, and (5.13) reverts to the isotropic form of Equation (5.7).

Equation (5.13) is plotted in Figure 5.2 for $\overline{K}_{Im}$=1.6 with various crack orientations, illustrating how the orthotropy influences the location and nature of the bifurcation. As would be expected, a crack propagating in the direction of least crack growth resistance requires a higher K_{II} or T-stress to alter its course. Conversely, a self-similar crack propagating along the direction of maximum crack growth resistance may turn in a compressive T-stress environment given sufficient fracture orthotropy.

One must take care when evaluating (5.13) to obtain maxima, and not minima. The minima occur to the right of the bifurcation line. In order to derive an expression for the value of $\overline{T}$ where the bifurcation occurs, we examine the limiting case of (5.13)

$$\lim \Delta\theta_c \to 0, \quad \overline{T} = \frac{2}{\Delta\theta_c}\left(\frac{K_{II}}{K_I} + \frac{2}{3}\Psi_I\left(\theta + \Delta\theta_c\right)\right) \tag{5.14}$$

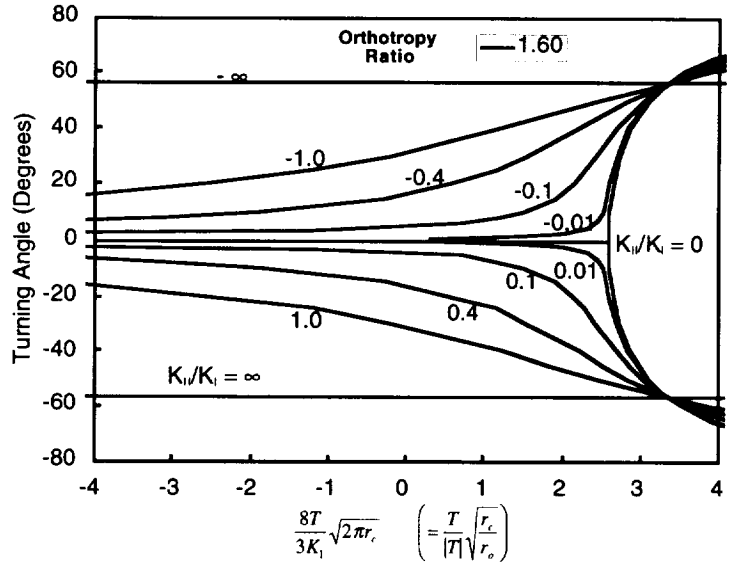

a. Crack Oriented at $\theta = 0°$

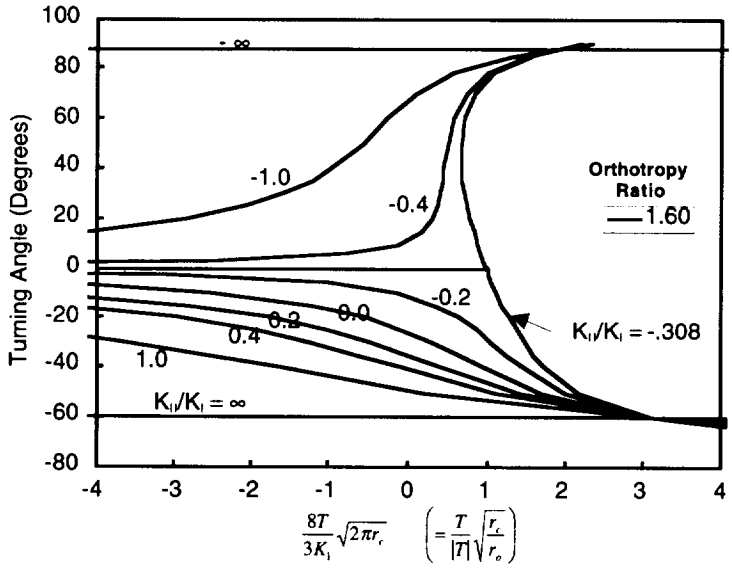

(b) Crack Oriented at $\theta = 45°$

Figure 5.2 Normalized Crack Turning Plots for an Elastically Isotropic Material with Fracture Orthotropy $\overline{K}_m = 1.6$, n=-1, Various Crack Orientations

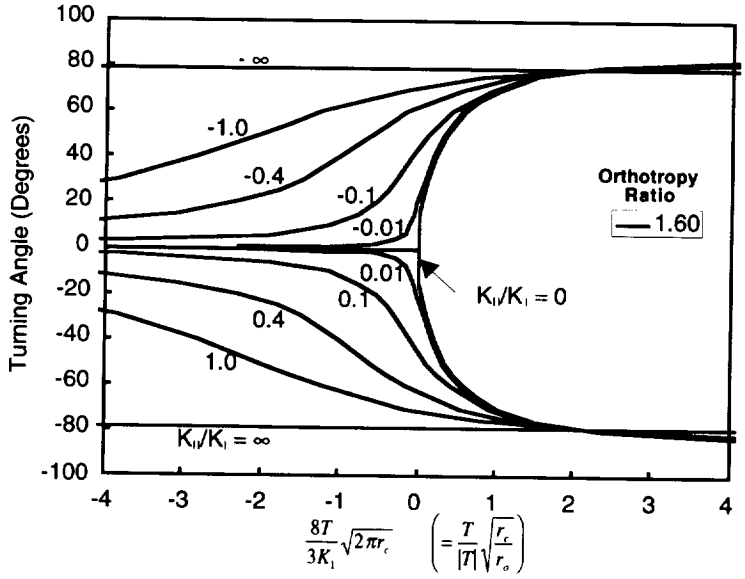

(c) Crack Oriented at $\theta = 90°$

Figure 5.2 Normalized Crack Turning Plots for an Elastically Isotropic Material with Fracture Orthotropy $\overline{K}_m = 1.6$, n=-1, Various Crack Orientations (Continued)

Note that the theory only predicts straight growth where $\overline{T}$ is below the bifurcation value and

$$\frac{K_{II}}{K_I} = \left(\frac{K_{II}}{K_I}\right)_{crit} = -\frac{2}{3}\Psi_I(\theta) = -\frac{2}{3}\Psi_{Io} \tag{5.15}$$

where Ψ_{Io} is defined as Equation (5.12) evaluated at $\Delta\theta_c = 0$. If K_{II}/K_I exceeds this value, then $\Delta\theta_c < 0$. The bifurcation value of $\overline{T}$ is obtained when we assume that (5.15) is satisfied and continue with the limit, from which we obtain

$$\overline{T}_{crit} = 1 + \frac{4}{3}\left(\Psi_{Io}{}^2 + \frac{4\beta(\beta + \cos 2\theta)}{n(1 + \beta\cos 2\theta)^2}\right) \tag{5.16}$$

where β is as given in (5.12).

5.2.4 2nd Order Maximum Shear Stress Theory with Fracture Orthotropy (Mode II Dominated)

The above theory is mode I dominant, inasmuch as σ_θ is analogous to mode I stress intensity. As discussed in Chapter 4, it has been observed that under certain conditions the crack propagates in the direction of maximum $\sigma_{r\theta}$. Following a similar development to the maximum tangential stress theory, the second-order orthotropic maximum shear stress theory can be obtained by maximizing via

$$\frac{d}{d(\Delta\theta)}\left(\frac{\sigma_{r\theta}(\Delta\theta)}{\overline{K}_{II}(\theta+\Delta\theta)}\right)=0 \tag{5.17}$$

to obtain

$$\overline{T}_{II}=\frac{2\cos\frac{\Delta\theta_c}{2}\left[\frac{K_I}{K_{II}}+4\Psi_{II}\left(\left(1-3\cos\Delta\theta_c\right)-\frac{K_I}{K_{II}}\sin\Delta\theta_c\right)\right]-2\left(9\sin\frac{3\Delta\theta_c}{2}+\sin\frac{\Delta\theta_c}{2}\right)+6\frac{K_I}{K_{II}}\cos\frac{3\Delta\theta_c}{2}}{3\left(2\cos 2\Delta\theta_c-\Psi_{II}\sin 2\Delta\theta_c\right)} \tag{5.18}$$

where Ψ_{II} is evaluated in terms of the mode II fracture resistance orthotropy ratio, and

$$\overline{T}_{II}\equiv\frac{8}{3}\frac{T}{K_{II}}\sqrt{2\pi r_c} \tag{5.19}$$

Selected plots of (5.18) are shown in Figures 5.3 and 5.4. In this case, there is no bifurcation, but one must be careful to obtain the global maximum or minimum of the greatest absolute value of the ratio in brackets in Equation (5.17). For the maximum stress theory, transition from mode I to mode II dominated fracture may be postulated to occur when

$$\max\left(\frac{\sigma_\theta(\Delta\theta)}{K_I(0)\overline{K}_I(\theta+\Delta\theta)}\right)\le\max\left|\frac{\sigma_{r\theta}(\Delta\theta)}{K_{II}(0)\overline{K}_{II}(\theta+\Delta\theta)}\right| \tag{5.20}$$

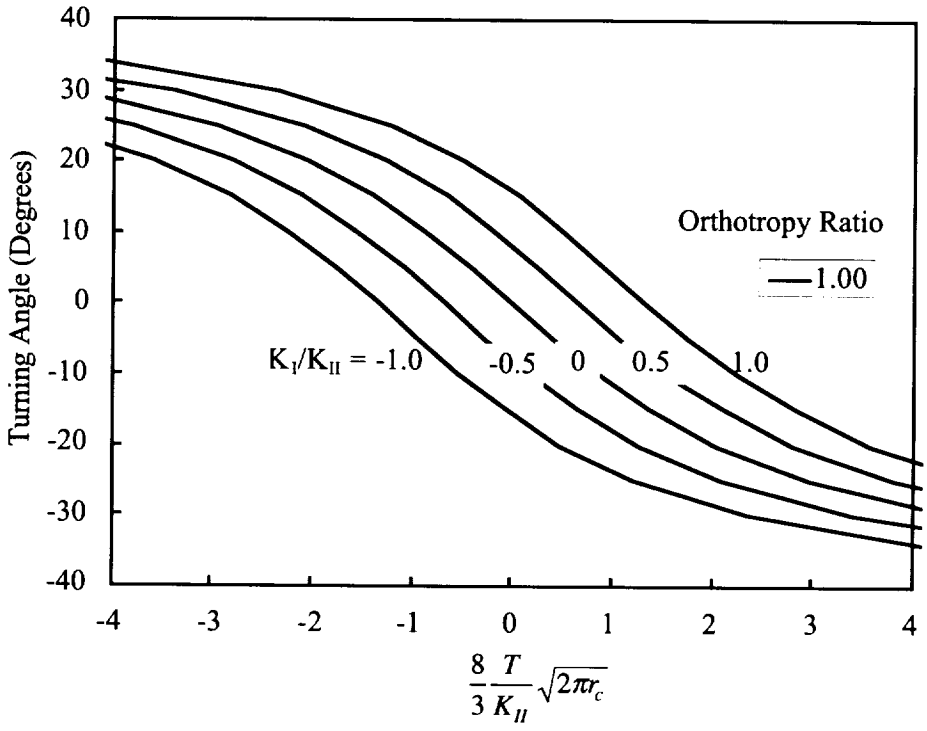

Figure 5.3 Predicted Effect of T-Stress on Kink Angle for Mode II Crack According to Maximum Shear Stress Theory, Isotropic Case

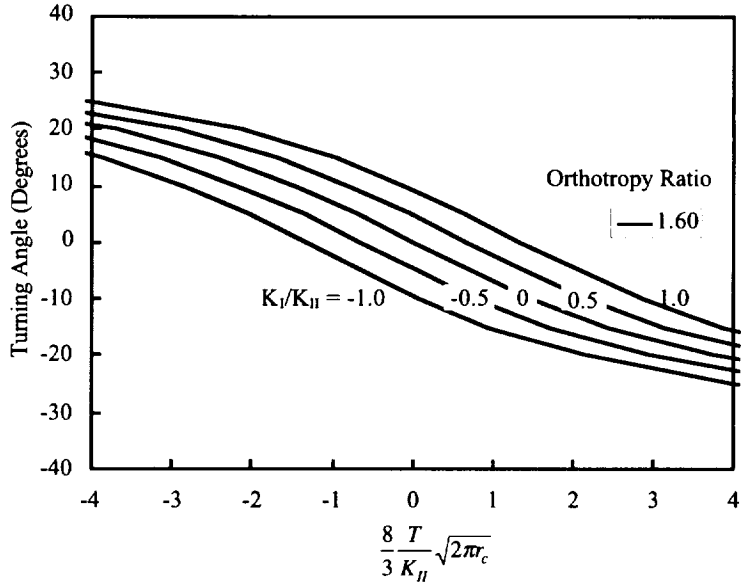

a. Crack Oriented at θ=0°

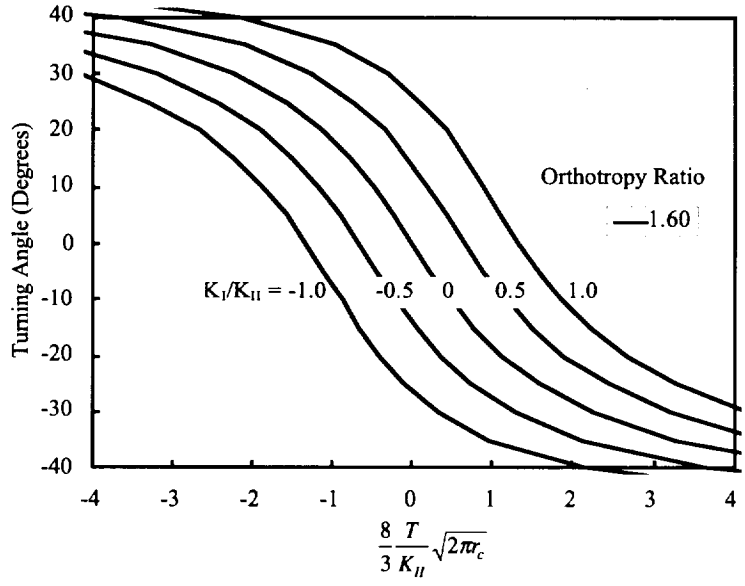

b. Crack Oriented at θ=90°

Figure 5.4 Predicted Effect of T-Stress on Kink Angle for Mode II Crack According to Maximum Shear Stress Theory, $\overline{K}_{IIm}$=1.6, n=-1

5.3 Second-Order Linear Elastic Virtual Kink Theory

Consider a lead crack under plane stress conditions with a plastic zone as shown in Figure 5.5a. Compared to an elastic crack, the plastic zone results in additional deformation that can be approximated by a virtual elastic crack kink as shown in Figure 5.5b. For self-similar crack growth, Wells [75], used the Irwin plastic zone correction as an approximation of the effective elastic kink length to obtain an estimate of the CTOD. While the appropriate choice of length may remain in

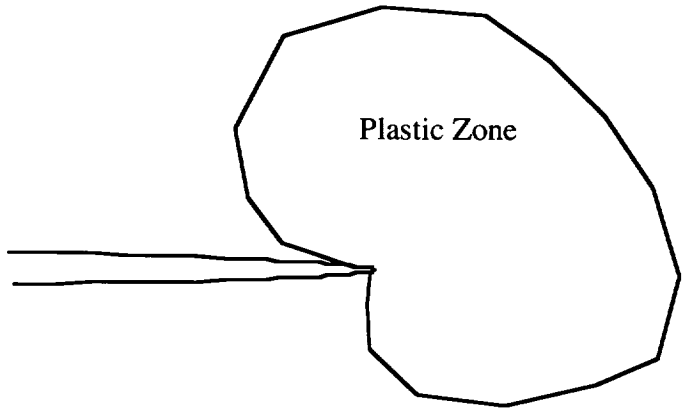

a) Physical crack tip and plastic zone

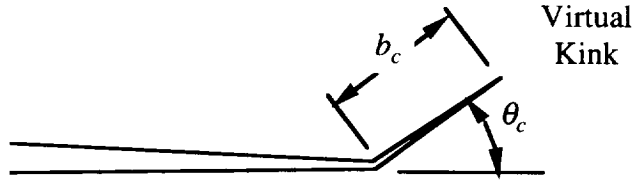

b) Physical crack with virtual kink

Figure 5.5 Crack Tip Plastic Zone Deformation Simulated by an Effective Virtual Kink

question, it is not unreasonable to assert that for a given material and loading, there is a unique kink length, b_c, and orientation, $\Delta\theta_c$, which will best simulate the deformation field as one moves away from the crack tip into the elastic region. *One might even postulate that a crack kink so defined would provide a reasonable approximation of the future crack trajectory. For a crack propagating under steady-state conditions, b_c would be expected to assume a constant, material-dependent value analogous to r_c.*

The direct implementation of such a criterion is problematic. Nevertheless, as linear elasticity is approached (as for so-called brittle materials, and also approximately for slow fatigue crack growth), the length of the virtual kink necessarily vanishes. In this limiting case, Cotterel and Rice [21] concluded, based on a maximum energy release rate argument, that the crack propagates in pure mode I, which is equivalent to the criterion $K_{II}=0$. For a finite (virtual) kink in the presence of non-zero T-stress, setting $K_{II}=0$ does not generally result in maximizing strain energy release rate, nor does it maximize K_I. Nevertheless, depending on the materials and loading conditions, cracks are observed experimentally to develop trajectories corresponding either to pure mode I or pure mode II cracking (see Chapter 4). Based on this evidence, an isotropic theory is proposed based on the concept that the virtual kink representing the process zone of an extending crack will develop in the direction of either pure mode I or pure mode II crack opening.

Isida and Nishino [51] (see also Kfouri [55]) give a solution for a crack in an infinite plate with a kink at one end subject to general in-plane loading. The stress intensity factors at the kink tip, (uppercase) K_I and K_{II}, are expressed in terms of lead crack (lowercase) stress intensities and T as

$$K_I = F_I^{(1)} k_I + F_I^{(3)} k_{II} - F_I^{(2)} T\sqrt{\pi a}$$
$$K_{II} = F_{II}^{(1)} k_I + F_{II}^{(3)} k_{II} - F_{II}^{(2)} T\sqrt{\pi a} \tag{5.21}$$

where a is the crack length, and $F_n^{(i)}$ are functions of the kink angle, $\Delta\theta$, and the normalized kink length, b/a, given in polynomial form by [51]. The crack length parameter can be eliminated by normalizing in the form

$$\frac{K_I}{k_I} = F_I^{(1)} + F_I^{(3)} \frac{k_{II}}{k_I} - \frac{F_I^{(2)}}{\sqrt{b/a}} \frac{3}{8\sqrt{2}} \overline{T}_b$$
$$\frac{K_{II}}{k_I} = F_{II}^{(1)} + F_{II}^{(3)} \frac{k_{II}}{k_I} - \frac{F_{II}^{(2)}}{\sqrt{b/a}} \frac{3}{8\sqrt{2}} \overline{T}_b \tag{5.22}$$

where $\sqrt{b/a}$ divides cleanly out of functions $F_n^{(2)}$, and $\overline{T}_b$ is defined with $b=b_c$ in a manner similar to Equation (5.6).

$$\overline{T}_b \equiv \frac{8}{3} \frac{T}{K_I} \sqrt{2\pi b_c} \tag{5.23}$$

For mode I dominated growth, values of the crack propagation angle, θ_c, can be obtained by varying $\Delta\theta$ to enforce $K_{II} = 0$ for various combinations of k_{II}/k_I and $\overline{T}$, as presented in Figure 5.6. Also shown for comparison is the second-order maximum tangential stress theory of Equation (5.7) with its characteristic length, r_c. The two theories are fairly equivalent (though not identical) if one recognizes that the characteristic lengths differ at the bifurcation by a constant factor,

$$b_c = 2.21 r_c \tag{5.24}$$

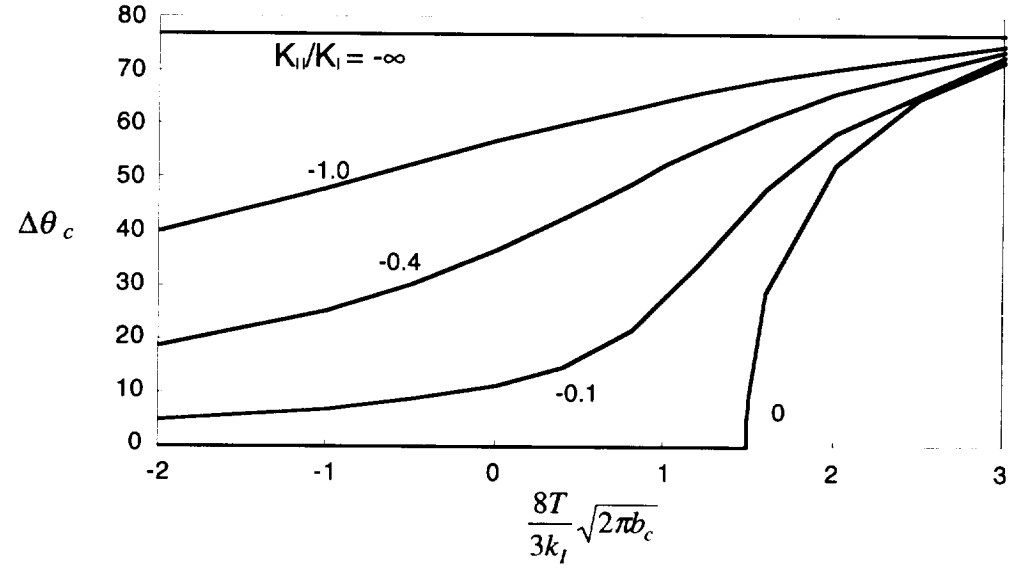

a) Virtual Kinked Crack with Pure Mode I Opening ($K_{II}=0$)

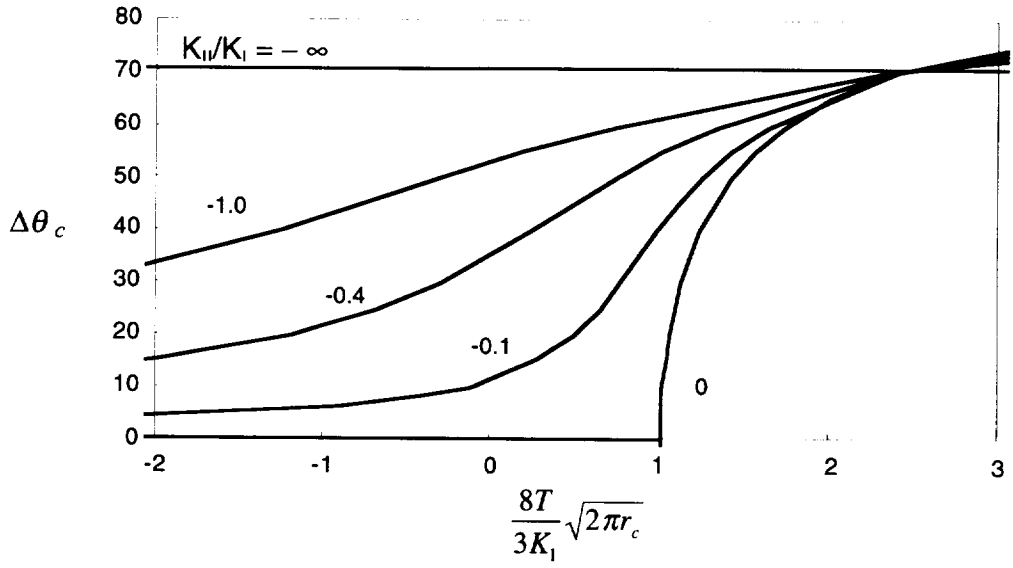

b) 2nd Order Maximum Tangential Stress Theory

Figure 5.6 Comparison of Mode I Virtual Kink Theory with Maximum Tangential Stress Theory

The corresponding mode II fracture behavior was not evaluated, but could easily be developed in the same manner. Nevertheless, from a linear elastic perspective, there is no apparent advantage to this theory over the the maximum stress theory, which is easier to implement, and has already been extended to include toughness orthotropy and modal transition.

5.4 Elastic-Plastic Crack Tip Opening/Virtual Kink Theory

Because the accelerated turning phenomenon sought is believed to be associated with the interaction of the process zone with the T-stress, it seems natural to directly consider crack turning in an elastic-plastic fracture model. Early work in this field showed that plasticity can affect the crack trajectory [36], and supported a notion that crack propagation and trajectory could be correlated with CTOD values [76,38]. Based on results from a small scale yielding (SSY) boundary layer crack tip model and laboratory experiments using 2024-T3 Arcan specimens, Sutton *et al* [40] recently developed curves which can be used to infer the crack growth direction from the ratio of the mode I and mode II CTOD components. These are plotted in Figure 5.7 in terms of the crack tip opening displacements using the notation of Sutton

$$\alpha = \arctan\left(\frac{D_{II}}{D_I}\right) \tag{5.25}$$

where D_I and D_{II} are the mode I and mode II components of crack opening displacement measured or simulated near (0.04 inches from) the tip of the crack. Also shown for comparison is the isotropic linear elastic maximum stress theory based on the observation that for the linear elastic case $D_{II}/D_I = K_{II}/K_I$.

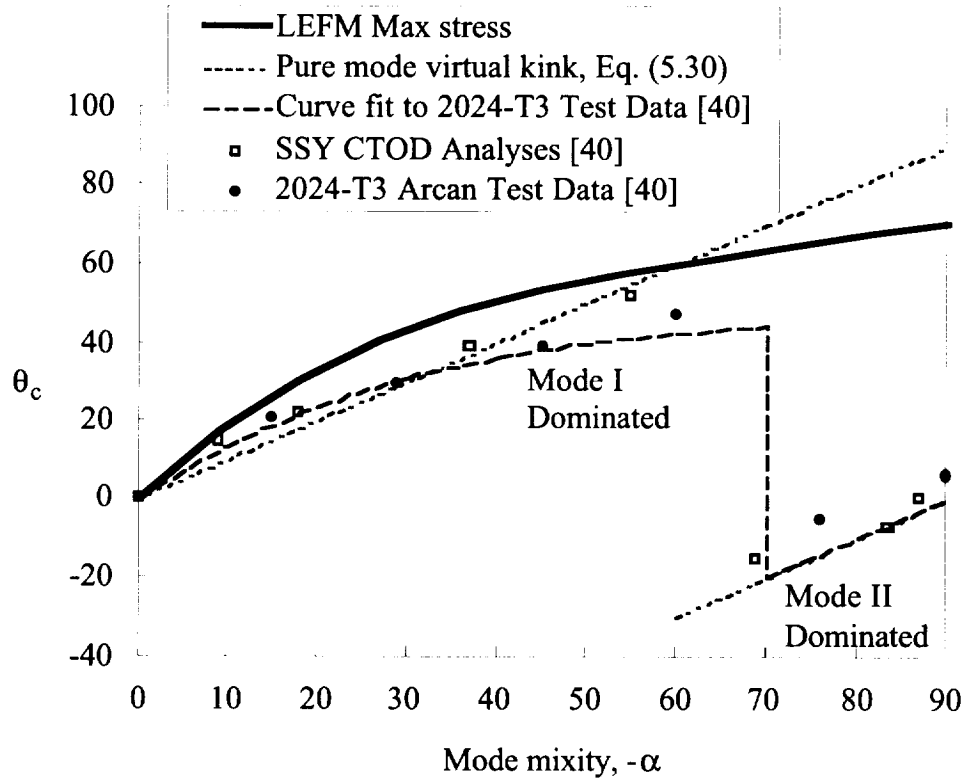

Figure 5.7 Comparison of Various CTOD related Crack-Turning Curves, Including the data of Sutton [40]

Sutton reported 2-D simulations[11] using an elastic/small-deformation plasticity model of a edge crack in a 30.4 inch radius circular plate of 2024-T3 aluminum. The crack tip was centered on the model, and traction boundary conditions were applied representing various amounts of K_I, K_{II} and T. For a given mode mixity, the CTOD components D_I and D_{II} were determined at a distance d=0.04 inches behind the crack tip as loading was increased until the total CTOD,

[11] Several of the details given here were not included in the referenced paper, but were provided via private correspondence with Dr. Sutton.

$$D = \sqrt{D_I^2 + D_{II}^2} \tag{5.26}$$

reached the critical value for propagation, D_c. The crack was then extended 0.0076 inches as a physical kink in several trial directions to find the kink angle, $\Delta\theta c$, that resulted in the maximum total CTOD a small distance back from the kink tip, or

$$\max \delta(\Delta\theta)\big|_{\alpha,T} \tag{5.27}$$

where

$$\delta = \sqrt{\delta_I^2 + \delta_{II}^2} \tag{5.28}$$

and δ_I and δ_{II} are the CTOD components near the kink tip. Angle predictions obtained from these analyses (with T=0) are included as datapoints in Figure 5.7. Significantly, the analyses also showed that the kink orientation that produced the critical CTOD also produced nearly pure mode I or mode II displacement near the kink tip, with a transition between the two modes occuring at about α=70 degrees. A corresponding similar trend was observed in the CTOD displacements and modal transition behavior observed in the Arcan test specimens.

Based on this observation of pure modal growth, which is consistent with the results of other investigators described (see Chapter 4), it is possible to infer some generality into Sutton's results by way of the virtual kink concept introduced earlier. For the kinked-crack representation of the elastic-plastic crack tip, the crack tip opening displacements may be approximated as indicated in Figures 5.8a and 5.8b, depending on whether the virtual kink is assumed to develop in pure mode I or pure mode II. Assuming the CTOD is obtained from an elastic-plastic simulation at some

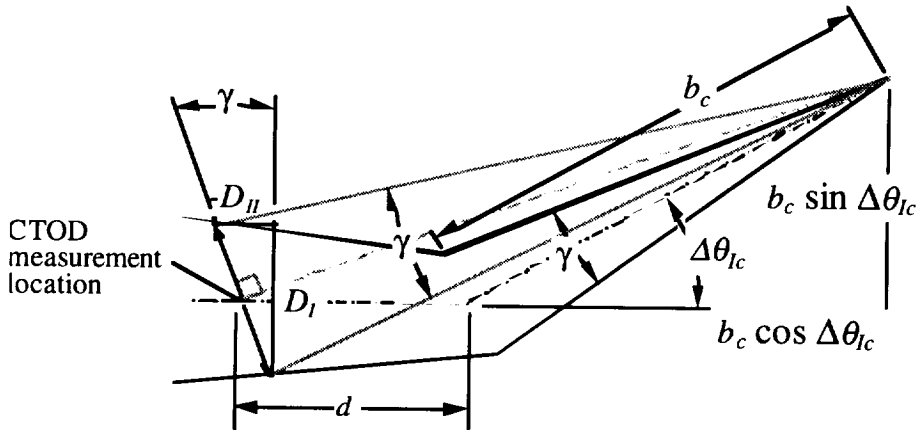

a). Pure Mode I

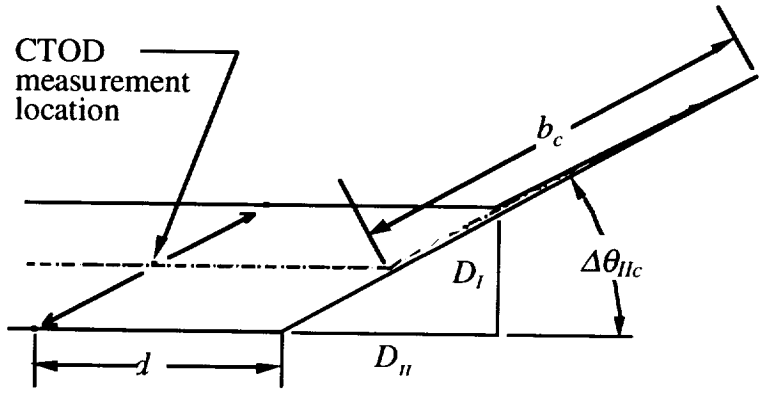

b) Pure Mode II

Figure 5.8 Approximate Method of Obtaining CTOD Mode Mixity for Pure Mode I and Mode II Virtual Crack Kinks

small distance, d, behind the physical crack tip (the physical crack tip being represented by the base of the kink), the following relations may be obtained.

$$\frac{D_{II}}{D_I} = \frac{-\sin\Delta\theta_{Ic}}{\cos\Delta\theta_{Ic} + d/b_c} \qquad \text{for a pure mode I kink} \qquad (5.29)$$

$$\approx -\tan\Delta\theta_{Ic} \qquad \text{(approximation for } d/b_c \rightarrow 0\text{)} \qquad (5.30)$$

$$\frac{D_{II}}{D_I} = \cot\Delta\theta_{Ic} \qquad \text{for a pure mode II kink} \qquad (5.31)$$

Clearly these equations are only crude approximations, but are most accurate and meaningful for small d/b_c. As d/b_c becomes large, D_{II}/D_I must approach the elastic K_{II}/K_I of the physical crack tip, and the effect of plasticity and the T-stress on the turning angle is lost. In the limit as $d/b_c \rightarrow 0$, the Equations simply state that for isotropic mode I dominant growth, the crack grows perpendicular to the CTOD, and for mode II dominant growth, the crack grows parallel to the CTOD.

With the plane stress plastic zone for 2024 on the order of inches, it is expected that d/b_c for Sutton's model is sufficiently small to allow the tangent approximation of Equation (5.30). Equations (5.30) and (5.31) are compared with test data and CTOD-based crack turning angle data in Figure 5.7, showing fair correlation for both mode I and mode II cases.

The point of this discussion lies in the fact that the development of Equations (5.30) and (5.31) make no assumption with regard to the T-stress, or even K_I or K_{II}. The underlying assumption is that the opening of the virtual kink will be either pure

mode I or pure mode II. Inasmuch as Figure 5.6a is also based on pure mode I opening of the virtual kink tip, it is apparent that several different combinations of K_I, K_{II}, and T acting about the physical crack tip can result in the same kink angle. This implies that D_{II}/D_I measured near an elastic-plastic crack tip will be fairly uniquely related to $\Delta\theta_c$, but may not be uniquely related to K_{II}/K_I if plasticity is significant, and the T-stress is substantially non-zero[12]. Sutton also attempted to show this by including T-stress in some of his analyses. Little change was observed in the results, but magnitude of the T-stress used was not disclosed.

Despite the above development, it is not suggested that Equations (5.30) and (5.31) be used as an elastic-plastic crack turning theory. The data from the boundary layer SSY analyses presented in Figure 5.7 are based on a more sound and likely accurate approach, and correlate better with test data. Also, for the purpose of analyzing a smoothly curving crack, the kink angles used in the simulation should be very small as convergence is obtained, thus of greatest importance is the accuracy of the slope of the curve at the origin in Figure 5.7. In this region, the virtual kink approximation appears to perform poorly, and the SSY analyses and test data seem to approach the linear elastic solution.

Sutton curve fit the 2024 Arcan test data as shown in Figure 5.7 and given by[13]

$$\Delta\theta_{Ic} = -36.5\tan^{-1}(2.2\alpha) \quad \text{for } \alpha < \alpha_c \quad \text{(mode I dominated)} \tag{5.32}$$

---

[12] Also worth mentioning is the likelihood that even as the crack tip nears a stiffener or other geometric feature, the virtual kink might still open in pure mode I or mode II. While the plastic zone shape would be distorted by the presence of such irregularities (which would likely affect the crack turning angle), the assumptions associated with the derivation of equations (5.30) and (5.31) are still valid with sufficiently small d, and the crack trajectory should remain a substantially unique function of D_{II}/D_I.

[13] For Equations (5.32) through (5.35), α is in degrees, but the inverse circular functions are evaluated in radians, with constants defined to give a result in degrees.

$$\Delta\theta_{IIc} = 57.3\frac{\alpha}{|\alpha|}\cos(\alpha) \qquad \text{for } \alpha \geq \alpha_c \quad \text{(mode II dominated)} \tag{5.33}$$

$$\alpha_c = 70° \tag{5.34}$$

Arguing that, like the linear elastic solution, the $\Delta\theta_c \sim \alpha$ relationship for the elastic plastic case should not be a strong function of material properties, particularly as $\alpha \rightarrow 0$, Sutton and his colleagues used these curves to predict both initiation and stable tearing crack paths in various aluminum alloys, with encouraging results. However, as part of their study, they also analyzed some of the L-T 7050-T7451 double cantilever beam specimens tested under the NASA IAS program and described in Chapter 7. Due to the significant toughness orthotropy of the 7050-T7451 plate material, cracks turned significantly faster than predicted using Equation 5.32. An extension of the approach to include fracture orthotropy is now presented.

5.5 Extension of Elastic-Plastic Theory to Materials with Fracture Orthotropy

The maximum stress theory for materials with fracture orthotropy discussed earlier predicts that cracks not growing along a material axis of symmetry will grow straight only if loaded at a specific mode mixity, which is a function of the orthotropy ratio and the orientation of the crack (Equation 5.15). At least qualitatively, this description is supported by experience and intuition. In essence, Equation (5.15) is the equivalent to the "criterion of local symmetry" for a crack in a body with fracture toughness orthotropy (an identical criterion can be developed for the linear elastic virtual kink theory described in Section 5.3).

Often, the toughness orthotropy does not appear to be associated with in-plane anisotropy of the yield strength. In 7050-T7451 plate machined to sheet, for example, a plane stress fracture toughness orthotropy ratio of 1.3 has been observed, but the 0 and 90 degree tensile properties are virtually identical [1]. 2024-T3 differs somewhat in the 0 and 90 degree tensile properties, but has less toughness orthotropy than 7050-T7451. Thus it would appear that those processes that result in toughness orthotropy might largely take place after strain localization, where the continuum theories break down.

From a modeling standpoint, this suggests the use of isotropic plasticity for modeling of the near tip stress and deformation field even in materials with fracture orthotropy. For the isotropic case, Sutton determined the elastic-plastic kink angle corresponding to the maximum kink CTOD as described by (5.27). For the orthotropic case, where the critical CTOD, D_c, is a function of orientation, one might determine the orthotropic turning angle according to

$$\max\left(\left.\frac{\delta(\Delta\theta)}{D_c(\theta+\Delta\theta)}\right|_{\alpha}\right) \tag{5.36}$$

Presumably, such an approach could predict transition in much the same way as Equation (5.27). While the CTOD orthotropy function in the denominator could be represented in the manner similar to Equation (4.5), the kink tip CTOD function in the numerator is unknown. One could evaluate (5.36) numerically in a manner similar to that used by Sutton. However, for small kink angles, such as would be needed for simulation of a continuously curving crack, an alternative approximation is suggested

based on the equivalent condition of local symmetry for fracture orthotropy. Only mode I growth is considered, though a similar approach is possible for mode II.

For a smoothly growing mode I crack in a *linear-elastic* material with fracture toughness orthotropy, the instantaneous kink angle $\Delta\theta_{I\,tot}$ must be infinitesimal, and Equation (5.15) must be satisfied at every point along the path. Under these circumstances, the mode mixity is generally non-zero (assuming the crack tip does not happen to be tangent to an axis of material symmetry). Thus, if one were to predict the turning angle assuming isotropy, an additional finite kink angle would be predicted as given by Equation (2.5) for the mode mixity corresponding to (5.15). We thus define an orthotropic correction angle of the same magnitude, but opposite sign, given by

$$\Delta\theta_{I\,orth} = 2\tan^{-1}\left(\frac{1-\sqrt{1+\frac{32}{9}\left[\Psi_I\left(\theta+\Delta\theta_{Ic}+\Delta\theta_{I\,orth}\right)\right]^2}}{\frac{8}{3}\Psi_I\left(\theta+\Delta\theta_{Ic}+\Delta\theta_{I\,orth}\right)}\right) \tag{5.37}$$

where $\Delta\theta_{Ic}$ is given by Equation (5.35), and

$$\Delta\theta_{I\,tot} = \Delta\theta_{Ic} + \Delta\theta_{I\,orth} \tag{5.38}$$

Equation (5.37) is implicit and self-convergent. For a sequence of finite kinks simulating a continuously curving crack, $\Delta\theta_{I\,tot}$ would be finite, but small for a convergent solution. For straight crack propagation the two components of turning in (5.38) cancel.

The orthotropic correction of (5.37) is defined in an exclusively linear elastic context, requiring evaluation of Ψ_I via Equation (5.12), which employs the fracture

toughness orthotropy ratio. Nevertheless, based on the work of Wells [75], the CTOD may be approximated for plane stress by

$$CTOD \sim \frac{K_I^2}{\sigma_y E} \tag{5.29}$$

Thus we obtain the ratio

$$\overline{K}_{Im} = \frac{K_{Ip}(90°)}{K_{Ip}(0°)} \approx \sqrt{\frac{D_c(90°)}{D_c(0°)}} \tag{5.40}$$

from which Ψ_I can be evaluated in an elastic-plastic context. Based on Equations (4.3) and (5.29), we can in similar fashion write

$$\overline{K}(\theta) = \frac{K_p(\theta)}{K_p(0^o)} \approx \sqrt{\frac{D_c(\theta)}{D_c(0^o)}} \tag{5.41}$$

from which it follows by Equation (4.6) that

$$D_c(\theta) = D_c(0°)\left[\cos^2\theta + \overline{K}_m \sin^2\theta\right]^2 \tag{5.42}$$

5.6 Summary

The concept of modeling a smoothly curving crack using a C^o continuous series of linear segments has been discussed in light of the recent results of Stone and Babuska. Their results are strictly valid only for first order, linear-elastic crack turning (K_{II}=0), but suggest that (1) for a convergent solution, the kink angles should approach

zero as the step size is reduced, and (2) the problem is probably sufficiently converged for engineering purposes when the kink angles fall below about 10 degrees.

Various second order crack kinking theories are then studied, including linear elastic maximum tangential and shear stress criteria for mode I and mode II dominated fracture, respectively, and a linear elastic theory assuming pure modal growth both in stress ($\sigma_{r\theta}$=0), and CTOD. These linear elastic theories predict either identical or very similar behavior, if one realizes that the corresponding process zone size parameters (r_c, b_c) differ in size for the various theories. The mode I second-order theory predicts a bifurcation behavior that results in crack kinking under self-similar loading if sufficient T-stress is present. The linear elastic maximum stress theories are extended to account for fracture toughness orthotropy, and to provide a linear elastic prediction for the point of modal transition based on the concept of fracture mode asymmetry.

An elastic-plastic crack turning approach based on the work of Sutton is discussed. Also, an angular correction to account for fracture orthotropy during a smoothly (albeit sharply) curving mode I growth pattern is suggested based on the linear elastic orthotropic theory.

CHAPTER 6.0

SOFTWARE IMPLEMENTATION

In this Chapter, the software implementation of second-order linear-elastic maximum tangential stress theory and the elastic-plastic CTOD crack turning theories will be described. The present effort builds on the framework of the FRANC2D fracture simulation environment, adding various features. In addition to the angle predicting algorithms themselves, a large portion of this Chapter describes the development of a domain integral T-stress calculation method with *a posteriori* error correction.

6.1 The FRANC2D Fracture Simulation Environment

FRANC2D (Fracture ANalysis Code in 2D), developed originally by Paul Wawrzyneck [77, 16] at Cornell University, provides an interactive, adaptive-mesh finite element modeling environment for two-dimensional problems. Cracks are modeled explicitly, and are allowed to develop along arbitrary curvatures (developed out of straight segments). The FRANC2D environment includes:

1. A preprocessor (CASCA) for building the initial (uncracked) geometric model, and meshing it with (isoparametric) quadratic triangular and quadrilateral elements.

2. Interactive databases for material properties and boundary conditions.

3. Adaptive meshing capability modify the mesh to include new or growing cracks.

4. Options for calculating stress intensity factors by different methods.

5. Options for crack kink angle prediction.

6. Postprocessing functions for viewing results, stress intensity history, etc.

During fracture simulation, a finite element model containing a crack is first run to determine the stress intensity factors. The kink angle is then calculated, and the model is remeshed locally to grow the crack an increment in the predicted direction. The cycle is then repeated to simulate further growth. For the purpose of the present study, stress intensity factors were calculated using the J-integral method. FRANC2D integrates around an eight-segment crack-tip rosette of triangular, quarter-point elements, resulting in stress intensity factors with accuracy typically well within one percent (for the highest stress intensity factor) with reasonably good mesh quality.

6.2 Second-Order Linear Elastic Crack Turning Algorithm

An algorithm was written to determine the crack kinking angle according to the maximum tangential stress theory using Equations (5.12) and (5.13). Equations (5.15) and (5.16) were used to ensure that the function was evaluated in the region of maximum (not minimum) tangential stress.

Implementation of the algorithm required some additional programming to support r_c as an additional material property, and to calculate the T-stress.

6.3 Calculation of the T-Stress

6.3.1 Literature Review

T-stress calculations have been performed by various authors. In one of the earliest studies, Larsson and Carlsson [78] evaluated the T-stress using finite elements. Later, Leevers and Radon [41] directly imposed the infinite series solution given by Williams [23] in a variational approach to obtain estimates of K_I and T simultaneously. They gave estimates of the T-stress in the form of the dimensionless parameter

$$B = \frac{T\sqrt{a}}{K_I} \tag{6.1}$$

Based on the convergence observed, Leevers and Radon estimated the error in the B values they provided for various specimen geometries to be less than three percent. Sham [79] used second-order weight functions and a work conjugate integral to calculate T-stresses in various specimen configurations. Fett [80,81] introduced a Green's function approach to calculate T-stresses, and analyzed numerous configurations. A more approximate displacement correlation method was outlined by Al-Ani and Hancock [82] which is nevertheless easy to implement in plate and shell codes, and has been utilized in various forms by other authors [9, 14, 15].

Cardew et al [83] and Kfouri [84] computed the T-stress using a modified J-integral based on unpublished work of Eshelby, and also gave results for selected specimens based on finite element analyses. Another type of path independent integral based on the Betti-Rayleigh reciprocal theorem has also been proposed by Sladek *et al* [85] and also by Yuan and Yang [86], and was shown to be mathematically equivalent to the J-integral method by Chen *et al* [87, 15]. By implementing the contour integral solution into a high polynomial order (p-version) finite element program, Chen obtained T-stresses that were claimed to be numerically

exact to at least five significant figures. The numerical accuracy was verified by way of an exact benchmark solution (a crack tip and surrounding region with the exact boundary conditions applied corresponding to arbitrary combinations of K_I, K_{II}, and T) and a theoretical error relationship

$$e_T = T_{FE} - T = \tilde{e}_T \frac{K_I}{\sqrt{r_1}} \tag{6.2}$$

where e_T is the error in the computed T-stress, r_1 is a characteristic dimension of the integration zone, and $\tilde{e}_T$ is a coefficient related to the discretization error in the vicinity of the integration zone.

Note that (6.2) predicts that the error in the computed T-stress is degraded as the size of the integration domain is reduced—a trend common to both integral methods described. Also, the integration must be performed about a straight segment at the crack tip. This means that when modeling a curvilinear crack, the integration radius cannot exceed the increment dimension, and as the step size is reduced, as required for path convergence, the accuracy of the T-stress solution will be simultaneously degraded.

Nevertheless, using the highly accurate solutions for simple geometries provided by Chen as benchmarks, together with the error estimation parameter, it was found that much of the error in the contour integral results is of a systematic nature, and can be corrected *a posteriori* for a given rosette geometry. Following a brief review of the contour integral solution based on the Betti-Rayleigh reciprocal theorem [15], an error correction scheme will be discussed, and correction parameters will be determined for the element type and rosette geometry of FRANC2D.

6.3.2 Contour Integral Methods

The Betti-Rayleigh reciprocal theorem can be written for a two-dimensional body bounded by a closed curve S without body forces as

$$\oint_S (T_i^* u_i - T_i u_i^*) dS = 0 \tag{6.3}$$

where T_i represents a set of surface tractions with resulting surface displacements u_i, and T_i^* and u_i^* are an independent set of surface tractions and corresponding surface displacements, referred to as *auxiliary fields*. By evaluating the integral at a crack tip around the closed four-segment path shown in Figure 6.1, and recognizing that segments C_+ and C_- are traction free, path independence can be shown with regard to the other two segments.

$$\int_C (T_i^* u_i - T_i u_i^*) dC = \int_{C_\varepsilon} (T_i^* u_i - T_i u_i^*) dC_\varepsilon \tag{6.4}$$

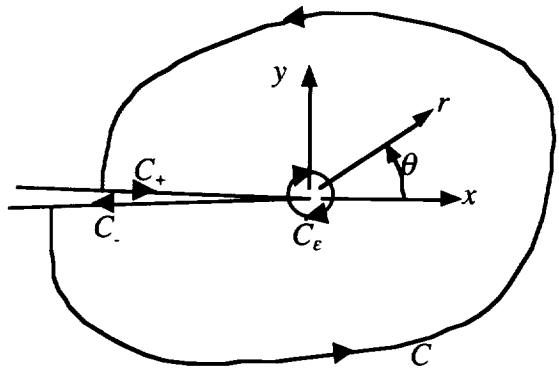

Figure 6.1 A Closed Contour Around a Crack Tip

By substituting $T_i = \sigma_{ij} n_j$ for each field, where n_j are components of the outward normal vector along the corresponding path segment, we obtain

$$\int_C (\sigma^*_{ij} u_i - \sigma_{ij} u^*_i) n_j dC = \int_{C_\varepsilon} (\sigma^*_{ij} u_i - \sigma_{ij} u^*_i) n_j \, dC_\varepsilon \tag{6.5}$$

Defining ε as a characteristic dimension of path C_ε, the right hand side can be evaluated analytically as $\varepsilon \to 0$ using the two-dimensional crack tip stress and displacement field solution given by Williams [23]

$$\begin{aligned} \sigma_{ij} &= \sum_{\lambda=-\infty}^{+\infty} A_\lambda r^{\frac{\lambda}{2}} f_{ij}^{\lambda}(\theta) \\ u_{ij} &= \sum_{\lambda=-\infty}^{+\infty} B_\lambda r^{\frac{\lambda}{2}+1} g_{ij}^{\lambda}(\theta) \end{aligned} \tag{6.6}$$

where $\frac{\lambda}{2}$ is the eigenvalue, and A_λ and B_λ are the corresponding coefficients for each eigenvalue. By choosing auxiliary fields corresponding to

$$\begin{aligned} \sigma^*_{ij} &\sim r^{-\frac{\lambda}{2}-2} \\ u^*_i &\sim r^{-\frac{\lambda}{2}-1} \end{aligned} \tag{6.7}$$

in Equation (6.5), coefficients of order $\frac{\lambda}{2}$ alone are obtained. T is of order $\lambda=0$, corresponding to auxiliary stresses and displacements in local Cartesian coordinates (see Figure 6.1) of

$$\begin{aligned} \sigma^*_{xx} &= \frac{\cos 2\theta + \cos 4\theta}{2\pi r^2} \\ \sigma^*_{yy} &= \frac{\cos 2\theta - \cos 4\theta}{2\pi r^2} \\ \sigma^*_{xy} &= \frac{\sin 4\theta}{2\pi r^2} \end{aligned} \tag{6.8}$$

$$u_x^* = -\frac{\kappa\cos\theta + \cos 3\theta}{8\pi rG}$$
$$u_y^* = \frac{\kappa\sin\theta - \sin 3\theta}{8\pi rG} \tag{6.9}$$

where G is the shear modulus, $\kappa=(3-\nu)/(4+\nu)$ for plane stress, and $\kappa=(3-4\nu)$ for plane strain problems. The T-stress is then obtained for $\varepsilon \rightarrow 0$ as

$$T = \frac{8G}{\kappa+1}\int_{C_\varepsilon}(\sigma_{ij}^* u_i - \sigma_{ij} u_i^*)n_j\, dC_\varepsilon \tag{6.10}$$

By virtue of the path independence of (6.5), an equivalent integral can be performed numerically using stresses and strains from the finite element analysis (superscript FE)

$$T = \frac{8G}{\kappa+1}\int_{C}(\sigma_{ij}^* u_i^{FE} - \sigma_{ij}^{FE} u_i^*)n_j\, dC \tag{6.11}$$

or the equivalent domain integral [15]

$$T = \frac{8G}{\kappa+1}\iint_{A}(\sigma_{ij}^* u_i^{FE} - \sigma_{ij}^{FE} u_i^*)q_{,j}\, dA \tag{6.12}$$

where A is a domain surrounding the crack tip bounded by curves Γ_0 and Γ_1, and function q is equal to unity on Γ_0 and zero on Γ_1. For the FRANC2D implementation, the domain A is the area comprising the outer ring of the crack tip rosette as illustrated in Figure 6.2. The integration zone radius, r_1, also shown in Figure 6.2, is twice the internal radius of the domain for the FRANC2D implementation.

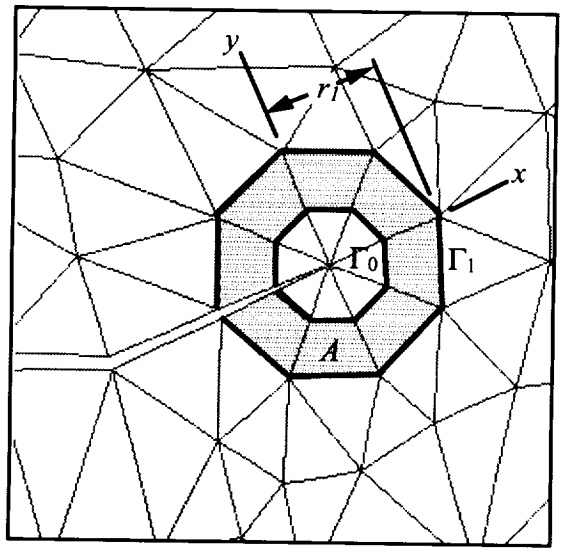

Figure 6.2 Rosette Configuration (Midside Nodes not Shown) and Integration Domain Used in FRANC2D Implementation

6.3.3 Error Correction Scheme

Equation (6.2) was derived by recognizing that the stress contribution of the singular terms in the stress field will converge far slower than the contribution of the non-singular terms, leaving an error in the coefficients of all terms proportional to the coefficients of the singular terms[13]. The square root term in the denominator was included due to dimensional considerations, consistent with the form of Equations (5.1) through (5.3). Based on a similar convergence rate argument, terms of higher order than T are expected to contribute little error to the computed value of T.

Unlike the error estimation expression given in [87,15], we have taken the liberty to write Equation (6.2) with no absolute value signs enforcing that the error measure always be positive. This represents an assertion which we now acknowledge—namely, that the sign and magnitude of $\tilde{e}_T$ is (at least on an average basis) a characteristic of the rosette configuration. Thus, if the value of $\tilde{e}_T$ were

[13] In spite of this argument, K_{II} was found to have no pollution effect on the T-stress in numerical experiments.

known for a given rosette configuration, the systematic error in a T-stress value calculated using that rosette could be estimated (and thus corrected) via Equation (6.2). The influence of scaling the rosette dimension is captured by way of the length parameter r_1.

The veracity of this assertion can be supported by rewriting (6.2) in the form of the relative error

$$e_{T_{rel}} = \frac{e_T}{T} = \tilde{e}_T \frac{K_I}{T\sqrt{r_1}} \tag{6.13}$$

The assertion that the relative error in T-stress scales with the dimensionless parameter $K_I/T\sqrt{r_1}$ is supported by the observation that geometrically similar finite element models which differ only in scale (which implies that the integration path is likewise scaled), should give numerically identical error fractions in the computed T-stress (or any other local stress measurement). In essence, the rosette may be considered as a finite element model with imposed boundary conditions representing K_I and T. Recognizing the similarity of all K_I and T fields relative to a characteristic length $(K_I/T)^2$, one may therefore conclude that the combination of such a field with a rosette model of fixed geometry and scale relative to the field characteristic length will be similar (and thus have comparable relative error) to all other rosette/field combinations with the same relative scaling ratio.

Because $\tilde{e}_T$ represents the discretization error in the vicinity of the integration zone, it should thus be relatively constant so long as the mesh geometry, or rosette, within the integration zone is geometrically similar for all problems. The mesh geometry outside of the integration zone is of secondary influence, and may change from problem to problem, thus its effect will be treated as a probabilistic source of

error. Nevertheless, provided that the external mesh is reasonably proportioned, the error introduced should be relatively small.

Based on some highly accurate T-stress solutions, we now proceed to numerically verify the foregoing assertions, and determine the value of the error parameter, $\tilde{e}_T$, for the rosette configuration of Figure 6.2.

6.3.4 High Accuracy Reference Solutions

Chen [87, 15] implemented the Betti Reciprocal type integral into a highly accurate p-finite element code, and analyzed various model configurations. First, a square model of a crack tip was constructed as shown in Figure 6.3, with a numerically exact external traction distribution imposed representing arbitrary combinations of K_I, K_{II}, and T.

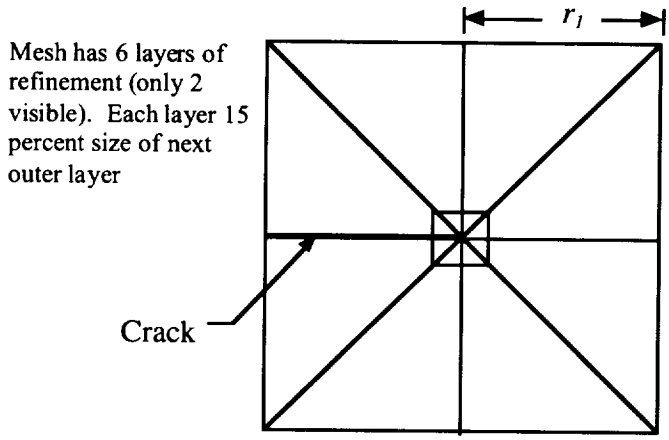

Figure 6.3 Rosette Configuration Used in p-element Implementation [87,15]

With this model, Chen showed that by increasing the polynomial order of the solution, the relative T-stress error could be reduced to about 10^{-6} with the rosette geometry used and an element shape function order, p =11. Extremely accurate stress intensities

were also obtained. The T-stress error data is re-plotted in Figure 6.4 in terms of $\tilde{e}_T$, showing that for the rosette of Figure 6.3, $\tilde{e}_T$ is characteristically negative for all p values evaluated, and is a logarithmic function of p. It was also verified by varying load (K_I) and r_1 that $\tilde{e}_T$ is constant for a given level of p.

Having established the extremely tight accuracy of the rosette geometry at high values of p, Chen then embedded the same rosette geometry within the meshes of various test specimen geometries to obtain solutions estimated to be within five significant figures of accuracy. The specimen geometries are summarized in Figure 6.5, and the results tabulated[14] in Table 6.1.

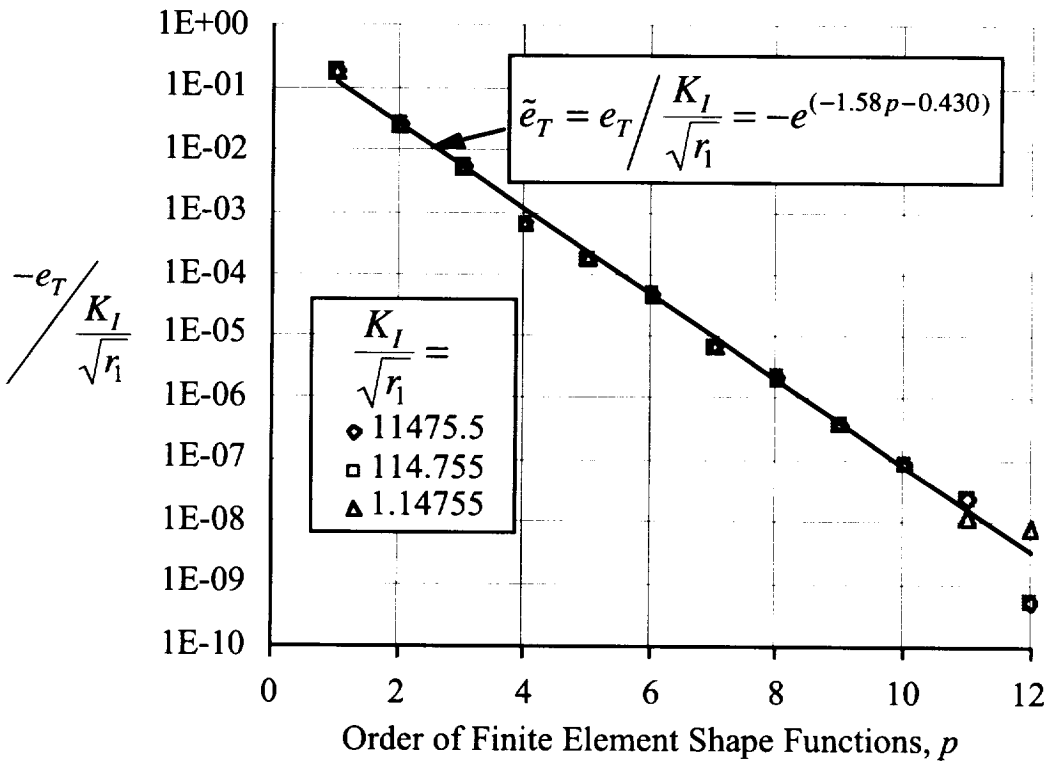

Figure 6.4 Accuracy Assessment of T-stress Computations Using p-version FEM [87]

[14] Chen also included a fairly comprehensive comparison to the results of previous authors not included here.

Table 6.1 High Accuracy Solutions for Selected Test Specimens, After [87,15]

Specimen Description	$K_I/\sigma\sqrt{\pi a}$	T/σ	$B = T\sqrt{\pi a}/K_I$
DCB (h/w=0.2, a/w=0.5)	3.9225	11.5745	2.9508
SENT (h/w=12, a/w=0.3)	1.6598	-0.61033	-0.36771
SENT (h/w=12, a/w=0.5)	2.8246	-0.42168	-0.14929
SENB (h/w=12, a/w=0.3)	1.1241	-0.079177	-0.070436

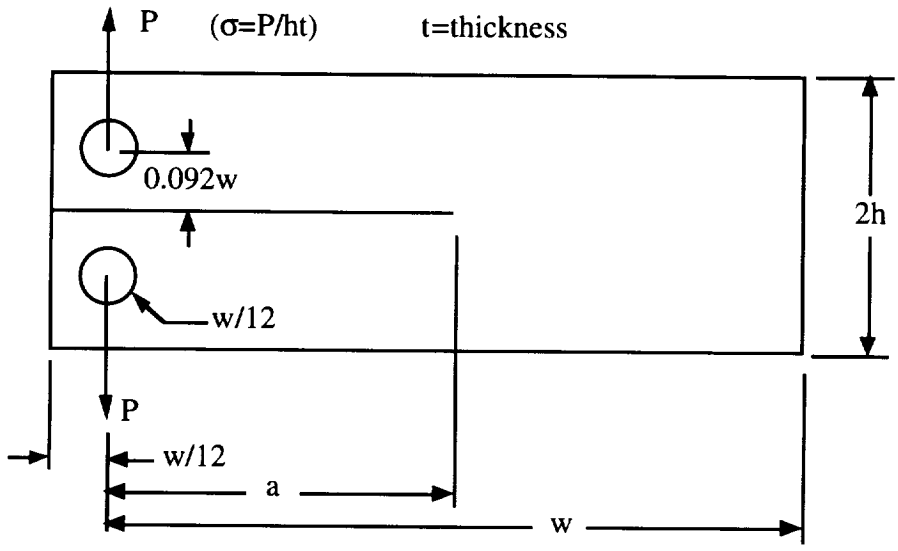

a. DCB

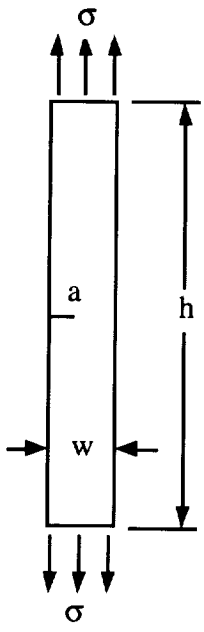

b. SENT

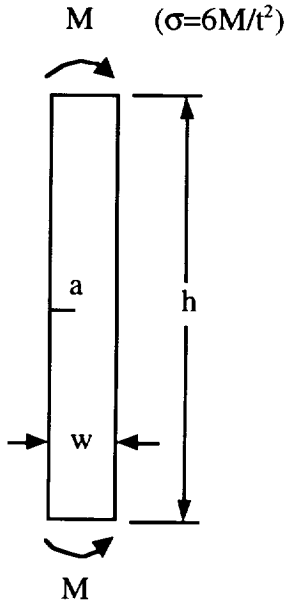

c. SENB

Figure 6.5 Summary of Reference Test Specimen Geometries, after [87,15]

6.3.5 Calibration of the FRANC2D Rosette Geometry

Using the data of Table 6.1 as a sort of calibration standard, the error parameter, $\tilde{e}_T$, was determined for the FRANC2D rosette configuration of Figure 6.2. To do this, FRANC2D models were created of the various specimen types[15] shown in Figure 6.5 using the FRANC2D rosette configuration, and the T-stresses were calculated using the methods of Section 6.3.2. A range of integration radii were included for each specimen configuration to provide more data points (each also representing a unique outer mesh). The error, e_T, in the as-calculated T-stress for each case was then determined by

$$e_T = T_{FE} - T_{ref} \tag{6.14}$$

where T_{ref} is the reference T-stress value from Table 6.1 corresponding to the specimen geometry and loading. As plotted in Figure 6.6, it is seen that the error for the FRANC2D rosettes is characteristically negative (the T-stress is underestimated by the FEM).

For each data point, a value of the error parameter was calculated by

$$\tilde{e}_T = \left(T_{FE} - T_{ref}\right) \Big/ \frac{K_I}{\sqrt{r_1}} \tag{6.15}$$

As would be expected, the $\tilde{e}_T$ values calculated in this way do not agree precisely, but vary according to some distribution function, and can be characterized in terms of mean and standard deviation values:

$$\tilde{e}_T = \tilde{e}_{T_M} \pm \tilde{e}_{T_{StD}} = -0.00825 \pm .00255 \tag{6.15}$$

(Mean) (Std. Deviation)

[15] The FRANC2D DCB specimen model neglected the loading holes with no loss of accuracy (point loads were used instead).

A corrected estimate, T_{cor}, of the T-stress can then be calculated by solving Equation (6.2) for T, and employing the mean value of $\tilde{e}_T$

$$T \approx T_{cor} = T_{FE} - \tilde{e}_{T_M} \frac{K_I}{\sqrt{r_1}} \tag{6.16}$$

The standard deviation of the remaining (random) error in T_{cor} can be estimated as

$$Std.\ Deviation \approx \tilde{e}_{T_{StD}} \frac{K_I}{\sqrt{r_1}} \tag{6.16}$$

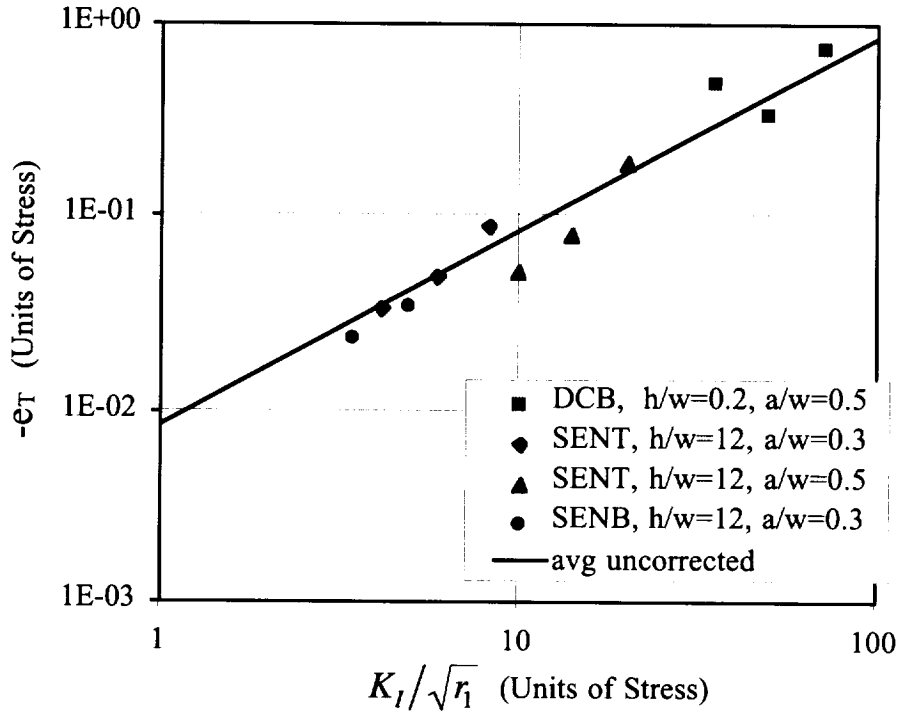

Figure 6.6 As-Calculated Error in T-stress Using FRANC2D

A plot of remaining error in the corrected data, e_{Tcor} is shown with lines denoting 50 and 90 percent confidence levels is given in Figure 6.7. The average error (50 percent confidence level) of the corrected solution was about one fifth of the original

error--a significant improvement in accuracy obtained with negligible additional computation.

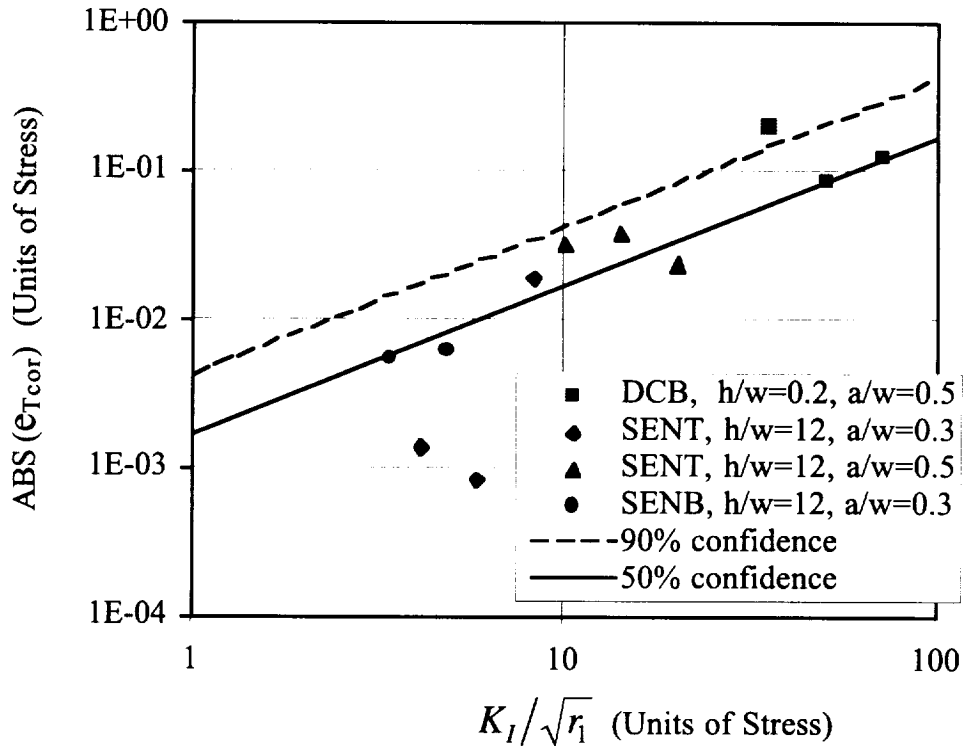

Figure 6.7 Corrected Error in T-stress Calculated by FRANC2D with Upper Bounds Representing Estimated Error

6.3.6 Other Details of Potential Significance with regard to T-stress Calculation

A few other observations arising in the course of the T-stress computation development effort include the following:

1. The presence of K_{II} was not found to incur any numerical pollution into T.

2. It was found necessary to start with an initially closed crack to get good T-stress results. As a programming expedience, FRANC2D historically has modeled the crack with a slight initial opening. The T-stress calculation was more sensitive to this than the calculation of K_I, thus in the present implementation, the code had to be modified to start with an initially closed crack.

3. The singular elements at the center of the rosette shown in Figure 6.2 were intentionally omitted from the integration domain, requiring the use of a two-layer rosette configuration. If included, the singular elements resulted in additional scatter in the T-stress calculations, making error correction less effective. The reason for this is not known, but may have something to do with the Gauss integration algorithm as applied to singular elements. An alternate path not chosen, would be to integrate throughout a single stage rosette without singular elements, and to correct both T and the stress intensities obtained from the J-integral by correction methods similar to those presented above. In this regard, it was found that the systematic component of relative error in K_I was a constant for a given rosette configuration, and is independent of scale.

4. Since the error in the T-stress depends on K_I, and not T, the relative error in T will of course be large if T is small compared to K_I. This is acceptable for the present crack turning application, because the influence of T is only significant as it becomes large compared to K_I.

6.4 FRANC2D/L Elastic-Plastic Crack Turning Implementation

FRANC2D/L is a modified version of FRANC2D maintained at Kansas State University. Its original purpose was to add the ability to model 2D assemblies such as joints and laminates, but has recently been modified by James [65]to include enhanced elastic-plastic crack simulation functionality. In addition to the capabilities described previously for FRANC2D, the elastic-plastic version of FRANC2DL includes the following capabilities relevant to the present work:

1. An isotropic hardening elastic-plastic finite element implementation (infinitesimal strain, small displacement).

2. An implementation of an inverse isoparametric mapping algorithm for mapping elastic-plastic state variables from a starting mesh to an arbitrarily remeshed geometry. This allows crack extension and local remeshing without losing the history-dependent plastic state information for the yielded material in the vicinity of the crack.

3. Implementation of a critical CTOD crack propagation criterion (Equation (5.26))

4. An implementation of the CTOD crack kinking criterion of Sutton *et al* [40] (Equations (5.32-5.34)) for elastic-plastic mixed-mode crack path modeling.

Item #2 is a particularly significant advancement, because it allows an elastic-plastic crack to propagate along a curvilinear path that is not known *a priori*, without losing the plastic history. The plastic history is vital to model a propagating crack,

and is responsible for such macroscopic phenomena as R-curve behavior. A complete description of the elastic-plastic finite-element implementation is given in [65]. The elastic-plastic version of FRANC2D/L was used with minor modification, except that the crack kinking implementation was modified to predict the crack turning angle according to Equation (5.35) with the orthotropic correction of Equation (5.38).

6.5 Summary

A description of the software implementation has been given for the linear elastic and elastic-plastic crack turning theories given in Chapter 5. For the second order linear elastic maximum tangential stress theory, the FRANC2D fracture code was used, and an implementation of a T-stress calculation algorithm is described that utilizes a domain integral approach based on the Betti reciprocal theorem. An *a posteriori* error correction scheme is also described that reduces the error of the T-stress calculation by a factor of five. An estimate of the remaining T-stress error is also provided based on available high-accuracy solutions.

The orthotropic correction to the elastic-plastic CTOD crack turning criterion was implemented into FRANC2D/L.

CHAPTER 7.0

TEST PROGRAM

A key phenomenon associated with crack turning to enhance the damage tolerance of aircraft structures is the ability to turn the crack at a fairly small radius (on the order of an inch or less) in a region of high T-stress that often occurs as the crack nears a stiffener [9]. While recent advances have brought us closer to being able to model these phenomena with some success at the structural component level [14,15], certain refinements of the present study are not yet available in shell codes[16], and require further evaluation at the coupon level. The FRANC2D and FRANC2D/L implementations described in the preceding chapter provide a means to study crack turning phenomena in a high T-stress environment with high fidelity models of simple test specimens.

In order to utilize the second-order orthotropic theory, the characteristic length, r_c, and the fracture orthotropy ratio, $\overline{K}_m$, must be known for the material being analyzed. Part of the purpose of this investigation is to develop an understanding of these properties and develop test methods to determine them empirically. Also, crack paths predicted by appropriate linear elastic and elastic-plastic methods will be compared with observed paths.

In the following, the test program will first be detailed, including a description of the specimens used, the test setup, the test procedure, and a documentation of the response of the various specimens. Selected results will then be discussed in more

[16] Specifically, the contour integral method of T-stress calculation is still problematic for curved shells, and the displacement correlation technique presently used has no component of correctable systematic error, thus the T-stress calculations are far less accurate than can be currently achieved for two-dimensional problems. For the elastic-plastic CTOD method, the state variable re-mapping method has not been implemented for shells.

detail, including an effort to extract key material parameters, and to compare observed fracture paths with FRANC2D and FRANC2D/L simulations.

7.1 Test Specimens

The Double Cantilever Beam (DCB) and Skew Double Cantilever Beam (SDCB) specimen concepts, shown in Figure 7.1, were used to achieve symmetric and mixed-mode fracture in a high T-stress environment. Specimen dimensions of h=2.4 inches, and w=12 inches were chosen[17], identical to the DCB configuration of a previous crack turning investigation [9]. The standard DCB and SDCB specimen configurations are shown in Figures 7.2 and 7.3, respectively (some deviations from these standards will be noted hereafter). The geometry was sized to allow about an inch of stable tearing without excessive plasticity for high strength aluminum alloys, and results in high T-stress, similar in magnitude to that which may occur in a pressurized fuselage as a crack approaches a stiffener [9]. Note that LEFM analyses given hereafter are continued as the crack approaches the edges of the specimen, but should be viewed with the understanding that plasticity becomes widespread as the shortest intact ligament decreases.

A total of 43 crack turning tests in four aluminum alloys were run overall, divided into four specimen sets based on material and test type. Of these, 23 DCB tests were performed at Boeing under the NASA IAS program [1], and eight DCB and 12 SDCB specimens were tested at Cornell under NASA grant. A detailed matrix of all crack turning specimens tested is given in Table 7.1. The source material lots for all specimens except specimen set No. 2 pertain to the IAS program, and material test

[17] As an exception, the SDCB specimens made from the IAS 7050-T74511 large extrusion material were modified from DCB specimens, leaving w=10.9 inches instead of 12 inches for these specimens. The slightly shorter length was not expected to make a significant difference in the specimen performance as long as the crack never grew closer than 4.8 inches from the end. This condition was satisfied for all specimens except those that grew straight.

results [88] for these lots are given in Table 7.2. Median stress strain curves for finite element analyses are given in Appendix 4.0.

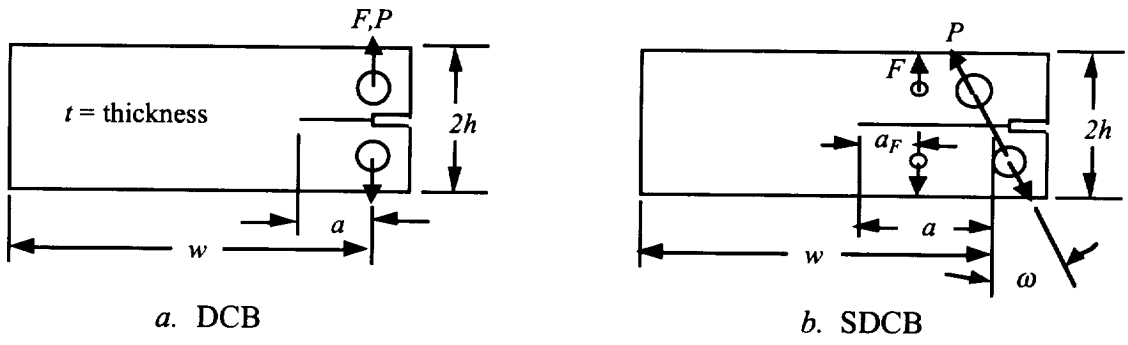

Figure 7.1 Illustration of DCB and SDCB Specimens. Specimens Precracked at Hole Set F to $a=a_i$, then Tested Using Hole Set.

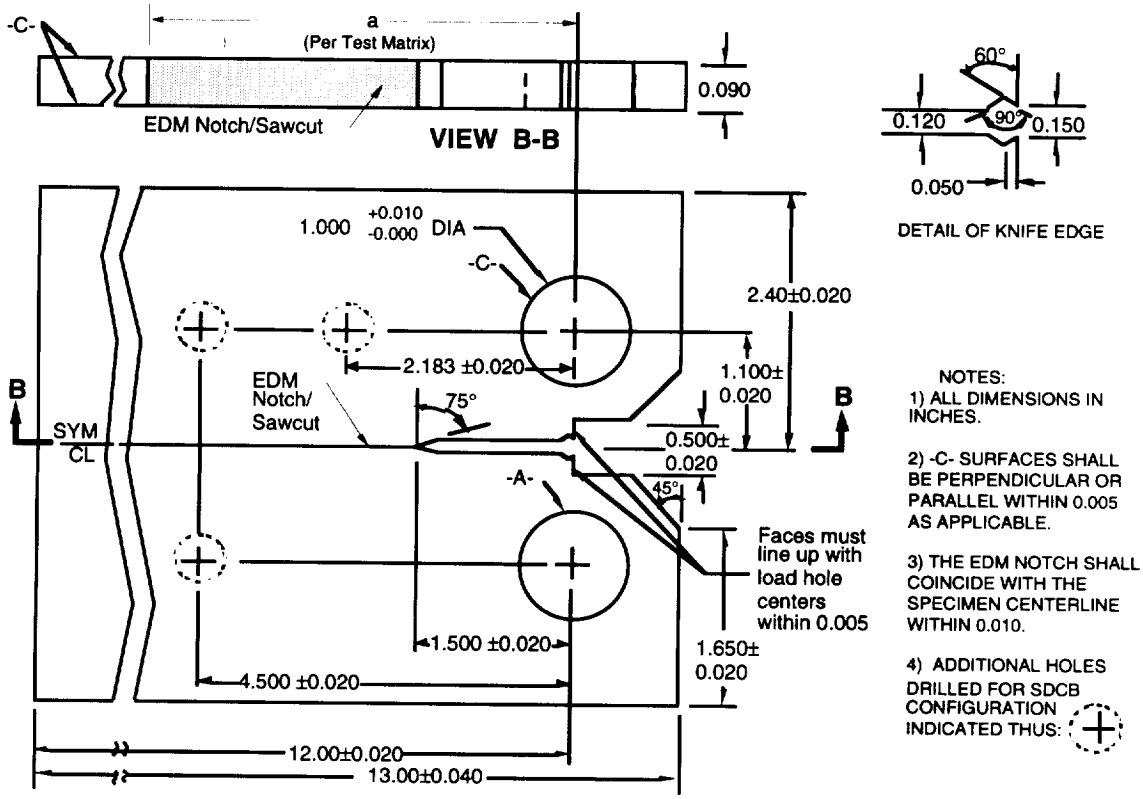

Figure 7.2. Double Cantilever Beam (DCB) Specimen, h=2.4, w=12 (Specimen Sets No.1,3)

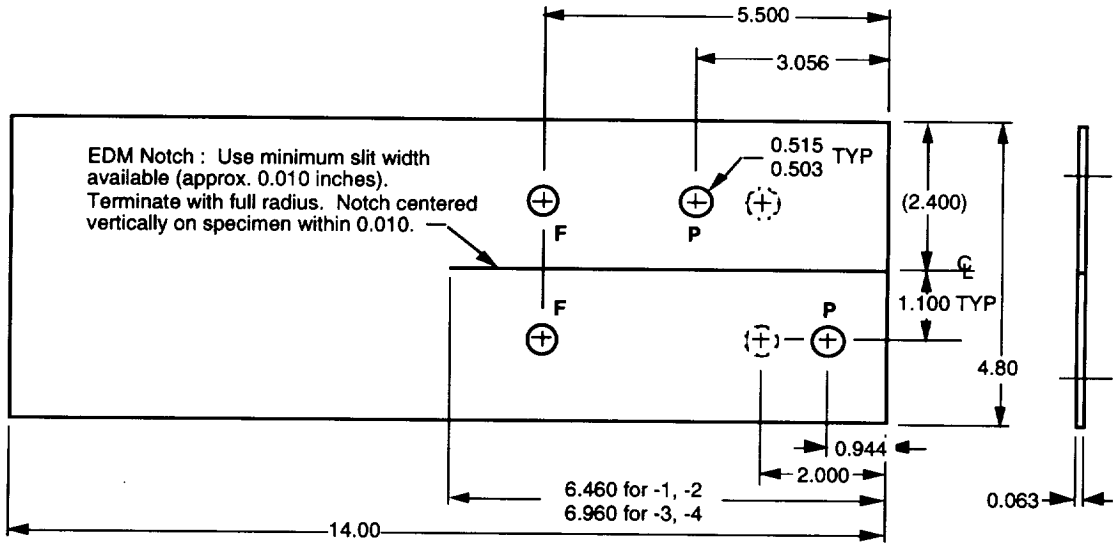

NOTES (UNLESS OTHERWISE NOTED:
1. ALL DIMENSIONS IN INCHES PER FOLLOWING TOLERANCES
   X.XX ± 0.020
   X.XXX ± 0.010
2. FOR ENG'G REFERENCE, K_{II}/K_I VALUES FOR SELECTED LOAD HOLES ARE AS FOLLOWS:

	K_{II}/K_I	
P, P	0.20	
F, F	0.00	(USE FOR PRE-CRACKING)

3. -1, -2 SPECIMENS USED FOR FATIGUE PLUS STATIC PRECRACKING
   -3, -4 SPECIMENS USED FOR FATIGUE PRECRACK ONLY
4. HOLE PATTERN FOR -5 DCB CONFIGURATION INDICATED THUS : ⊕

Figure 7.3 Skew Double Cantilever Beam (SDCB) Specimen, h=2.4, w=12 (Specimen Set No. 4)

The test specimen geometries show some evolution, the first two specimen sets being entirely of the DCB type. While the DCB configuration is the most sensitive to T-stress/process zone interactions associated with the second-order theory, a random perturbation also exists in every specimen due to imperfections and small-scale material inhomogeneity. The SDCB specimen provides a finite asymmetry designed to be sufficiently larger than specimen imperfections to allow a more reproducible, and hopefully more informative, behavior.

Table 7.1 Crack Turning Specimen Test Matrix

Specimen Set No. 1
t=0.090 inches, h=2.4, w=12
DCB Specimens from 1.5 inch 7050-T7451 Plate (Pechiney Lot #75394/011), tested at Boeing [1]

Specimen ID	Nominal Starter Notch Length, a (in)	Precrack,R=.05, 5 Hz. Max Load (lb)	Fatigue Precrack, (in)
rc-LT-15-2	2.0	320/variable	Fatigue Crack to Failure
rc-LT-15-3	6.5	71	0.04
rc-LT-15-4	2.0	165	0.04
rc-LT-15-5	3.0	129	0.04
rc-LT-15-6	7.0	65	0.04
rc-LT-15-7	4.5	98	0.04
rc-LT-15-8	5.0	94	0.04
rc-LT-15-9	5.5	84	0.04
rc-LT-15-10	6.0	78	0.04
rc-TL-15-1	6.5	78	0.04
rc-TL-15-2	2.0	320/variable	Fatigue Crack to Failure
rc-TL-15-4	2.0	165	0.04
rc-TL-15-5	3.0	129	0.04
rc-TL-15-6	4.0	106	0.04
rc-TL-15-7	4.5	98	0.04
rc-TL-15-8	5.0	94	0.04
rc-TL-15-9	5.5	84	0.04
rc-TL-15-10	6.0	78	0.04

Specimen Set No. 2
t=0.090 inches, h=2.4, w=12
DCB Specimens from 2324-T39, 7475-T7351, and 7050-T76511 (misc. material lots), tested at Boeing [1]

Specimen ID	Nominal Starter Notch Length, a (in)	Fatigue Precrack, R=.05, 5 Hz., 0.04 in Max Load (lb)	Comments
rc-TL-2324-1	5.0	113	cut from .95 inch plate
rc-TL-2324-2	5.0	113	cut from .95 inch plate
rc-TL-7475-1	5.0	113	cut from 1.75 inch plate
rc-TL-7475-2	5.0	113	cut from 1.75 inch plate
rc-TL-7050-1	5.0	113	cut from scrap extrusion

Table 7.1 Crack Turning Specimen Test Matrix (Continued)

Specimen Set No. 3
t=0.090 inches, h=2.4; w=12 for DCB, 10.9 for SDCB specimens
Specimens from IAS 7050-T76511 large extrusion [1], tested at Cornell

Type	Specimen ID	Nominal Starter Notch Length, a (in)	Fatigue Precracking R=.05, 3-5 Hz. Max Load (lb)	Precrack (in)	ω	K_{II}/K_I After Precrack
DCB	rc-LT-EXT1-2	3.0	200	0.04 fatigue	0	0
DCB	rc-LT-EXT1-3	5.0	106	0.04 fatigue	0	0
DCB	rc-LT-EXT1-4	5.0	108	0.04 fatigue	0	0
SDCB	rc-LT-EXT1-6	4.4	370	0.04 fatigue + 0.5 static	44.78°	0.21
SDCB	rc-LT-EXT1-7	4.9	270	0.04 fatigue	44.78°	0.21
DCB	rc-TL-EXT1-2	3.0	200	0.04 fatigue	0	0
DCB	rc-TL-EXT1-3	5.0	106	0.04 fatigue	0	0
DCB	rc-TL-EXT1-4	5.0	168	0.04 fatigue	0	0
SDCB	rc-TL-EXT1-5	4.4	360	0.04 fatigue + 0.5 static	44.78°	0.21
SDCB	rc-TL-EXT1-7	4.9	300	0.04 fatigue	44.78°	0.21

Specimen Set No. 4
t=0.063 inches, h=2.4, w=12
Specimens from IAS 7475-T7351 plate [1], tested at Cornell

Type	Specimen ID	Nominal Starter Notch Length, a (in)	Precracking Load, R=.05, 3-5 Hz. Max Load (lb)	Precrack (in)	ω	K_{II}/K_I After Precrack
SDCB	S7475LT-1	4.46	200	0.04 fatigue + 0.5 static	43.83°	0.20
SDCB	S7475LT-2	4.46	106	0.04 fatigue + 0.5 static	43.83°	0.20
SDCB	S7475LT-3	4.96	108	0.04 fatigue	43.83°	0.20
SDCB	S7475LT-4	4.96	370	0.04 fatigue	43.83°	0.20
DCB	S7475LT-5	4.96	270	0.04 fatigue	0	0
SDCB	S7475TL-1	4.46	200	0.04 fatigue + 0.5 static	43.83°	0.20
SDCB	S7475TL-2	4.46	106	0.04 fatigue + 0.5 static	43.83°	0.20
SDCB	S7475TL-3	4.96	168	0.04 fatigue	43.83°	0.20
SDCB	S7475TL-4	4.96	360	0.04 fatigue	43.83°	0.20
DCB	S7475TL-5	4.96	300	0.04 fatigue	0	0

Table 7.2 Average Material Properties for IAS Material Lots

Alloy	Orientation	Ultimate Tensile Strength (ksi)	Yield Strength (ksi)	Modulus (ksi)	Maximum R-curve Fracture Toughness (ksi$\sqrt{in}$)
7050-T7451 1.5 inch Plate	L	77.5	68.3	10.6	
	T	76.2	66.3	10.7	
	S	73.0	62.0	10.4	
	L-T				108
	T-L				83
7050-T74511 Extrusion (skin, under stiffener)	L	77.9	68.4	10.7	
	T	75.2	64.7	10.7	
7475-T7351 1.5 inch Plate	L	76.5	66.6	10.4	
	T	75.4	65.4	10.6	
	S	75.7	63.1	11.4	
	L-T				145
	T-L				141

Note: A modulus of 10.4 MSI was used for all analyses of plate alloys based on MIL-HDBK-5 data.

Specimen set No.1 was fabricated at Boeing Seattle from IAS lots of 1.5 inch 7050-T7451 plate, machined to nominal thickness of 0.090 inches, h=2.4, w=12. The plate specimen blanks were cut through the midplane before machining to obtain two specimens per blank, and specimens were excised adjacent to the original exterior faces of the plate. This set includes specimens in both L-T and T-L orientations of the DCB configuration shown in Figure 7.2. Testing took place at the Boeing Long Beach facility [1].

Specimen set No. 2 was fabricated at Boeing Long Beach. Specimens 0.090 inch thick, with h=2.4, w=12, were taken from remnants of various materials, including 7050-T76511 extrusion, 7475-T7351 plate, and 2324-T39 plate. The specimen

configuration was of DCB type, and equivalent to that of Figure 7.2, but with modified grip geometry [1]. Tests were run in the T-L orientation only, in order to get a first assessment as to whether the orthotropy of these alloys was sufficiently mild to allow crack turning from the preferred fracture orientation (like a longitudinal fuselage crack approaching an integral frame pad). Testing took place at the Boeing Long Beach facility [1].

Specimen set No. 3 was fabricated at Boeing Seattle from 30 inch wide 7050-T74511 extrusions from the IAS program. The panels were extruded by Alcoa in the shape shown in Figure 7.4, and subsequently straightened in a rolling process. Specimens excised from these panels were not tested under the IAS program, but were provided to Cornell for testing. Those tested as DCB specimens retained the original h=2.4, w=12 dimensions (Figure 7.2). Four of the specimens were modified to be SDCB specimens by drilling additional holes, resulting in an effectively shorter specimen of w=10.9. Testing took place at the Cornell Winter Lab.

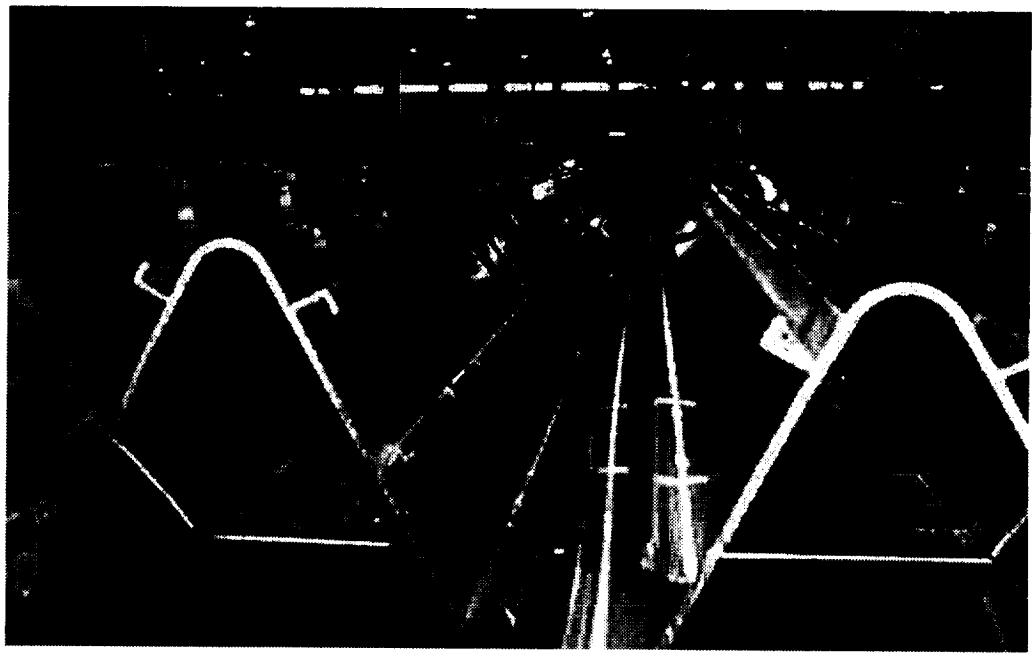

Figure 7.4 As-Extruded Shape of 7050-T74511 Material

Specimen set No. 4 was fabricated at Cornell from remnants of a 0.063 inch thick R-curve panel machined from 1.5 inch thick 7475-T7351 plate (IAS lot). This was the same lot of material used to fabricate a crown fuselage panel for a barrel test under the IAS program. The specimens were made long enough to accommodate the staggered load holes of the SDCB configuration and still retain the standard dimensions h=2.4, w=12 (Figure 7.3). Testing took place at the Cornell Winter Lab.

7.2 K_I, K_{II}, and T for Initial (Straight) Cracks in DCB/SDCB Specimens

For most analyses, the stress intensity factors and T-stress are determined numerically from FRANC2D. However, the following equations are useful for specimen design and analyses when the crack is straight.

The SDCB specimen loads the specimen with both mode I and mode II components

$$\begin{aligned} P_I &= P\cos(\omega) \\ P_{II} &= P\sin(\omega) \end{aligned} \tag{7.1}$$

The DCB represents the special case where ω=0. The stress intensity factor for the mode I component can be calculated based on results from Gross and Srawley [89].

$$K_I = \frac{P_I}{t}\sqrt{\frac{12}{h}}\left(\frac{a}{h}+.687\right) \tag{7.2}$$

This equation was found to agree within one percent down to a/h=0.5 with a full range expression given by Foote and Buchwald [90]. For real specimens, the grip may have an effect at this extreme, but the specimens tested were of significantly larger a/h and the effect of grip configuration was neglected. The mode II stress intensity factor is derived using a beam theory approach in Appendix 3.0, and is given by

$$K_{II} = \frac{2P_{II}}{t\sqrt{h}} \tag{7.3}$$

This equation was verified with FRANC2D to within less than 0.5 percent error down to a/h=0.5. To avoid the influence of the opposite end of the current specimen, Equations (7.2) and (7.3) should not be (and were not) used for crack lengths within $2h$ of the far end of the specimen. Combining Equations (7.1) through (7.3) we obtain

$$\frac{K_{II}}{K_I} = \frac{\tan\omega}{\sqrt{3}\left(\frac{a}{h} + .687\right)} \tag{7.4}$$

Equation (7.4) was used to calculate the K_{II}/K_I ratios for the precracked SDCB specimens in Table 7.1.

The T-stress can be evaluated in terms of r_o (defined as in (5.5)) for the current specimen aspect ratio (h/w=0.2) using an equation given in [9]

$$\frac{r_o}{h} = .0114\left[1 + .7214\left(\frac{h}{a}\right) + .2879\left(\frac{h}{a}\right)^2\right]^2 \tag{7.3}$$

for crack lengths ranging within $1 \leq a/h \leq 3$. Thus the present specimen is capable of achieving combinations of K_I and T corresponding to r_o values ranging from 0.110 $\geq r_o \geq .044$ (note that this is more approximate for the reworked 7050-T74511 SDCB specimens, which have h/w=0.22).

7.3 Test Procedure

Testing required use of a servohydraulic test machine, an anti-buckling guide, and a data recording system. Red dye penetrant was used on pre-torn SDCB to mark

the extent of the crack after pre-tearing. The setup at the Cornell Winter Laboratory is shown in Figure 7.5. The test procedure for DCB/SDCB specimens is as follows.

1. Wipe specimen clean as required. Solvent permissible, but avoid removing specimen ID.

2. Measure specimen thickness, w, $2h$, and initial notch length, a. (specimens may be lightly scribed as required to facilitate measurements).

3. Mount specimen in test machine. Fill space between clevises and specimen faying surface with shims to restrict out-of-plane movement of the specimen. Make sure shim thickness is distributed symmetrically about the specimen, and that the top and bottom clevises are shimmed to match.

4. Fatigue precrack using hole pair D at load indicated in table, R=0.05, 3-5 Hz, for at least 0.04 inches growth. A higher starting precrack load is permissible subject to the precracking guidelines of ASTM E647-93. Total growth should be at least 0.04 but not exceed 0.10 inches. Measure and record final crack length on both sides of specimen.

5. If static precracking is specified in the test matrix, load slowly to statically tear specimen approximately 0.5 inches to final precrack length. Record the critical load at the end of tearing, load vs. head deflection during tearing, and final crack length measured on each side. Afterwards, apply red dye penetrant to crack tip and let dry overnight before proceeding.

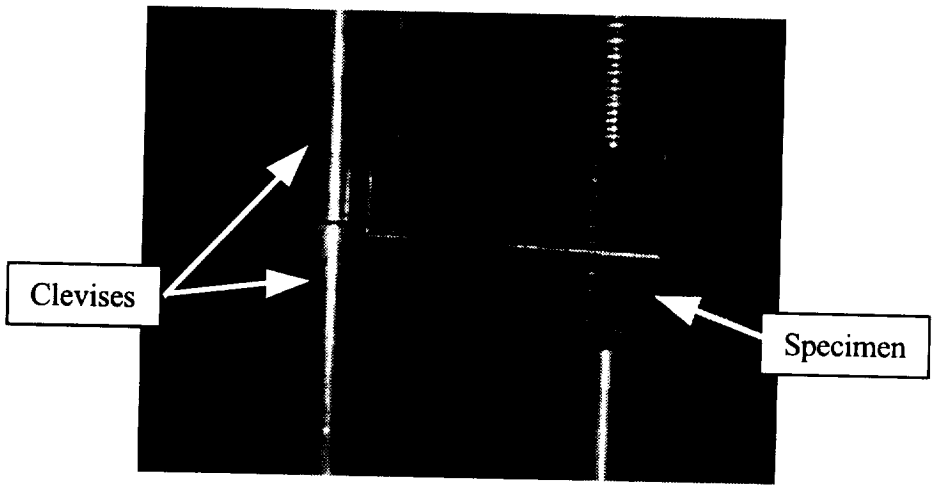

a. DCB (Shown without Anti-Buckling Guide)

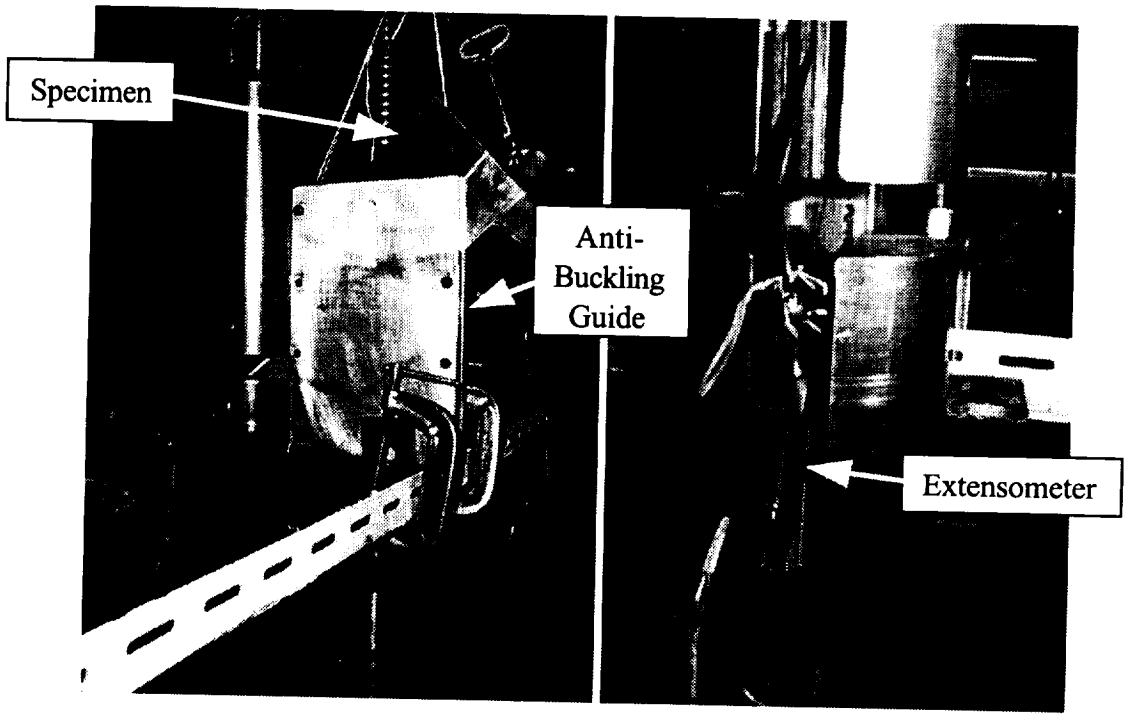

b. SDCB

Figure 7.5 Test Setup

6. Remount specimen using hole pair P (for DCB specimens, this is the same hole pair used for precracking). Mount antibuckling guide over specimen and gently finger tighten screws to achieve sliding fit. Support antibuckling guide so that its weight is not carried through the loading pins, leaving sufficient clearance at the specimen lower edge to permit specimen deflection during testing.

7. Mount clip gage or extensometer at mouth of crack. Gage shall be calibrated to a range of 0.5 inches or the maximum range available.

8. Load specimen at 0.05 in/min or less (during final stages of failure after crack turning, higher rates may be used), recording load, clip gage, and stroke data at 1.0 samples/sec. Continue until specimen failure or until deflection is limited by interference with the anti-buckling guide. NOTE: Continue testing even if deflection exceeds clip gage range.

7.4 Results

A detailed summary of specimen data, including specimen measurements, precrack measurements, and maximum loads, is given in Tables 7.3-7.6. Load/Crack Opening Displacement (COD) plots for DCB/SDCB fracture specimens were prepared for the range of validity for the clip gage or extensometer used. As illustrated in Figure 7.6, the distance, S, between the effective point of load application and the point at which the CTOD was measured, was not the same for all specimens. This dimension is noted on each COD plot or corresponding caption, given in Figures 7.7-7.13. Specimen photographs are presented in Figures 7.14-7.19, and crack paths for all specimens are given in Figures 7.20-7.26. Selected data is also tabulated in Appendix 4.

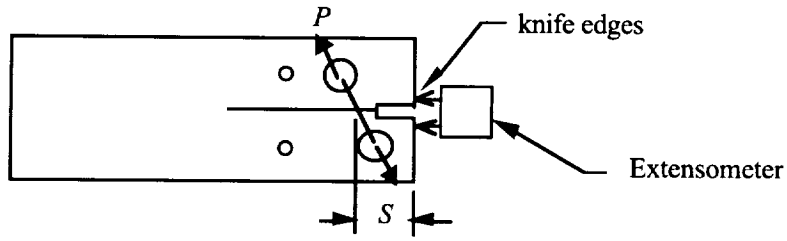

Figure 7.6 Schematic of COD Measurement Position, S

Table 7.3. Summary of 7050-T7451 Static Crack Turning Tests (Set No.1)

Specimen ID	Crack Front Type After Initiation	Thickness (in)	w (in)	2h (in)	a_n (notch) (in)	a_i (precrack) (in)	r_o (a_i) (in)	Max Load (lb)
rc-LT-15-3	slant	0.0923	11.997	4.800	6.472	6.532	0.047	879
rc-LT-15-4	slant	0.0922	11.997	4.797	2.006	2.048	0.137*	2757
rc-LT-15-5	slant	0.0924	11.996	4.799	2.989	3.031	0.084	1863
rc-LT-15-6	V-shear	0.0917	11.996	4.799	6.961	7.002	0.045	896
rc-LT-15-7	slant	0.0922	11.996	4.799	4.500	4.546	0.058	1467
rc-LT-15-8	V-shear	0.0926	11.998	4.800	5.007	5.054	0.054	1200
rc-LT-15-9	slant	0.0917	11.950	4.799	5.536	5.584	0.051	1178
rc-LT-15-10	slant	0.0910	11.998	4.801	5.999	6.042	0.049	1122
rc-TL-15-1	V-shear	0.0925	11.997	4.800	6.492	6.536	0.046	960
rc-TL-15-4	slant	0.0931	12.000	4.800	2.006	2.050	0.137*	1858
rc-TL-15-5	slant	0.0919	11.994	4.798	3.000	3.047	0.083	1427
rc-TL-15-6	slant	0.0935	12.000	4.800	3.998	4.050	0.064	1298
rc-TL-15-7	V-shear	0.0922	11.996	4.799	4.502	4.557	0.058	1254
rc-TL-15-8	slant	0.0910	11.997	4.805	4.997	5.047	0.054	1066
rc-TL-15-9	slant	0.0924	11.985	4.799	5.512	5.557	0.051	1003
rc-TL-15-10	slant	0.0920	11.997	4.799	6.002	6.047	0.049	943

* r_o values calculated slightly out of bounds of validity of Equation (7.3)

Table 7.4. Summary of Static Crack Turning Tests of DCB Specimens of 2324-T39, 7475-T7351, and 7050-T76511 Alloys (Set No.2)

Specimen ID	Crack Front Type After Initiation	Thickness (in)	w (in)	2h (in)	a_n (notch) (in)	a_i (precrack) (in)	r_o (a_i) (in)	Max Load (lb)
rc-TL-2324-1	slant	0.0858	12.001	4.800	4.988	5.053	0.054	1044
rc-TL-2324-2	slant	0.0915	11.999	4.792	4.995	5.049	0.054	1169
rc-TL-7475-1	slant*	0.0906	12.003	4.792	4.992	5.049	0.054	1359
rc-TL-7475-2	V-shear	0.0898	11.999	4.793	4.999	5.048	0.054	1331
rc-TL-7050-1	slant	0.0985	11.997	4.804	4.993	5.054	0.054	1306

* The crack passed through a small region of V shear (about 0.08 inches) adjacent to the precrack, but completed most of the turn as a slant crack.

Table 7.5 Summary of DCB/SDCB Tests of 7050-T74511 Extrusion (Set No.3)

Specimen ID	Crack Front Type After Initiation	Thickness (in)	2h (in)	a_n (notch) (in)	a_i (precrack*) (in)	ω (in) (in)	r_o (a_i) (in)	Max Precrack Load (lb)	Max Load (lb)
rc-LT-EXT1-2	slant	0.0880	4.800	3.00	3.05	0	0.083	200	2011
rc-LT-EXT1-3	V-shear	0.0911	4.804	4.99	5.03	0	0.054	106	1489
rc-LT-EXT1-4	slant	0.0915	4.809	5.01	5.05	0	0.054	109	1434
rc-LT-EXT1-6	slant	0.0913	4.801	4.40	4.54, 4.91	45.45	0.049	3633	1518
rc-LT-EXT1-7	V-shear	0.0923	4.803	4.91	4.98	45.09	0.055	270	1595
rc-TL-EXT1-2	slant	0.0925	4.799	3.00	3.11	0	0.082	200	2035
rc-TL-EXT1-3	slant	0.0954	4.802	5.01	5.06	0	0.054	106	1243
rc-TL-EXT1-4	V-shear	0.0913	4.808	4.50	5.00	0	0.055	168	1405
rc-TL-EXT1-5	slant	0.0909	4.804	4.41	4.45,5.01	45.03	0.048	3017	1701
rc-TL-EXT1-7	slant	0.0910	4.804	4.91	5.09	45.21	0.054	300	1418

* Where applicable, both fatigue and static precrack lengths are given respectively.

r_o is calculated based on the final precrack length, including both fatigue and static propagation.

Table 7.6 Summary of DCB/SDCB Tests of 7475-T7351 Plate (Set No. 4)

Specimen ID	Crack Front Type After Initiation	Thickness (in)	2h (in)	a_n (notch) (in)	a_i (precrack*) (in)	ω (in) (in)	r_o (a_i) (in)	Max Precrack Load (lb)	Max Load (lb)
S7475LT-1	slant	0.0649	4.808	4.46	4.56,4.98	43.68	0.055	2194	1113
S7475LT-2	slant	0.0654	4.800	4.45	4.53,4.96	43.88	0.055	2172	1222
S7475LT-3	V-shear	0.0628	4.803	4.98	5.05	43.73	0.054	270	1144
S7475LT-4	slant	0.0631	4.800	4.95	5.01	43.78	0.049	270	1022
S7475LT-5	slant	0.0631	4.799	4.95	5.02	0	0.054	91	874
S7475TL-1	slant	0.0643	4.802	4.46	4.55,5.01	43.89	0.055	1999	1084
S7475TL-2	slant	0.0650	4.802	4.46	4.50,5.05	43.80	0.054	2076	1049
S7475TL-3	slant	0.0655	4.800	4.95	5.00	43.88	0.055	270	949
S7475TL-4	slight V-shr	0.0636	4.799	4.96	5.00	43.97	0.048	270	967
S7475TL-5	slant	0.0624	4.808	4.96	5.00	0	0.055	91	819

* Where applicable, both fatigue and static precrack lengths are given respectively.

r_o is calculated based on the final precrack length, including both fatigue and static propagation.

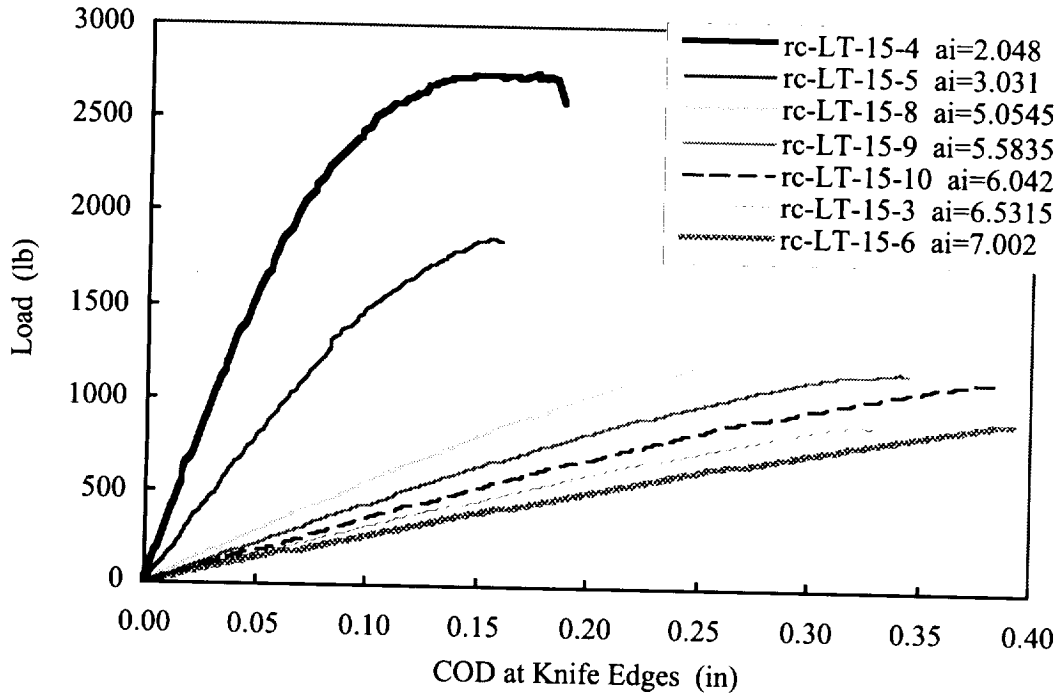

Figure 7.7 L-T Load/COD Curves for 7050-T7451 DCB Specimens, S= 1.0 inch

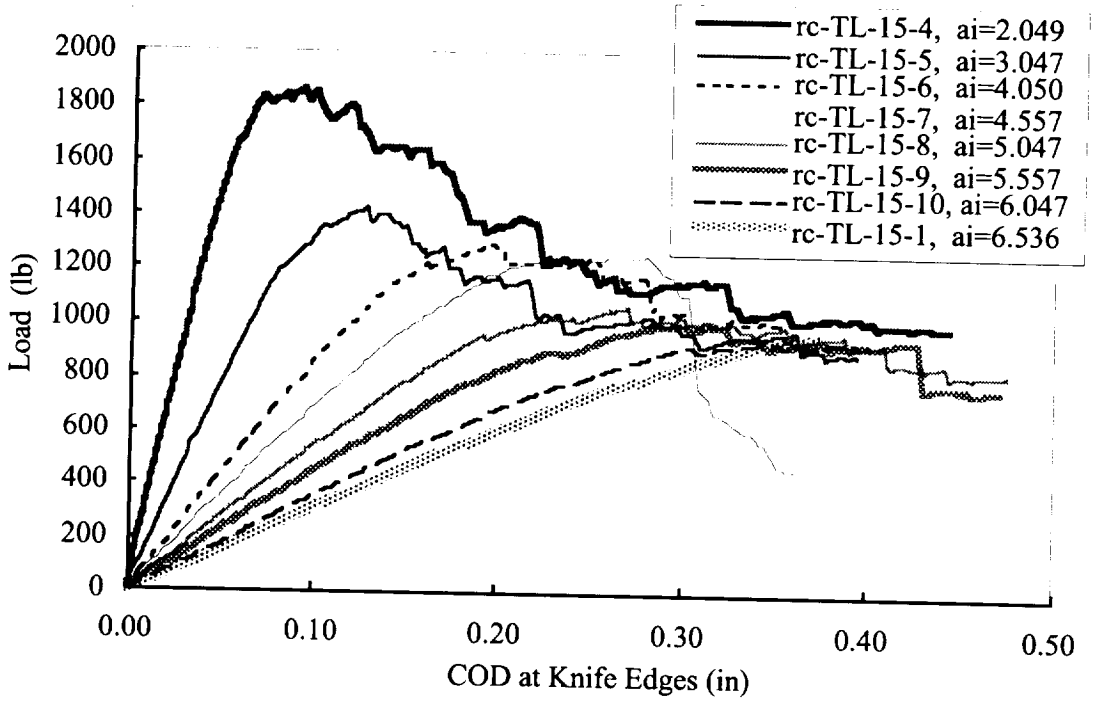

Figure 7.8 T-L Load/COD Curves for 7050-T7451 DCB Specimens, S= 1.0 inch

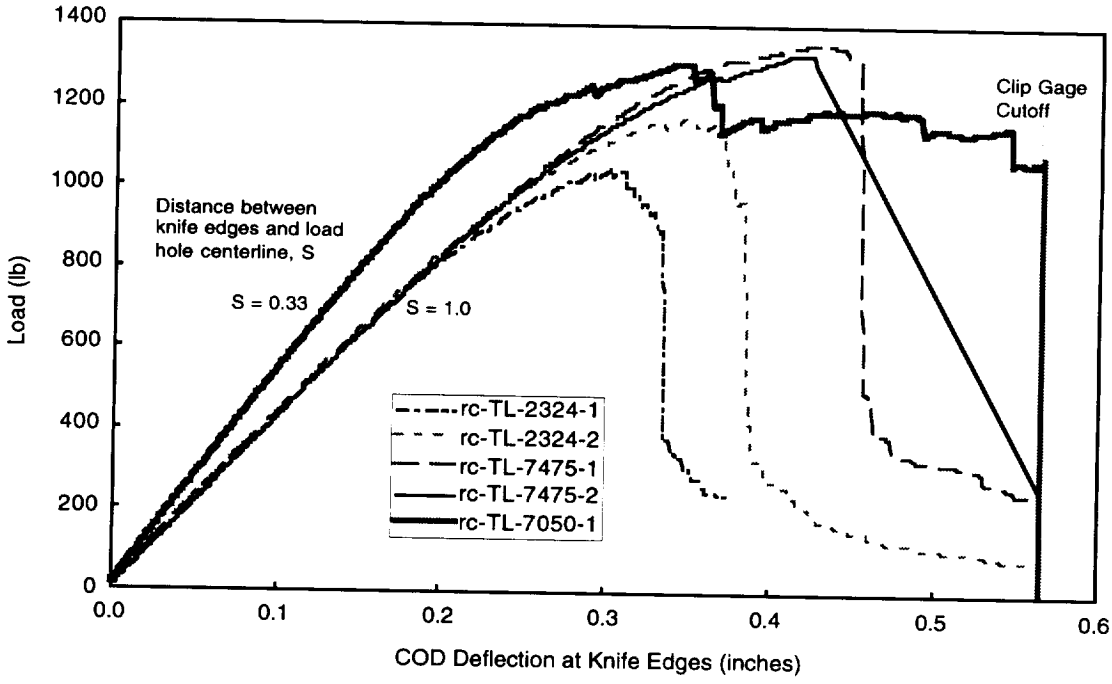

Figure 7.9 T-L Load/COD Curves for DCB Specimens of 2324-T39, 7475-T7351, and 7050-T76511 Alloys

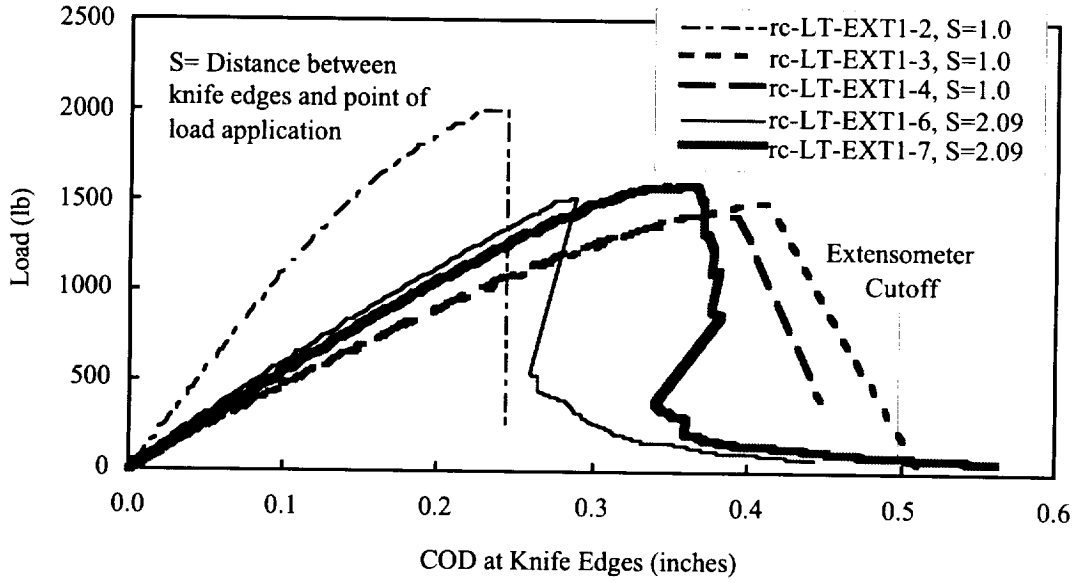

Figure 7.10 L-T Load/COD Curves, 7050-T74511 Extrusion DCB/SDCB Specimens

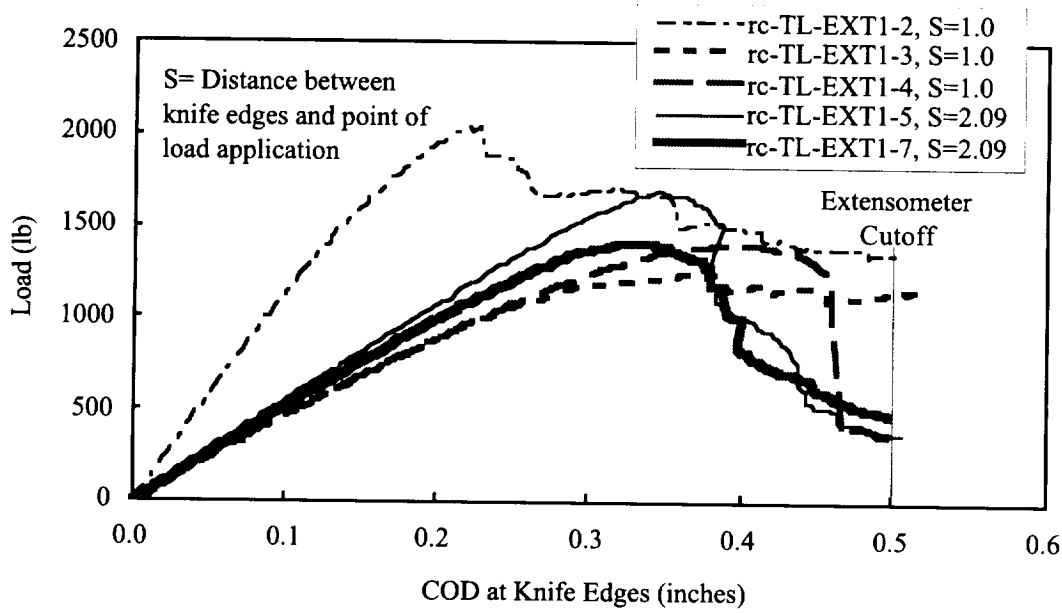

Figure 7.11 T-L Load/COD Curves, 7050-T74511 Extrusion DCB/SDCB Specimens

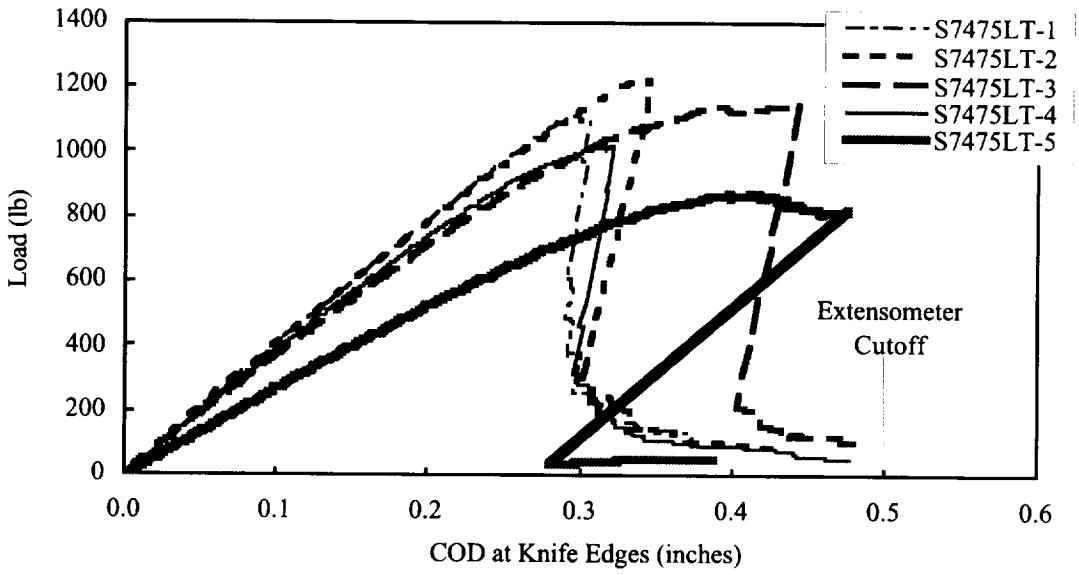

Figure 7.12 L-T Load/COD Curves, 7475-T7351 DCB/SDCB Specimens, S= 2.0 in.

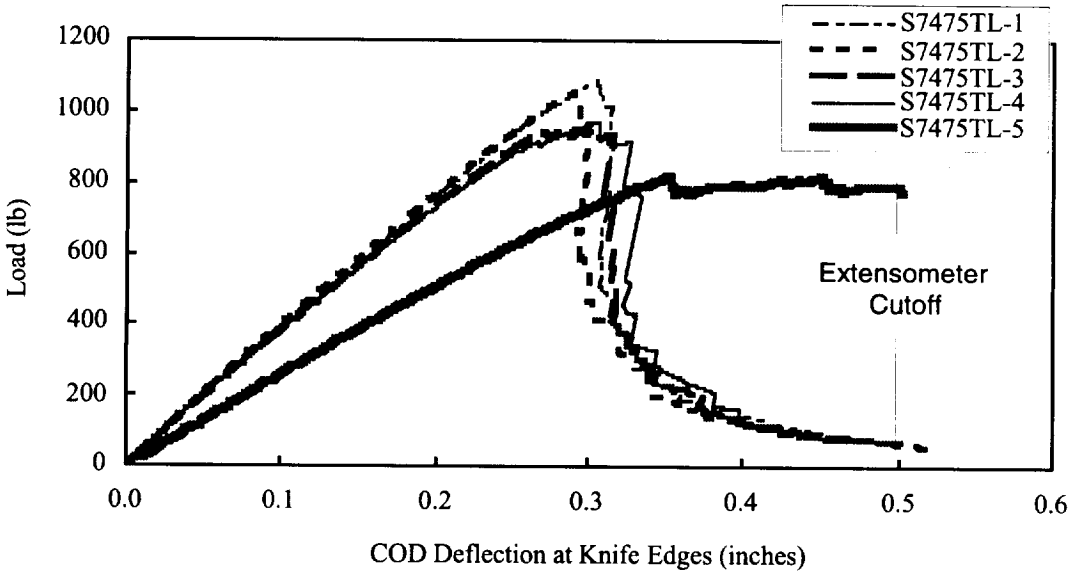

Figure 7.13 T-L Load/COD Curves, 7475-T7351 DCB/SDCB Specimens, S= 2.0 in.

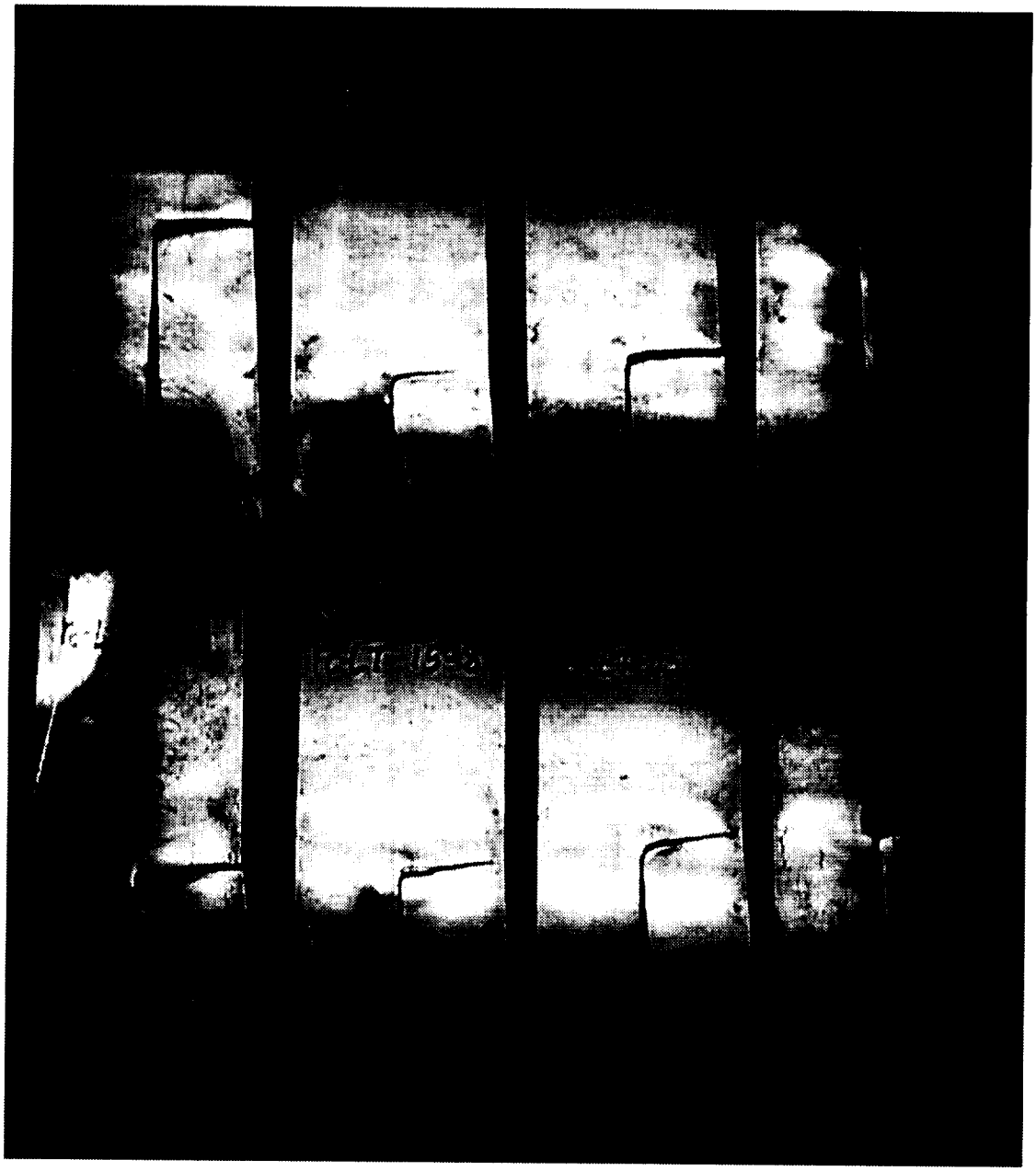

Figure 7.14 7050-T7451 Static Crack Turning Specimens (Set No. 1), L-T Orientation

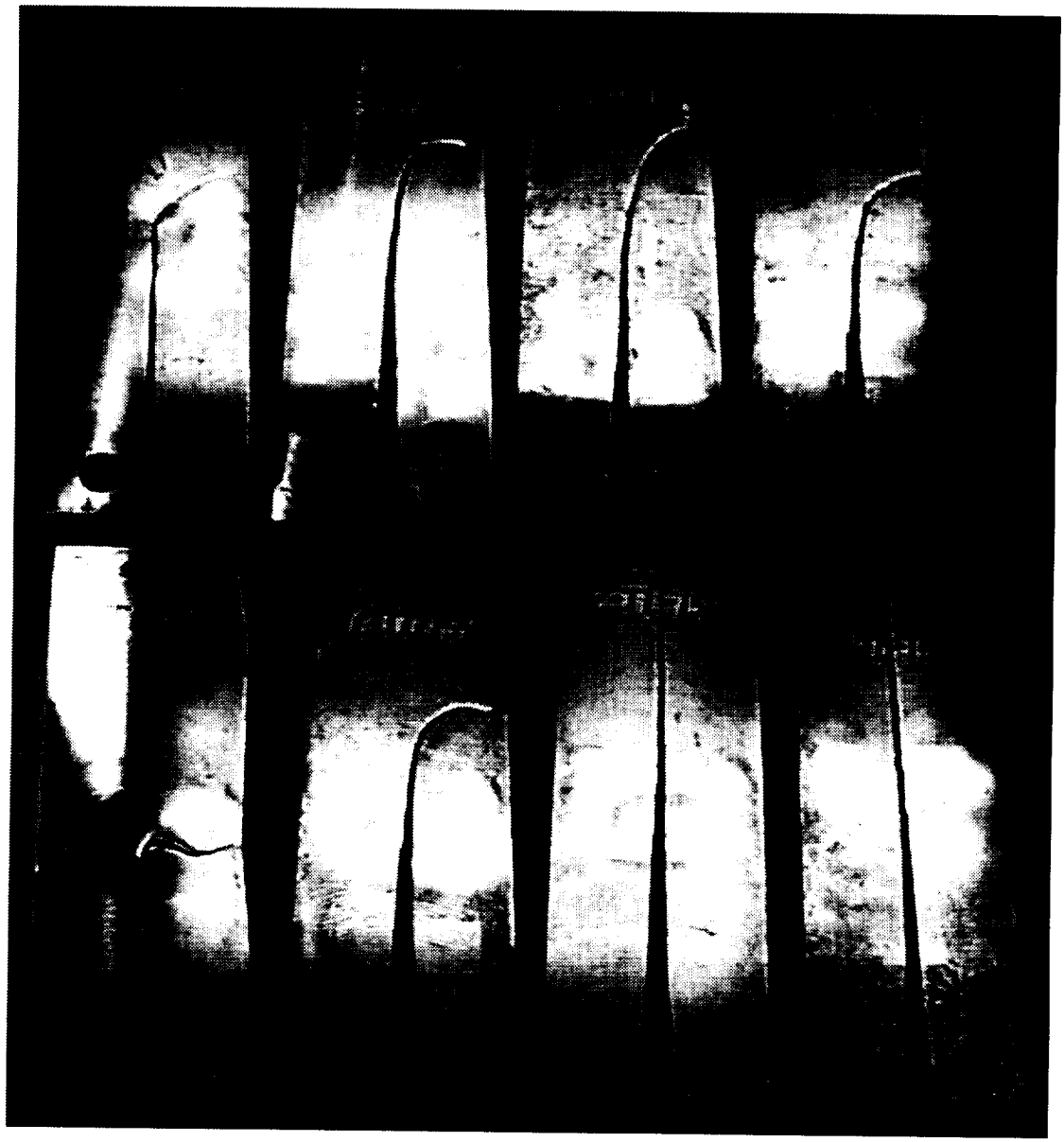

Figure 7.15 7050-T7451 Static Crack Turning Specimens (Set No.1), T-L Orientation

Figure 7.16 7050-T7451 Fatigue Crack Turning Specimens, Shown with Static Specimens with Same Starting Crack Length (2 inches)

Figure 7.17 2324-T39, 7475-T7351, and 7050-T76511 Alloy Static Crack Turning Specimens (Set No.2), T-L Orientation

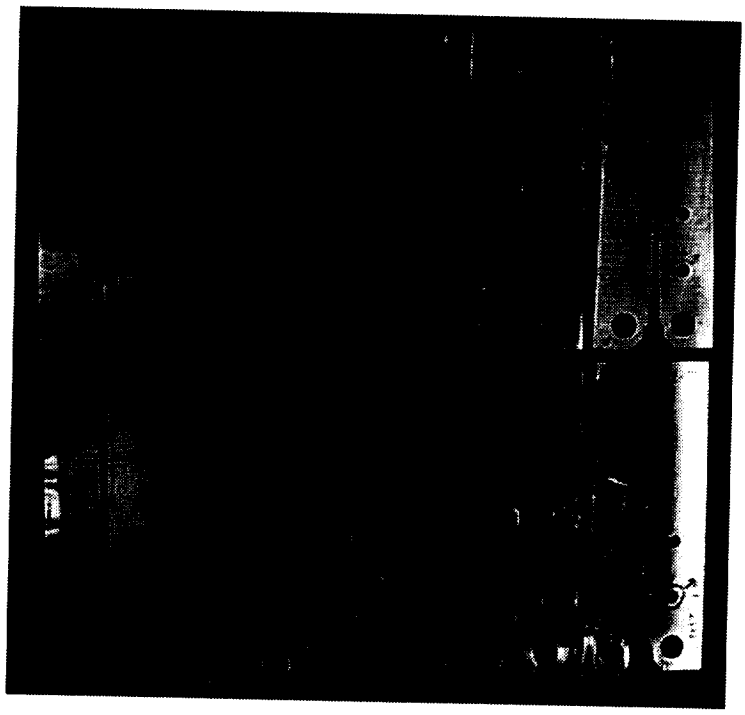

Figure 7.18 7050-T74511 Static Crack Turning Specimens (Set No. 3), L-T and T-L Orientation

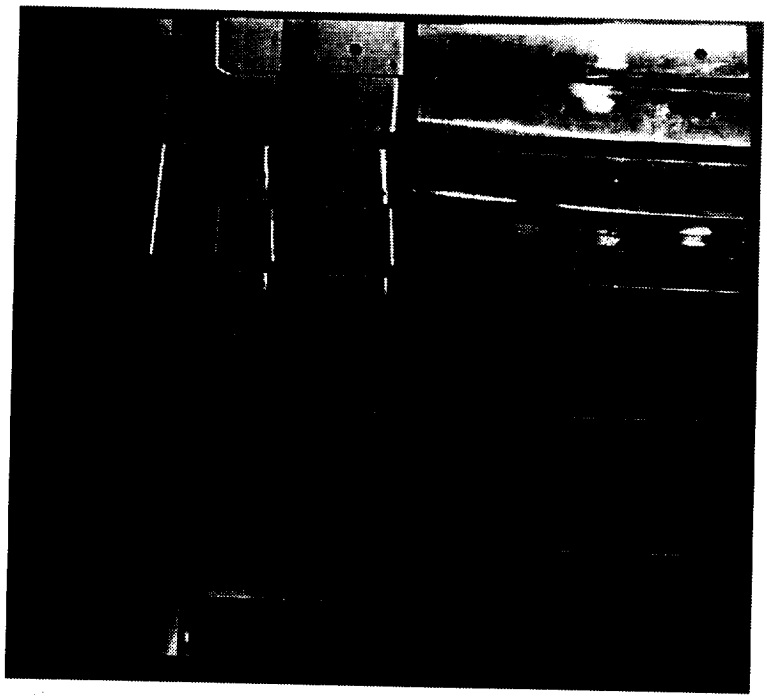

Figure 7.19 7475-T7351 Static Crack Turning Specimens (Set No. 4), L-T and T-L Orientation

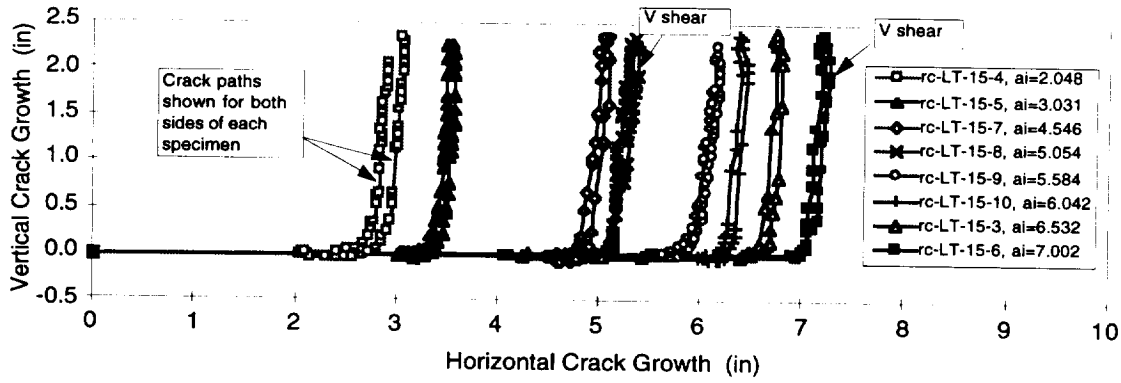

Figure 7.20 Crack Paths, 7050-T7451 Crack Turning Specimens, L-T Orientation

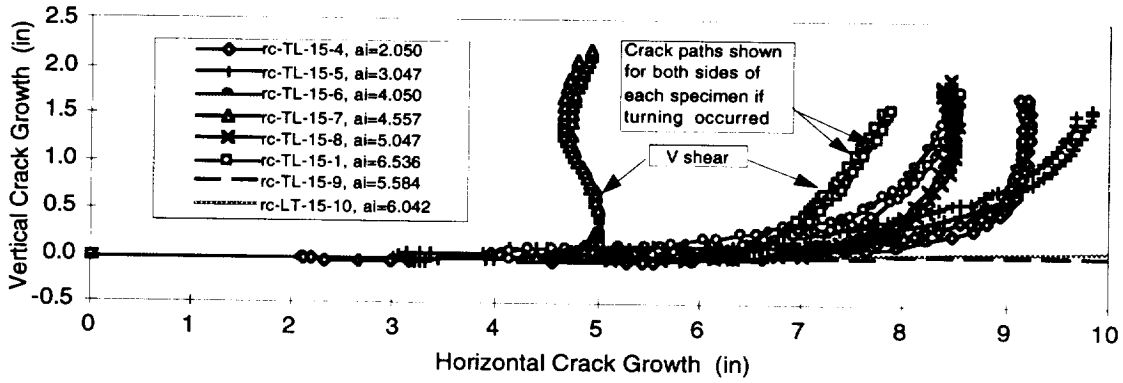

Figure 7.21 Crack Paths, 7050-T7451 Crack Turning Specimens, T-L Orientation

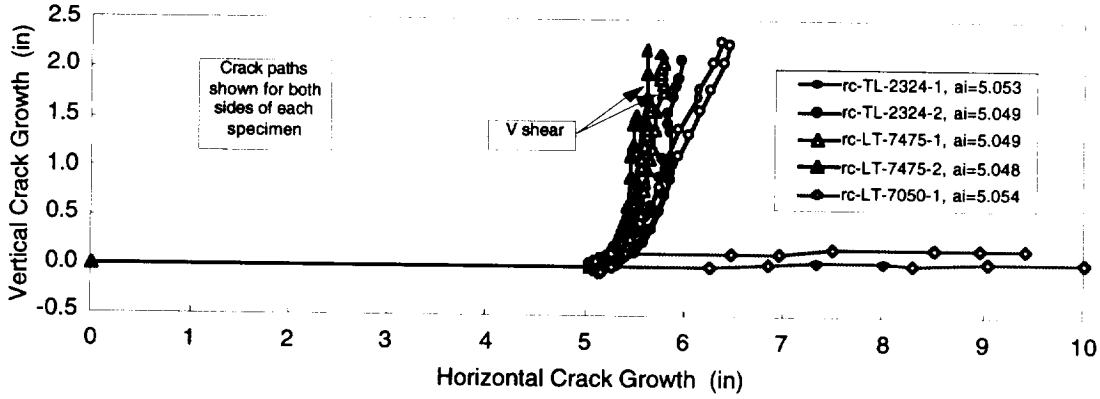

Figure 7.22 Crack Paths, 2324-T39 Plate, 7475-T7351 Plate, and 7050-T76511 Extrusion Alloy Crack Turning Specimens, T-L Orientation

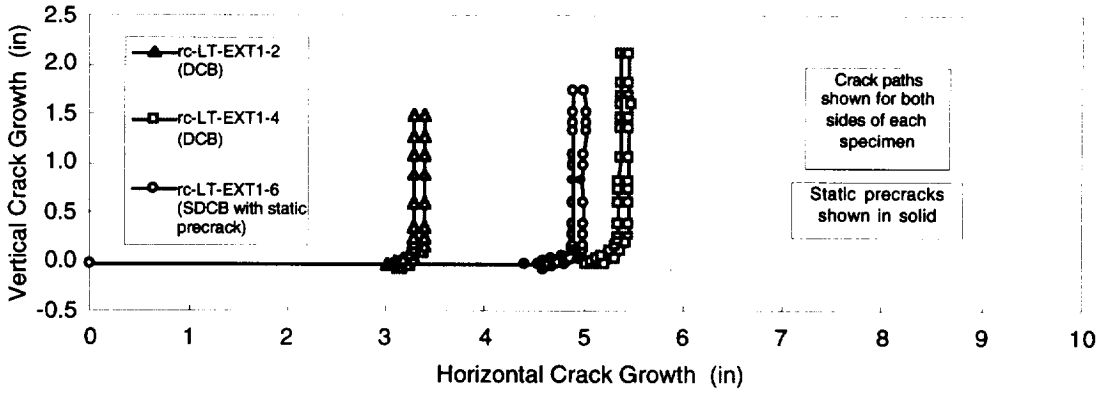

Figure 7.23 Crack Paths, 7050-T74511 Extrusion Crack Turning Specimens, L-T Orientation (Excluding V-ShearFailures)

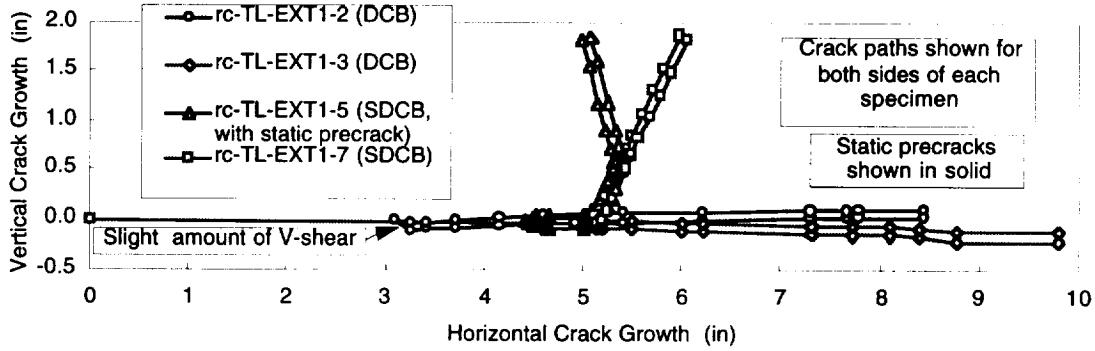

Figure 7.24 Crack Paths, 7050-T74511 Extrusion Crack Turning Specimens, T-L Orientation (Excluding V-ShearFailures Except as Noted)

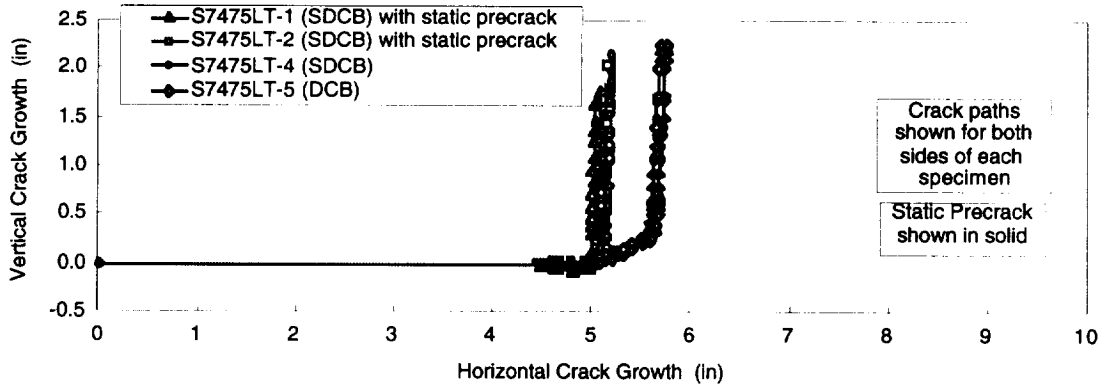

Figure 7.25 Crack Paths, 7475-T7351 Crack Turning Specimens, L-T Orientation (Excluding V-ShearFailures)

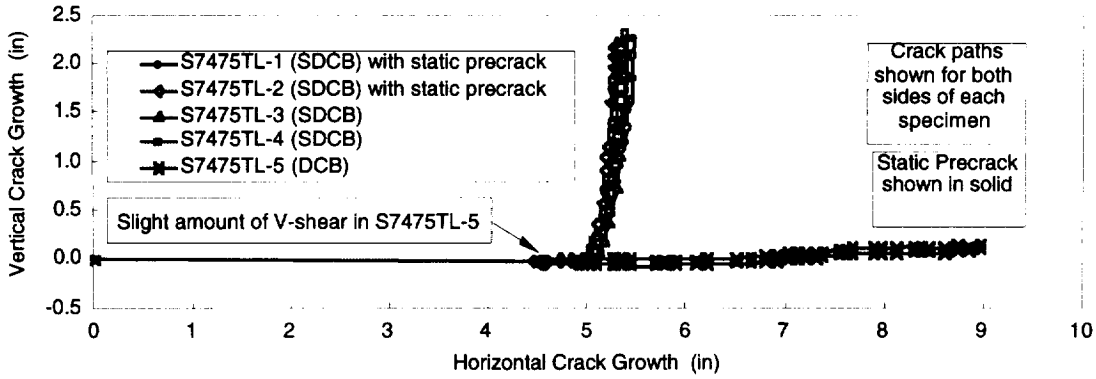

Figure 7.26 Crack Paths, 7475-T7351 Crack Turning Specimens, T-L Orientation

7.5 Discussion

The results of the various specimen sets will now be discussed in greater detail. From the first specimen set, which was made up of symmetric (DCB) specimens, a great deal was learned about the effect of perturbations and orthotropy on the crack path. This configuration was found to be less than optimal for the determination of r_c, but for the orthotropic material tested, was useful for developing the T-L R-curve necessary for determination of $\overline{K}_m$. The orthotropic elastic-plastic method showed good correlation with both the crack path and the load-deflection curve.

The second specimen set, also of symmetric (DCB) configuration, was not analyzed because lot material data was not available, but was intended to provide early results on the likelihood of turning a crack from the favored (T-L) crack orientation in various materials, and is included for completeness.

The third and fourth specimen sets included both DCB and SDCB specimen configurations. The materials were chosen from the extremes observed in set No. 2; set No. 3 was of the highly orthotropic extruded 7050-T74511, and set No. 4 was of the more isotropic 7475-T7451 plate. Emphasis will be on the analysis of the SDCB specimens in the 7475-T7451 material, since that material was found among the most

promising for integral structures during the IAS program, and thus a more complete material data set is available for that material.

7.5.1 7050-T7451 Plate DCB Specimens (Set No. 1)

7.5.1.1 Statically Loaded Specimens

When tested in the stable tearing regime, the 7050-T7451 plate specimens behaved very differently in the L-T and T-L orientations. The L-T specimens transitioned from the flat notch to a slant crack, and then turned quite sharply to a nearly right angle within less than an inch of the initial notch tip. Most of the T-L specimens transitioned from flat to slant, but then took several inches to turn, if they turned at all. Also a few of the specimens failed in a "V-shear" mode (see Figure 7.27 for a description of the different failure modes). The V-shear mode is a somewhat

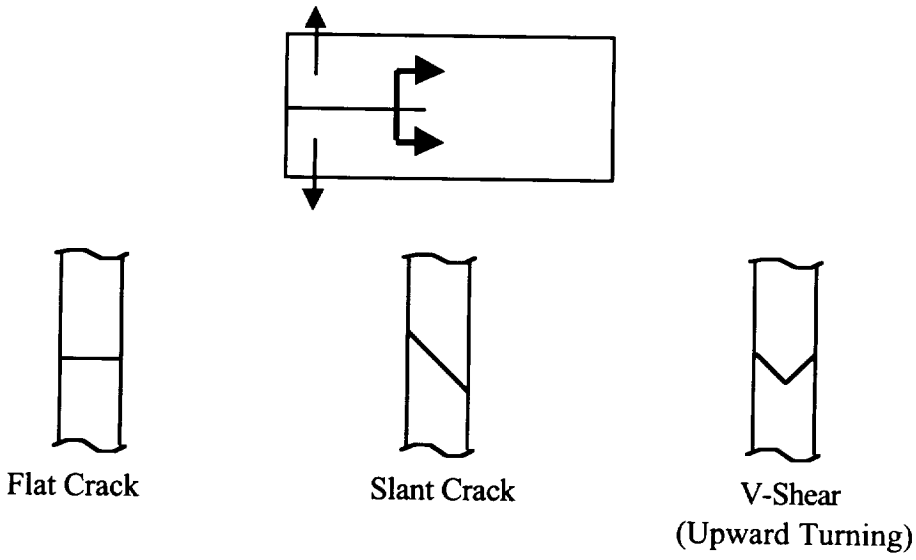

Figure 7.27 Crack Failure Types for Thin Sheet Specimens

randomly occurring asymmetric mode that nearly always results in turning at a fairly sharp angle or radius, and is beyond the scope of the theories developed under the present program[18].

With the exception of the V-shear failures, since the specimens were otherwise geometrically comparable except for the grain orientation, the difference in crack path could only be attributed to the orthotropy of the fracture properties of the 7050-T7451 plate material. Recalling the discussion of Chapter 4, the applicable fracture resistance parameter for determining the orthotropy ratio must correspond to the failure regime, which is stable tearing. Based on NASA 24 inch wide R-curve tests [91] for the 1.5 inch plate material machined down to 0.06 inches thickness, the L-T and T-L fracture toughnesses at a crack extension of about 0.4 inches are 99 and 76 ksi$\sqrt{in}$, giving a $\overline{K}_m$ value for stable tearing of about 1.3. This was the highest toughness value obtained for the T-L testing, but the NASA L-T data continued out to a maximum value of 108 ksi$\sqrt{in}$. Because several of the T-L crack turning specimens exhibited a significant amount of straight growth, it was possible to reduce R-curve data from load/deflection data, as presented in Figure 7.28. Details regarding the data reduction method for the DCB specimen are given in [1].

[18] Note however, that if turning is desirable, the possibility of V-shear failure is not all bad, and in fact it has been suggested that this mode be studied and exploited. V-shear appears to be a mestable state associated with the initiation of stable tearing from a fatigue precrack, and when present, reverts to a slant crack after a short segment of growth. It has been observed to reoccur briefly in structures when a slant crack transitions to the opposite orientation.

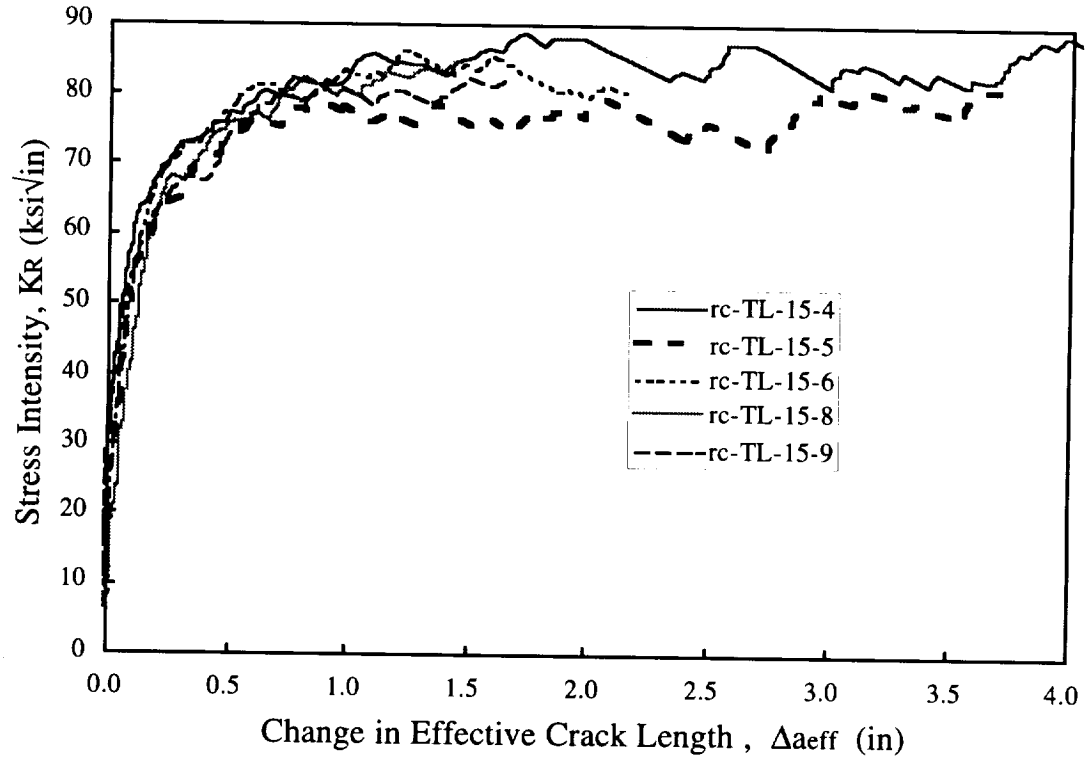

Figure 7.28 R-Curve Data Extracted from T-L 7050-T7451 Crack Turning Specimens in the Straight Crack Growth Region

Since the R-curves were taken from load-deflection data, all the points were not equally critical, as the specimen tore in small finite crack extensions, thus producing somewhat rough curves as shown. The most quasi-static points were probably the peaks, which if connected would be a better representation of the true K_R curve. In any case, it appears that the curves agree well with the NASA data at 0.4 inches growth, and reach a maximum, relatively constant value after 1.5 inches of growth of about 83 ksi√in. Taking the ratio with the top of the R-curve L-T value (108 ksi√in), we again calculate $\overline{K}_m$=1.3. Apparently the ratio is fairly constant within this range.

Determination of the characteristic length, r_c, for stable tearing has been accomplished in a previous investigation [9] by plotting the average minimum turning radius as a function of r_o (calculated per Equation (5.5)). The turning radius is

determined by laying a circle template over the specimen, finding the radius which best matches the radius of curvature at the turning point (average of the radii on each side). A value for r_c can be estimated for isotropic materials by extrapolation to the r_o value at which crack turning occurs with zero radius.

The test matrix for Specimen set No. 1 was originally set up to evaluate r_c in the manner described above (thus including several starting notch dimensions, corresponding to multiple r_o values). However, as fracture orthotropy has become better understood, it has become apparent that the test data cannot be meaningfully reduced in this manner for highly orthotropic materials. This is because the expected critical (bifurcation) value of r_o is different in each direction, and falls out of the range of r_o values tested with the current specimen geometry. Also, turning from the symmetric test configuration was observed to occur over a fairly smooth (albeit often tight) curve, rather than the sharp kink predicted by the second-order linear-elastic theory. Nevertheless, literature values (of unknown accuracy) for 2000 and 7000 series aluminum alloys [8, 9] are on the order of 0.05-0.06 inches, and Appendix A.1 gives values in the 0.05-0.08 range depending on the orientation. It was thus desired to perform a sensitivity study for r_c values in this vicinity to see if the crack paths could be correlated with the second-order orthotropic theory using the FRANC2D implementation described in Chapter 5.

FRANC2D calculates K_I, K_{II}, and T at for a given crack configuration, calculates the new crack direction based on Equation (5.13), extends the crack a specified increment, remeshes the region around the crack tip, and reruns the analysis to calculate the new crack trajectory. An example of a mesh used for analysis of a DCB specimen of L-T orientation is shown Figure 7.29.

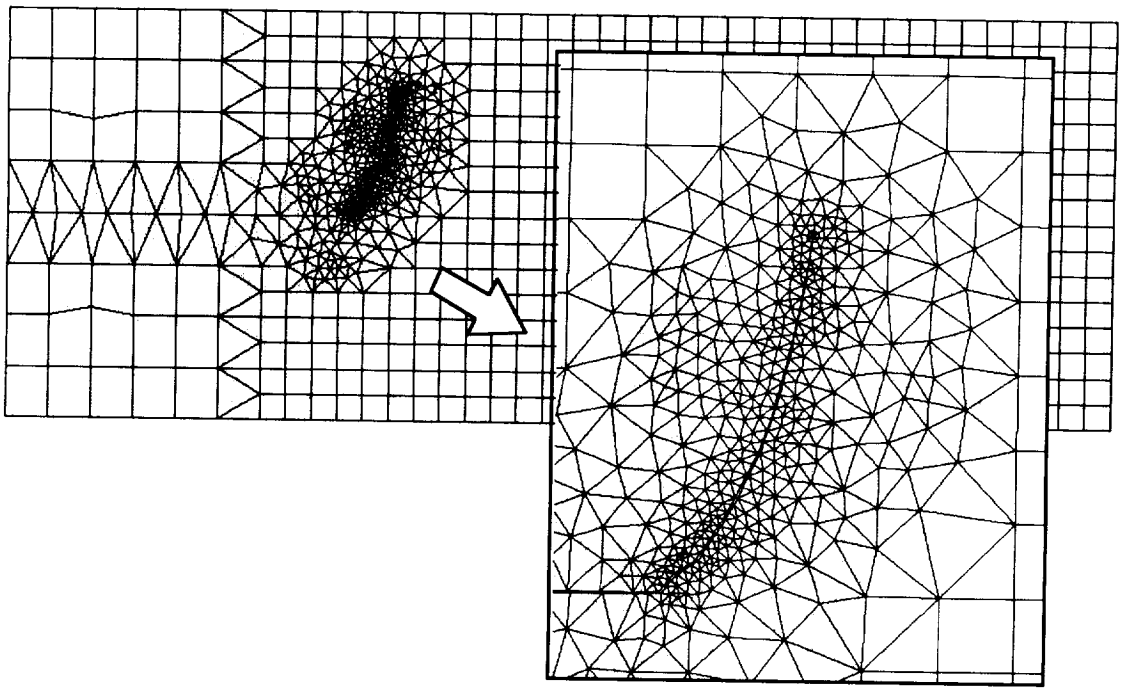

Figure 7.29 FRANC2D Mesh for Analysis of a DCB Specimen

7.5.1.1.1 Perturbation Effects

Unfortunately, the symmetric nature of the specimens is a drawback from a crack-path correlation standpoint for T-L specimens. An analysis of a DCB specimen of a hypothetical material with substantial fracture orthotropy ($\overline{K}_m$=1.67) and various angular perturbations applied at the first step is presented in Figure 7.30. In cases where the crack turns gradually, such as T-L specimens with high orthotropy, the perturbation sensitivity is most significant. Note that the sharply turning L-T curves plot together (independent of perturbation).

Modeling a perfectly symmetric specimen will typically result in a (slightly) non-zero K_{II}, related to discretization error of the mesh, thus only a theoretical line is given for this the unperturbed T-L case in Figure 7.30. In real specimens, perturbation

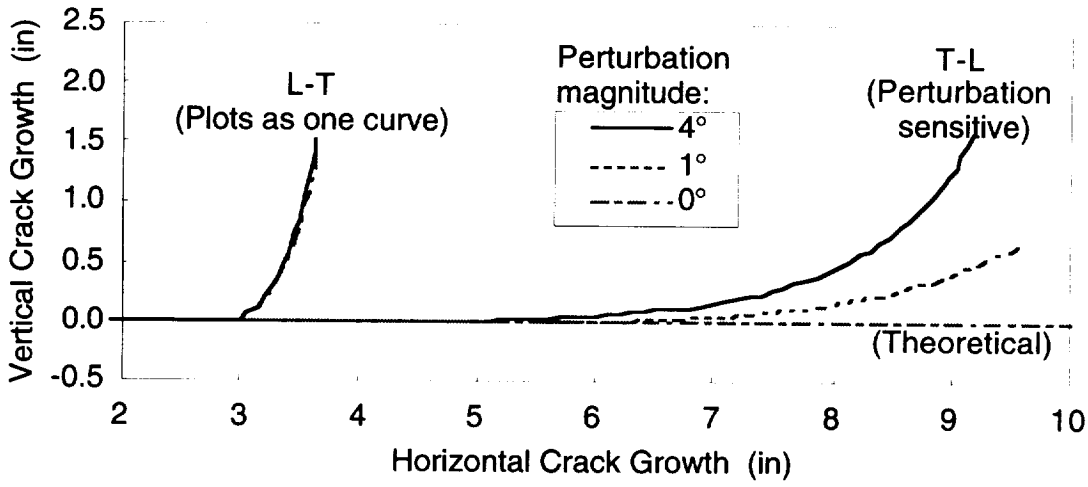

Figure 7.30 FRANC2D Crack Path Sensitivity Study for a DCB Specimen with Various Perturbation Angles Applied at the First Step ($\overline{K}_m$=1.3, a_i=3.0 in, r_c=0.05 in, Step Size = 0.1 in)

could potentially result from manufacturing imperfections in the specimen geometry, the effects of gravity on the specimen, and the natural meandering nature of the crack tip due material inhomogeneity. Gravitational effects were largely ruled out as a major contributor, since the specimens did not all turn the same direction (up or down) in the test machine. Geometric irregularities in the specimens, while potentially significant, were small enough that they were difficult to quantify in a meaningful way, though it was evident that the precracks were sometimes observably out of alignment with the starting notches (and this varied through the thickness). Nevertheless, visual inspection of the specimens suggested that even in fairly nominally straight regions of stable tearing, the natural meandering of the crack appeared to provide a potentially significant source of perturbation.

In an attempt to quantify the inherent perturbation distribution of a meandering (stably tearing) crack in 7050-T7451 plate, a high resolution scan of a 2.5 inch length of substantially straight crack growth in specimen rc-TL-15-4 was sampled for angular slope (point to point) at various increment lengths. The data and a curve fit to a

logarithmic distribution is given in Figure 7.31, and shows that there is about an eighty percent likelihood of an angular perturbation exceeding an angle of one degree over a typical 0.010 inch length of crack propagation.

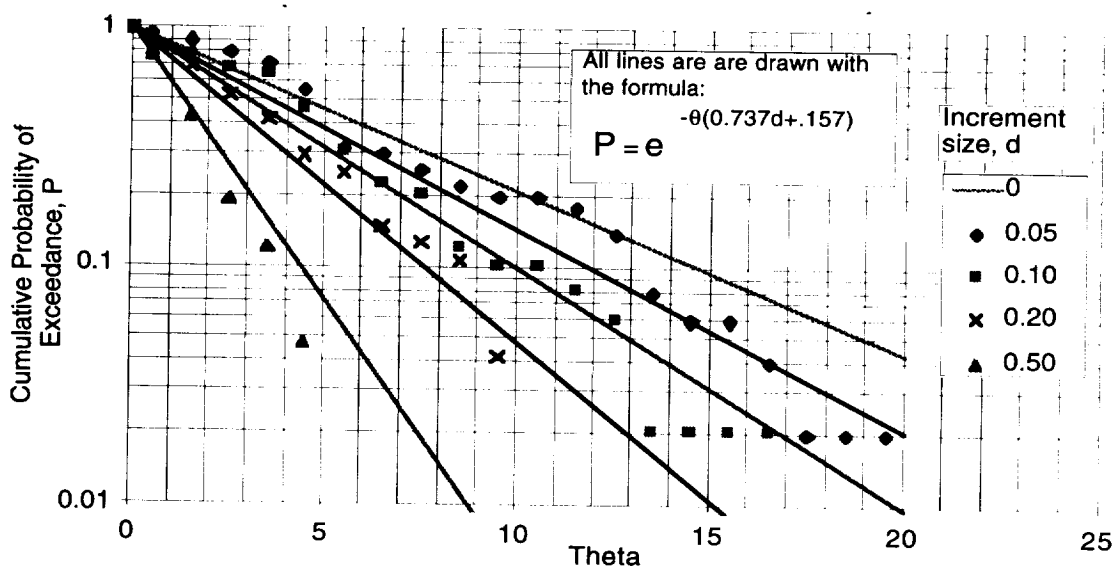

Figure 7.31 Perturbation Distribution for 7050-T7451 Plate, Obtained from Nominally Straight Stable Tearing Region of Specimen

7.5.1.1.2 Correlation with Second-Order Turning Theory, Including Toughness Orthotropy

With substantial random perturbation due to material inhomogeneity, and the potential for geometric imperfections, one would expect a noticeable amount of scatter in the crack paths for nominally self-similar specimens such as the DCB. However, we observe that after a finite amount of crack growth, including an amount of perturbation induced turning, the specimen geometry is no longer symmetric. At this point its future path should be more predictable, since the nominal asymmetry is then larger compared to random perturbations[19].

Specimens rc-TL-15-5 and rc-TL-15-8 were analyzed in this manner with

[19] By the same logic, real physical problems would not be expected to be highly perturbation sensitive unless they are nearly symmetric.

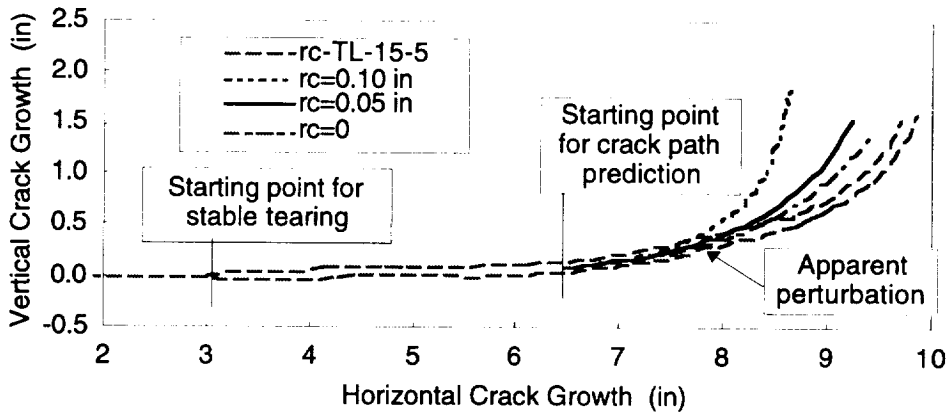

a) Specimen rc-TL-15-5

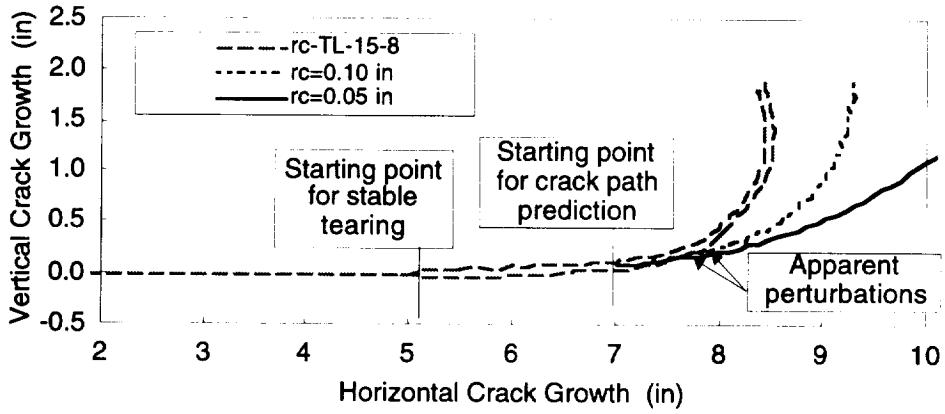

b) Specimen rc-TL-15-8

Figure 7.32 Correlation of Observed and Predicted Crack Paths for Selected 7050-T7451 Specimens (L-T Orientation, $\overline{K}_m = 1.3$, Step Size = 0.1 in)

correlation of various analyses shown in Figures 7.32a and 7.32b. The models included the actual crack path up until the vertical (asymmetric) growth component was about 0.1 inches, and the crack path was predicted analytically from that point, using an orthotropy ratio $\overline{K}_m$=1.3, and a crack increment step size of 0.1 inches.

From Figures 7.32a and 7.32b, we observe that with the level of orthotropy present, the choice of r_c has a modest effect on the predicted (T-L) crack. An r_c value

of approximately 0.10 inches gives the best results in an average sense, overestimating the turning in one case and underestimating in the other. The remaining disparity in the crack paths appears to result from perturbations observed along the crack path presumably due to material inhomogeneity. Also, for 7475-T7451 the steady state Irwin plastic zone is about 0.5 in (T-L) to 0.7 in (L-T), and the LEFM approximation becomes increasingly poor as uncracked ligament decreases.

In the L-T orientation, all specimens turn fairly sharply to nearly 90 degrees, as shown in Figure 7.20. The FRANC2D analysis in Figure 7.30 illustrates that this result is predicted for an orthotropy ratio of 1.3 almost independent of the perturbation magnitude. The results are re-plotted in Figure 7.33 with comparison to the crack path of specimen rc-LT-15-5. Clearly, the correlation is favorable, and is in this case enhanced by an r_c value of at least 0.05 inches, but insensitive to higher values. A value of r_c=0.1 gives the best correlation with both T-L and L-T results.

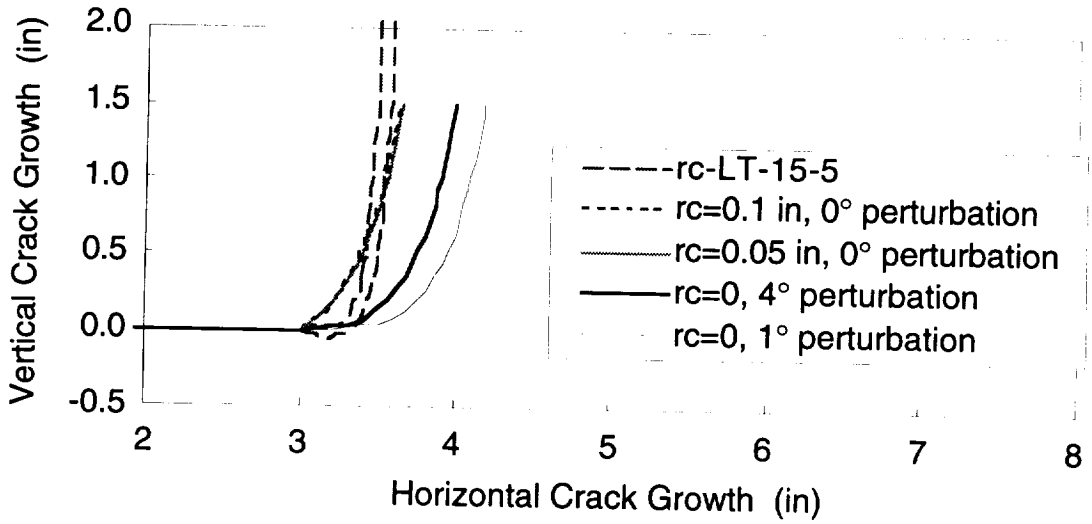

Figure 7.33 Correlation of Observed and Predicted Crack Paths for Selected 7050-T7451 Specimens Using the Second Order Elastic Theory with Toughness Orthotropy (L-T Orientation, $\overline{K}_m$ = 1.3, Step Size = 0.1 in)

7.5.1.1.3 Correlation with Elastic-Plastic CTOD Method, Including Toughness Orthotropy

The elastic plastic method first requires determination of the critical crack tip opening displacement, D_c. For the isotropic case, this is accomplished [40] by running simulations of a fracture test assuming various value of D_c, and choosing the value that results in the best match of the observed load-deflection curve. With fracture orthotropy, the same approach applies, with recognition that D_c is a function of orientation. The approach that was taken was to determine $D_c(0°)$ from a straight-growing specimen of T-L orientation. FRANC2D/L then uses Equation (5.42) to estimate the critical CTOD for other orientations[20].

Specimen rc-TL-15-9 grew quite straight, and was chosen for determination of D_c. Figure 7.34 shows good correlation of the observed response to that predicted by a simulation using $D_c(0°)$=0.0026 inches, thus this value was chosen for use in subsequent analyses. There is also evidence of an initial, slightly higher critical CTOD at the initiation of stable tearing, as has been observed by other authors [38], though this was neglected for the present study.

Simulating a length of the actual crack path, as was done for the linear elastic method, was not practical for the elastic-plastic method, because the path is history dependent, and must be grown, not simply modeled geometrically, to obtain the proper plastic history. The actual fatigue precrack angles for these specimens were small, leaving the actual crack path subject to random perturbations as discussed earlier. Thus specimens rc-TL-15-5 and rc-LT-15-5 were modeled from the nominal initial precrack configuration (a=3.0 inches), but with a small angle kink in the last 0.1

---

[20] Note that the value of $\overline{K}_m$ used herein is based on fracture toughness data, allowing a consistent orthotropy ratio for both linear elastic and elastic-plastic studies. In practice, it may be advantageous to determine both $D_c(0°)$ and $D_c(90°)$ directly from fracture specimens, then obtain $\overline{K}_m$ from Equation (5.40).

inch of the precrack to provide an initial perturbation. Perturbation angles of 1.0 and 4.0 degrees were modeled for each specimen, and compared with actual measured paths in Figures 7.35 and 7.36. Inasmuch as the average random perturbation angle for a 0.1 inch increment is about three degrees based on Figure 7.31, correlation between predicted and observed trajectories is quite satisfactory. For the L-T specimen, predicted curves are smooth, and resemble the observed path better than the linear-elastic prediction.

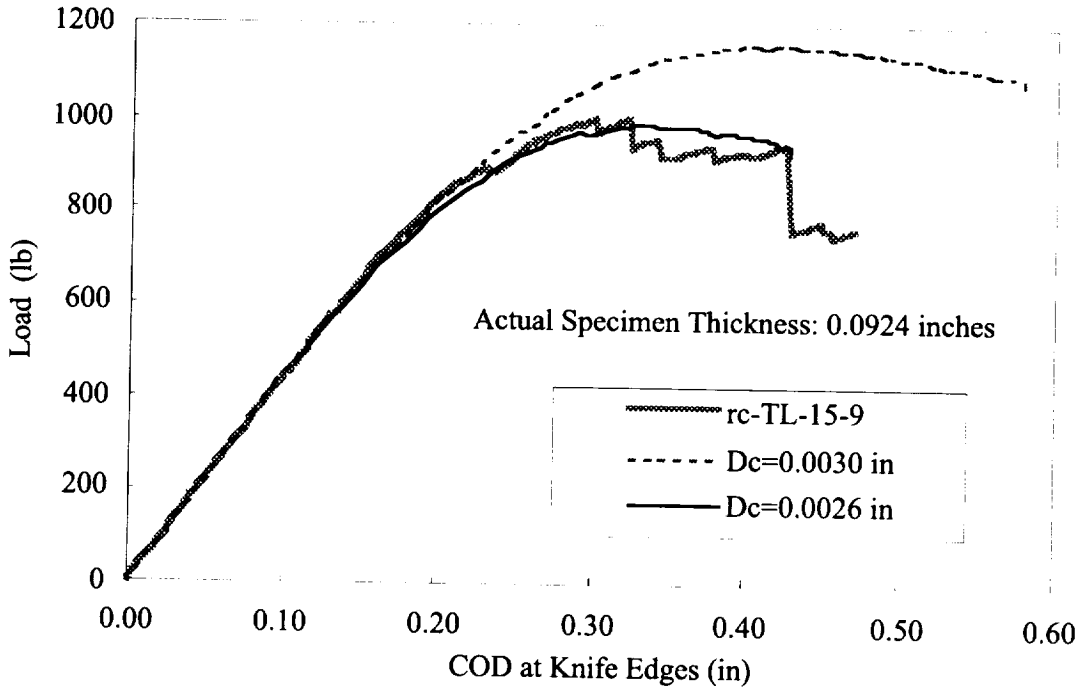

Figure 7.34 Correlation of Observed and Predicted Load vs.COD for Specimen rc-TL-15-9 *(T-L Orientation , Straight Crack Growth, Elastic-Plastic Method)*

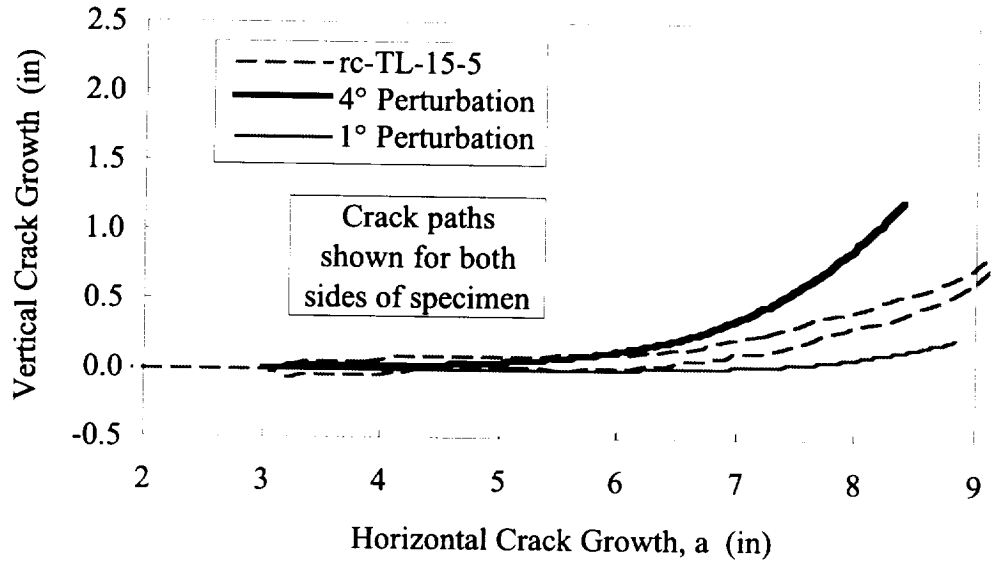

Figure 7.35 Correlation of Observed and Predicted Crack Paths for Specimen rc-TL-15-5 *(T-L Orientation , Natural Crack Growth, Elastic-Plastic Method,* $\overline{K}_m = 1.3$*)*

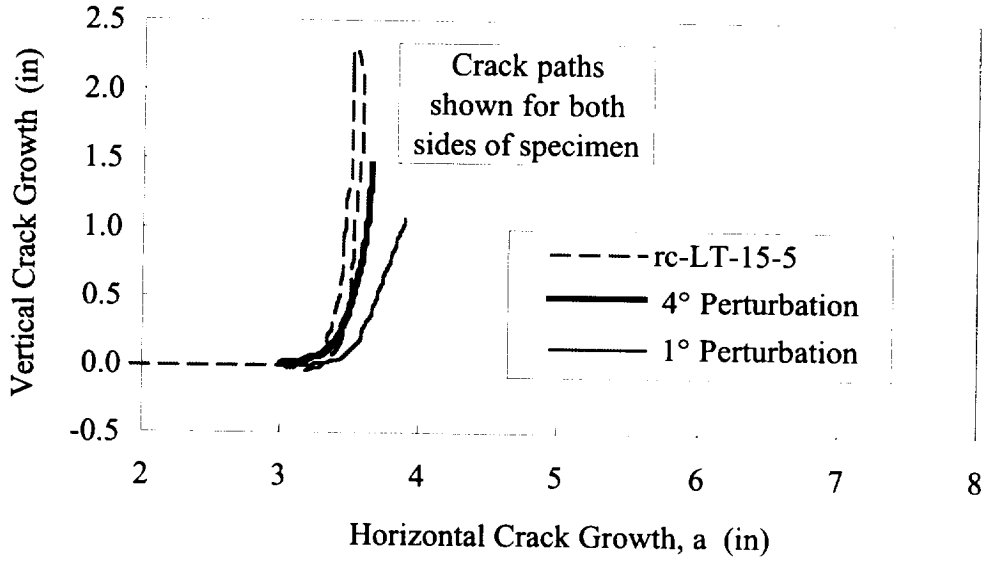

Figure 7.36 Correlation of Observed and Predicted Crack Paths for Specimen rc-TL-15-9 *(L-T Orientation , Natural Crack Growth, Elastic-Plastic Method,* $\overline{K}_m = 1.3$*)*

7.5.1.2 Fatigue Loaded Specimens

Inasmuch as r_c is expected to scale with the plastic zone size, it is expected to be negligible for slow fatigue crack growth. The fracture orthotropy ratio can be obtained from a comparison of L-T and T-L fatigue crack growth rate data, shown in Figure 7.37, taken from the straight growth regions of specimens rc-LT-15-2 and rc-TL-15-2. Extrapolating the data into approximately parallel lines in this regime of growth, it is apparent that to obtain the same crack growth rate in either orientation, one would have to load the L-T crack about 10 percent more than the T-L crack, thus the orthotropy ratio is about 1.1.

With r_c=0, and a nominally symmetric, gradually turning crack, a high degree of perturbation sensitivity is expected. The FRANC2D analysis thus utilized the actual crack path up to 0.1 inches of asymmetric growth in the same manner as was done in Figure 7.32. The resulting correlation shown in Figure 7.38 is very favorable for the L-T case. Correlation was somewhat worse for the T-L case, possibly because the stress intensity for growth was getting high enough that the T-stress had an effect which was not modeled since we assumed r_c=0 for fatigue crack growth.

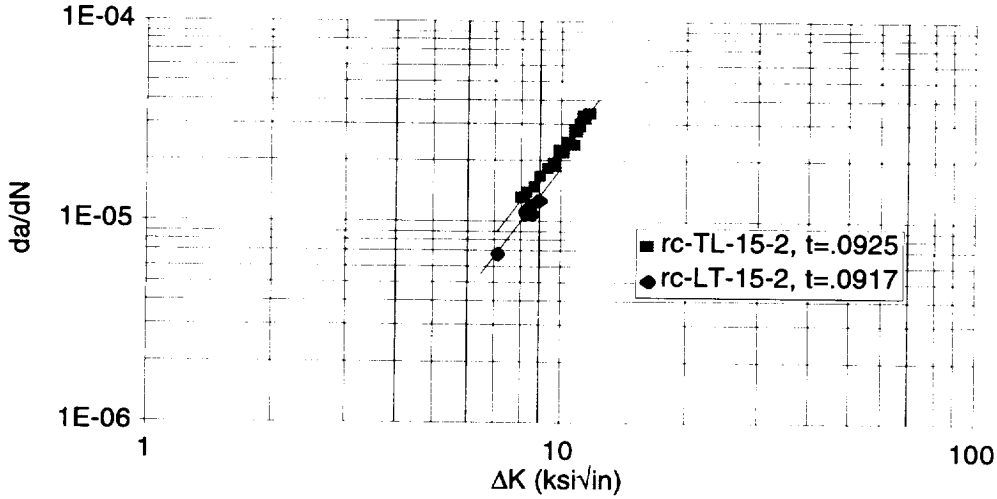

Figure 7.37 Comparison of T-L and L-T Fatigue Crack Growth Data Taken from DCB Specimens, Stress Ratio=0.05

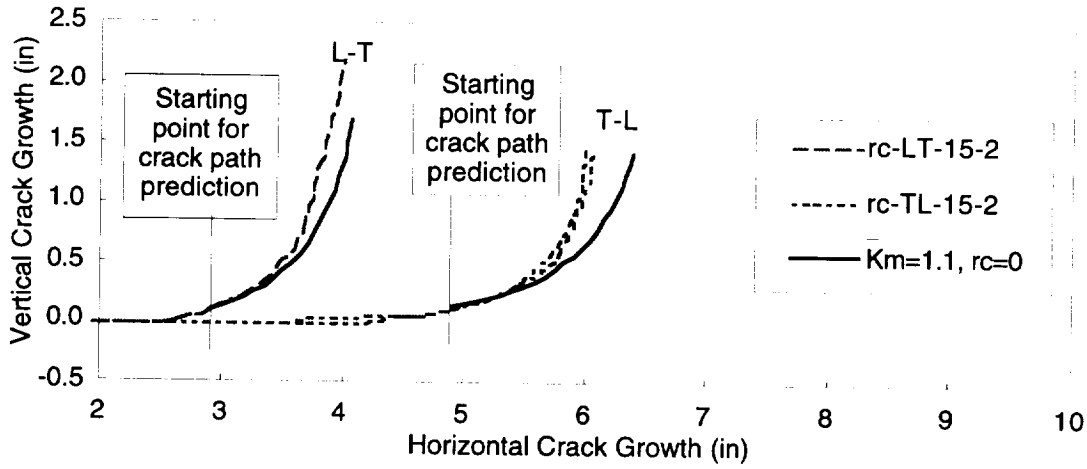

Figure 7.38 Comparison of T-L and L-T Fatigue Crack Paths Taken from DCB Specimens, Stress Ratio=0.05

7.5.2 2324-T39, 7475-T7351, and 7050-T76511 DCB Specimens (Set No. 2)

The primary purpose of these tests was to obtain information about the orthotropy of these alloys, and the likelihood of turning a crack from the T-L orientation. This information was needed to support a material selection decision for a large panel test under the IAS program requiring a sufficiently isotropic material to enable crack turning of a longitudinal fuselage crack (T-L). Only T-L specimens were tested with the underlying assumption that $\overline{K}_m \geq 1$. Based on results reported in [9] for 2024-T3 DCB tests, one would expect that fairly isotropic T-L specimens would turn sharply due to the high T-stress environment. From the curves plotted in Figure 7.22, 2324-T9 plate clearly falls into this category, while 7050-T76511 does not. It was also concluded that 7475-T7351 was sufficiently isotropic to turn a T-L crack, though it was observed that both 7475-T7351 specimens exhibited a small amount of V-shear behavior, which could have influenced the results.

Without performing further testing at the time, the project went on to build and test a large fuselage barrel test panel out of 7475-T7351 plate for testing with a two-bay crack. While the panel performed well in residual strength, the crack did not turn

appreciably [92]. As will be discussed with regard to specimen set No. 4, an (L-T) DCB specimen cut later from the same lot of material as the test panel did not turn either (though also with a small amount of V-shear). Based on a rudimentary estimate of the T-stress made for the fuselage panel during the IAS program, the panel had less T-stress than the specimen, thus would not have been expected to turn the crack.

Further crack path analysis was not performed on these specimens.

7.5.3 7050-T74511 Extrusion DCB and SDCB Specimens (Set No. 3)

Large extrusions with integrated skin and stiffeners have been identified as a potentially cost-effective approach for both wing and fuselage applications. However, because of the directional nature of the processing, extrusions were expected to manifest substantial toughness orthotropy, making cracks difficult to turn from the preferred T-L orientation. For fuselage applications, it is preferable to turn both longitudinal and transverse cracks, should they impinge upon either frame or longeron. For wing applications, it may be sufficient to turn cracks from the L-T to the T-L orientation as they impinge upon a longitudinal stiffener.

As shown in Figures 7.23 and 7.24, cracks in the L-T DCB specimens turned immediately about a small radius to a near 90 degree angle, and cracks in the T-L DCB specimens grew straight, as would be expected for a material with significant toughness orthotropy[21]. Due to the high toughness orthotropy, among other things, this material was deselected from the IAS fuselage program before any R-curves were run, thus the degree of orthotropy could not be determined in the usual manner. (While T-L R-curves could be developed from the straight growing DCB specimens, there was excessive turning for R-curve development in the L-T specimens).

---

[21] V-shear specimens have been excluded from the crack path plots for this set, as well as the discussion. To get an idea of the V-shear crack paths, see specimen photographs. V-shear failure was always accompanied by severe turning, regardless of initial crack orientation.

As an alternative, it was noted that specimen rc-TL-EXT1-7, an SDCB specimen, turned sharply at 64.5 degrees from the initial crack length, a_i=6.18 inches, and grew nearly in a straight line crack extension for about 2.2 inches. Because the path is straight, we should theoretically be able to assume that the K_{II}/K_I ratio represents the critical value given in Equation (5.15) with θ=64.5 degrees. For a given orthotropy ratio and orientation, the critical K_{II}/K_I ratio should be relatively constant. A FRANC2D analysis of this problem reveals that the K_{II}/K_I ratio varies along the straight path described as shown in Figure 7.39. The variation is so dramatic that (even changing sign), that it is difficult to imagine that the material properties are constant along the crack, unless there were an unanticipated axis of minimum toughness lying along the crack path. If that were the case, then a nearly identical crack path would have been expected in specimen rc-TL-EXT1-5, which did not occur.

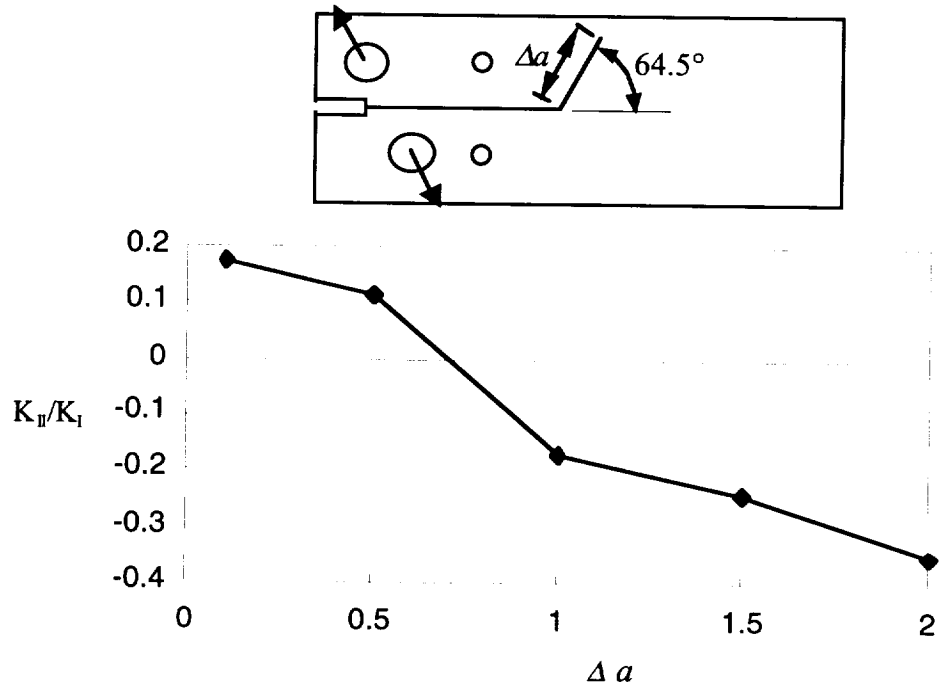

Figure 7.39 K_{II}/K_I Values Predicted by FRANC2D Along a Straight Crack Extension Following a 64.5° Kink, Specimen rc-TL-EXT1-7

Various explanations might exist for the observed anomalies. It is well known that the grain structure varies considerably within extruded shapes, potentially resulting in heterogeneous fracture properties. Also, the specimens were not very flat, indicating potentially significant residual stresses, and potentially giving rise to undesireable and potentially nonuniform frictional loading from the anti-buckling guide. To further complicate matters, 30 percent of the specimens failed in V-shear mode.

As a result of these anomalies, and in the absence of R-curve data, it was not possible to reduce meaningful values for $\overline{K}_m$ and r_c for the 7050-T74511 extrusion material from the specimens provided.

7.5.4 7475-T7351 Plate DCB and SDCB Specimens (Set No. 4)

7475-T7351 plate has an excellent combination of strength, fracture toughness, and stress-corrosion resistance, and was the material of choice for the IAS fuselage test program. It was desired to determine the values of $\overline{K}_m$ and r_c for this material.

Forty inch wide R-curve tests were run at NASA Langley Research Center [93] on the same lot of material used for the IAS widebody barrel test, and are plotted in Figure 7.40. For a given value of effective crack extension, Δa_{eff}, the L-T fracture resistance is about 10 percent higher than the T-L value, thus $\overline{K}_m$=1.1.

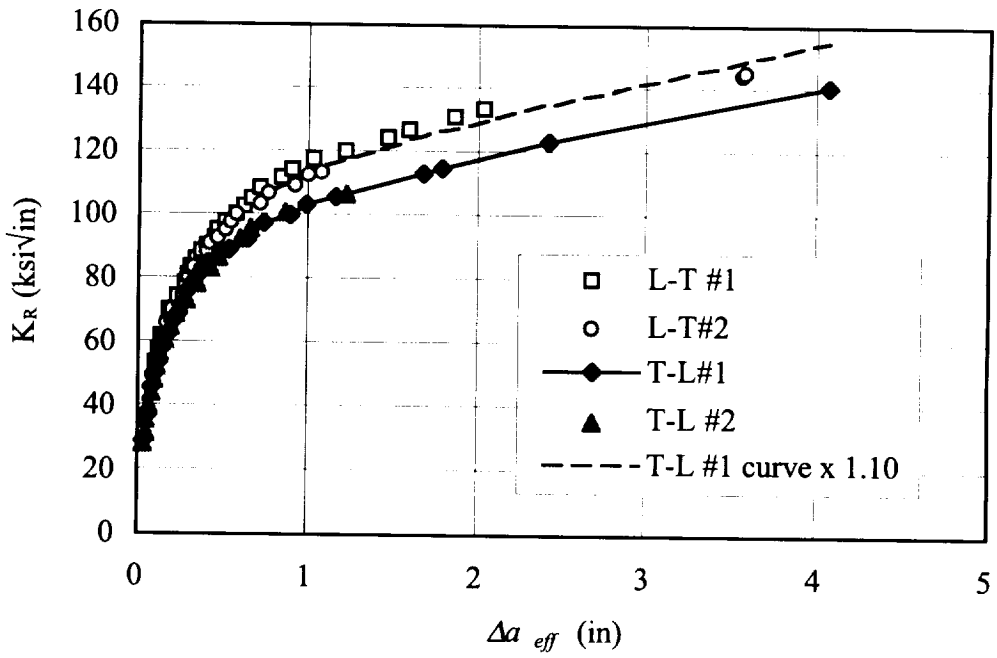

Figure 7.40 Determination of Stable Tearing Fracture Toughness Orthotropy Ratio, $\overline{K}_m$, from 7475-T7451 R-Curve Data

7.5.4.1 Correlation with 2nd-Order Linear-Elastic Theory, Including Toughness Orthotropy

For the SDCB specimen geometry of Figure 7.3, Equations (7.4) and (7.5) give K_{II}/K_I=0.20, and r_o=0.0546 inches for the precracked starter notch configuration. Based on these conditions, the initial kink angle predicted by the second-order, linear-elastic, maximum circumferential stress theory is given in Figure 7.41 as a function of initial crack orientation for various values of r_c. Plotted for comparison are the actual kink angles observed in each of the 7475-T7351 SDCB specimens, measured from high-resolution optical scans of the specimens. The initial crack orientation plotted along the ordinate is defined relative to the longitudinal (rolling) axis of the plate material, and reflects the measured angle at the crack tip after precracking. Data is shown for both T-L (0°) and L-T (90°) specimens, excluding specimen

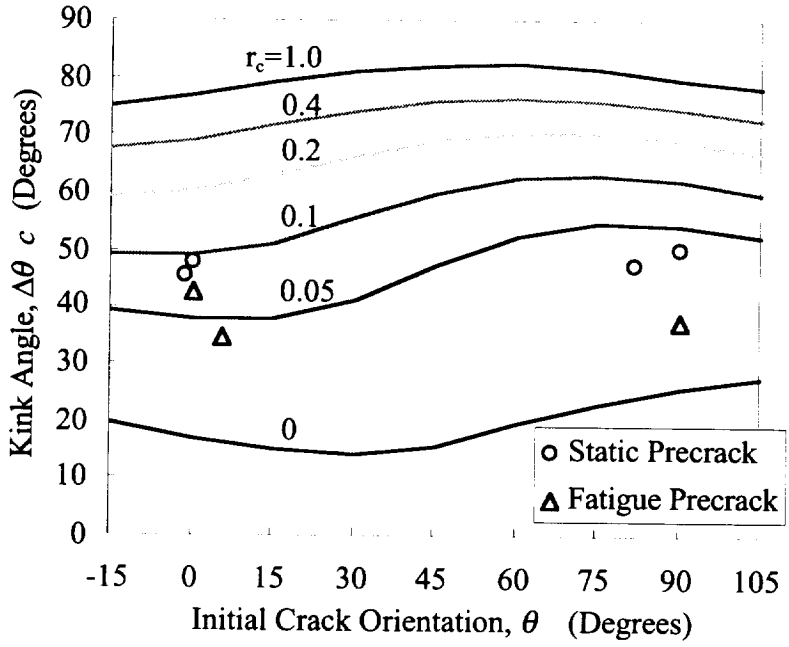

Figure 7.41 Determination of r_c from Crack Kinking Data, K_{II}/K_I=0.2

S7475-LT-3, which failed in V-shear. The kink angle is measured relative to the precrack angle, and each data point represents an average of angles measured on each side of the specimen.

From Figure 7.41 we observe that the measured angles for static precracked specimens are higher then for specimens precracked with fatigue loading only. This may reflect an increase in process zone size corresponding to the increased crack growth resistance, K_R, of the statically precracked specimens. However, the difference is small in terms of r_c, particularly considering the rather large K_R gradient evident in the first 0.5 inches of stable tearing in Figure 7.40. Also, accurate measurement of the kink angle is more difficult for the fatigue precracked specimens because the crack transitions to a slant crack while it kinks, as shown in Figure 7.42. For this reason, kink angles measured from the statically precracked specimens are considered to be more reliable and representative, and correspond to r_c values of approximately 0.08

inches in the T-L orientation and 0.04 inches in the L-T orientation, or an average value of 0.06 inches. Clearly, first-order theory (r_c=0) is incapable of predicting the correct turning angles.

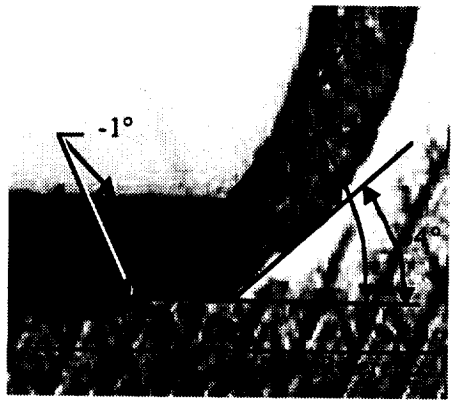

a. S7475-TL-2 (Static Precrack)

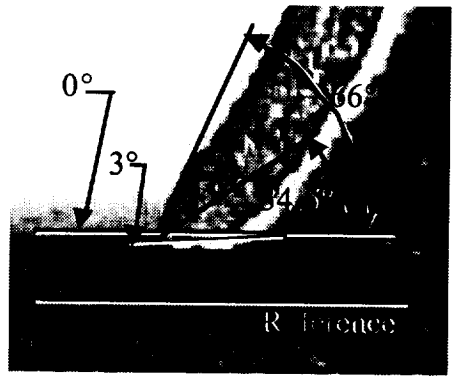

b. S7475-TL-3 (Fatigue Precrack Only)

Figure 7.42 Measurement of Initial Crack Kink Angle in Specimens with and without Static Precracking

Based on the values of $\overline{K}_m$ and r_c determined above, DCB specimens S7475LT-5 and S7475TL-5 were analyzed the second-order linear elastic maximum tangential stress theory with toughness orthotropy. The fatigue precracks developed at the notch tips were at 29° and -9° to the notch orientation, respectively, and

initiated slightly off-center (see first three points of each crack path given in Appendix 4.0). These details were included in FRANC2D models of the specimens, providing a small initial asymmetry.

Predicted and observed crack paths are given in Figures 7.43 and 7.44, respectively. Correlation is quite satisfactory in the L-T orientation, though the observed crack path seems to show more severe turning as the crack orientation "snaps" into the preferred, longitudinal grain orientation. Similar behavior was found in other 7475-T7451 specimens, indicating that the fracture resistance function, $\overline{K}(\theta)$ may have a more pronounced minimum than the simple function given by Equation (4.6). This would also explain why the T-L specimen turned less than predicted by the model. Nevertheless, based on the previous discussion with regard to Figure 7.30, one would also expect that a slightly curving crack such as in the T-L case, the path is

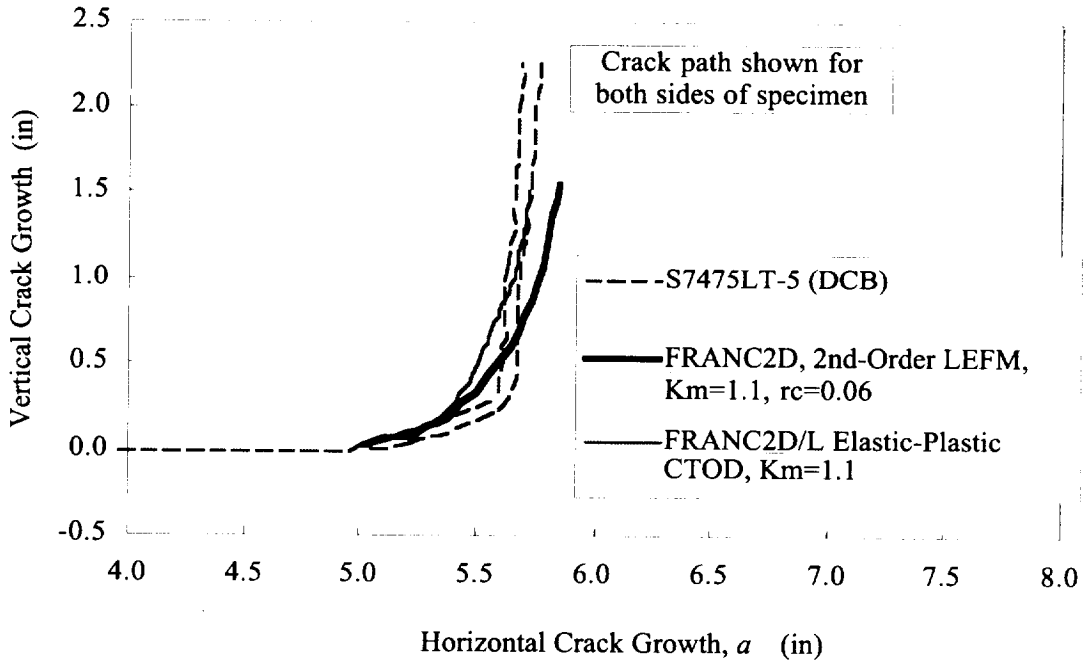

Figure 7.43 Correlation of Observed and Predicted Crack Paths for Specimen S7475LT-5 *(L-T Orientation)*

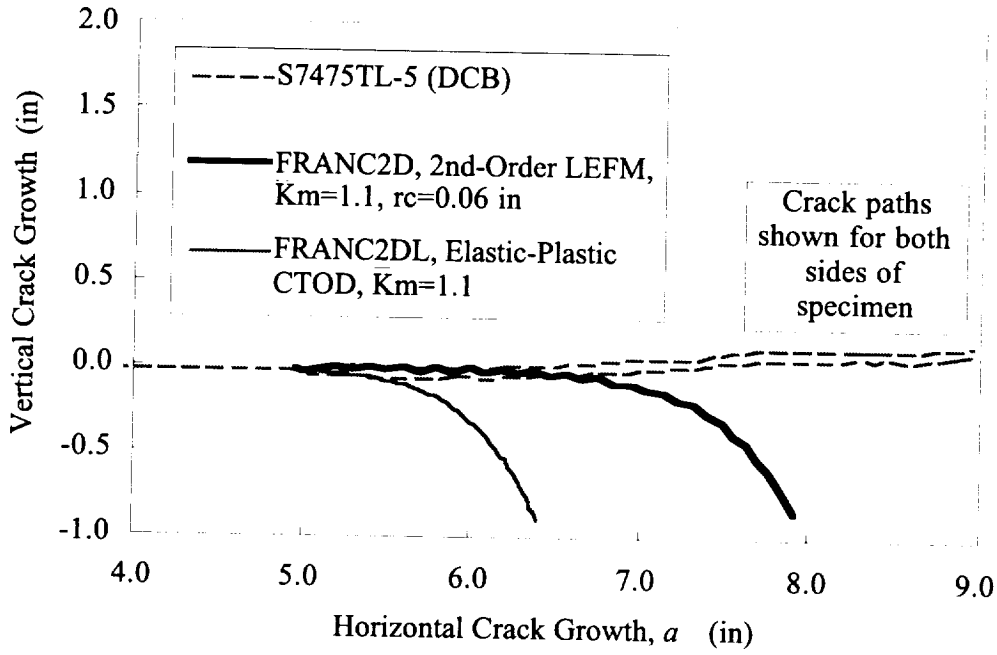

Figure 7.44 Correlation of Observed and Predicted Crack Paths for Specimen S7475LT-5 *(L-T Orientation)*

sensitive to the random perturbations due such as those described in Figure 7.31. It is likely that if several additional specimens were tested, some would show gradual turning as predicted[22].

7.5.4.2 Correlation with the Elastic-Plastic CTOD Method, Including Toughness Orthotropy

Specimen S7475TL-5 is of T-L (0°) orientation, grew essentially straight, and was used as a basis to determine $D_c(0°)$. The results of FRANC2D/L simulations based on various values of $D_c(0°)$ are compared with observed load/COD data for this specimen in Figure 7.45. The simulations assumed the crack grew straight, neglecting the small deviations from straightness observed in the actual specimen. For the most part, the observed response fell between the simulated curves for $D_c(0°)$=0.0028 and

[22] Note from Figures 7.15 and 7.21 that most of the T-L 7050-T7451 specimens turned, even though that material was found to have higher toughness orthotropy than 7475-T7451.

$D_c(0°)$=0.0030 inches, thus a critical value of 0.0029 inches was assumed for subsequent analysis. There was also evidence of an initial, higher critical CTOD at the initiation of stable tearing, as has been observed by other authors [38], though this was neglected for the present study.

Assuming $D_c(0°)$=0.0029 inches, $\overline{K}_m$=1.1, DCB specimens S7475TL5 and S7475LT5 were analyzed using the elastic-plastic implementation in FRANC2D/L. For these analyses, the initial measured angles associated with the fatigue precrack were included in the starting notch configurations as was done for the second-order LEFM analyses performed in the preceding section, giving a small initial deviation from symmetry. Predicted crack paths are included in Figures 7.43 and 7.44, and load/COD plots are compared with observed response in Figures 7.46 and 7.47, respectively.

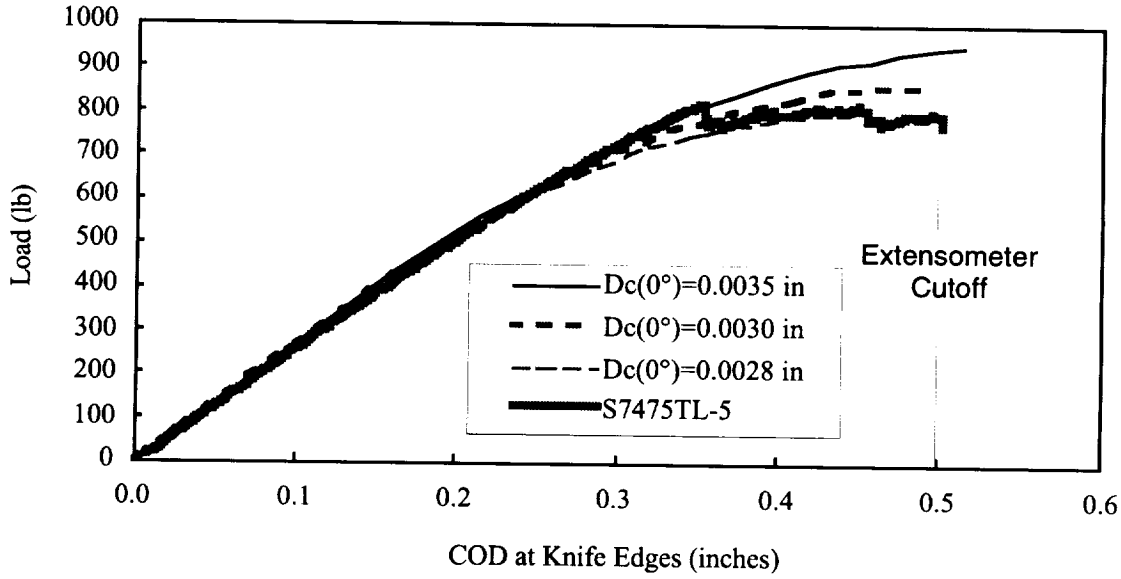

Figure 7.45 Correlation of Observed and Predicted Load vs. COD for Specimen S7475TL-5 *(T-L Orientation , Straight Crack Growth Assumed)*

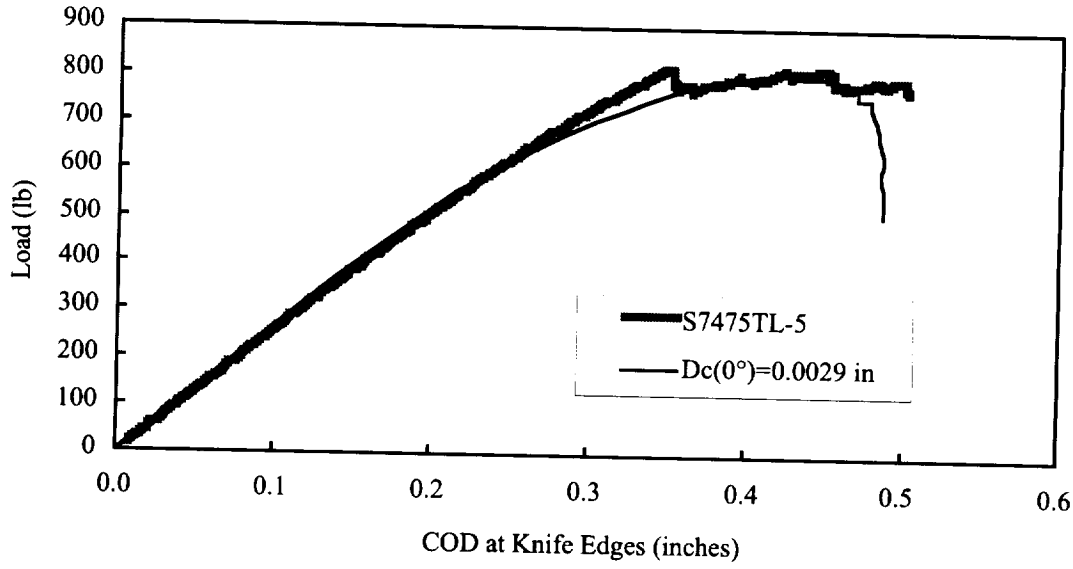

Figure 7.46 Correlation of Observed and Predicted Load vs.COD for Specimen S7475TL-5 *(T-L Orientation, Natural Crack Growth from Fatigue Precrack),* $\overline{K}_m$=1.1

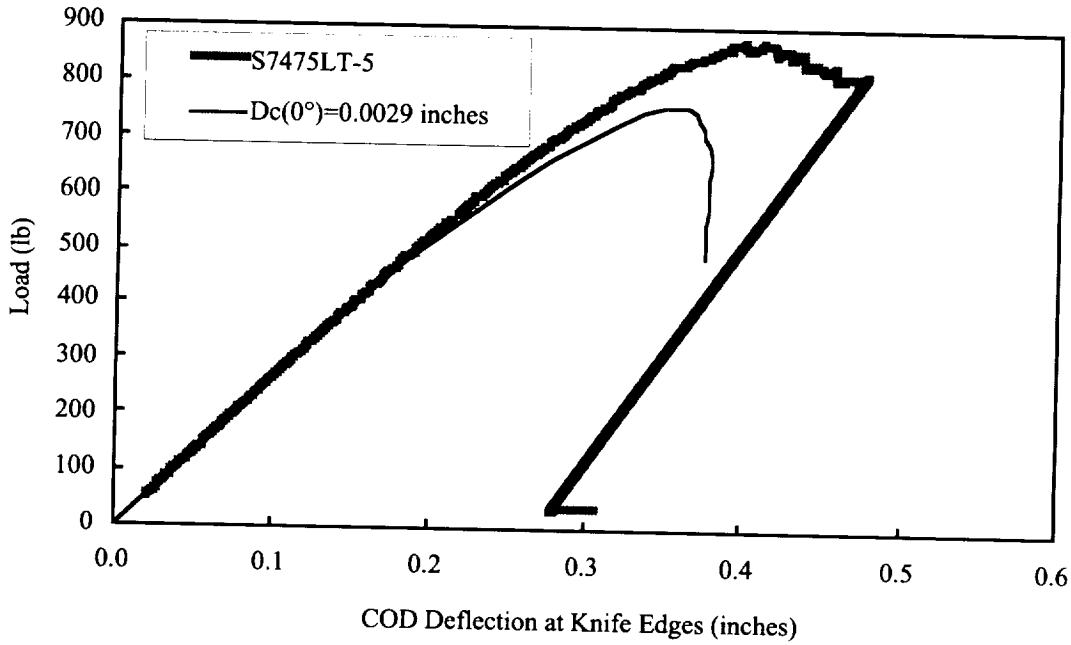

Figure 7.47 Correlation of Observed and Predicted Load vs.COD for Specimen S7475LT-5 *(L-T Orientation),* $\overline{K}_m$=1.1

The predicted crack path for specimen S7475LT5 (90°) compares well to the measured response, and is very similar to the predicted behavior of the second-order linear elastic theory. The predicted load/COD curve is somewhat conservative for this specimen. This may be in part due to the use of the transverse tensile properties for the analysis, even though the primary loading is in the longitudinal direction (which has slightly higher strength per Table 7.2). Also of potential significance in this regard are the effects of deviations in the crack path, and errors associated with the approximate nature of Equation (5.40).

For specimen S7475TL5 (0°), the predicted response indicated crack turning somewhat more severe than the second-order linear elastic analysis, compared to the relatively straight growth observed in the specimen. As suggested earlier, there is evidence from the L-T crack path that for this lot of material, the toughness function has a more pronounced minimum at θ=0° than assumed, which would explain the disparity between analysis and observation in the L-T orientation. The predicted load/COD curve matches well with the observed behavior in the region where the predicted path is relatively straight, as would be expected.

7.6 Summary

A test program has been described including test results from 31 DCB and 12 SDCB specimens, fabricated from four aluminum materials--7050-T7451 plate, 7050-T74511 extrusion, 2324-T39 plate, and 7475-T7351 plate—and divided into four specimen sets. These sets will be described in chronological order, with a review of the highlights of their purpose and what was learned.

The first specimen set, comprised of DCB specimens cut from 7050-T7451 plate, was intended to provide data for determination of the characteristic length, r_c, using an extrapolation method used under a previous test program for 2024-T3 (a

material with more isotropic toughness). As it turned out, the intended method to obtain r_c was not applicable, and statically loaded specimen showed a very significant effect of fracture toughness orthotropy. Toughness data from the same lot of material indicated that $\overline{K}_m$=1.3 for this alloy in the stable tearing regime.

Analyses using the second-order linear-elastic maximum tangential stress theory with $\overline{K}_m$=1.3 showed that in the regime of T-stress found in the DCB specimens, crack trajectory was dominated by the toughness orthotropy, and sensitivity of the crack path to r_c was minor. For T-L cracks, the path was found to curve gently, and was found to be heavily influenced by random perturbations, and the perturbation distribution was quantified. For L-T cracks, some effect of r_c was noted up to r_c=0.05 inches, beyond which the predicted crack path became insensitive to the characteristic length. Use of r_c=0.05 did improve crack path prediction, and is recommended for this alloy in the stable tearing regime.

Elastic-plastic fracture simulation of T-L and L-T specimens from Specimen set #1 showed comparable predictions to the second-order linear elastic method, though the smooth shape of the tightly turning crack in the L-T specimen was better predicted by the elastic-plastic method, and is free of the zig-zag oscillation observed in the linear elastic prediction.

Specimen set No. 1 also had two specimens for which the crack was propagated in fatigue. There was a distinct difference in the nature of the crack path compared to the stable tearing specimens, showing evidence that the effective fracture resistance orthotropy was different for fatigue loading than for stable tearing. Based on *da/dN* data from straight crack growth regions of the specimens, a fracture resistance orthotropy ratio of $\overline{K}_m$=1.1 was determined for the 7050-T7451 plate at a crack growth rate of about 10^{-5} inches/cycle. Use of this orthotropy value and $r_c \rightarrow 0$ resulted in satisfactory correlation of the analysis and test data, supporting the

hypothesis that process zone size interacts with T-stress (via r_c) and fracture orthotropy to influence the crack path. With regard to fracture orthotropy, this confirmed the notion expressed in Chapter 4 that the fracture resistance orthotropy ratio must be based on the material response in the appropriate fracture regime. Presumably, the fracture resistance orthotropy varies with *da/dN* to the degree that the T-L and L-T *da/dN* vs ΔK curves differ, and approaches constant value in the stable tearing regime.

Specimen set No. 2 was tested to provide early information during the IAS program on the ability to turn cracks in various alloys from the preferred (T-L) orientation, and is included for completeness. Specimen set No. 3 indicated that 7050-T74511 extrusion was rather prone to spurious and unpredictable behavior, and is a warning that it may be inherently difficult to reliably predict crack paths in materials made by processes that result in nonuniform grain structure and/or residual stresses.

Specimens set No. 4 included both DCB and SDCB specimens machined from 7475-T7351 plate material—the material of choice for the IAS integral fuselage program. Using a novel data reduction approach, r_c for this material was estimated to be 0.06 inches based on SDCB specimen kink data. A fracture toughness orthotropy ratio, $\overline{K}_m$=1.1, was determined for this material based on IAS wide panel R-curve data. Using this information, simulations run with both elastic and elastic-plastic turning methods showed good correlation with observed test results.

CHAPTER 8.0

SUMMARY, CONCLUSIONS, AND RECOMMENDATIONS FOR FUTURE WORK

8.1 Overview

This chapter presents a summary of the contributions of the present work, conclusions drawn, and recommendations for future work as appropriate. The overall purpose of the work is to develop improved crack path prediction methods necessary to aid in the design of damage tolerant aircraft structure where skin and stiffening elements are integrated as one-piece. A discussion of the background to the problem is given in the first chapter, describing how crack turning can provide a measure of fail safety for integral structures, and identifying process zone interaction with T-stress and fracture toughness anisotropy as potentially significant factors requiring further study. Chapters 2-5 discuss various details with regard to crack turning theory, starting with first-order (T-stress free) isotropic theories, and adding the effects of T-stress and orthotropy along the way. Chapter 6 describes the software implementation of selected elastic and elastic-plastic methods, including accurate T-stress calculation methods, and Chapter 7 presents test results and crack path correlation with numerical analyses. The contributions of each chapter beginning with Chapter 2 will now be summarized in more detail.

8.2 Chapter 2: Isotropic Crack Turning Theory in Two Dimensions

This chapter is largely introductory in nature, providing a description of various isotropic crack turning theories found in the literature, including both linear elastic and elastic-plastic theories. The linear-elastic theories described are later described as "first-order", because they include only the mode I and mode II

components (K_I, K_{II}) of the leading term in the crack tip stress field expansion, but neglect the T-stress and higher-order terms. The elastic-plastic theory of Shih also neglects the far-field T-stress, and may thus also be described as first-order in this sense. These theories give the kink angle as a function of K_{II}/K_I, and predict very similar results, particularly as K_{II} becomes small compared to K_I. In the limit as K_{II} vanishes, the predicted kink angle is zero, as for a smoothly curving crack. Based on the resulting assertion that a naturally curving crack follows the path that satisfies K_{II}=0, all the first-order theories thus predict the same crack path—a path which tends to diverge in a positive T-stress environment, as shown by Cotterell and Rice.

Following this discussion, test data are shown that indicate that process zone size effects the rate of crack path divergence in a positive T-stress environment—a phenomenon not possible to predict based on the first order theories—and the question is asked: Why?

8.3 Chapter 3: Crack Path Instability in a Material with a Cohesive Process Zone

This chapter attempts to address the question posed in the preceding chapter by an original study of the crack path instability of a slightly curvilinear crack in an isotropic material with a cohesive process zone at the crack tip, propagating in a positive T-stress environment. The cohesive zone is intended to represent a strain localization region of smaller size than the total plastic zone would be in the usual Dugdale sense (that is, the stress intensity factor at the tip of the cohesive crack is non-zero). Further, it is assumed that the crack propagates under steady state conditions (the cohesive zone is of constant length), and the tip of the cohesive crack follows the path corresponding to zero mode II stress intensity, as suggested by Cotterell and Rice. The solution neglects second and higher order terms involving the deviation of the crack from a straight path.

Because the crack is (initially) slightly curved, there is a finite mode II stress intensity, K_{II}^{P},associated with the cohesive tractions at the crack tip. Therefore, for the total mode II stress intensity at the crack tip to vanish, there must be a *non-zero* far-field component, K_{II}, equal and opposite in sign to K_{II}^{P}. In order to enable development of an estimate for K_{II}^{P}, expressions are developed for the crack flank displacements in the vicinity of the slightly curved crack, due to both far-field loading and local cohesive tractions. The normal traction is taken as a steady state function of the flow stress and distance from the crack tip, and includes strain softening. The tractions and displacements in the cohesive zone interact by way of a simple constitutive relationship based on the strain localization concept. The constitutive relationship is considered for both plane-stress Von Mises strain localization in a cohesive crack surface normal to the plate, and a Tresca shear strain localization surface at 45 degrees to the plane of the plate. A closed form expression involving shear and normal tractions is integrated along the cohesive zone to obtain an estimate of K_{II}^{P} in terms of the assumed steady-state normal traction function, flow stress, and crack tip curvature.

A solution is then developed using Laplace transform techniques for the future path of an initially curved semi-infinite crack with a cohesive process zone propagating in an infinite elastic medium. The solution indicates that in a positive T-stress environment, an increase in process zone size results in an increase in crack path instability, agreeing at least qualitatively with experimental findings.

8.4 Chapter 4: Fracture Resistance Orthotropy and Modal Transition

This chapter serves initially as an introduction to the work of various authors with regard to fracture resistance anisotropy (fracture resistance that is a function of direction), fracture mode asymmetry (fracture resistance that varies with fracture

mode), and modal transition (transition between mode I and mode II failure, depending on mode-mixity). In addition, a few important original contributions are presented, as will now be described.

Among the original contributions is the recognition that the crack growth resistance, $K_p(\theta)$, used to characterize the orthotropic fracture behavior, must be determined in a regime consistent with the failure process. That is, the fracture resistance may (and typically does) vary more as a function of orientation in the stable tearing regime, than during slow fatigue crack growth. Thus, the orthotropy ratio, $\overline{K}_m$, is not a material constant, but a state variable, though it may be approximated as a constant within a given fracture regime. This was supported by test data in Chapter 7 for thin sheet coupons propagated under static or fatigue loading. While the mechanism behind the change in orthotropy ratio in the different fracture regimes is not well understood (granted that stable tearing and fatigue fracture have inherent phenomenalogical differences), it is hoped that current multi-scale studies of fracture processes may shed light on this issue.

Two additional contributions relate to the interpolation function that estimates the fracture resistance at an arbitrary crack orientation angle based on the principal values of the fracture resistance. First, some motivation was given to the choice of the exponent in the interpolation function of Equation (4.1), in view of the fact that in prior work the exponent is arbitrarily selected, and the different authors are in disagreement. Second, and most significant, is the extension of the fracture orthotropy interpolation function to three dimensions, interpolating between the six principal fracture resistance values corresponding to this case. While this contribution was not carried on in the subsequent stages of the present work, it provides an important building block for follow-on work in three-dimensional crack turning studies with fracture resistance orthotropy.

8.5 Chapter 5: Crack Turning Theories with Process Zone Effects and Fracture Resistance Orthotropy

This chapter builds upon the work of prior authors to develop two enhanced approaches for crack turning simulation, a linear elastic approach and an elastic-plastic approach. These methods are the proposed workhorse methods for implementation in the following chapter.

The linear-elastic approach includes both the "second order" (process zone related) effect of the T-stress, and the effect of fracture resistance orthotropy. Both of these influences had been studied independently in prior work, but their unification and full development in the present work, is both original and significant. The inclusion of the T-stress into the orthotropic theory predicts more rapid turning in a positive T-stress environment as the process zone related characteristic length, r_c, is increased. provide a linear elastic prediction for the point of modal transition based on the concept of fracture mode asymmetry.

Several original variants of the second order linear elastic crack kinking theories are also discussed, including fracture orthotropic maximum tangential and shear stress criteria for mode I and mode II dominated propagation, and a modal transition condition based on fracture mode asymmetry. Other variants include second-order isotropic theories assuming pure modal growth both in stress ($\sigma_{r\theta}$=0 for mode I), and CTOD. It is shown that the various second-order mode I theories predict either identical or very similar behavior, if one realizes that the corresponding process zone size parameters differ in scale for the various theories.

The elastic-plastic crack turning approach described builds heavily on the work of Sutton [40] with regard to using the mode I and mode II components of the CTOD (D_I and D_{II}) to determine the crack path. The present contribution extends the method to include fracture resistance orthotropy by way of an angular correction based on linear elastic orthotropic theory. The enhancement is only valid for (nearly) smoothly

curving cracks, and would not be expected to correctly account for orthotropy for large angle sharp kinking behavior.

Also, early in the chapter, the concept of modeling a smoothly curving crack using a C^o continuous series of linear segments was discussed in light of the theoretical convergence study Stone and Babuska. Their results are strictly valid only for first order, linear-elastic crack turning (K_{II}=0), but infer that (1) for a convergent solution, the kink angles should approach zero as the step size is reduced, and (2) the problem is probably sufficiently converged for engineering purposes when the kink angles fall below about 10 degrees. As is evident in the results of Chapter 7, the second-order linear elastic theory does not tend to converge in this manner, but results in a sharply zig-zagging path that does not become smooth as the step size is refined. Yet, the path does converge in an average sense to a reasonable approximation of the actual behavior. On the other hand, the elastic-plastic method converges to a smooth path, and is in this respect more realistic.

8.6 Chapter 6: Software Implementation

The software implementation of second-order linear-elastic maximum tangential stress theory and the elastic-plastic CTOD crack turning theories are described in this chapter. The present effort builds on the framework of the FRANC2D fracture simulation environment, adding various features necessary to utilize the enhanced crack turning criteria. Two variants of the code were produced, a version of FRANC2D for the second-order elastic-plastic method, and a version of FRANC2D/L for the elastic-plastic method. FRANC2D/L was chosen for the elastic-plastic method to build on a prior implementation of the isotropic CTOD method by a colleague.

A large portion of the chapter describes a domain integral T-stress calculation method with *a posteriori* error correction. The domain integral approach, based on the

Betti-Rayleigh reciprocal theorem, is included for completeness, but is entirely attributable to colleagues and prior authors. However, the error estimation and correction methods are original to the present work, and significantly improve the accuracy of the T-stress calculations in FRANC2D.

8.7 Chapter 7: Test Program

This Chapter describes test results from 31 DCB and 12 SDCB specimens, fabricated from four aluminum materials--7050-T7451 plate, 7050-T74511 extrusion, 2324-T39 plate, and 7475-T7351 plate. While some of these results have been included in prior publications related to the corresponding contracts funding the work, they are combined here with the most recent results, and compared with analyses based on the foregoing methods as applicable. Further detail of the test data is given in the appendices in tabulated form to allow future authors to study the results in light of new developments and theories.

For a detailed review of the results of each specimen set, the reader is referred to the chapter summary at the end of Chapter 7. A summary of overall findings is as follows:

- Symmetric cracks in a high T-stress exhibit considerable crack path instability (as expected from both present and prior theories).

- Both fracture resistance orthotropy and ("second order") process zone size effects influence the crack path instability. Increased process zone size (higher loading) tends to produce more rapid crack turning in fairly isotropic materials. However, the orthotropy ratio itself is a function of process zone size (failure regime), and may change sufficiently between different failure regimes to offset or overpower the "second order" process

zone size effects associated with including the process zone size directly in the crack turning theory.

- In order for the elastic and elastic-plastic theories to correctly account for the fracture resistance orthotropy, an orthotropy ratio must be determined appropriate to the regime of failure (do not use the fracture toughness ratio to predict the fracture resistance ratio in the slow fatigue regime). For the 7050-T7451 plate material tested in 0.090 inch thick specimens, the orthotropy ratio was far greater for stable tearing (1.3) , than for fatigue crack propagation (1.1).

- The use of asymmetric specimens such as the SDCB is recommended for determination of the characteristic length, r_c, for the linear elastic theory as explained in the text.

- For slow fatigue crack propagation (less than about 10^{-4} for the 7050-T7451 aluminum plate alloy tested), the process zone size was sufficiently small to assume r_c=0 for the level of T-stress in the specimens tested (about r_o=0.04 inches). This is probably a reasonable approach for fatigue cracking in most structural applications. The elastic-plastic method is not intended, nor is it necessary for crack path analysis of fatigue cracking.

- Due to random "bumps" in the crack path apparently due to local material inhomogeneity, the crack path is constantly under the influence of random perturbations. This caused an apparent scatter in T-L DCB specimens, which have only slight crack path instability because the crack starts out in the favored crack orientation. This scatter, however was anticipated based on analyses of specimens with slight initial angular perturbations. It is

suggested that a perturbation analyses of a similar sort could help the designer anticipate structural situations where the crack path is highly sensitive to random perturbations. In general, where rather sharp crack turning is predicted by the analysis, it appears that random effects are less likely.

- V-shear failures (as opposed to the usual slant crack) were observed in several specimens, typically resulting in sharper turning than would be anticipated by analysis. For the most part, however, it appears that the occurrence of V-shear is largely an artifact of the test method—starting a stable tear from a fatigue precrack with minimal plastic zone. It was never observed in a statically precracked specimen, and would thus appear to be less probable in real structural situations where a fatigue crack grows at gradually increasing ΔK until it becomes unstable. The propensity for V-shear also appears to be material (and/or possibly thickness) dependant.

- Crack turning analyses in prototype 7050-T74511 large extrusion appeared to exhibit somewhat spurious behavior, and suggesting caution when attempting to predict crack trajectories in materials processed in a manner that might result in grain heterogeneity or residual stresses.

8.8 Recommendations for Future Work

Among a myriad of possibilities, there are at least two obvious tracks for future work—application of either the linear elastic or elastic-plastic methods into shell codes. Due to the work of a colleague [15], the second order elastic theory with fracture resistance orthotropy has already been implemented into the shell capability

of FRANC3D. However, the T-stress calculation method is presently limited to a rather crude displacement correlation technique for curved shells. The development of path integrals for shell applications could enhance the accuracy of the solution.

With regard to the elastic-plastic method, the re-mapping technique for plastic state variables has yet to be implemented for shells. Also, it has been shown [94, 95] that the residual strength prediction using the elastic-plastic CTOD method is improved by the use of a band of plane strain or—better yet—solid elements immediately adjacent to the crack. State variable mapping for such conditions has yet to be worked out. Mesh size along the crack path is presently limited by the method itself to 0.020 inches. If one is analyzing a 40 inch crack in an airplane, the problem size becomes extremely large. In order for this to become practical for real applications where significant stable tearing occurs before the crack reaches the region of interest, it would be extremely beneficial if one could directly specify a fully meshed crack tip with a reasonable estimate of the steady-state plastic history built-in *a priori* in a region just preceding the region of interest. The crack could then be grown a short distance to fine tune the plastic history, and the analysis would be obtained in a more painless way than developing the elastic-plastic history from scratch.

APPENDIX 1.0

THEORETICAL APPROXIMATION OF THE STRAIN LOCALIZATION ZONE SIZE PRECEDING A CRACK TIP.

In Chapter 3, a strain localization concept was introduced to motivate the use of a cohesive zone ahead of the crack tip in a crack turning model. In the following, an attempt is made to develop a theoretical expression to approximate the size of the strain localization zone.

A1.1 Strain Localization Concept

A simple tensile test of a strain hardening material yields the familiar engineering and true stress-strain plots shown schematically in Figure 3.1. In accordance with a well-known plastic instability theory attributed to Considere, the maximum load, F, occurs when the specimen rate of area reduction equals the rate of strain hardening

$$dF = \sigma dA + A d\sigma = 0 \tag{A1.1}$$

Rearranging,

$$\frac{d\sigma}{\sigma} = -\frac{dA}{A} = d\varepsilon$$

$$\frac{d\sigma}{d\varepsilon} = \sigma \tag{A1.2}$$

It is equally well established that the point of maximum load (zero stiffness) also defines the onset of localized deformation or necking in the specimen compliance becomes infinite, as is implied in Equation (A1.1). All along the specimen a stiffness of zero is approached as large strains reduce the cross sectional area in an initially uniform manner. At first this offset by strain hardening , but as the maximum load is

approached, the stiffness vanishes. Due to some imperfection one segment reaches that point first, and necking begins there.

Once localized deformation has begun, the location of the future failure of the specimen has been determined. As fracture develops, the processes which occur after the onset of localized deformation may differ from material to material, but the location of fracture is set in a macroscopic sense at the onset of plastic instability.

Assuming strain hardening of the exponential form,

$$\sigma = k\varepsilon^m \tag{A1.3}$$

and substituting this into Equation (A1.2), one obtains the true plastic strain at the engineering ultimate stress

$$\varepsilon_{ult} = m \tag{A1.4}$$

Noting that $S = \sigma e^{-\varepsilon}$ (where e is the base of the natural log) we obtain from (A1.3) and (A1.4) the engineering ultimate stress of the material in terms of k and m

$$S_{ult} = km^m e^{-m} \tag{A1.5}$$

Defining σ_o as the 0.2 percent offset yield strength, we have $k = \sigma_o (.002)^{-m}$ and

$$\frac{\sigma_o}{S_{ult}} = \left(\frac{.002e}{m}\right)^m \tag{A1.6}$$

Swift [96] developed similar relationships for plastic instability and necking in sheet material under tensile plane stress conditions. Necking is also observed in front of the crack tip, and is believed to play a significant role in crack path formation in sheet metal.

A crack growing in a thin sheet is illustrated in Figure 3.3, with the necking region shown in the vicinity of the crack tip well within the bounds of the plastic zone, since necking must occur after some plastic deformation as in the tensile test. It is further asserted based on observation that the crack will eventually develop along the necking line, and that the future crack path is therefore known out to the onset of necking (barring some abrupt change in the load environment). In order to support this notion, it is observed that the sectional load (load/in) distribution ahead of a propagating crack and normal to the future crack path must have a maximum a finite distance away from the crack tip as shown schematically in Figure A1.1.

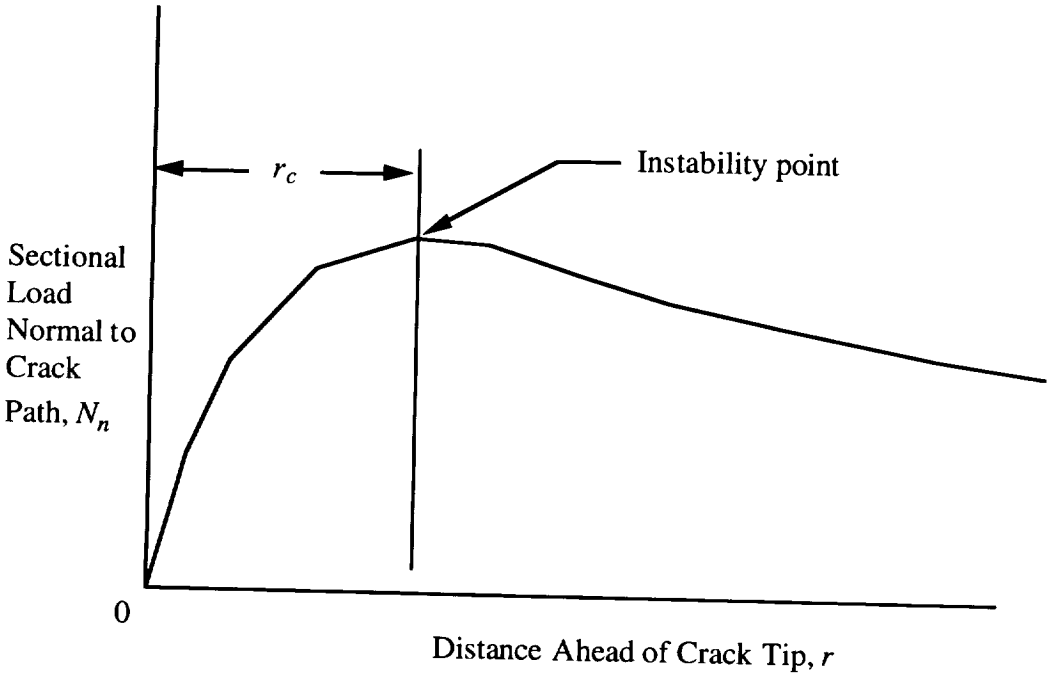

Figure A1.1 Schematic of Sectional Load Distribution ahead of Crack Tip

McMeeking [97], using nonlinear finite element computations, has shown this to be true for the self-similar plane strain stationary crack due to crack blunting. The

sectional load distribution of Figure A1.1 is also supported by the argument that all real materials must exhibit strain softening behavior across any real failure interface down to zero load. Strain softening is a result of the advanced stages of deformation localization, including void growth and coalescence for metallic materials. The interface has finite residual strength until the last two atoms of a given interface separate, (and even as they separate, they do so with a smooth load/displacement relationship). Given that the atomic bonds, even in a tensile test, must break in some sequence, and cannot separate at exactly the same moment, it follows that in the limit of absolute displacement control the failure of any interface could be defined as a quasi-static progression of damage as the load drops smoothly (at some scale) to zero. The failure interface of a slow stable tearing interface approaches this limit of absolute displacement control [98]

It is now suggested that in a manner equivalent to the Considere criterion mentioned previously, the onset of localized deformation coincides with the instability point defined by

$$dN_n = 0 \tag{A1.7}$$

where N_n is the sectional load normal to the future crack path. It can be argued that for elastic-plastic strain hardening materials, this point marks the local onset of plastic instability, whether in plane strain or plane stress. Likewise, one would expect that the path of localized deformation marks the future crack path just like necking in the tensile specimen predetermines the eventual failure location. The instability point marks the end of the known future crack path, and might well represent the point where the material is "deciding" where it the crack will go next. Presumably as the crack grows, the instability point would migrate to the location where N_n is maximized. Thus, the distance from the physical crack tip to the instability point, r_c, could be

considered as a physical representation of the characteristic length associated with crack turning.

A1.2 Theoretical Development

For the purposes of this study, the strain localization zone shall be assumed to be straight, and of approximately constant length for a given material and thickness. In order to obtain an estimate of the length, the simple case of a self-similar crack will suffice. For the plane strain case, McMeeking and Parks [99] have shown using a large deformation analysis that the maximum stress occurs for materials with moderate strain hardening at a distance approximately given by

$$r_c \approx \frac{J}{\sigma_o} \tag{A1.8}$$

where for small scale yielding and mode I loading, the strain energy release rate J, is related to the stress intensity factor by

$$J = \frac{K_I^2}{E} \tag{A1.9}$$

Thus for plane strain we may write

$$r_c \approx \frac{K_I^2}{\sigma_o E} \tag{A1.10}$$

It should be cautioned, however, that while this expression is a reasonable estimate for T=0, it has been shown [82] that for plane strain, the distance to the maximum stress point varies with the T-stress, particularly if it is negative. Also, void growth was not considered, and could result in a longer distance to the peak stress point if it takes place prematurely.

For the plane stress case, thickness strain (necking) is possible. We can thus rewrite (A1.7) as

$$dN_n = dN_\theta = td\sigma_\theta + \sigma_\theta dt = 0 \tag{A1.11}$$

$$\frac{d\sigma_\theta}{\sigma_\theta} = -\frac{dt}{t} = -d\varepsilon_z \tag{A1.12}$$

Assuming incompressibility,

$$-d\varepsilon_z = d\varepsilon_\theta(1+\rho) \tag{A1.13}$$

where $\rho = \frac{\varepsilon_r}{\varepsilon_\theta}$

Using the Von Mises yield condition, the differential equivalent strain can be expressed as

$$d\bar{\varepsilon} = d\varepsilon_\theta \frac{2}{\sqrt{3}}\left(1+\rho+\rho^2\right) \tag{A1.14}$$

Combining (A1.12), (A1.13), and (A1.14) and noting that for a constant ρ, the equivalent stress conforms to the equality $\frac{d\bar{\sigma}}{\bar{\sigma}} = \frac{d\sigma_\theta}{\sigma_\theta}$ we obtain

$$\frac{d\bar{\sigma}}{d\bar{\varepsilon}} = \frac{\bar{\sigma}\sqrt{3}(1+\rho)}{2\left(1+\rho+\rho^2\right)} \tag{A1.15}$$

Employing an exponential strain hardening relationship for the equivalent stress and strain similar to (A1.7), we obtain the critical strain and stress at the instability point.

$$\bar{\varepsilon}_{\text{crit}} = \frac{2\text{m}\left(1+\rho+\rho^2\right)}{\sqrt{3}(1+\rho)} \tag{A1.16}$$

$$\bar{\sigma}_{\text{crit}} = \text{k}\left[\frac{2\text{m}\left(1+\rho+\rho^2\right)}{\sqrt{3}(1+\rho)}\right]^{\text{m}} \tag{A1.17}$$

Assuming the necking region in plane stress is somewhat larger than the crack blunting effected zone in plane strain (which will be observed hereafter), we can obtain an estimate of ρ based on the Hutchinson Rice Rosengren (HRR) asymptotic field for plane stress cracks in strain hardening materials [34, 35]. This inherently involves the assumption of proportional flow, which for a propagating crack is less than desirable. Directly ahead of a straight propagating crack, the flow should be fairly proportional, but the deviation from proportionality will have an unknown effect on the results forward of the crack. Also of concern is the fact that the HRR field is derived based on the assumption of small strain theory. The very existence of plastic instability is by definition a large strain effect. Nevertheless, McMeeking and Parks did observe in their analysis that the plane strain HRR field was valid up to the point of maximum stress. Note also that true stress and strain and engineering stress and strain are fairly close up until plastic instability for most structural materials.

Proceeding with the above cautions in mind, the effective stress given by the HRR solution, written here in terms of the far field stress intensity factor, is

$$\overline{\sigma} = \sigma_o \left[\frac{K_I^2}{\alpha \sigma_o^2 I_n r} \right]^{\frac{1}{n+1}} \sigma_e(n,\theta) \tag{A1.18}$$

For $\theta = 0$, Hutchinson normalized the σ_e term to unity for the plane stress case. The Ramberg-Osgood material parameters α and n are related to the exponential strain hardening parameters from Equation (A1.7) by

$$k = \sigma_o^{(1-1/n)} \left(\frac{E}{\alpha} \right)^{1/n} \tag{A1.19}$$

$$m = 1/n \tag{A1.20}$$

Hutchinson gives numerical results for I_n and ρ which are functions of the exponent n. For the propagating crack, we may assume that K_I is equal to the propagating value, which for stable tearing may be denoted K_c. We may thus approximately equate (24) and (25) at $r = r_c$, and to obtain after some rearrangement

$$r_c \approx \left(\frac{\sqrt{3}}{2} \frac{\sigma_o \alpha n (1+\rho)}{E(1+\rho+\rho^2)} \right)^{\frac{(n+1)}{n}} \left[\frac{K_c^2}{\alpha \sigma_o^2 I_n} \right] \tag{A1.21}$$

Equation (A1.21) can be combined with equations (A1.5), (A1.19), and (A1.20) to obtain an expression in terms of the engineering ultimate strength

$$r_c \approx \left(\frac{\sqrt{3}}{2} \frac{(1+\rho)}{(1+\rho+\rho^2)} \right)^{(1+1/n)} \frac{n}{I_n e^{1/n}} \left[\frac{K_c^2}{S_{ult} E} \right] \tag{A1.22}$$

For $n < 7$, ρ makes little contribution, and I_n is nearly linear at least up to the maximum value of $n = 13$ given by Hutchinson, and probably well beyond. Thus, in this range we can further approximate with no significant loss of accuracy

$$r_c \approx \left(\frac{\sqrt{3}}{2} \right)^{(1+1/n)} \left(\frac{n}{(3.38 - .039n) e^{1/n}} \right) \left[\frac{K_c^2}{S_{ult} E} \right] \tag{A1.23}$$

If a suitable value for n is not available, one can obtain an approximation using the ratio of yield and ultimate strength from the implicit equation

$$\frac{\sigma_o}{S_{ult}} = (.002 n e)^{1/n} \tag{A1.24}$$

which was obtained by combining equations (A1.6) and (A1.20).

A1.3 Calculated Values

Calculated r_c values for 2024-T3 and 7050-T7451 aluminum alloys are given in Tables A1.1 and A1.2 respectively, based on Equations (A1.23) and (A1.24). For the 2024-T3 sheet, the mechanical properties are B basis values from MIL-HDBK-5G [100] corresponding to the load orientation, and the fracture toughness is the maximum R-curve value obtained based on 48 inch wide R-curve panels reported by Gruber et al [101]. The 7050-T7451 data is from the IAS lot of 1.5 inch plate, with the fracture toughness based on R-curves in 0.090 inch thick specimens cut from the plate [93]. Despite many obvious shortcomings in the preceding development, the calculated values appear to be fairly reasonable.

Table A1.1 Calculation of r_c for 2024-T3

0.063 inch, 2024-T3 clad sheet							r_c
Crack Orient.	S_y (ksi)	S_{ult} (ksi)	n	K_c (ksi$\sqrt{in}$)	E (ksi)	$K_c^2/S_{ult}E$ (in$^{1/2}$)	Plane Stress (in)
T-L	42	62	8.04	180	10500	0.050	0.098

Table A1.2 Calculation of r_c for 7050-T7451

7050-T7451 Plate machined to sheet (IAS Lot release and R-curve data)							r_c
Crack Orient.	S_y (ksi)	S_{ult} (ksi)	n	K_c (ksi$\sqrt{in}$)	E (ksi)	$K_c^2/S_{ult}E$ (in$^{1/2}$)	Plane Stress (in)
L-T	68.0	77.4	18	108	10300	0.0146	0.080
T-L	68.3	76.9	19.1	83	10300	0.0087	0.051

APPENDIX 2.0

MIXED-MODE TRACTION RELATIONSHIP FOR COHESIVE SLANT CRACK

A cross section of the cohesive zone for a slant crack in a thin sheet loaded globally in mixed mode II/I is illustrated in Figure A2.1 where the s and n axes are defined as in Figure 3.4a. The cohesive interface may be modeled as the q-s slip plane, deforming in shear according to the Tresca yield criterion with a shear flow stress τ_o. Local crack flank relative deflections are of mixed-mode II/III character, and are related to the global mode II/I relative deflections by

$$\frac{\Delta u_s}{\Delta u_n} = \frac{\Delta u_s}{\Delta u_q \sin\alpha} \tag{A2.1}$$

The principal shear strain acts at a (small) angle

$$\zeta = \tan^{-1}\frac{\Delta u_s}{\Delta u_q} \approx \frac{\Delta u_s \sin\alpha}{\Delta u_n} \tag{A2.2}$$

measured from the q axis within the q-s plane. Assuming proportional loading, the principal shear stress, τ_o, also acts at this angle, thus the shear stress components must satisfy

$$\begin{aligned} \tau_s &= \tau_o \sin\zeta \\ \tau_q &= \tau_o \cos\zeta \end{aligned} \tag{A2.3}$$

Hence for small ζ

$$\frac{\tau_s}{\tau_q} \approx \zeta \tag{A2.4}$$

whence we obtain from Figure A2.1 and Equations (A2.2) and (A2.4),

$$\frac{\tau_s}{\tau_n} = \frac{\tau_s \sin\alpha}{\tau_q} = \frac{\Delta u_s}{\Delta u_n}\sin^2\alpha \tag{A2.5}$$

Recognizing that $T_s << T_n$, we observe that the maximum shear stress occurs at $\alpha=\pi/4$. Thus the value of c defined by equation (3.36) for this case is

$$c = \sin^2\left(\frac{\pi}{4}\right) = \frac{1}{2} \tag{A2.6}$$

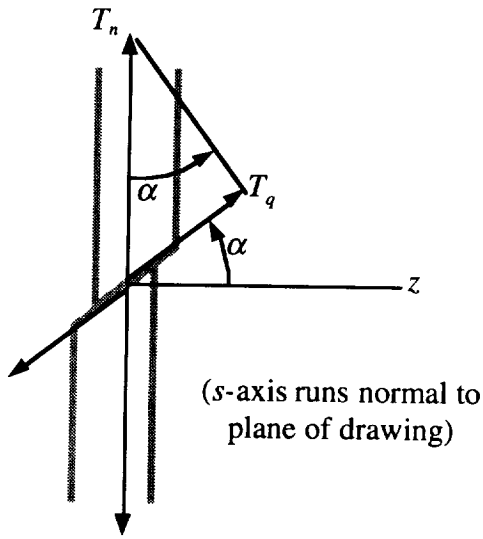

Figure A2.1 Schematic of Tractions on Cross-Section of Slant Crack Cohesive Zone

APPENDIX 3.0

DERIVATION OF STRESS INTENSITY SOLUTION FOR MODE II LOADED DCB SPECIMEN

Consider a linear elastic DCB specimen loaded in pure mode II as shown in Figure A3.1

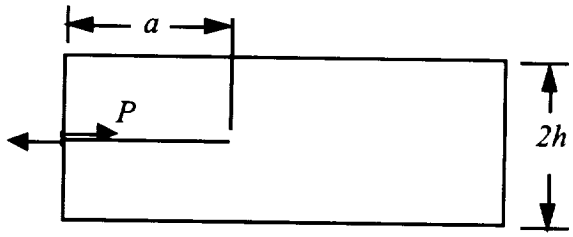

Figure A.3.1 Mode II Loaded DCB Specimen

We define the energy release rate as given by Irwin [102, 103],

$$G = \frac{-d\Pi}{dA} \tag{A3.1}$$

where dA is an increment of new crack area (half of the new free surface area of both upper and lower surfaces) created by an incremental crack extension,

$$dA = t\,da \tag{A3.2}$$

Π is the potential energy supplied by the internal strain energy and external forces, respectively

$$\Pi = U - F \tag{A3.3}$$

When applying a constant load, P, a crack opening displacement, Δ, occurs between the points of load application, thus

$$F = P\Delta$$

$$U = \int_0^{\Delta} P d\Delta = \tfrac{1}{2} P\Delta$$

Thus

$$\Pi = -U = -\tfrac{1}{2} F \tag{A3.4}$$

We now idealize the upper half of the specimen as a beam, and decompose the loading into two components, statically equivalent to the actual loading, as shown in Figure A3.2.

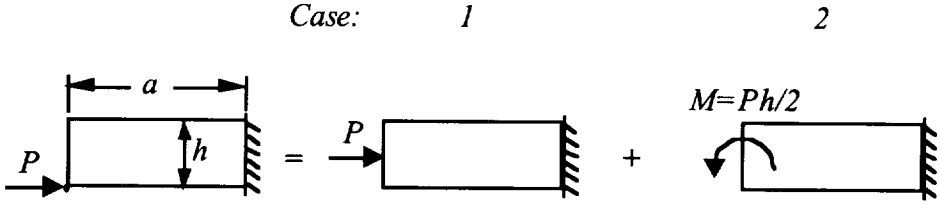

Figure A.3.2 Statically Equivalent Load Components

Applying superposition of load cases 1 and 2, and multiplying by two to include energy contributions from both upper and lower surfaces, we can combine (A.3.1) and (A.3.4) to obtain

$$G = \frac{-d\Pi}{dA} = \frac{dU}{dA} = \frac{2}{t}\left(\frac{dU_1}{da} + \frac{dU_2}{da}\right) \tag{A3.5}$$

From beam theory, we can write

$$\frac{dU_1}{da} = \frac{\tfrac{1}{2} P\epsilon da}{da} = \frac{P^2}{2Eht}$$

$$\frac{dU_2}{da} = \frac{\frac{1}{2}Md\theta}{da} = \frac{M^2}{2EI} = \frac{(Ph/2)^2}{2E(th^3/12)} = \frac{3P^2}{2Eh}$$

Substituting these expressions back into (A3.5), we obtain

$$G = \frac{4P^2}{Eht^2} \tag{A3.6}$$

from which the stress intensity factor is obtained as

$$K_{II} = \sqrt{GE} = \frac{2P}{t\sqrt{h}} \tag{A3.7}$$

APPENDIX 4.0 TABULATED DCB/SDCB TEST DATA

Table A4.1 Tabulated Tensile Stress-Strain Curves for Use in Elastic-Plastic Analyses

7050-T7451 Plate		7475-T7451 Plate	
Strain	Stress	Strain	Stress
(in/in)	(Ksi)	(in/in)	(Ksi)
0.00000	0.00	0.00000	0.00
0.00648	66.70	0.00635	65.40
0.01007	67.92	0.01007	66.32
0.01997	70.87	0.02011	69.35
0.03018	72.45	0.03021	71.03
0.04016	74.09	0.04013	72.80
0.05058	75.30	0.05052	74.10
0.06003	75.96	0.06001	74.85
0.07765	76.40	0.06982	75.28
0.20000	76.40	0.08009	75.40
		0.20000	75.40

Notes: Curves were developed from median IAS tensile specimens. First segment of each curve is defined by the MIL-HDBK-5 modulus up to the yield strength of the specimen, after which the points follow the test data up to the maximum stress. An additional segment indicates constant stress after the maximum stress is reached, because FRANC2DL cannot handle strain softening. Engineering stresses and strains specified.

Table A4.2 Summary of 7050-T7451 Fatigue Crack Turning Tests (Set#1)

Specimen rc-LT-15-2					Crack Front Type	Thickness (in)	w (in)	2h (in)
					flat	0.0917	11.996	4.799
Load (lb)	ΔN	x ave (in)	y ave (in)	Curvilinear Δa avg	Δa/ΔN (in/cycle)	Curvilinear a (in)	ΔK (ksi√in)	Theta (deg)
(notch)	0	2.004	0.000	2.004		2.004		
320	5000	2.031	0.000	0.027	5.40E-06	2.031	6.99	0.00
320	4000	2.059	0.000	0.027	6.87E-06	2.059	7.04	0.00
368	6000	2.126	0.003	0.068	1.13E-05	2.126	8.20	2.12
368	6000	2.197	0.000	0.071	1.18E-05	2.197	8.36	-2.02
368	8000	2.284	-0.001	0.087	1.09E-05	2.284	8.53	-0.66
368	15000	2.475	0.007	0.191	1.27E-05	2.475	8.83	2.25
331	4000	2.512	0.006	0.037	9.25E-06	2.512		-0.77
350	10000	2.626	0.022	0.116	1.16E-05	2.627	Crack	7.71
350	10000	2.755	0.052	0.133	1.33E-05	2.760	Curves	13.30
350	5000	2.830	0.073	0.077	1.55E-05	2.837		15.39
350	5000	2.903	0.095	0.076	1.53E-05	2.914		17.13
350	5000	2.981	0.132	0.086	1.72E-05	3.000		25.08
350	5000	3.063	0.175	0.093	1.87E-05	3.093		27.80
350	5000	3.163	0.230	0.114	2.28E-05	3.207		28.59
350	5000	3.259	0.290	0.113	2.27E-05	3.320		32.22
350	5000	3.367	0.377	0.138	2.76E-05	3.458		38.82
350	3000	3.432	0.438	0.090	2.99E-05	3.548		43.20
350	3000	3.499	0.514	0.101	3.35E-05	3.649		48.63
350	3000	3.582	0.616	0.132	4.40E-05	3.781		51.00
350	2000	3.633	0.729	0.124	6.18E-05	3.904		65.61
331	1000	3.659	0.772	0.050	5.02E-05	3.954		58.84
265	4000	3.690	0.889	0.122	3.04E-05	4.076		74.99
212	4000	3.722	0.975	0.091	2.28E-05	4.167		69.48
212	2000	3.749	1.044	0.074	3.70E-05	4.241		68.99
212	2000	3.764	1.147	0.105	5.23E-05	4.346		81.75
212	2000	3.808	1.337	0.195	9.75E-05	4.541		76.96
212	500	3.853	1.471	0.141	2.82E-04	4.682		71.18
159	1000	3.855	1.507	0.037	3.65E-05	4.718		87.65
Failure		3.895	1.700	0.197	n/a	4.916		78.15
Failure		3.948	1.900	0.207	n/a	5.122		75.29
Failure		3.998	2.200	0.304	n/a	5.427		80.54

Table A4.2 Summary of 7050-T7451 Fatigue Crack Turning Tests (Set #1) (Continued)

Specimen rc-TL-15-2						Crack Front Type	Thickness (in)	w (in)	2h (in)
						flat	0.0925	11.995	4.798
Load (lb)	ΔN	x ave (in)	y ave (in)	Curvilinear Δa avg	Δa/ΔN (in/cycle)	Curvilinear a (in)	ΔK (ksi√in)	Theta (deg)	
(notch)	0	2.003	0.000	2.003		2.003			
368	4000	2.035	0.000	0.032	8.00E-06	2.035	- -	0.00	
368	6000	2.115	0.000	0.080	1.33E-05	2.115	8.09	0.00	
368	10000	2.254	0.000	0.140	1.40E-05	2.254	8.33	0.00	
368	10000	2.403	0.000	0.149	1.49E-05	2.403	8.64	0.00	
368	10000	2.570	0.000	0.167	1.67E-05	2.570	8.99	0.00	
368	10000	2.756	0.000	0.186	1.86E-05	2.756	9.37	0.00	
368	3000	2.813	-0.003	0.058	1.92E-05	2.813	9.63	-2.99	
368	7000	2.969	-0.003	0.156	2.23E-05	2.969	9.86	0.00	
368	5000	3.082	-0.003	0.113	2.25E-05	3.082	10.16	0.00	
368	6000	3.232	-0.003	0.150	2.50E-05	3.232	10.44	0.00	
368	6000	3.402	-0.003	0.170	2.83E-05	3.402	10.79	0.00	
368	4000	3.522	-0.003	0.121	3.01E-05	3.522	11.11	0.00	
368	5000	3.682	0.019	0.161	3.22E-05	3.683	11.41	7.68	
368	4000	3.820	0.019	0.138	3.45E-05	3.821	11.73	0.00	
331	4000	3.916	0.019	0.096	2.40E-05	3.917	10.78	0.00	
331	6000	4.086	0.019	0.171	2.84E-05	4.088	11.04	0.00	
331	7000	4.319	0.035	0.234	3.34E-05	4.321	11.44	3.93	
331	4000	4.457	0.053	0.139	3.47E-05	4.460	11.80	7.66	
331	4000	4.604	0.065	0.147	3.69E-05	4.607	12.08	4.67	
331	4000	4.753	0.085	0.150	3.76E-05	4.758	12.37	7.65	
331	4000	4.915	0.126	0.167	4.18E-05	4.925		14.20	
331	3000	5.049	0.162	0.139	4.62E-05	5.063	Crack	14.84	
314	1000	5.084	0.175	0.038	3.78E-05	5.101	Curves	20.11	
314	2000	5.170	0.198	0.089	4.43E-05	5.190		15.06	
314	2000	5.255	0.231	0.092	4.59E-05	5.282		21.40	
314	2000	5.339	0.268	0.092	4.59E-05	5.373		23.77	
314	1000	5.383	0.295	0.051	5.09E-05	5.424		31.35	
283	1000	5.404	0.308	0.025	2.51E-05	5.449		31.16	
283	3000	5.501	0.372	0.116	3.88E-05	5.566		33.62	
283	3000	5.623	0.466	0.154	5.12E-05	5.719		37.73	
283	2000	5.730	0.558	0.141	7.06E-05	5.861		40.69	
283	1000	5.775	0.627	0.083	8.27E-05	5.943		56.60	
283	1000	5.829	0.730	0.116	1.16E-04	6.059		62.44	
212	1000	5.844	0.745	0.021	2.12E-05	6.080		45.00	
212	2000	5.883	0.830	0.094	4.68E-05	6.174		65.35	
212	1000	5.894	0.903	0.074	7.44E-05	6.248		81.11	
170	1000	5.913	0.919	0.025	2.45E-05	6.273		39.21	
170	2000	5.949	1.011	0.099	4.93E-05	6.371		68.90	
170	1500	5.977	1.124	0.117	7.80E-05	6.488		75.90	
170	1000	6.008	1.280	0.158	1.58E-04	6.647		78.90	
170	276	6.014	1.375	0.096	3.47E-04	6.742		86.40	
170	121	6.025	1.468	0.093	7.70E-04	6.836		82.91	

Table A4.3 Summary of 7050-T7451 Specimen Crack Paths (Set #1)

rc-TL-15-1				rc-TL-15-4				rc-TL-15-5				rc-TL-15-6			
1		2		1		2		1		2		1		2	
x	y	x	y	y	x	y	x	x	y	x	y	x	y	x	y
0.00	0.00	0.00	0.00	0.00	0.00	0.00	0.00	0.00	0.00	0.00	0.00	0.00	0.00	0.00	0.00
6.48	0.00	6.47	0.00	0.00	5.38	0.00	2.09	2.99	0.00	3.05	0.00	3.99	0.00	4.00	0.00
6.54	0.01	6.50	0.00	0.03	5.78	-0.02	2.10	3.04	0.01	3.06	-0.01	4.04	0.03	4.03	0.01
6.57	0.01	6.53	0.02	0.05	6.21	-0.03	2.19	3.11	0.02	3.11	-0.02	4.13	0.06	4.06	0.01
6.60	0.01	6.57	0.03	0.07	6.45	-0.04	2.30	3.25	0.04	3.14	-0.04	4.32	0.09	4.10	-0.01
6.64	0.02	6.62	0.05	0.08	6.59	-0.04	2.63	3.34	0.05	3.18	-0.05	4.56	0.09	4.13	-0.03
6.67	0.04	6.66	0.06	0.11	6.75	-0.04	2.96	3.87	0.05	3.24	-0.05	4.69	0.10	4.29	-0.03
6.70	0.06	6.71	0.09	0.13	6.88	-0.04	3.14	4.13	0.09	3.30	-0.04	4.97	0.11	4.35	-0.02
6.72	0.08	6.74	0.13	0.14	7.07	0.03	3.96	4.40	0.09	3.42	-0.03	5.21	0.13	4.45	-0.01
6.75	0.11	6.80	0.18	0.13	7.37	-0.05	4.56	4.51	0.10	3.91	-0.03	5.45	0.13	4.55	0.00
6.78	0.14	6.83	0.21	0.17	7.58	-0.06	5.29	4.85	0.09	3.98	-0.03	5.61	0.14	4.76	-0.01
6.80	0.16	6.86	0.21	0.19	7.72	-0.05	5.44	5.06	0.09	4.26	0.00	5.72	0.15	4.87	0.01
6.82	0.20	6.88	0.21	0.22	7.85	-0.04	5.55	5.31	0.09	4.54	0.01	5.87	0.17	5.00	0.02
6.83	0.24	6.94	0.26	0.22	7.94	-0.02	5.93	5.55	0.11	4.80	0.01	6.04	0.20	5.05	0.02
6.85	0.26	6.99	0.31	0.23	7.98	0.00	6.34	5.82	0.12	5.08	0.01	6.18	0.21	5.18	0.03
6.86	0.27	7.07	0.41	0.26	8.10	0.01	6.61	6.09	0.12	5.31	0.01	6.40	0.25	5.35	0.03
6.89	0.31	7.18	0.51	0.30	8.21	0.06	6.84	6.34	0.14	5.58	0.00	6.55	0.26	5.47	0.04
6.91	0.33	7.27	0.62	0.32	8.35	0.06	7.01	6.45	0.15	5.80	0.01	6.68	0.30	5.55	0.05
6.93	0.36	7.30	0.67	0.39	8.55	0.08	7.12	6.58	0.16	6.11	0.02	6.83	0.34	5.69	0.06
6.96	0.39	7.34	0.70	0.41	8.65	0.08	7.42	6.71	0.17	6.19	0.03	6.99	0.37	5.75	0.07
7.02	0.46	7.38	0.75	0.47	8.75	0.10	7.64	6.74	0.19	6.39	0.04	7.14	0.40	5.87	0.08
7.07	0.51	7.43	0.82	0.52	8.83	0.14	7.92	6.85	0.21	6.51	0.05	7.28	0.42	5.99	0.08
7.10	0.54	7.50	0.94	0.58	8.92	0.22	8.21	6.93	0.23	6.61	0.07	7.39	0.44	6.09	0.10
7.13	0.57	7.56	1.01	0.58	8.96	0.28	8.46	7.08	0.25	6.89	0.10	7.47	0.46	6.20	0.12
7.16	0.60	7.61	1.11	0.59	8.99	0.33	8.67	7.22	0.27	6.98	0.13	7.60	0.53	6.42	0.15
7.20	0.65	7.70	1.23	0.63	9.05	0.40	8.80	7.37	0.31	7.18	0.14	7.68	0.58	6.53	0.17
7.22	0.69	7.72	1.28	0.68	9.08	0.49	8.94	7.45	0.32	7.39	0.17	7.79	0.67	6.65	0.20
7.32	0.78	7.75	1.34	0.81	9.13	0.55	8.99	7.59	0.36	7.61	0.23	7.89	0.75	6.75	0.22
7.34	0.81	7.78	1.40	0.88	9.15	0.61	9.00	7.74	0.41	7.77	0.29	7.98	0.83	6.89	0.26
7.39	0.88	7.82	1.48	0.98	9.18	0.63	8.98	7.83	0.42	7.89	0.31	8.04	0.92	7.04	0.28
7.46	0.99	7.85	1.54	1.06	9.20	0.66	8.98	7.96	0.44	8.01	0.34	8.11	1.01	7.09	0.29
7.52	1.09	7.87	1.58	1.19	9.21	0.73	9.01	8.05	0.46	8.17	0.37	8.23	1.20	7.12	0.30
7.57	1.17			1.31	9.22	0.79	9.03	8.24	0.52	8.28	0.39	8.30	1.32	7.29	0.33
7.59	1.20			1.41	9.23	0.88	9.06	8.35	0.55	8.39	0.43	8.36	1.44	7.36	0.34
7.62	1.24			1.48	9.23	0.94	9.08	8.46	0.58	8.55	0.48	8.42	1.56	7.43	0.34
7.66	1.31			1.57	9.22	1.01	9.11	8.56	0.60	8.68	0.52	8.44	1.62	7.50	0.37
7.71	1.41			1.64	9.20	1.09	9.14	8.65	0.61	8.82	0.58	8.44	1.68	7.63	0.42
7.78	1.55			1.69	9.20	1.17	9.14	8.77	0.67	8.95	0.64			7.70	0.46
				1.73	9.19	1.25	9.15	8.86	0.72	9.05	0.71			7.87	0.62
						1.31	9.16	8.92	0.74	9.14	0.76			7.94	0.66
						1.41	9.16	9.08	0.84	9.26	0.84			8.02	0.74
						1.53	9.17	9.19	0.93	9.35	0.90			8.09	0.82
						1.59	9.15	9.26	0.97	9.44	0.98			8.15	0.91
						1.65	9.14	9.35	1.06	9.52	1.06			8.22	1.02
						1.72	9.12	9.43	1.14	9.56	1.10			8.29	1.11
								9.49	1.20	9.60	1.15			8.34	1.20
								9.55	1.29	9.64	1.22			8.38	1.27
								9.59	1.34	9.68	1.28			8.43	1.35
								9.65	1.47	9.72	1.35			8.49	1.47
								9.68	1.55	9.75	1.41			8.52	1.55
										9.79	1.49			8.54	1.65
										9.81	1.54			8.56	1.75
										9.82	1.58			8.56	1.78
										9.83	1.63				

Table A4.3 Summary of 7050-T7451 Specimen Crack Paths (Set #1) (Continued)

rc-TL-15-7			rc-TL-15-8				rc-TL-15-9				rc-TL-15-10			
	2		1		2		Average				Average			
y	x	y	y	x	y	x	x	y	x	y	x	y	x	y
0.00	0.00	0.00	0.00	0.00	0.00	0.00	5.60	0.00			6.04	0.00		
0.00	4.25	0.00	0.00	5.01	0.00	5.08	10.00	0.00			10.00	0.07		
0.00	4.32	0.00	0.02	5.07	0.00	5.11								
0.01	4.41	0.01	0.04	5.15	-0.02	5.13		(straight)				(straight)		
0.03	4.50	0.01	0.06	5.20	-0.03	5.63								
0.05	4.55	0.00	0.06	5.31	-0.02	5.86								
0.06	4.59	0.01	0.05	5.47	-0.01	5.92								
0.08	4.63	0.02	0.07	5.68	-0.01	6.15								
0.10	4.69	0.04	0.06	5.87	-0.01	6.34								
0.12	4.73	0.06	0.08	6.04	0.02	6.55								
0.14	4.78	0.07	0.07	6.12	0.03	6.61								
0.16	4.81	0.08	0.09	6.23	0.04	6.79								
0.19	4.85	0.10	0.08	6.29	0.05	7.00								
0.22	4.88	0.13	0.08	6.36	0.06	7.09								
0.25	4.91	0.15	0.08	6.44	0.09	7.25								
0.28	4.94	0.17	0.10	6.51	0.12	7.44								
0.30	4.98	0.22	0.11	6.57	0.19	7.57								
0.32	4.99	0.24	0.11	6.70	0.22	7.73								
0.45	5.00	0.28	0.13	6.78	0.25	7.81								
0.48	5.00	0.43	0.12	6.89	0.32	7.92								
0.53	5.00	0.47	0.13	6.92	0.41	8.03								
0.59	4.99	0.52	0.13	7.00	0.48	8.09								
0.64	4.98	0.60	0.15	7.07	0.58	8.18								
0.72	4.95	0.67	0.16	7.22	0.66	8.25								
0.80	4.93	0.72	0.18	7.36	0.75	8.30								
0.92	4.90	0.79	0.23	7.50	0.83	8.36								
0.98	4.88	0.85	0.26	7.60	0.94	8.43								
1.07	4.85	0.91	0.31	7.75	1.01	8.45								
1.13	4.83	0.96	0.36	7.85	1.10	8.49								
1.18	4.78	1.03	0.46	7.99	1.18	8.51								
1.26	4.76	1.08	0.58	8.10	1.26	8.51								
1.30	4.73	1.14	0.74	8.22	1.36	8.51								
1.35	4.72	1.19	0.93	8.34	1.43	8.52								
1.37	4.71	1.24	1.08	8.39	1.49	8.51								
1.43	4.74	1.29	1.17	8.43	1.56	8.50								
1.47	4.74	1.44	1.26	8.43	1.64	8.48								
1.51	4.74	1.51	1.37	8.43	1.71	8.47								
1.60	4.74	1.61	1.46	8.43	1.80	8.45								
1.69	4.75	1.66	1.57	8.41	1.84	8.44								
1.79	4.77	1.73	1.68	8.39	1.92	8.44								
1.89	4.79	1.80	1.76	8.37										
1.97	4.80	1.86	1.81	8.36										
2.06	4.81	1.90	1.83	8.36										
2.09	4.83	1.93	1.84	8.37										
	4.84	1.97												
	4.86	2.03												
	4.88	2.10												
	4.90	2.14												
	4.91	2.17												
	4.91	2.20												

Table A4.3 Summary of 7050-T7451 Specimen Crack Paths (Set #1) (Continued)

rc-LT-15-3				rc-LT-15-4				rc-LT-15-5				rc-LT-15-6			
1		2		1		2		1		2		1		2	
x	y	x	y	y	x	y	x	y	x	y	x	x	y	x	y
0.00	0.00	0.00	0.00	0.00	0.00	0.00	0.00	0.00	0.00	0.00	0.00	0.00	0.00	0.00	0.00
4.24	0.00	5.46	0.03	0.00	2.12	0.00	2.03	0.00	3.01	0.00	3.00	4.06	0.00	4.10	0.00
4.30	0.01	6.41	0.03	-0.02	2.12	0.02	2.06	-0.02	3.03	0.01	3.03	4.11	-0.02	4.33	-0.01
4.70	0.03	6.47	0.05	-0.03	2.13	0.04	2.08	-0.02	3.08	0.03	3.05	4.62	-0.02	4.59	-0.01
4.75	0.00	6.52	0.05	-0.04	2.31	0.04	2.42	-0.04	3.17	0.03	3.10	4.70	-0.01	4.65	0.00
5.02	0.00	6.58	0.06	-0.04	2.41	0.05	2.50	-0.02	3.22	0.03	3.18	4.88	-0.01	4.89	0.00
5.12	0.02	6.63	0.09	-0.04	2.49	0.07	2.59	-0.01	3.27	0.05	3.23	5.10	-0.02	4.95	-0.01
5.41	0.00	6.65	0.13	-0.03	2.57	0.12	2.68	0.01	3.31	0.07	3.28	5.53	-0.01	5.35	-0.01
6.40	0.00	6.67	0.18	-0.01	2.65	0.20	2.72	0.04	3.35	0.12	3.31	6.51	0.00	5.50	0.00
6.44	0.01	6.68	0.31	0.02	2.73	0.26	2.76	0.09	3.38	0.21	3.33	6.94	0.00	5.53	0.02
6.51	0.05	6.70	0.49	0.08	2.81	0.34	2.76	0.15	3.41	0.27	3.37	6.96	0.01	6.21	0.03
6.57	0.14	6.72	0.66	0.15	2.85	0.35	2.78	0.24	3.44	0.38	3.38	7.00	0.03	6.90	0.03
6.62	0.55	6.75	0.85	0.20	2.87	0.54	2.79	0.35	3.46	0.47	3.40	7.03	0.07	6.94	0.03
6.65	0.67	6.78	1.64	0.25	2.90	0.62	2.80	0.44	3.48	0.51	3.42	7.05	0.09	6.96	0.04
6.69	1.39	6.78	2.10	0.38	2.93	0.66	2.82	0.51	3.49	0.69	3.43	7.06	0.15	6.98	0.05
6.72	1.59	6.77	2.21	0.54	2.94	0.92	2.82	0.65	3.50	0.95	3.44	7.06	0.35	7.02	0.09
6.72	2.10	6.74	2.34	0.65	2.95	1.13	2.83	0.79	3.51	1.01	3.46	7.05	0.37	7.04	0.11
6.72	2.31	6.73	2.35	0.68	2.97	1.19	2.85	1.07	3.52	1.06	3.46	7.05	0.54	7.04	0.14
6.70	2.36	6.73	2.41	1.14	2.98	1.29	2.85	1.11	3.53	1.09	3.46	7.08	0.79	7.05	0.29
6.73	2.39			1.17	3.00	1.36	2.83	1.22	3.53	1.22	3.46	7.09	0.95	7.08	0.32
				1.26	3.00	1.45	2.86	1.30	3.54	1.33	3.47	7.10	1.17	7.11	0.37
				1.29	3.00	1.53	2.86	1.39	3.55	1.41	3.49	7.12	1.39	7.13	0.40
				1.40	3.00	1.62	2.86	1.44	3.56	1.51	3.49	7.18	1.77	7.13	0.55
				1.57	3.00	1.64	2.87	1.58	3.57	1.63	3.49	7.18	2.03	7.15	0.74
				1.66	3.03	1.75	2.88	1.74	3.57	1.71	3.49	7.16	2.21	7.17	0.97
				1.75	3.03	1.81	2.89	1.95	3.57	1.96	3.49	7.16	2.27	7.17	1.26
				1.86	3.04	1.87	2.90	2.05	3.57	2.13	3.49	7.18	2.36	7.20	1.32
				1.98	3.06	1.98	2.90	2.08	3.57	2.27	3.49	7.20	2.39	7.21	1.51
				2.09	3.06	2.09	2.89	2.19	3.56					7.23	1.69
				2.20	3.06			2.29	3.54					7.26	1.90
				2.30	3.05									7.26	1.94
				2.35	3.04									7.25	2.15
														7.22	2.26
														7.21	2.36
														7.20	2.39

Table A4.3 Summary of 7050-T7451 Specimen Crack Paths (Set #1) (Continued)

rc-LT-15-7				rc-LT-15-8				rc-LT-15-9				rc-LT-15-10			
1		2		1		2		1		2		1		2	
x	y	x	y	y	x	y	x	y	x	y	x	x	y	x	y
0.00	0.00	0.00	0.00	0.00	0.00	0.00	0.00	0.00	0.00	0.00	0.00	0.00	0.00	0.00	0.00
4.50	0.00	4.48	0.00	0.00	4.69	0.00	4.90	0.00	5.56	0.00	5.53	5.99	0.00	6.02	0.00
4.56	-0.03	4.52	-0.01	0.00	4.92	0.00	4.98	0.00	5.60	0.00	5.53	6.06	-0.02	6.06	0.04
4.59	-0.05	4.54	0.00	0.01	4.99	0.03	5.03	-0.02	5.63	0.01	5.59	6.08	-0.04	6.12	0.04
4.61	-0.06	4.58	0.03	0.02	5.03	0.08	5.07	-0.02	5.71	0.04	5.63	6.15	-0.04	6.17	0.07
4.70	-0.06	4.68	0.03	0.09	5.10	0.11	5.10	0.00	5.77	0.07	5.70	6.16	-0.03	6.20	0.09
4.73	-0.05	4.71	0.04	0.11	5.12	0.15	5.13	0.02	5.83	0.09	5.77	6.19	-0.03	6.21	0.13
4.80	-0.04	4.75	0.05	0.17	5.12	0.22	5.13	0.05	5.86	0.11	5.80	6.23	0.00	6.23	0.16
4.84	-0.01	4.79	0.06	0.25	5.12	0.24	5.14	0.09	5.90	0.14	5.84	6.26	0.04	6.24	0.24
4.89	0.05	4.80	0.07	0.34	5.12	0.64	5.15	0.15	5.93	0.21	5.87	6.30	0.11	6.25	0.27
4.90	0.11	4.80	0.10	0.46	5.15	0.79	5.18	0.20	5.95	0.32	5.91	6.31	0.16	6.26	0.38
4.93	0.27	4.82	0.18	0.59	5.16	0.80	5.23	0.26	5.97	0.44	5.95	6.33	0.23	6.28	0.95
4.95	0.63	4.83	0.22	0.74	5.16	0.88	5.24	0.29	5.98	0.56	5.97	6.34	0.31	6.32	1.17
5.01	1.21	4.85	0.50	0.90	5.15	1.00	5.26	0.35	5.99	0.58	5.98	6.36	0.92	6.32	1.39
5.02	1.25	4.88	0.70	1.03	5.15	1.25	5.27	0.40	6.01	0.87	6.00	6.39	1.23	6.38	1.98
5.03	1.51	4.91	1.00	1.13	5.16	1.40	5.29	0.47	6.02	1.04	6.02	6.43	1.90	6.37	2.14
5.07	1.65	4.93	1.06	1.19	5.16	1.51	5.31	0.57	6.03	1.06	6.04	6.45	2.00	6.35	2.27
5.07	2.13	4.95	1.24	1.28	5.20	1.60	5.32	0.63	6.04	1.19	6.04	6.45	2.11	6.36	2.40
5.06	2.18	4.98	1.52	1.51	5.21	1.77	5.34	0.70	6.06	1.23	6.05	6.40	2.28		
5.05	2.34	4.98	1.56	1.55	5.21	1.90	5.35	0.80	6.06	1.40	6.07	6.40	2.36		
5.07	2.38	5.00	1.91	1.64	5.23	1.96	5.37	0.85	6.07	1.48	6.08				
		5.00	2.08	1.74	5.23	2.24	5.37	1.00	6.09	1.59	6.09				
		4.99	2.21	1.86	5.23	2.29	5.35	1.09	6.10	1.68	6.10				
		5.01	2.36	1.95	5.27	2.35	5.35	1.17	6.10	1.79	6.11				
		5.02	2.38	2.02	5.27			1.26	6.10	1.80	6.12				
				2.07	5.27			1.32	6.12	2.12	6.12				
				2.12	5.27			1.37	6.13	2.15	6.12				
				2.17	5.27			1.44	6.14						
				2.21	5.27			1.56	6.16						
				2.30	5.27			1.71	6.18						
								1.76	6.18						
								1.89	6.18						
								1.99	6.19						
								2.06	6.19						
								2.10	6.19						
								2.17	6.16						
								2.20	6.15						
								2.26	6.16						

Table A4.4 Summary of 7475-T7351 Specimen Crack Paths (Set #4)

S7475LT-1				S7475LT-2				S7475LT-4				S7475LT-5			
Back		Front		Front		Back		Front		Back		Front		Back	
x	y	x	y	x	y	x	y	x	y	x	y	x	y	x	y
0.000	0.000	0.000	0.000	0.000	0.000	0.000	0.000	0.000	0.000	0.000	0.000	0.000	0.000	0.000	0.000
4.464	-0.017	4.464	-0.017	4.452	-0.010	4.452	0.000	4.954	-0.017	4.954	-0.017	4.952	-0.008	4.952	0.001
4.562	-0.022	4.562	-0.022	4.533	-0.031	4.533	-0.002	5.014	-0.020	5.014	-0.020	5.017	0.032	5.017	0.032
4.600	-0.045	4.600	-0.002	4.620	-0.060	4.620	0.006	5.020	-0.027	5.020	0.002	5.040	0.007	5.040	0.059
4.640	-0.050	4.640	0.004	4.680	-0.060	4.680	0.008	5.100	0.007	5.068	0.053	5.080	0.008	5.080	0.074
4.800	-0.060	4.800	-0.008	4.780	-0.051	4.780	0.017	5.123	0.042	5.092	0.077	5.140	0.021	5.140	0.091
4.900	-0.054	4.900	-0.002	4.920	-0.060	4.920	0.010	5.148	0.080	5.092	0.080	5.200	0.042	5.200	0.113
4.986	-0.052	**4.960**	-0.010	**4.960**	-0.068	**4.960**	0.004	5.158	0.150	5.094	0.150	5.260	0.065	5.260	0.129
5.029	-0.009	4.981	0.023	5.000	-0.056	5.000	0.004	5.159	0.235	5.095	0.235	5.320	0.086	5.320	0.156
5.054	0.093	4.983	0.100	5.050	-0.030	5.050	0.074	5.154	0.280	5.093	0.280	5.400	0.129	5.400	0.206
5.062	0.300	4.992	0.300	5.108	0.040	5.026	0.040	5.160	0.389	5.094	0.389	5.520	0.191	5.500	0.256
5.050	0.400	4.984	0.400	5.114	0.060	5.042	0.060	5.169	0.520	5.102	0.520	5.570	0.220	5.539	0.277
5.060	0.480	4.993	0.480	5.114	0.080	5.052	0.080	5.174	0.550	5.111	0.550	5.605	0.265	5.563	0.310
5.058	0.580	4.996	0.580	5.114	0.160	5.053	0.160	5.165	0.580	5.106	0.580	5.638	0.323	5.582	0.351
5.075	0.720	5.003	0.716	5.123	0.210	5.053	0.210	5.167	0.660	5.106	0.660	5.650	0.400	5.584	0.420
5.071	0.840	5.010	0.840	5.125	0.300	5.053	0.300	5.172	0.720	5.107	0.720	5.668	0.490	5.603	0.490
5.072	0.960	5.003	0.960	5.120	0.580	5.051	0.580	5.176	0.780	5.114	0.780	5.670	0.570	5.608	0.570
5.083	1.100	5.011	1.100	5.112	0.660	5.053	0.660	5.174	0.890	5.106	0.890	5.672	0.610	5.602	0.610
5.082	1.260	5.015	1.260	5.128	0.810	5.063	0.810	5.174	0.960	5.115	0.960	5.673	0.650	5.614	0.650
5.080	1.360	5.013	1.360	5.131	0.980	5.067	0.980	5.188	1.040	5.118	1.040	5.678	0.680	5.617	0.680
5.099	1.480	5.036	1.480	5.129	1.060	5.080	1.060	5.184	1.080	5.125	1.080	5.672	0.780	5.612	0.780
5.078	1.640	5.013	1.640	5.136	1.180	5.066	1.180	5.194	1.180	5.124	1.180	5.672	0.920	5.613	0.920
5.080	1.760	5.014	1.760	5.140	1.250	5.076	1.250	5.184	1.220	5.116	1.220	5.679	1.080	5.622	1.080
				5.143	1.320	5.073	1.320	5.180	1.330	5.115	1.330	5.687	1.200	5.635	1.200
				5.152	1.380	5.091	1.380	5.181	1.360	5.111	1.360	5.706	1.320	5.650	1.320
				5.153	1.440	5.088	1.440	5.188	1.520	5.125	1.520	5.702	1.400	5.643	1.400
				5.179	1.580	5.114	1.580	5.187	1.660	5.123	1.660	5.722	1.500	5.655	1.500
				5.180	1.640	5.113	1.640	5.202	1.760	5.142	1.760	5.724	1.660	5.656	1.660
				5.174	1.680	5.114	1.680	5.202	1.800	5.132	1.800	5.732	1.720	5.668	1.720
				5.182	1.740	5.116	1.740	5.198	1.860	5.135	1.860	5.732	2.000	5.673	2.000
				5.182	1.800	5.114	1.800	5.191	1.960	5.123	1.960	5.745	2.100	5.678	2.100
				5.158	2.040	5.093	2.040	5.191	2.140	5.134	2.140	5.749	2.180	5.692	2.180
				5.174	2.200	5.103	2.200	5.194	2.280	5.135	2.280	5.758	2.260	5.685	2.260

Note: Bold signifies end of static precrack.

Table A4.4 Summary of 7475-T7351 Specimen Crack Paths (Set #4) (Continued)

S7475TL-1				S7475TL-2				S7475TL-3				S7475TL-4			
Front		Back		Back		Front		Back		Front		Back		Front	
x	y	x	y	x	y	x	y	x	y	x	y	x	y	x	y
0.000	0.000	0.000	0.000	0.000	0.000	0.000	0.000	0.000	0.000	0.000	0.000	0.000	0.000	0.000	0.000
4.464	-0.013	4.464	-0.013	4.456	-0.023	4.456	-0.023	4.953	-0.027	4.953	-0.027	4.955	-0.008	4.955	-0.008
4.554	-0.021	4.554	-0.021	4.500	-0.024	4.500	-0.024	5.000	-0.026	5.000	-0.026	5.000	-0.007	5.000	-0.007
4.585	-0.049	4.585	-0.002	4.509	-0.041	4.509	-0.015	5.011	-0.034	5.006	-0.006	5.020	-0.016	5.010	0.011
4.740	-0.046	4.740	0.010	4.528	-0.045	4.528	-0.002	5.032	-0.033	5.011	0.003	5.046	-0.011	5.012	0.027
4.850	-0.052	4.850	0.009	4.580	-0.059	4.580	-0.002	5.043	-0.028	5.016	0.014	5.090	0.060	5.036	0.087
4.940	-0.060	4.940	0.002	4.880	-0.058	4.880	0.000	5.072	-0.001	5.037	0.039	5.129	0.153	5.079	0.180
5.014	-0.057	5.014	0.002	4.960	-0.050	4.956	0.014	5.120	0.074	5.074	0.110	5.170	0.257	5.116	0.296
5.045	-0.030	5.022	0.009	5.032	-0.037	5.016	0.021	5.171	0.200	5.115	0.221	5.229	0.487	5.171	0.507
5.078	0.000	5.036	0.034	5.071	0.002	5.029	0.039	5.216	0.386	5.160	0.400	5.249	0.660	5.190	0.672
5.109	0.060	5.055	0.079	5.108	0.080	5.050	0.100	5.282	0.720	5.220	0.720	5.263	0.820	5.200	0.831
5.157	0.200	5.102	0.221	5.143	0.200	5.084	0.220	5.319	1.060	5.259	1.060	5.287	0.960	5.226	0.973
5.210	0.360	5.158	0.383	5.174	0.360	5.111	0.370	5.322	1.180	5.264	1.180	5.320	1.249	5.259	1.261
5.239	0.460	5.186	0.480	5.207	0.540	5.150	0.569	5.316	1.306	5.257	1.306	5.340	1.480	5.280	1.480
5.276	0.640	5.218	0.653	5.224	0.700	5.160	0.709	5.333	1.417	5.274	1.417	5.348	1.620	5.291	1.620
5.301	0.780	5.243	0.795	5.240	0.900	5.179	0.900	5.334	1.560	5.274	1.560	5.350	1.753	5.292	1.753
5.320	0.960	5.264	0.972	5.247	1.040	5.181	1.040	5.358	1.780	5.297	1.780	5.370	1.840	5.312	1.850
5.345	1.120	5.300	1.142	5.260	1.149	5.205	1.160	5.364	1.920	5.303	1.920	5.394	2.000	5.338	2.017
5.378	1.205	5.320	1.220	5.300	1.360	5.242	1.360	5.362	2.090	5.304	2.090	5.405	2.140	5.344	2.153
5.397	1.340	5.340	1.352	5.304	1.400	5.243	1.400	5.370	2.240	5.310	2.240	5.437	2.280	5.382	2.300
5.416	1.520	5.366	1.531	5.294	1.600	5.235	1.600								
5.438	1.611	5.380	1.625	5.298	1.760	5.236	1.760								
5.458	1.851	5.396	1.860	5.304	1.840	5.250	1.839								
5.461	2.080	5.403	2.079	5.320	1.960	5.258	1.960								
5.477	2.260	5.415	2.260	5.320	2.060	5.259	2.060								
				5.314	2.180	5.251	2.180								

S7475TL-5			
Back		Front	
x	y	x	y
0.000	0.000	0.000	0.000
4.957	-0.018	4.957	-0.018
5.001	-0.025	5.001	-0.025
5.035	-0.047	5.035	-0.017
5.090	-0.047	5.090	0.002
5.240	-0.051	5.240	0.003
5.280	-0.049	5.280	0.007
5.340	-0.057	5.340	0.006
5.440	-0.060	5.440	0.003
5.680	-0.067	5.680	-0.003
5.780	-0.066	5.780	-0.006
5.900	-0.057	5.900	-0.001
6.100	-0.058	6.100	0.002
6.200	-0.055	6.200	0.007
6.220	-0.049	6.220	0.010
6.500	-0.041	6.500	0.013
6.640	-0.034	6.640	0.021
6.800	-0.017	6.800	0.039
6.920	-0.016	6.920	0.045
7.020	0.000	7.020	0.062
7.123	0.000	7.123	0.061
7.200	0.011	7.200	0.064
7.310	0.011	7.310	0.070
7.372	0.027	7.372	0.077
7.540	0.043	7.540	0.097
7.620	0.043	7.620	0.100
7.680	0.053	7.680	0.112
7.890	0.057	7.890	0.116
7.960	0.063	7.960	0.117
8.120	0.056	8.120	0.112
8.280	0.073	8.280	0.128
8.380	0.066	8.380	0.129
8.440	0.075	8.440	0.125
8.600	0.062	8.600	0.121
8.740	0.080	8.740	0.143
8.840	0.085	8.840	0.141
8.960	0.097	8.960	0.153

Note: Bold signifies end of static precrack.

REFERENCES

[1] R. G. Pettit, J. J. Wang, C. Toh, *Integral Airframe Structures (IAS)—Validated Feasibility Study of Integrally Stiffened Metallic Fuselage Panels for Reducing Manufacturing Cost*, Boeing Report CRAD-9306-TR-4542, NASA contract NAS1-20014, Task 34, November, 1998 (See also NASA CR-2000-209342, May 2000).

[2] T. Swift, "Application of Damage Tolerance Technology to Type Certification", SAE Paper #811062, Aerospace Congress and Exp., Anaheim, CA October 1981.

[3] H. F. Hardrath et al, NACA Tech Note #3856, 1956.

[4] C. C. Poe, "Crack Propagation in Stiffened Panels", ASTM STP 486, 1971.

[5] J. Maclin, "Performance of Fuselage Pressure Structure", *1991 International Conference on Aging Aircraft and Structural Airworthiness*, Washington D.C., November 19-21, 1991, NASA Conference Pub 3160 (1992).

[6] T. Swift, "The Applications of Fracture Mechanics in the Development of the DC-10 Fuselage", in *Fracture Mechanics of Aircraft Structures* , AGARD-AG-176 by H. Liebowitz, Neuilly sur Seine, France, pp. 226-287, 1974.

[7] T. Swift, "Damage Tolerance in Pressurized Fuselage", 11th Plantema Memorial Lecture, 14th Symposium of the ICAF, *New Materials and Fatigue Resistant Aircraft*, Ottawa, Canada, 1987.

[8] M. Kosai, A. S. Kobayashi, M. Ramulu, "Tear Straps in Aircraft Fuselage", *Durability of Metal Aircraft Structures*: Proc. of International Workshop on Structural Integrity of Aging Airplanes, Atlanta Technology Publications, Atlanta, GA, pp. 443-457, 1992.

[9] R. G. Pettit, J. C. Newman, M. S. Domack, *Crack Turning Damage Tolerance Approach for Integrally Stiffened Structure*, 19th ICAF Symposium, Edinburg, June 1997.

[10] *National Transportation Safety Board Aircraft Accident Report, Aloha Airlines Flight 243, Boeing 737-200, N73711, Near Maui, Hawaii, April 28, 1988*, NTSB/AAR-89/03, 1989.

[11] M. Kosai, A. Shimamoto, C. T. Yu, S. I. Walker, A. S. Kobayashi, and P. Tan; Axial Crack Propagation and Arrest in Pressurized Fuselage", FAA/NASA Symposium on Advanced Structural Integrity Methods for Airframe Durability and Damage Tolerance, NASA Conf. Pub. 3274, Part 1, pp. 375-392, 1994.

[12] M. Miller, K. Kaelber, and R. E. Worden, "Finite Element Analysis of Pressure Vessel Panels", *Durability of Metal Aircraft Structures*: Proc. of International Workshop on Structural Integrity of Aging Airplanes, Atlanta Technology Publications, Atlanta, GA, pp. 337-339, 1992.

[13] D. O. Potyondy, Discrete Crack Growth Analysis Methodology for Cracks in Pressurized Fuselage Structures", FAA/NASA Symposium on Advanced Structural Integrity Methods for Airframe Durability and Damage Tolerance, NASA Conference Publication 3274, Part 2, pp. 581-601, 1994.

[14] B. Knops, *Numerical Simulation of Crack Growth in Pressurized Fuselages*, Ph.D. Thesis, Delft University of Technology, September, 1994.

[15] C.-S. Chen, *Crack Growth Simulation and Residual Strength Prediction in Thin Shell Structures*, Ph. D. Dissertation, Cornell University, January, 1999.

[16] P. A. Wawrzynek, A. R. Ingraffea, "Interactive Finite-Element Analysis of Fracture Processes: An Integrated Approach", *Theoretical and Applied Fracture Mechanics*, Vol. 8, 1987, pp. 137-150.

[17] F. Erdogan, G. C. Sih; "On the Extension of Plates under Plane Loading and Transverse Shear", *Journal of Basic Engineering*, Vol. 85D, No. 4, pp. 519-527, 1963.

[18] I. Finnie, A. Saith; "A Note on the Angled Crack Problem and the Directional Stability of Cracks", *International Journal of Fracture* , Vol.9, pp.484-486,1973.

[19] M. B. Buczek , C. T. Herakovich, "A Normal Stress Criterion for Crack Extension Direction in Orthotropic Composite Materials", *J. Composite Materials*, Vol. 19, pp. 544-553, 1985.

[20] M. Ramulu, A. Kobayashi, "Dynamic Crack Curving—a Photoelastic Evaluation", *Experimental Mechanics*, Vol. 23, pp. 1-9, 1983

[21] B. Cotterell, J. R. Rice, "Slightly Curved or Kinked Cracks", *International Journal of Fracture*, Vol. 16, pp. 155-169, 1980.

[22] T. J. Boone, P. A. Wawrzynek, and A. R. Ingraffea, *Engineering Fracture Mech.*, Vol. 26, No. 2, pp. 185-201, 1987.

[23] M. L. Williams, "On the Stress Distribution at the Base of a Stationary Crack", ASME Transactions, *Journal of Applied Mechanics*, Vol. 24, pp. 109-114, 1957.

[24] G. P. Cherapanov, *Mechanics of Brittle Fracture*, McGraw-Hill, New York, 1979.

[25] M. A. Hussain, S. L. Pu, and J. H. Underwood, "Strain Energy Release Rate for a Crack Under Combined Mode I and Mode II", *Fracture Analysis*, ASTM STP 560, Philadelphia, pp. 2-28, 1974.

[26] G. C. Sih, "Strain-Energy-Density Factor Applied to Mixed-Mode Crack Problems", *International Journal of Fracture*, Vol. 10, pp. 305-321, 1974.

[27] S. K. Maiti, R. A. Smith, *International Journal of Fracture*, Vol. 23, pp. 281-295, 1983.

[28] Theocaris, P. S., "Variation on the Theme of Fracture Criteria", *Engineering Fracture Mechanics*, Vol. 33, pp. 205-214 (1989).

[29] M. Shirmohamadi, *Stable Crack Growth Trajectories and Fracture Due to Interacting Cracks*, Ph. D. Dissertation, University of California at Berkely, 1995.

[30] T. M. Maccagno, J. F. Knott, "The Fracture Behaviour of PMMA in Mixed Modes I and II", *Engineering Fracture Mechanics*, Vol. 34, No. 1, pp. 65-86, 1989.

[31] T. M. Maccagno, J. F. Knott, "The Low Temperature Brittle Fracture Behaviour of Steel in Mixed Modes I and II", *Engineering Fracture Mechanics*, Vol. 38, No. 2/3, pp. 111-128, 1991.

[32] L. P. Pook, "The Effect of Crack Angle on Fracture Toughness", *Engineering Fracture Mechanics*, Vol. 3, pp. 205-218, 1971.

[33] A. F. Liu, Crack Growth and Failure of Aluminium Plate Under In-Plane Shear", *AIAA Journal*, vol. 12, pp. 180-185, 1974.

[34] J. W. Hutchinson, "Singular Behaviour at the End of a Tensile Crack in a Hardening Material", *Journal of the Mechanics and Physics of Solids*, Vol. 16, pp. 13-31, 1968.

[35] J. R. Rice, G. F. Rosengren, "Plane Strain Deformation Near a Crack Tip in a Power-Law Hardening Material", *Journal of the Mechanics and Physics of Solids*, Vol. 16, pp. 1-12, 1968.

[36] C. F. Shih, "Small-Scale Yielding Analysis of Mixed Mode Plane-Strain Problems", Fracture Analysis, ASTM STP 560, American Society for Testing and Materials, pp. 187-210, 1974.

[37] N. Hallback, F. Nilsson, "Mixed-Mode I/II Fracture Behaviour of an Aluminium Alloy", *Journal of the Mechanics and Physics of Solids*, Vol. 42, No. 9, pp. 1345-1374, 1994.

[38] B. E. Amstutz, M. A. Sutton, D. S. Dawicke, and J. C. Newman, "An Experimental Study of CTOD for Mode I/Mode II Stable Crack Growth in Thin 2024-T3 Aluminum Specimens", *Fracture Mechanics: 26th Volume*, ASTM STP 1256, American Society for Testing and Materials, pp. 257-271, 1995.

[39] C. Dalle Donne, H. Doker, "Plane Stress Crack Resistance Curves of an Inclined Crack Under Biaxial Loading", *Multiaxial Fatigue and Deformation Testing Techniques*, ASTM STP 1280, American Society for Testing and Materials, pp. 243-263, 1997.

[40] M. A. Sutton, X. Deng, F. Ma, J. C. Newman, M. James, "Development and Application of a COD-Based Mixed-Mode Fracture Criterion", *International Journal for Solids and Structures*, (in press).

[41] P. S. Leevers, J. C. Radon, "Inherent Stress Biaxiality in Various Fracture Specimen Geometries", *International Journal of Fracture*, Vol. 19, pp. 311-325, 1982.

[42] Y. Sumi, S. Nemat-Nasser, L. M. Keer, "On Crack Path Instability in a Finite Body", *Engineering Fracture Mechanics*, Vol. 22, pp. 759-771, 1985.

[43] K. Zaal, *A Survey of Crack Path Stability Criteria and Their Application to Crack Flapping Phenomena in Stiffened Structures*, Report LR-681, TU Delft, Faculty of Aerospace Engineering, The Netherlands, September, 1992.

[44] W. F. Hosford, R. M. Caddell, *Metal Forming, Mechanics and Metallurgy*, 2nd Edition, Prentice Hall, Englewood Cliffs, NJ, pp. 68-79, 1993.

[45] Dugdale, D.S., "Yielding in Steel Sheets Containing Slits", *Journal of the Mechanics and Physics of Solids*, Vol. 8, pp. 100-104, 1960.

[46] Barenblatt, G. I., "The Mathematical Theory of Equilibrium Cracks in Brittle Fracture", *Advances in Applied Mechanics*, Vol. VII, Academic Press, pp. 55-129, 1962.

[47] W. Becker, D. Gross, "About the Dugdale Crack Under Mixed Mode Loading", *International Journal of Fracture*, Vol. 37, pp163-170, 1987.

[48] J. Li, "Elastic-Plastic Study of Mixed Mode Semi-Infinite Crack by Using the Dugdale Model", *International Journal of Fracture*, Vol. 90, pp. L27-L31, 1998.

[49] F. Erdogan, "On the Stress Distribution on Plates with Collinear Cuts Under Arbitrary Loads", *Proceedings, Fourth U.S. National Congress of Applied Mechanics*, p. 547, 1962

[50] FRAN2D/L fracture simulation software and documentation available from Kansas State University, www.mne.ksu.edu/~franc2d.

[51] M. Isida, T. Nishino, "Formulae of Stress Intensity Factors at the Tips of Kinked Cracks Under Various Loadings", *Engineering Fracture Mechanics*, Vol. 36, No. 5, pp. 697-711, 1990.

[52] G. R. Irwin, "Analysis of Stresses and Strains Near the End of a Crack Transversing a Plate", ASME Transactions, *Journal of Applied Mechanics*, Vol. 24, p. 361, 1957.

[53] H. Tada, P. C. Paris, G. Irwin, *Stress Analysis of Cracks Handbook*, 2nd Ed, Paris Productions/Del Research Corp., St Louis, 1985.

[54] F. Lemant, A. Pineau, Mixed Mode Fracture of a Brittle Orthotropic Material—Example of Strongly Textured Zinc Sheets, *Engineering Fracture Mechanics*, Vol. 14, pp. 91-105, 1981.

[55] A. P. Kfouri, "Crack Extension Under Mixed-Mode Loading in an Anisotropic Mode-Asymmetric Material in Respect of Resistance to Fracture", *Fatigue & Fracture of Engineering Materials & Structures*, Vol. 19, No. 1, pp. 27-38, 1996.

[56] R. J. Goode, "Identification of Fracture Plane Orientation, Materials Research and Standards (MIRSA)", *ASTM*, Vol. 12, No. 9, 1972. (see also ASTM E1823).

[57] Vaughn, H. "Crack Propagation and the Principal-Tensile Stress Condition for Mixed-Mode Loading", *Engineering Fracture Mechanics*, Vole 59, pp. 393-397, 1998.

[58] T. M. Maccagno, J. F. Knott, "The Mixed Mode I/II Fracture Behaviour of Lightly Tempered HY130 Steel at Room Temperature", *Engineering Fracture Mechanics*, Vol. 41, No. 6, pp. 805-820, 1992.

[59] M. Arcan, Z. Hasin, A. Volodshin, "A Method to Produce Uniform Plane-Stress States with Applications to Fiber-Reinforced Materials", *Experimental Mechanics*, Vol. 18, pp.141-146, 1978.

[60] B. E. Amstutz, M. A. Sutton, D. S. Dawicke, and M. L. Boone, "Effects of Mixed Mode I/II Loading and Grain Orientation on Crack Initiation and Stable Tearing in 2024-T3 Aluminum", *Fatigue and Fracture Mechanics*: 27th Volume, ASTM 1296, American Society for Testing and Materials, Philadelphia, 1995.

[61] N. Hallback, "The Influence of Finite Geometry and Material Properties on Mixed-Mode I/II Fracture of Aluminum", *International Journal of Fracture*, Vol. 87, pp. 151-188, 1997.

[62] A. K. Ghosal, R. Narasimhan, "A Finite Element Analysis of Mixed-Mode Fracture Initiation by Ductile Failure Mechanisms", *Journal of the Mechanics and Physics of Solids*, Vol. 42, pp. 953-978, 1994.

[63] A. P. Kfouri, M.W. Brown, "A Fracture Criterion for Cracks Under Mixed-Mode Loading", *Fatigue & Fracture Mechanics of Engineering Structures & Materials*, Vol. 18, No. 9, pp. 959-969, 1995.

[64] Y. J. Chao, S. Liu, "On the Failure of Cracks Under Mixed-Mode Loads", *International Journal of Fracture*, Vol. 87, pp. 201-223, 1997.

[65] M. James, *A Plane Stress Finite Element Model for Elastic Plastic Mode I/II Crack Growth*, Ph.D. Dissertation, Department of Mechanical and Nuclear Engineering, Kansas State University, 1998.

[66] T. J. Stone, I Babuska, "A Numerical Method with *a Posteriori* Error Estimation for Determining the Path Taken by a Propagating Crack", *Computational Methods in Applied Mechanics and Engineering*, Vol. 160, pp. 245-271, 1998.

[67] J. G. Williams, P. D. Ewing, "Fracture Under Complex Stress--The Angled Crack Problem", *International Journal of Fracture Mechanics*, Vol. 8, pp. 441-446, 1972.

[68] G. R. Irwin, "Plastic Zone Near a Crack and Fracture Toughness", *Proc. 7th Sagamore Conf.*, p. IV-63, 1960.

[69] J. R. Rice, M. A. Johnson, "The Role of Large Crack Tip Geometry Changes in Plane Strain Fracture", *Inelastic Behavior of Solids*, McGraw Hill, pp. 641-690, 1969.

[70] I. Constable, J. G. Williams, L.E. Culver, "Notch Root Radii Effects in the Fatigue of Polymers", *International Journal of Fracture Mechanics*, Vol. 6, No. 3, pp. 279-285, 1970.

[71] M. Ramulu, A. S. Kobayashi, "Dynamic Crack Curving—A Photoelastic Evaluation", *Experimental Mechanics*, Vol. 23, pp.1-9, 1983.

[72] P. S. Theocaris, N. P. Andrianopoulos, N. P., "A Modified Strain Energy Density Criterion Applied to Crack Propagation", *Journal of Applied Mechanics*, Vol. 49, No. 1, pp. 81-86, 1982.

[73] A. S. Selvaratinam, J. G. Goree, "T-Stress Based Fracture Model for Cracks in Isotropic Materials," *Engineering Fracture Mechanics*, Vol. 60, N0. 5-6, pp. 543-561, 1998.

[74] R. Streit, I. Finnie, "An Experimental Investigation of Crack-Path Directional Stability", *Experimental Mechanics*, Vol. 20, pp. 17-23, 1980.

[75] A. A. Wells, "Unstable Crack Propagation in Metals: Cleavage and Fast Fracture", *Proceedings of the Crack Propagation Symposium*, Vol. 1, Paper 84, Cranfield, UK, 1961.

[76] J. C. Newman, D. S. Dawicke, M. A. Sutton, C. A. Bigelow, "A Fracture Criterion for Widespread Cracking in Thin Sheet Aluminum Alloy", 17th Symposium of the International Committee on Aeronautical Fatigue (ICAF 93), Stockholm, 1993.

[77] P. A. Wawrzynek, *Interactive Finite Element Analysis of Fracture Processes: an Integrated Approach*, M. S. Thesis, Cornell University, 1987.

[78] S. G. Larsson, A. J. Carlsson, "Influence of Non-Singular Stress Terms and Specimen Geometry on Small-Scale Yielding at Crack Tips in Elastic-Plastic Materials, *Journal of the Mechanics and Physics of Solids*, Vol. 21, pp. 263-277, 1973.

[79] Sham, T.-L. Sham, "The Determinationof the Elastic T-term Using Higher Order Weight Functions", *International Journal of Fracture*, Vol. 48, pp. 81-102, 1991.

[80] T. Fett, "A Green's Function for T-stresses in an edge-cracked rectangular plate, *Engineering Fracture Mechanics*, Vol. 57, pp. 365-373, 1997

[81] T. Fett, *A Compendium of T-stress Solutions*, Institut fur Materialforschung, Karlsruhe, Report FZKA 6057, February 1998.

[82] A. M. Al-Ani and J.W. Hancock, "J-Dominance of Short Cracks in Tension and Bending", *Journal of the Mechanics and Physics of Solids,* Vol. 39, No.1, pp. 23-43, 1991.

[83] G. E. Cardew, M. R. Goldthorpe, I. C. Howard, A. P. Kfouri, "On the Elastic T-term", *Fundamentals of Deformation and Fracture: Eshelby Memorial Symposium*, 1985.

[84] A. P. Kfouri, "Some Evaluations of the Elastic T-term using Eshelby's Method", *International Journal of Fracture*, Vol. 30, pp. 301-315, 1986.

[85] J. Sladek, E. B. Becker, R. S. Durham, "A Contour Integral Computation of Mixed-Mode Stress Intensity Factors", International Journal of Fracture, Vol. 12, pp. 359-368, 1976.

[86] F. G. Yuan, S. Yang, "The Application of Fracture Mechanics to Stitched Warp-kit Fabric Composites", AIAA Paper #98-2025, *39th AIAA/ASME/ASCE/AHS/ASC Structures, Structural Dynamics, and Materials Conference*, Long Beach, CA, April 1998.

[87] C.-S. Chen, R. Krause, R. G. Pettit, L. Banks-Sills, A. R. Ingraffea, "Numerical Assessment of T-Stress Computation Using a P-Version Finite Element Method", submitted to *International Journal of Fracture*, 2000.

[88] R. K. Bird, *Evaluation of Tensile and Fatigue Behavior of Candidate Alloys and Product Forms for IAS*, Integral Airframe Structures Program—Joint NASA Industry Workshop, NASA Langley Research Center, November, 1998 (unpublished).

[89] B. Gross and J. E. Srawley, *Stress Intensity Factors for Single-Edge Notch Specimens Subjected to Splitting Forces*, NASA TN D-3295, 1966.

[90] R. M. L. Foote and V. T. Buchwald, "An Exact Expression for the Stress Intensity Factor for a Double Cantilever Beam", International Journal of Fracture, Vol. 29, pp. 125-134, 1985

[91] M. S. Domack, *Fatigue Crack Growth Rate and Fracture Toughess Testing at NASA Langley Research Center*, Integral Airframe Structures Program—Joint NASA Industry Workshop, NASA Langley Research Center, April, 1998 (unpublished).

[92] J. Munroe, K. Wilkins, M. Gruber *Integral Airframe Structure (IAS) Validated Feasibility Study of Integrally Stiffened Metallic Fuselage Panels for Reducing Manufacturing Cost—Final Report*, NASA Contract NAS1-20267, The Boeing Company (Seattle), November, 1998 (See also NASA CR-2000-209337).

[93] M. Domack, W. Johnston, unpub. data, NASA Langley Research Center, 2000.

[94] J. C. Newman, Jr., B. C. Booth, K. N. Shivakumar, "An Elastic-Plastic Finite-Element Analysis of the J-resistance Curve Using a CTOD Criterion", *Fracture Mechanics: Eighteenth Symposium, ASTM STP 945*, American Society for Testing and Materials, Philadelphia, pp. 665-685, 1988.

[95] D. S. Dawicke, J. C. Newman, Jr., Residual Strength Predictions for Multiple Site Damage Cracking Using a Three-Dimensional Finite-Element Analysis and a CTOA Criterion", *Proceedings of the 29th National Symposium on Fatigue and Fracture Mechanics* (1997), American Society of Testing and Materials, pp. 815-829, 1999.

[96] H. W. Swift, "Plastic Instability Under Plane Stress", *Journal of the Mechanics and Physics of Solids*, Vol. 1, pp. 1-18, 1952.

[97] R. M. Mc Meeking, "Finite Deformation Analysis of Crack-Tip Opening in Elastic-Plastic Materials and Implications for Fracture", *Journal of the Mechanics and Physics of Solids*, Vol. 25, pp. 357-381, 1977.

[98] A. R. Ingraffea, "Theory of Crack Initiation and Propagation in Rock", *Fracture Mechanics of Rock*, Academic Press/Harcourt Brace Jonavich, pp.71-110, 1987.

[99] R. M. McMeeking, D. M. Parks, "On Criteria for J-Dominance of Crack Tip Fields in Large-Scale Yielding", ASTM STP 668, American Society for Testing and Materials, Philadelphia, pp. 175-194, 1979.

[100] MIL-HDBK-5G, *Metallic Materials and Elements for Aerospace Vehicle Structures*, Vol. 1, pp. 3-73, November, 1994.

[101] M. L. Gruber, C. J. Mazur, K. E. Wilkins, R. E. Worden, *Investigation of Fuselage Structure Subject to Widespread Fatigue Damage*, Federal Aviation Administration Report DTFA03-94-C-00065,pp. 12-13, October 1995.

[102] Irwin, G. R., "Onset of Fast Crack Propagation in High Strength Steel and Aluminum Alloys", *Sagamore Research Conference Proceedings*, Vol. 2, pp. 289-305, 1956.

[103] T. L. Anderson, Fracture Mechanics, Fundamentals and Applications, 2nd Edition, CRC Press, New York, pp. 41-43, 1994.